Topological phenomena and proximity-induced superconductivity in carbon nanotubes

DISSERTATION ZUR ERLANGUNG DES DOKTORGRADES
DER NATURWISSENSCHAFTEN (DR. RER. NAT.) DER FAKULTÄT FÜR PHYSIK
DER UNIVERSITÄT REGENSBURG

vorgelegt von

Lars Milz

aus Düsseldorf

im Jahr 2018

Promotionsgesuch eingereicht am: 20.06.2018

Die Arbeit wurde angeleitet von: Prof. Dr. Milena Grifoni

Prüfungsausschuss:
Vorsitzender: PD Dr. F. Bruckmann
1. Gutachter: Prof. Dr. M. Grifoni
2. Gutachter: Prof. Dr. C. Strunk
weiterer Prüfer: Prof. Dr. J. Fabian

Termin Promotionskolloquium: 07.12.2018

In liebevoller Erinnerung an Bella

„Can you hear me? It has been a glorious time to be alive doing research in theoretical physics. Our picture of the universe has changed a great deal in the last 50 years and I'm happy if I have made a small contribution. The fact that we humans who are ourselves mere collections of fundamental particles of nature have been able to come as close to an understanding of the laws governing us and our universe is a great triumph. I want to share my excitement and enthusiasm about this quest. So remember to look up at the stars and not down at your feet. Try to make sense of what you see and wonder about what makes the universe exist. Be curious. And however difficult life may seem, there is always something you can do and succeed at. It matters that you do not just give up. Thank you for listening.“

Stephen Hawking last words to the world (2018)

„This guy loves Majorana fermions! “

Simon Trebst about Alexei Kitaev (2017)

Teile dieser Dissertation wurden veröffentlicht:

Topology and zero energy edge states in carbon nanotubes with superconducting pairing,
W. Izumida, L. Milz, M. Marganska, and M. Grifoni,
Phys. Rev. B, **96**, 125414 (2017)

Majorana quasiparticles in semiconducting carbon nanotubes,
M. Marganska, L. Milz, W. Izumida, C. Strunk, and M. Grifoni,
Phys. Rev. B, **97**, 075141 (2018)

Transverse profile and 3D spin canting of a Majorana state in carbon nanotubes,
L. Milz, W. Izumida, M. Grifoni, M. Marganska,
Phys. Rev. B, **100**, 155417 (2019)

Contents

Danksagungen

Ich möchte mich bei Prof. Dr. Milena Grifoni für die Möglichkeit bedanken meine Doktorarbeit zu schreiben. Ich bin froh, die Chance gehabt zu haben an einem so interessanten Thema und in einer so tollen Gruppe zu arbeiten.

Ein weiterer großer Dank geht an Dr. Magdalena Marganska-Lyzniak für die Betreuung meiner Arbeit. Liebe Magda, ich habe die Zusammenarbeit mit dir die letzten fünf Jahre sehr genoßen. Mit dir die Übung für deiner Vorlesung *Topology in condensed matter physics* zu organisieren war sehr lehrreich und hat mir Spaß gemacht. Auch wenn wir uns Übungen ausgedacht haben, die wir selbst nicht lösen konnten.

Ebenfalls möchte ich mich bedanken bei Prof. Dr. Wataru Izumida. Er hat mein Verständnis vom Zusammenspiel von Topologie und Kohlenstoffnanoröhren auf ein neues Level gebracht.

Vielen Lieben Dank auch an meine Kollegen: Andreas Costa, Andrea Donarini, Tobias Frank, Maria Camarasa Gomez, Patrick Grössing, Petra Högl, Michael Kammermeier, Raphael Kozlovsky, Nico Leumer, Sebastian Pfaller, Sonja Predin, Benjamin Siegert, Sergey Smirnov, Matthias Stosiek, Davide Mantelli, Martin Wackerl, Heng Wang, Felix Weiner, Paul Wenk, Klaus Zollner und Allen die ich vergessen habe. Insbesondere möchte ich mich bei meinen Kollegen im Büro: Daniel Hernangomez Perez und Michael Niklas für die schöne Zeit bedanke. Weiter möchte ich mich bei Robert Hrdina, Sylvia Hrdina und Claudia Zange für die ganze Hilfe bedanken.

Auch ein Physiker hat mal Freizeit und daher danke ich meinen Freunden für die schöne Nicht-Physiker-Zeit mit euch. Bei Adrian und Basti für die ganzen Retro-Nerd Nächte mit sehr vielen Energiedrinks und LoL zocken.

Ein Dank geht auch an Dani, Domi, Jonas, Luzi und Phillip für die vielen schönen Abenden, die ich mit euch verbringen durfte. Weiter möchte ich mich bei Florian Geißler bedanken für die schöne Zeit auf Physikkonferenzen und außerhalb der Universität.

Ein lieben Dank geht an Chris und Steffi. Euer Sohn Ben ist wahrscheinlich das einzige Kind, dass ich kenne, welches Higgs-Feldtheorie total interessant findet. Ich hoffe noch auf viele weitere schöne Zeit mit euch.

Ein großer Dank geht an Bernhard, Kathi und Ulrike für eure ganze Unterstützung und das ihr mich sofort in eure Familie aufgenommen habt.

Besonders bedanke ich mich bei meiner kleinen Schwester Jana und meinen Eltern Johanna und Detlef Milz. Leider sage ich euch zu selten, wie toll ihr seid und wie froh ich bin euch zu haben. Daher denkt immer daran: Ohne euren Hilfe und Unterstützung wäre dies hier alles nicht möglich gewesen.

Zu guter letzt ein Dank an die Liebe meines Lebens: Felizia Merkau. Danke für alles! Ohne dich hätte ich es niemals geschafft!

Abstract

Over the past decade Majorana fermions have been of great interest in condensed matter physics. Under special conditions they arise as quasiparticles in superconductors, where they are zero energy eigenstates of the Bogoliubov-de Gennes Hamiltonian and of the particle-hole symmetry operator. Theoretically such quasiparticles were predicted to appear in the elusive one-dimensional p-wave superconductors; but it is also possible to engineer *s*-wave systems in such a way that they mimic p-wave superconductivity. In this thesis we deal with the description and analysis of topological superconductivity in carbon nanotubes coupled to an s-wave superconductor.

In the first part we introduce the concept of topology in the condensed matter context. Further, we discuss in a topologically nontrivial system the appearance of protected edge states, and we adress the so-called bulk-edge correspondence. Then, under the assumption of a short-ranged pairing potential, a mean-field Hamiltonian for the carbon nanotubes including curvature, spin-Âŋorbit coupling, valley mixing and a magnetic field is derived.

In the second part we analyse a minimal model for topological superconductivity in a carbon nanotube with time-reversal symmetry. We can relate the number of edge states in the superconducting finite length carbon nanotube to the corresponding topological invariant and also prove the bulk-edge correspondence. Next we turn to a setup where time-reversal symmetry is broken. In the presence of a perpendicular magnetic field and valley mixing the topological superconducting phase diagram of semiconducting carbon nanotubes is shown. In particular, regions in the magnetic field chemical potential plane possibly hosting localized Majorana modes are discussed. Finally, we show that the spatial profile of Majorana bound states can be derived analytically with good accuracy.

Introduction

The dynamics of many-body system can be understood by effective field theories describing the low-energy excitation of the system. Most systems are fermionic many-particle systems whose behavior is determined by a fermionic theory. Historically, fermionic effective field theories are well known due to the Landau-Fermi liquid theory and Landau theory of symmetry breaking. Both theories are also called the „Standard model“ of condensed matter theory [1, 2].

In the Landau-Fermi liquid theory, the low-energy excitations are tranformed to the excited states of non-interacting fermionic system [3, 4]. Formally, such low-energy excitations - the so-called quasiparticles - are described as non-interacting fermions with renormalized properties and the low-energy properties of the convectional metals, semiconductors, superconductors and superfluids are determined by them. For example phonons, plasmons and magnons are well known quasiparticles in solids [5]. But also excitation like spinons and holons in Tomonaga-Luttinger liquids[1] are quasiparticles in condensed matter systems [6].

The Landau theory of symmetry breaking defines a classification scheme of phases of matter and the description of phase transitions [7, 8]. By definition, a phase of matter is a specific configuration of a many-body system and a transition between two phases is determined by discontinuities in the model. A discontuinity occurs because both phases have different symmetries, i.e. a phase transition is simply a transition that changes the symmetry.

However, due to the discovery of the integer [9] and fractional quantum Hall effect [10] new kind of phases occur in condensed matter physics. In general, the transition of quantum Hall states can not be classified by symmetry breaking theory, but by a quantity that describes the topological properties of the states [11]. The reason is that in contrast to Landau's theory symmetry breaking, quantum Hall states have the same symmetries. The discovery of topological insulators was a breakthrough in this field, because topological insulators can be used for modern electronic circuits [12–14].

In 2016, D. J. Thouless and J. M. Kosterlitz won together with F. D. M. Haldane the Nobel Prize in physics for the description of topological effects in condensed matter theory. D. J. Thouless, J. M. Kosterlitz and independently W. L. Berezinskii discovered the so-called Berezinskii-Kostelitz-Thouless (BTK) transition [15, 16]. In a two-dimensional superconductors, the BTK transition is defined as a transition without spontaneous symmetry breaking in which vortices and anti-vortices are paired or not [2, 17]. Generally, topology consider the properties of topological spaces[2], i.e. spaces that remain invariant under continuous deformations. There are several of categories of topological spaces. A good review about topology concepts used in physics can be found in Refs. [18–20].

In this thesis we are interested in gapped phases of quantum matter that can be distinguished

[1] Tomonaga-Luttinger liquid is a system of interacting fermions in one-dimension.
[2] These topological spaces do not necessarily have to be geometrical objects.

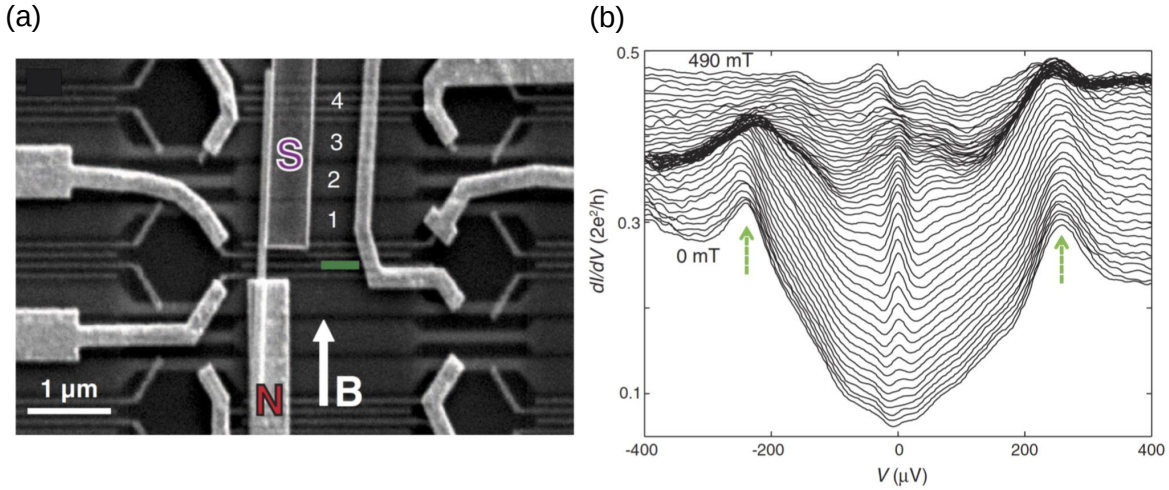

Figure 1: (a) The experimental setup where an InSb nanowire is connected by normal and superconducting contacts. (b) In the experiment the differential conductance $\frac{dI}{dV}$ is measured as a function of the bias voltage V and the magnetic field. A zero-bias peaks appears for magnetic field at 100 mT. One possible explanation of the zero-bias peak is the emergence of Majorana fermions. (Source: Ref. [21]).

topologically. These kind of phases are called topological phases and can not be classified by the Landau's symmetry breaking theory. Topological phases are characterized by a topological invariant in the bulk system. The transitions between them are called topological phase transitions. Thus, the BTK transition is a topological transition and the quantum Hall states are topological phases. From a topological point of view, two gapped states are equivalent if they can be adiabatically transformed without closing the energy gap and breaking the symmetries. Then it follows from the *bulk-edge correspondence* that gapless edge states emerge for a finite system [22].

In topological superconductors, these gapless edge states behave similar to a Majorana fermion, known from elementary particle physics [23]. E. Majorana predicted an elementary fermionic particle which is its own antiparticle, and suspected that neutrinos could be one of these fermions. Nowadays it is known that neutrinos are not Majorana fermions. In condensed matter context, edge states in a topological superconductors are called Majorana fermions, because it is no longer possible to distinguish between quasiparticle and hole. The similarity results from the particle-hole symmetry in superconducors and the fact that the corresponding quasiparticles are superpositions of electrons and holes. In general, Majorana fermions can be described by a second quantized operator γ with the property $\gamma^\dagger = \gamma$. Their existence has been predicted in various systems: p-wave superconductors [24], superfluid ^{3}He [1], topological insulator-superconductor hybrid systems [25], semiconducting nanowire - s-wave superconductor hybrid systems [26–29], quantum spin liquids [30] and also iron chains on s-wave superconductor [31].

In the following we will discuss mostly the nanowire proposals and their carbon nanotube analogs. Although the experiments are by now very advanced [32], a definite proof that

the reported signatures [21, 33–36] are really due to the topologically nontrivial Majorana bound states (MBS) is still missing. The first experimental setup has been realized in the Delft group of L. P. Kouwenhoven, see Fig. 1(a), where an InSb wire is contacted with superconducting and normal metal electrodes. The existence of the Majorana bound state is probed by measuring the tunneling current I in dependence of the voltage bias V and an external magnetic field along the wire. A zero-bias peak emerging at a finite magnetic field is a hint of the possible existence of a Majorana bound state in the experiment see Fig. 1(b).

Majorana bound states have other unusual properties which are important for future electronics in quantum computing technology. In two-dimensional systems it can be shown that they are non-abelian anyons [37]. Anyons are quasiparticles whose many-body wavefunction acquires an arbitrary phase under exchange of two anyons [38]. While the nature of topological states of matter is interesting in its own right, the observation that systems with non-abelian anyons can be used to construct a quantum computer that is naturally immune to errors has focused much more attention in this field [39]. Basically, in a topological quantum computation anyons are used for encoding and manipulating information non-locally which protects them from the influence of external perturbations [38].

Since the number of transistors in electronic circuits doubles every two years according to Moore's law, further miniaturization will sooner or later encounter technical and physical limits. When reaching the scale of some nanometers, the size of molecules, quantum processes become important. Such sizes have already been reached by now. Additionally, the local heat production can impair the device operations and requires more effective cooling techniques. Therefore, the industry researches a number of alternative device technologies where carbon based electronic elements play a major role [40]. A combination of carbon based electronic elements and quantum computing via non-abelian anyons might be a big revolution in future electronics.

Outline

This thesis is devoted to a description and analysis of topological superconductivity in proximitized carbon nanotubes. We discuss the topological origin of zero energy bound states in the two cases with and without time-reversal symmetry.

In the first chapter we will introduce topological concepts in the context of condensed matter physics. We discuss the question why we must use topological tools for certain state of matters and introduce the concept of geometric phases. Then, we show the correlations between the topological invariant, describing topological properties of the system, and the system's symmetries. With this we are able to define topological invariants for specific systems.

The second chapter is dedicated to Majorana bound states in topological superconductors. We prove the existence of these states in a one-dimensional p-wave superconductor, the Ki-

taev chain, and their emergence in nanowires with Rashba spin-orbit coupling and a parallel magnetic field in contact with an s-wave superconductor. At the end we discuss experimental realizations.

In the third chapter we describe how the electronic spectra of carbon nanotubes are obtained based on the dispersion relation of graphene, including curvature effects, spin-orbit coupling and the finite size of carbon nanotubes. Then, we investigate the effects of applied magnetic fields and valley mixing in the energy spectrum of carbon nanotubes. Furthermore, we introduce a mean-field model of the superconducting correlations in carbon nanotubes.

In chapter 4 we investigate a minimal model for topological superconductivity in carbon nanotubes. We discuss the emergence of edges states in the presence of time-reversal symmetry. We notice that the formation of edge states depends not only on the chemical potential and the pairing potentials, but also on the chirality and the boundary shape of the nanotubes since they strongly affect the coupling of the two valleys. We show that the edge states emerge in the parameter region of nontrivial topological invariant. Finally, a 1D continuum model is introduced which allows us to obtain analytically the condition for the emergence of the edges states. By comparing it with the condition for nontrivial winding number, we find that these two conditions are identical, hence proving the bulk-edge correspondence.

We dedicate chapter 5 to the description of edge states in superconducting carbon nanotubes in the presence of a magnetic field. The starting point of our investigation is a microscopic tight-binding model for the carbon nanotube lattice, with external influences such as the substrate potential, superconducting pairings, magnetic field (perpendicular and axial) and disorder added in real space. The emergence of localized zero energy states above a critical magnetic field strength is demonstrated in the real space. Using the knowledge of the components of the wave functions, we prove the Majorana nature of the localized states. The effective model from chapter 3 allows us to gain the knowledge of the symmetries and topological invariants. We construct the topological phase diagram and examine the stability of Majorana modes in the non-trivial phase.

The final chapter is devoted to the full 3D spatial profile of Majorana wave function in a carbon nanotube - superconductor hybrid system. We show that it can be derived analytically with great accuracy compared to the numerical results. We can also extract from it some experimentally relevant information like the spin canting angle of a Majorana bound state, which has been shown [41] to influence the electronic transport through a Majorana device.

1. Topology in condensed matter physics

In this chapter we introduce topological conecpts in condensed matter physics. We start with a review of Berry's geometric phase and show the relations between symmetries of the systems and the possibility of topological properties in quantum systems. In the end we define the topological invariants which characterize topological properties. The results of this chapter have been published in Phys. Rev. B **96**, 125414 (2017) and Phys. Rev. B **97**, 075141 (2018).

1.1. Geometric phase

Sir M. Berry introduced a geometric phase, the so-called Berry phase, and explained the connection to classical electrodynamics [42]. He recognized that the phase factor is related to a gauge potential and depends highly on the path in the parameter space. The geometric phase is derived by the assumption of adiabtic transport and given by an abelian factor for non-degenerate eigenstates. However, the result of M. Berry can be generalized for degenerate eigenstates [43] and for non-adiabatic transport [44]. We discuss the formal derivation of the geometric phase done by Sir M. Berry for the case of a adiabatic abelian geometric phase. Fore a more detailed account of geometric phases see Ref. [45].

1.1.1. Berry phase, connection and curvature

For the derivation of the Berry phase we consider a Hamiltonian $\mathcal{H} = \mathcal{H}(\mathbf{R})$ which can be characterized by a vector of parameter $\mathbf{R} = (R_1, R_2, \dots)$. This vector depends on the time $t \in [0; T]$ and moves adiabatically along a path $\mathcal{C}$. Formally, the eigenstates $|n(\mathbf{R})\rangle$ can not be fully determined by the equation of motion $\mathcal{H}(\mathbf{R})|n(\mathbf{R})\rangle = E_n(\mathbf{R})|n(\mathbf{R})\rangle$ since the $U(1)$ gauge freedom of the eigenstate. We will assume that the phase of the eigenstate is well-defined and single-valued. Due to the adiabatic theorem [45], we must determine only the phase factor of the eigenstate which is described by the time-dependent Schrödinger equation

$$i\hbar\frac{d}{dt}|\Psi_n(t)\rangle = \mathcal{H}(\mathbf{R}(t))|\Psi_n(t)\rangle,$$

where the solution $|\Psi_n(t)\rangle$ is given by

$$|\Psi_n(t)\rangle = e^{i\gamma_n(t)}\exp\left(-\frac{i}{\hbar}\int_0^t dt' E_n\left(\mathbf{R}\left(t'\right)\right)\right)|n(\mathbf{R}(t))\rangle. \tag{1.1}$$

The energy-dependent phase is the well-known dynamical phase. The second phase is defined as $\gamma_n(t) = \int_0^t d\mathbf{R}\cdot\mathcal{A}_n(\mathbf{R})$, where the vector-valued function $\mathcal{A}_n(\mathbf{R})$ is the corresponding *Berry connection*. Formally, the Berry connection is given by

$$\mathcal{A}_n(\mathbf{R}) = i \langle n(\mathbf{R}(t))| \frac{\partial}{\partial \mathbf{R}} |n(\mathbf{R}(t))\rangle , \tag{1.2}$$

and depends on the gauge. A gauge transformation yields

$$|n(\mathbf{R}(t))\rangle \to \left|n'(\mathbf{R}(t))\right\rangle = e^{i\zeta_n(\mathbf{R})} |n(\mathbf{R}(t))\rangle ,$$

the Berry connection transforms to

$$\mathcal{A}_{n'}(\mathbf{R}) = \mathcal{A}_n(\mathbf{R}) - \frac{\partial}{\partial \mathbf{R}} \zeta_n(\mathbf{R}) .$$

Thus, the second phase $\gamma_n(t)$ will also transform $\gamma_n(T) \to \gamma_n(T) + \zeta_n(\mathbf{R}(0)) - \zeta_n(\mathbf{R}(T))$. In the case of a closed path, i.e. $\mathbf{R}(T) = \mathbf{R}(0)$, it follows $\zeta_n(\mathbf{R}(0)) - \zeta_n(\mathbf{R}(T)) = 2\pi N$ with $N \in \mathbb{Z}$, because $e^{i\zeta_n(\mathbf{R})}$ is a single-valuedness function. Consequently, the phase angle $\gamma_n = \gamma_n(T) = \oint_{\mathcal{C}} d\mathbf{R} \cdot \mathcal{A}_n(\mathbf{R})$, known as the *Berry phase*, is a gauge-invariant quantity and can be measured in experiments [45].

In analogy to electrodynamics, the Berry connection can be interpreted as a magnetic flux. Therefore, it is possible to define a gauge-invariant field strength tensor $\mathcal{F}_n^{\mu\nu}$ which is defined as

$$\mathcal{F}_n^{\mu\nu}(\mathbf{R}) = \nabla_\mu \mathcal{A}_n^\nu(\mathbf{R}) - \nabla_\nu \mathcal{A}_n^\mu(\mathbf{R}) , \tag{1.3}$$

where $\nabla_\mu = \frac{\partial}{\partial R_\mu}$. The field stength tensor $\mathcal{F}_n^{\mu\nu}$ is known as the *Berry curvature tensor*. For a three-dimensional parameter space the Berry curvature and Berry connection are related by $\mathcal{F}_n = \nabla \times \mathcal{A}_n(\mathbf{R})$ with $\mathcal{F}_n^{\mu\nu}(\mathbf{R}) = \epsilon_{\mu\nu\lambda} \mathcal{F}_n^\lambda(\mathbf{R})$, where $\epsilon_{\mu\nu\lambda}$ is the antisymmetric Levi-Civita tensor. Then, due to Stokes theorem the Berry phase can be expressed in terms of the Berry curvature. Explicity, the relation is given by

$$\gamma_n = \int_{S(\mathcal{C})} d\mathbf{S} \cdot \mathcal{F}_n(\mathbf{R}) , \tag{1.4}$$

with $S(\mathcal{C})$ being a surface bounded by the closed path $\mathcal{C}$. In contrast to the Berry phase, which is defined on a closed path, the Berry curvature depends on the local geoemetry of the parameter space given by the vector $\mathbf{R}$. For degenerate eigenstates, the Berry connection is defined as a matrix of dimension equal to the degeneracy.

1.1.2. The Berry phase in Bloch bands

Now we want to discuss a particular case of Berry phase physics related to solids. In several experiments the influence of the berry phase was measured. For example, in magneto-oscillatory effects [46, 47] or in one-dimensional systems, where the geometric phase is called *Zak phase* [48], in which the influence can be measured in adiabatic transport [49, 50] and the electric polarization [51, 52]. As discussed in the introduction, the physical behavior in solids can be understood by a non-interacting Hamiltonian $\mathcal{H} = \frac{p^2}{2m} + V(\mathbf{r})$. Due to the periodic lattice potential $V(\mathbf{r}) = V(\mathbf{r} + \mathbf{a})$, the electronic states fulfill the condition $\Psi_{n\mathbf{q}}(\mathbf{r} + \mathbf{a}) = e^{i\mathbf{q}\cdot\mathbf{a}}\Psi_{n\mathbf{q}}(\mathbf{r})$, where $\mathbf{a}$ is the Bravais lattice vector of the corresponding lattice, n the band index and $\hbar\mathbf{q}$ is the crystal momentum belonging to the first Brillouin zone. Bloch's theorem implies that the wave function can be written as $u_{n\mathbf{q}}(\mathbf{r}) = e^{-i\mathbf{q}\cdot\mathbf{r}}\Psi_{n\mathbf{q}}(\mathbf{r})$ wich satisfies the periodic boundary condition $u_{n\mathbf{q}}(\mathbf{r}) = u_{n\mathbf{q}}(\mathbf{r} + \mathbf{a})$. In this new basis, the Hamiltonian becomes $\mathcal{H} \to \mathcal{H}(\mathbf{q}) = e^{-i\mathbf{q}\cdot\mathbf{r}}\mathcal{H}e^{i\mathbf{q}\cdot\mathbf{r}}$ where

$$\mathcal{H}(\mathbf{q}) = \frac{(\mathbf{p} + \hbar\mathbf{q})^2}{2m} + V(\mathbf{r}). \tag{1.5}$$

Then the connection to the Berry phase is quite simple, since the parameter space is the first Brillouin zone, $\mathcal{H}(\mathbf{R}) \to \mathcal{H}(\mathbf{q})$ with $\mathbf{R} \to \mathbf{q}$ and $|n(\mathbf{R})\rangle \to |u_n(\mathbf{q})\rangle$. Analogously, we can define also the Berry connection $\mathcal{A}_n(\mathbf{q}) = i\langle u_n(\mathbf{q})|\nabla_{\mathbf{q}}|u_n(\mathbf{q})\rangle$ and Berry curvature $\mathcal{F}_n(\mathbf{q}) = \nabla_{\mathbf{q}} \times \mathcal{A}_n(\mathbf{q})$. Both will be used later for the definition of the topological invariants.

1.2. Symmetries and symmetry classes

Until the 1980's, only convectional phases are known which are described by Landau's symmetry breaking theory. Due to the discovery of the quantum Hall effect and later topological insulators, a new kind of phase, the topological phase, is introduced in the condensed matter context. In general, a topological phase of matter is defined as a state of a quantum system in which the bulk is described by a topological invariant and edge states emerges at the edges for a finite system. In order to understand the physics of topological phases we need to address the connection between symmetries and topological invariants.

There exist a zoo of topological phases which are characterized by different topological invariants. The classification of topological phases can not be described by Landau's symmetry breaking theory because topological different phases of a system has the same symmetries. The topological properties of a system is classified by symmetry classes which depends on the dimensionality and symmetries of the system. Here in this thesis we will introduce the simplest classification scheme for gapped systems, like insulators and superconductors, with a mean-field theory. Formally, a system is described by the following Hamiltonian

$$\mathcal{H} = \sum_{i,j} \Psi_i^\dagger H_{ij} \Psi_j, \tag{1.6}$$

where H_{ij} is the matrix element of the $N \times N$ Hamiltonian matrix, $\Psi_i^\dagger$ is the creation operator, Ψ_i the annihilation operator and i the quantum number of the particle. Usually, the quantum number i includes the lattice position of the particle and the corresponding spin quantum numbers. For fermionic operators these operators obey the anticommutation relations

$$\{\Psi_i, \Psi_j^\dagger\} = \delta_{ij} \text{ and } \{\Psi_i, \Psi_j\} = 0. \tag{1.7}$$

In general, the system has certain symmetries, for example lattice symmetries, which can be grouped together in the group G. Then, for an element of the symmetry group $g \in G$ exists a linear representation $U = D(g)$, the symmetry operator, with $U\mathcal{H}U^{-1} = \mathcal{H}$ or $[U, \mathcal{H}] = 0$. Due to the Wigner theorem [53], symmetries can be only realized either by a unitary or antiunitary symmetry operator. In the case of an unitary symmetry operators, the Hamiltonian can be transformed into a block-diagonal form, where the blocks are labled as $H^{(\lambda)}$ and λ is a certain irreducible representation of the corresponding symmetry group G [54, 55]. One well-known example is the lattic Hamiltonian for a solid. Due to the discrete translation symmetry of the lattice, the Hamiltonian can be brought into a block-diagonal form, where a block is labeled by the crystal momentum $\mathbf{k}$.

For the classification scheme, we consider the block Hamiltonians $H^{(\lambda)}$ and the corresponding behavior under anti-unitary symmetries. Then, the Hamiltonians can be classified depending on the absence or presence of antiunitary symmetries, which we will introduce next, and the dimensionality of the system. Then, the Hamiltonian is an element of the corresponding symmetry class. The term symmetry class was introduced in the random matrix theory and we will describe the connection to the topological properties and the symmetry classes later in this thesis.

The classification scheme describes the topological properties of an generalized system. Even in solids with a particular lattice structures, topological phases have a much more complicated nature [56–60]. Such systems are so-called *topological crystalline insulators and superconductors* and can be also classified [61–63]. Furthermore We will show later in this thesis that the superconducting carbon nanotubes are an example of such a topological crystalline superconductor.

1.2.1. Time-reversal symmetry

The first important symmetry for the topological classification of quantum matter is time-reversal symmetry. By definition, the time-reversal transformation reverse the time $\mathcal{T}$: $t \to -t$

and commutes with the Hammiltonian $[\mathcal{H}, \mathcal{T}] = 0$. Moreover, the time-reversal symmetry is an antiunitary symmetry which implies $\mathcal{T} = U_{\mathcal{T}} K$ with the property $U_{\mathcal{T}}^{\dagger} = U_{\mathcal{T}}^{-1}$, $U_{\mathcal{T}}$ is a unitary matrix and K the complex conjugation operator. In general, every Hamiltonian is invariant when the time-reversal symmetry is applied twice. This implies $\mathcal{T}^2 = U_{\mathcal{T}} K U_{\mathcal{T}} K = U_{\mathcal{T}} U_{\mathcal{T}}^{\star} = e^{i\phi}\mathbb{1}$ and $U_{\mathcal{T}} = e^{i\phi} U_{\mathcal{T}}^{T} = e^{i\phi}\left(e^{i\phi} U_{\mathcal{T}}\right) = e^{2i\phi} U_{\mathcal{T}} \Rightarrow e^{i\phi} = \pm 1$ by using $U_{\mathcal{T}}^{\star} = e^{i\phi} U_{\mathcal{T}}^{\dagger} \Rightarrow U_{\mathcal{T}}^{T} = e^{i\phi} U_{\mathcal{T}}$. Thus, the time-reversal symmetry squares to $\mathcal{T}^2 = \pm 1$ where for particles with integer spin it holds $\mathcal{T}^2 = 1$ and $\mathcal{T}^2 = -1$ for half-integer spin.

For a Hamiltonian with well-defined momentum $\mathbf{k}$, time-reversal invariance is given by

$$\mathcal{T}\mathcal{H}(\mathbf{k})\mathcal{T}^{-1} = U_{\mathcal{T}}\mathcal{H}^{\star}(\mathbf{k})U_{\mathcal{T}}^{-1} = \mathcal{H}(-\mathbf{k}). \tag{1.8}$$

The eigenstate $\Psi(\mathbf{k})$ of the Hamiltonian $\mathcal{H}(\mathbf{k})$ is given by $\mathcal{H}(\mathbf{k})\Psi(\mathbf{k}) = E(\mathbf{k})\Psi(\mathbf{k})$ with the energy $E(\mathbf{k})$. In the case of time-reversal invariance, $\mathcal{T}\Psi(\mathbf{k})$ is an eigenstate of $\mathcal{H}(-\mathbf{k})$ with the energy $E(-\mathbf{k})$. Due to Kramers theorem, which is important for topological insulators, every eigenstate for half-integer spin systems is doubly degenerate [64].

1.2.2. Particle-hole symmetry

In the case of superconducting system the mean-field dynamics is described within the Bogoliubov - de Gennes (BdG) formalism, which we will discuss later in more detail. The BdG Hamiltonian, like all BdG Hamiltonians, is by construction invariant under a particle-hole operation. In general, the particle-hole operation maps the positive energy solutions onto their negative energy solutions. The BdG Hamiltonians with translational invariance which we will consider in this thesis are of the form

$$\mathcal{H}_{\mathrm{BdG}}(\mathbf{k}) = \begin{pmatrix} H_0(\mathbf{k}) & \Delta \\ -\Delta^{\star} & -H_0(-\mathbf{k}) \end{pmatrix}, \tag{1.9}$$

where $H_0(\mathbf{k})$ is the Bloch Hamiltonian and $\Delta = -\Delta^T$ is the pairing matrix. Like for the time-reversal symmetry also particle-hole symmetry is an antiunitary symmetry and can be represented by $\mathcal{P} = U_P \mathcal{K}$ with $\mathcal{P}^2 = \pm 1$. Particle-hole symmetry leads to the condition

$$\mathcal{P}\mathcal{H}(\mathbf{k})\mathcal{P}^{-1} = U_P\mathcal{H}^{\star}(\mathbf{k})U_P^{-1} = -\mathcal{H}(-\mathbf{k}). \tag{1.10}$$

which implies that the Hamiltonian anticommutes with $\mathcal{P}$ and the particle-hole symmetry operator is given by $\mathcal{P} = \tau_x \mathcal{K}$, where $\tau_{x,y,z}$ are the Pauli matrices. We can transform the BdG Hamiltonian in the so-called *Majorana basis*, i.e. the basis of eigenstates of $\mathcal{P}$, obtained by a transformation U_M, $\mathcal{H}_M = U_M \mathcal{H} U_M^{-1}$ [22]. The unitary matrix U_M is given by

$$U_M = \frac{1}{\sqrt{2}} \begin{pmatrix} 1 & 1 \\ -i & i \end{pmatrix}. \tag{1.11}$$

The Majorana basis is important later for the definition of topological invariants. The particle-hole symmetry operator transforms as $U_M \mathcal{P} U_M^{-1} = \mathbb{1}\mathcal{K}$ and the BdG Hamiltonian can be expressed as

$$iX(\mathbf{k}) = \frac{1}{2} \begin{pmatrix} R_-(\mathbf{k}) + S_- & i(R_+(\mathbf{k}) - S_+) \\ -i(R_+(\mathbf{k}) + S_+) & R_-(\mathbf{k}) - S_- \end{pmatrix}, \tag{1.12}$$

where $R_\pm(\mathbf{k}) = H_0(\mathbf{k}) \pm H_0(-\mathbf{k}) = \pm R_\pm(-\mathbf{k})$ and $S_\pm = \Delta \pm \Delta^\star = -S_\pm^T$. Furthermore, it is possible to define a gauge transformation such that Δ is a real matrix. Then it follows that $S_+ = 2\Delta$ and $S_- = 0$.

1.2.3. Chiral symmetry

With both the particle-hole $\mathcal{P}$ and the time-reversal symmetries $\mathcal{T}$, the Hamiltonian is also invariant under a product of both, i.e. $C = \mathcal{T} \cdot \mathcal{P} = U_\mathcal{T} U_P^\star$. In contrast to previous discussed symmetries, the symmetry C, the so-called chiral symmetry or sometimes sublattice symmetry, is given by an unitary symmetry operator and anticommutes with the corresponding Hamiltonian $\{H, C\} = 0$ with $C^2 = 1$. The absence of one of the symmetry leads to the absence of chiral symmetry. However, if both symmetry are absent then chiral symmetry can be either present or abesent.

In general, the chiral symmetry, connecting positive and negative energy solutions at the same momentum $\mathbf{k}$ which can be expressed in the following condition

$$C\mathcal{H}(\mathbf{k})C^{-1} = -\mathcal{H}(\mathbf{k}). \tag{1.13}$$

For the eigenstate Ψ satisfying $\mathcal{H}\Psi = E\Psi$ there exists a paired state $C\Psi$ with the energy $-E$, that is, $\mathcal{H}C\Psi = -EC\Psi$. In this thesis we will have BdG Hamiltonians of the form

$$\mathcal{H} = \begin{pmatrix} H_0(\mathbf{k}) & \Delta_C \\ \Delta_C & -H_0(\mathbf{k}) \end{pmatrix} = H_0(\mathbf{k})\tau_z + \Delta_C \tau_x, \tag{1.14}$$

where $H_0(\mathbf{k})$ is the Bloch Hamiltonian of the system with the property that there exist a transformation $\tilde{U}$ with $\tilde{U} H_0(\mathbf{k}) \tilde{U}^{-1} = H_0(-\mathbf{k})$, $\Delta_C = \tilde{U}\Delta\tilde{U}^{-1}$ is the real pairing matrix and the chiral symmetry operator is given by $C = \tau_y$. In such a case we can use the chiral symmetry to determine the spectrum of the system. The unitary transformation

$$U_C = \frac{1}{2}\begin{pmatrix} 1+i & 1+i \\ -1+i & 1-i \end{pmatrix}, \tag{1.15}$$

rotates the Pauli matrices for the particle-hole basis as $U_C^\dagger \tau_x U_C = \tau_y$, $U_C^\dagger \tau_y U_C = \tau_z$ and $U_C^\dagger \tau_z U_C = \tau_x$. In this basis the chiral symmetry operator $\tilde{C} = \tau_z$ is diagonal and the Hamiltonian is given by

$$\mathcal{H}_C(\mathbf{k}) = \begin{pmatrix} 0 & D(\mathbf{k}) \\ D^\dagger(\mathbf{k}) & 0 \end{pmatrix}, \tag{1.16}$$

where $D(\mathbf{k}) = H(\mathbf{k}) - i\Delta_C$ and we call this basis the *chiral basis*. Since $\mathcal{H}_C(\mathbf{k})$ has a block-off diagonal form, $\mathcal{H}_C^2(\mathbf{k})$ is block-diagonal. In order to obtain the energy spectrum we write down the BdG equation in chiral basis

$$\mathcal{H}_C(\mathbf{k})\Psi(\mathbf{k}) = \begin{pmatrix} 0 & D(\mathbf{k}) \\ D^\dagger(\mathbf{k}) & 0 \end{pmatrix}\begin{pmatrix} \chi_n^\pm(\mathbf{k}) \\ \eta_n^\pm(\mathbf{k}) \end{pmatrix} = \pm E_n(\mathbf{k})\begin{pmatrix} \chi_n^\pm(\mathbf{k}) \\ \eta_n^\pm(\mathbf{k}) \end{pmatrix}, \tag{1.17}$$

where $n \in \{1, \cdots, N\}$ is the quantum number, like band index or spin index. The energies are positive $E_n(\mathbf{k}) > 0\ \forall n$. Multiplying the equation from the left by $\mathcal{H}_C(\mathbf{k})$ yields

$$\mathcal{H}_C^2(\mathbf{k})\Psi(\mathbf{k}) = \begin{pmatrix} D(\mathbf{k})D^\dagger(\mathbf{k}) & 0 \\ 0 & D^\dagger(\mathbf{k})D(\mathbf{k}) \end{pmatrix}\begin{pmatrix} \chi_n^\pm(\mathbf{k}) \\ \eta_n^\pm(\mathbf{k}) \end{pmatrix} = E_n^2(\mathbf{k})\begin{pmatrix} \chi_n^\pm(\mathbf{k}) \\ \eta_n^\pm(\mathbf{k}) \end{pmatrix}, \tag{1.18}$$

which follows from the block-diagonal form of the chiral symmetry. Thus, the eigenvalue problem can be reduced to solving the equation

$$\det\left(\mathcal{H}_C^2(\mathbf{k}) - E^2\mathbb{1}\right) = \det\left(D(\mathbf{k})D^\dagger(\mathbf{k}) - E^2\mathbb{1}\right) = \det\left(D^\dagger(\mathbf{k})D(\mathbf{k}) - E^2\mathbb{1}\right) = 0.$$

Thus, the energy spectrum can be easily determined for systems with chiral symmetry. We will use this property later for the energy spectrum of superconducting carbon nanotubes.

1.2.4. Symmetry classes

Originally, E. Wigner introduced random matrix theory for the description of nuclear systems [65, 66]. Later, random matrix theory was used to describe disordered systems in the context of condensed matter physics. In general, random matrix theory can be used to determine universal properties for different systems with the same symmetries. Formally, Hamiltonians

Classes	Cartan label	$\mathcal{T}^2$	$\mathcal{P}^2$	C^2
Standard (Wigner-Dyson) classes	A (unitary)	0	0	0
	AI (orthogonal)	+1	0	0
	AII (symplectic)	-1	0	0
Chiral classes	AIII (chiral unitary)	0	0	1
	BDI (chiral orthogonal)	+1	+1	1
	CII (chiral symplectic)	-1	-1	1
BdG classes	D	0	+1	0
	C	0	-1	0
	DIII	-1	+1	1
	CI	+1	-1	1

Table 1: The three chategories of the ten ranom matrix ensembles labled with the Cartan label. The ten ensembles can be characterized by the behavior of time-reversal $\mathcal{T}$, particle-hole $\mathcal{P}$ and chiral C symmetries.

are assumed as random matrices. Therefore, random matrix theory is a good starting point of a classification of physical systems in mathematical physics.

At the beginning of random matrix theory, only one ensemble of random matrices was known. Afterwards, F. Dyson generalized the idea of E. Wigner and introduced three ensembles by studying the behavior of random matrices under time reversal, where he demonstrated that the irreducible blocks are either unitary, orthogonal or symplectic matrices in dependence of the transformation which diagonalizes the matrix [67]. Due to chiral symmetry in quantum chromodynamics, three ensembles were added [68, 69] and later for systems with particle-hole symmetry, like superconductors, the final four ensembles were introduced [70]. Thus, the ensembles can be categoriezed in three groups as shown in Tab. 1. In total, there are ten different combinations of symmetries, see Tabel 1, and the behavior of the corresponding symmetry operators, discussed in the chapters of the corresponding symmetries. The labels of the ten ensembles are introduced by M. Zirnbauer [71]. He recognized the relation of the random matrix ensembles and so-called symmetric spaces by proving that the corresponding time-evolution operator $e^{it\mathcal{H}}$ with the Hamiltonian $\mathcal{H}$ is an element of the symmetric space. The symmetric spaces are characterized by E. Cartan and labeled by the *Cartan label* [72, 73]. The result of E. Cartan is listed in Tab. 2 in the last column with the corresponding Cartan labels in the first column. In the context of the topological classification, the ten ensembles are also called symmetry classes and the result of the classification is called the *tenfold way*.

We will show the relation by two simple examples. Due to Stone's theorem the time-evolution operator $U_t = e^{-it\mathcal{H}} \in U(N)$ a well-defined quantity $\forall t \in \mathbb{R}$, where the $N \times N$ matrix is the Hamiltonian $\mathcal{H}$ of the system [74]. The group $U(N)$ is a Lie group and thus the Hamiltonian must be an element of the corresponding Lie algebra $\mathcal{H} \in \mathfrak{u}(N)$. The first example is a system without symmetries. Then, the Hamiltonian is a Hermitian matrix which implies $e^{-it\mathcal{H}} \in U(N)$. From Tab. 2 we see that this space is labled as A.

The second example is a system with time-reversal symmetry where $\mathcal{T}^2 = 1$. For such systems, the corresponding Hamiltonian can be brought into a real symmetric form. By definition, a

Cartan label	$\mathcal{T}^2$	$\mathcal{P}^2$	C^2	Time-evolution operator $e^{it\mathcal{H}}$
A	0	0	0	$U(N)$
AI	+1	0	0	$U(N)/O(N)$
AII	-1	0	0	$U(2N)/Sp(2N)$
AIII	0	0	1	$U(N+M)/U(N)\times U(M)$
BDI	+1	+1	1	$SO(N+M)/SO(N)\times SO(M)$
CII	-1	-1	1	$Sp(N)/Sp(2N)\times Sp(2M)$
D	0	+1	0	$O(N)$
C	0	-1	0	$Sp(2N)$
DIII	-1	+1	1	$O(2N)/U(N)$
CI	+1	-1	1	$Sp(2N)/U(N)$

Table 2: The relation of the ten random matrix ensembles and the corresponding spaces for the time-evolution operators.

general hemitian matrix $\tilde{\mathcal{H}}$ can be decomposed into a symmetric and antrisymmetric part $\tilde{\mathcal{H}} = \frac{1}{2}\left(\tilde{\mathcal{H}} + \tilde{\mathcal{H}}^T\right) + \frac{1}{2}\left(\tilde{\mathcal{H}} - \tilde{\mathcal{H}}^T\right) = \tilde{\mathcal{H}}_S + \tilde{\mathcal{H}}_A$ where $\tilde{\mathcal{H}}_S = \tilde{\mathcal{H}} - \tilde{\mathcal{H}}_A$ with $\tilde{\mathcal{H}}_A^T = -\tilde{\mathcal{H}}_A$. Since $e^{it\tilde{\mathcal{H}}} \in U(N)$ it follows that $e^{it\tilde{\mathcal{H}}_A} \in O(N)$

$$e^{it\tilde{\mathcal{H}}_A}\left(e^{it\tilde{\mathcal{H}}_A}\right)^T = e^{it\tilde{\mathcal{H}}_A}e^{it\tilde{\mathcal{H}}_A^T} = e^{it\tilde{\mathcal{H}}_A}e^{-it\tilde{\mathcal{H}}_A} = 1.$$

Thzs, the time-evolution operator is given by $e^{it\tilde{\mathcal{H}}_S} \in U(N)/O(N)$ which corresponds to the Cartan label AI.

1.2.5. Classification of topological insulators and superconductors

Non-interacting gapped systems were topologically classified using different methods. One method is to use the bulk-edge correspondence for the classification [22, 75], using the presence of gapless edge states at the interface of two different phases. This method can be generalized for fermionic disordered systems using an effective low-energy field theory, the so-called *nonlinear σ model*. Originally, the term nonlinear σ model is introduced in the context of high-energy physics by M. Gell-Mann and M. Lévy. Later, F. Wegner derived nonlinear σ models[3] for disordered systems [77], where the presence of topological gapless edge states implies further terms to the nonlinear σ model which evades Anderson localization [78] and can be viewed as a physical proof of the bulk-edge correspondence [79]. The result for the topological classification in dependence of the spatial dimension and symmetry class is shown in Tab. 3. For differentiation between different topological ground states we can use topological invariants, which can be expressed in terms of the Berry connection or curvature.

[3] There exists a remarkable correspondence between random matrix theory, a phenomenological theory for disordered systems, and the nonlinear σ model [76].

Cartan label	$d=1$	$d=2$	$d=3$
A	0	$\mathbb{Z}$	0
AI	0	0	0
AII	0	$\mathbb{Z}_2$	$\mathbb{Z}_2$
AIII	$\mathbb{Z}$	0	$\mathbb{Z}$
BDI	$\mathbb{Z}$	0	0
CII	$\mathbb{Z}$	0	$\mathbb{Z}_2$
D	$\mathbb{Z}_2$	$\mathbb{Z}$	0
C	0	$\mathbb{Z}$	0
DIII	$\mathbb{Z}_2$	$\mathbb{Z}_2$	$\mathbb{Z}$
CI	0	0	$\mathbb{Z}$

Table 3: The result of the topological classification of the systems in dependence of the spatial dimensionality. Topological non-trivial systems can be characterized by an $\mathbb{Z}$ or a $\mathbb{Z}_2$ topological invariant, respectively.

1.3. Topological invariants

For the definition of topological invariants, insulators and superconductors in the absence of disorder are considered, which implies a translational invariance. B. Simon noted that non-interacting gapped systems can be mathematically described as vector bundles and the Berry connection is the connection of a vector bundle and the Berry phase is equivalent to the corresponding holonomy [39, 45, 80]. Vector bundles can be classified by the so-called characteristic classes. With the characteristic classes it is possible to define topological invariants in terms of Berry connection and curvature for explicit calculations [18]. There are two important characteristic classes for the classification of physical systems. The first one is the so-called Chern class and the second one is the Chern-Simons class. In general, the Chern number is defined for systems with translational invariance in terms of the Berry curvature $\mathcal{F}$ of the system in the following way

$$\mathrm{Ch}_n = \frac{1}{n!}\left(\frac{i}{2\pi}\right)^2 \int_{\mathcal{C}} \mathrm{Tr}\left(\mathcal{F}^n\right),$$

where $n = \frac{d}{2}$ and $\mathcal{C}$ is the parameter space manifold. The Chern number is only defined for even-dimensional parameter space and without chiral symmetry. Therefore, the topological invariant coming from the Chern class is not the invariant which we need for describing the topological properties of the system studied in this thesis, a carbon nanotube. The fundamental topological invariant in 1D is Zak's phase [48] in one band carrying a generic index n,

$$\gamma_n = \frac{i}{2\pi}\int_{\mathrm{BZ}} dk\ \mathcal{A}_n\left(k\right), \tag{1.19}$$

where $\mathcal{A}_n\left(k\right)$ is the Berry connection in band n, $\mathcal{A}_n\left(k\right) = \langle\Psi_n\left(k\right)|\partial_k|\Psi_n\left(k\right)\rangle$, and $|\Psi_n\left(k\right)\rangle$ is

the eigenfunction of a 1D bulk Hamiltonian for eigenvalue E_n. We discussed that the Berry connection is gauge dependent quantity, so is Zak's phase, and a gauge transformation changes γ_n only by an integer. The more frequently used invariant is therefore $W = \exp(2\pi i \sum_l \gamma_l)$, where l are the indices of filled bands, which is gauge independent, although in general not quantized. The presence of discrete symmetries restricts the values which γ_l can take. Mathematically, the Zak phase is the Chern-Simons invariant for the one-dimensional system which is defined as [18]

$$\mathrm{CS}_1 = \frac{i}{2\pi} \int_{\mathcal{C}} \mathrm{Tr}\left(\mathcal{A}\right). \tag{1.20}$$

The Chern-Simons invariant can be expressed in terms of the Berry connection $\mathcal{A}$ and in contrast to the Chern invariant well-defined for odd-dimensional parameter spaces $\mathcal{C}$. In general, the Chern-Simons invariant is not quantized but due to the presence of symmetries it may take discrete values. In systems with chiral symmetry, in the gauge given by the chiral basis the winding number can be shown to be $\mathbb{Z} \ni w_l = 2\gamma_l$, therefore $W = \exp(i\pi \sum_l w_l) = \pm 1$. In systems with particle-hole symmetry the topological invariant W can be evaluated using the representation of the Hamiltonian in the Majorana basis.

1.3.1. Winding number

Mathematically, the winding number is defined as quantity which counts how many times a closed curve circles around a point. The winding number is an important invariant for system with chiral symmetry. If the Hamiltonian has chiral symmetry $\{C, \mathcal{H}\} = 0$, we have shown that one consequence is that in a basis where C is block-diagonal the Hamiltonian $\mathcal{H}$ has a block off-diagonal form (1.16). One can introduce the winding number as a one-dimensional topological invariant [81, 82]

$$\nu = -\frac{1}{4\pi i} \int_{\mathrm{BZ}} dk\ \mathrm{Tr}\left(\tilde{C}\mathcal{H}_C^{-1}\left(k\right)\partial_k \mathcal{H}_C\left(k\right)\right). \tag{1.21}$$

Then, the winding number can be expressed only in terms of the Hamiltonian

$$\nu = -\frac{1}{4\pi i} \int dk\ \mathrm{Tr}\left[\tilde{C}\mathcal{H}_C^{-1}\partial_k \mathcal{H}_C\right] = \frac{1}{2\pi}\mathrm{Im} \int dk\ \partial_k \ln\left(\det\left(D\right)\right) = \frac{1}{2\pi} \int dk\ \partial_k \arg\left(\det\left(D\right)\right),$$

where we have used the two relations $\mathrm{Tr}\left[D^{-1}\partial_k D\right] = \partial_k \ln\left(\det\left(D\right)\right)$ and $\ln\left(\det\left(D^\dagger\right)\right) = \mathrm{Re}\left(\ln\left(\det\left(D\right)\right)\right) - i\mathrm{Im}\left(\ln\left(\det\left(D\right)\right)\right)$. Therefore, we see that the value of the winding number depends on the trajectory of $\det\left(D\right)$ in the complex plane as k changes in the Brillouin zone.

Alternatively, it is also possible to define the winding number in terms of the flat-band Hamiltonian [75]. For this we need the solution of the BdG equation in the chiral basis (1.18). The eigenfunctions $\Psi_{\pm,n}(k)$ of the Hamiltonian, with the eigenvalue $\pm E_n(k)$, where $-$ $(+)$ refers to the filled (empty) state, can be written as [83]

$$\Psi_{\pm,n}(k) = \begin{pmatrix} \chi_n^{\pm}(k) \\ \eta_n^{\pm}(k) \end{pmatrix} = \frac{1}{\sqrt{2}} \begin{pmatrix} u_n \\ \pm \frac{1}{E_n(k)} D^{\dagger}(k) u_n \end{pmatrix}. \tag{1.22}$$

One can check that the function satisfies the BdG equation $\mathcal{H}_C(k)\Psi_n(k) = \pm E_n(k)\Psi_n(k)$ with the relation $D(k)D^{\dagger}(k)u_n = E_n^2(k)u_n$. *A priori* the eigenvectors u_n may depend on k. Nevertheless, since u_n are eigenvectors of $D(k)D^{\dagger}(k)$ which is Hermitian, they form an orthogonal set. We can perform a unitary transformation into a basis in which $DD^{\dagger}$ is diagonal, and the eigenvectors u_n are independent of k. This transformation is continuous in k, which is assured by the continuity of the original eigenvectors $u_n(k)$. In the following, we shall work implicitly in that transformed basis. The projector onto the filled states is given by

$$P = \sum_n \Psi_{-,n}(k)\Psi_{-,n}^{\dagger}(k) = \frac{1}{2}\mathbb{1} - \frac{1}{2}Q. \tag{1.23}$$

The operator Q acts as a flat-band Hamiltonian having the energy $+1$ for the empty states and -1 for the filled states independent of k since $Q\Psi_{\pm,n}(k) = (I-2P)\Psi_{\pm,n}(k) = \pm\Psi_{\pm,n}(k)$. In the matrix form, we have

$$Q = \begin{pmatrix} 0 & q(k) \\ q^{\dagger}(k) & 0 \end{pmatrix}, \tag{1.24}$$

where $q(k) = \sum_l \frac{1}{E_n(k)} u_n u_n^{\dagger} D(k) = U(k)D(k)$ and the matrix

$$U(k) = \sum_l \frac{1}{E_n(k)} u_n u_n^{\dagger} \tag{1.25}$$

has been introduced. Using the flat-band Hamiltonian, a winding number is defined as [75]

$$\nu' = \frac{1}{2\pi i} \int dk \mathrm{Tr}\left[q^{-1}(k)\partial_k q(k)\right], \tag{1.26}$$

where the integral is taken over the whole one-dimensional Brillouin zone. The winding number ν' counts winding of $q(k)$. The proof of $\nu = \nu'$ is presented in appendix A. The connection to the Chern-Simons invariant (1.20) can be shown by using the fact that the

Berry connection of the system can be expressed as $\mathcal{A} = q^{-1}(k)\,\partial_k q(k)$ with the chiral eigenstate (1.22) [84]. Therefore, due to chiral symmetry the Chern-Simons invariant is $\frac{1}{2}$ of the winding number.

1.3.2. $\mathbb{Z}_2$ invariant

We have shown that the winding number can be related to the Chern-Simons number by using the chiral symmetry. In one-dimensional systems with particle-hole symmetry the $\mathbb{Z}_2$ topological invariant $\mathcal{M} = \pm 1$ can be defined using the representation of the Hamiltonian in the Majorana basis (1.12). Hence, the topological invariant $\mathcal{M}$ is called *Majorana number*. At the time reversal invariant momenta $\tilde{k} = 0, \frac{\pi}{a}$, $X\left(\tilde{k}\right)$, defined in Eq (1.12), it has the particularly simple form

$$X\left(\tilde{k}\right) = \begin{pmatrix} 0 & H_0\left(\tilde{k}\right) - \Delta \\ -\left[H_0\left(\tilde{k}\right) + \Delta\right] & 0 \end{pmatrix}. \tag{1.27}$$

where we used a gauge transform to transform the pairing matrix to a real matrix. We see that the matrix $X\left(\tilde{k}\right)$ is real and skew symmetric $X\left(\tilde{k}\right) = -X^T\left(\tilde{k}\right)$. For skew-symmetric matrices it is possible to define the so-called *Pfaffian* with $\mathrm{Pf}^2\left[X\left(\tilde{k}\right)\right] = \det\left(X\left(\tilde{k}\right)\right)$. The topological invariant $\mathcal{M}$ can then be expressed through the Pfaffian of $X(k)$ at $\tilde{k} = 0, \frac{\pi}{a}$. The relation due to the partucle-hole symmetry between the Chern-Simons invariant (1.20) and the Majorana number is derived in appendix A. Then, it follows

$$\mathcal{M} = \mathrm{sgn}\left(\mathrm{Pf}\left[X\left(\frac{\pi}{a}\right)\right]\mathrm{Pf}\left[X(0)\right]\right) = (-1)^{\frac{\mathrm{CS}_1}{2\pi}} = \pm 1. \tag{1.28}$$

With the $\mathbb{Z}_2$ invariant we are able to determine the topological features of systems with particle-hole symmetry. In the case of the superconducting carbon nanotubes we have particle-hole symmetry and also chiral symmetry. Especially, we will show that in the presence of a magnetic field, perpendicular to the nanotube axis, we can still use both invariants. The winding number gives more information about the topological properties than the pfaffian because it is a integer invariant and the pfaffian is a $\mathbb{Z}_2$ invariant. Furthermore, the winding number is more stable since a parallel magnetic field breaks the chiral symmetry. Thus, the winding number is not well-defined anymore but the pfaffian is still defined. However, in the case of a magnetic field parallel to the nanotube axis, the pfaffian turned out to be unreliable because it only looks at $k = 0$ and $k = \frac{\pi}{a}$!

2. Majorana fermions and topological superconductivity

In this chapter we give a short overview of the BCS theory for superconductors. Then, we introduce Majorana fermions in quantum field and condensed matter theory. Majorana fermions, particles being their own antiparticle predicted already eighty years ago, have remained elusive to experimental observation so far. Hence, recent proposals to observe quasiparticles with the Majorana property in one-dimensional p-wave superconductor and s-wave superconductor hybrid systems containing semiconducting elements have raised big attention. Further, we demostrate topological properties of both systems and the existence of Majorana states. Finally, we discuss realizations and signatures of Majorana states in epitaxially grown superconductor-semiconducting nanowires, which are by now the most advanced experimentally, and the emergence of a zero bias transport peak at finite magnetic field.

2.1. Introduction to superconductivity

Superconductivity is a quantum effect of many-body systems at low temperature which is defined by vanishing electrical resistivity and the presence of diamagnetism. Microscopically, superconductivity is driven by an attractive effective interaction between electrons near the Fermi surface. This leads to the formation of bound states with energy lower than the energy of two free electrons, which produces an instability of the Fermi sea. The attractive effective interaction between electrons is a consequence of the electron-phonon coupling which dominates the electron-electron interaction due to screening effects.

The basic theory of superconductivity was formulated by Bardeen, Cooper and Schrieffer (BCS) in 1957 [85]. We introduce the BCS theory by considering the case of s-wave superconductors. We start with the pairing Hamiltonian of an interacting electron system [86]

$$H - \mu N = \sum_{\mathbf{k},s} \xi(\mathbf{k})\, c^{\dagger}_{\mathbf{k}s} c_{\mathbf{k}s} + \sum_{\mathbf{k},\mathbf{k}'} V_{\mathbf{k}\mathbf{k}'} c^{\dagger}_{\mathbf{k}\uparrow} c^{\dagger}_{-\mathbf{k}\downarrow} c_{-\mathbf{k}'\downarrow} c_{\mathbf{k}'\uparrow}, \tag{2.1}$$

where $\xi(\mathbf{k}) = \varepsilon(\mathbf{k}) - \mu$ is the single particle energy measured with respect to the chemical potential μ and

$$V_{\mathbf{k}\mathbf{k}'} = \begin{cases} -V_0 < \hbar\omega_D & \text{for } |\xi(\mathbf{k})|,\ |\xi(\mathbf{k}')| < \hbar\omega_D, \\ 0 & \text{otherwise,} \end{cases}$$

with ω_D the Debye frequency. In general, the Coulomb interaction is repulsive and it is screened in a metal. The screening of the Coulomb interaction can be described by the random phase approximation [87]. The idea behind the BCS theory is that electrons interact attractively $V_0 > 0$ within a small energy window in the vicinity of the Fermi energy. The

attractive interaction leads to a formation of bound states of two electrons in the electronic states $|\mathbf{k}\uparrow\rangle$ and $|-\mathbf{k}\downarrow\rangle$ which induces an instability of the Fermi sea.

Bogoliubov also realized that superconductivity can be understood with the help of mean-field theories [88][4]. This approximation leads to the mean-field BCS grand canonical Hamiltonian

$$H_{\mathrm{BCS}} - \mu N = E_{\mathrm{BCS}} + \sum_{\mathbf{k},s} \xi\left(\mathbf{k}\right) c^{\dagger}_{\mathbf{k}s} c_{\mathbf{k}s} - \sum_{\mathbf{k}} \left(\Delta\left(\mathbf{k}\right) c^{\dagger}_{\mathbf{k}\uparrow} c^{\dagger}_{-\mathbf{k}\downarrow} + \Delta^{\star}\left(\mathbf{k}\right) c_{-\mathbf{k}\downarrow} c_{\mathbf{k}\uparrow} \right), \tag{2.2}$$

where $\Delta\left(\mathbf{k}\right) = -\sum_{\mathbf{k}'} V_{\mathbf{k}\mathbf{k}'} \langle c_{-\mathbf{k}'\downarrow} c_{\mathbf{k}'\uparrow} \rangle$ is the superconducting order parameter and E_{BCS} the condensate energy. In the limit $T \to 0$ E_{BCS} is equal to the BCS ground state energy. In the mean-field Hamiltonian (2.2), the electron number is not conserved leading to eigenstates without definite electron number. In contrast, the pairing Hamiltonian (2.1) commutes with the electron number operator. In general, the number of electrons is conserved in superconductors and it is possible to describe superconductivity with fixed electron number [89].

By introducing a new fermionic basis, the energy spectrum of the BCS Hamiltonian (2.2) can be analytically solved. The fermionic basis, the so-called *Bogoliubov transformation*, is defined in the following way

$$\begin{pmatrix} \gamma_{\mathbf{k}\uparrow} \\ \gamma^{\dagger}_{-\mathbf{k}\downarrow} \end{pmatrix} = \begin{pmatrix} u^{\star}\left(\mathbf{k}\right) & v\left(\mathbf{k}\right) \\ -v^{\star}\left(\mathbf{k}\right) & u\left(\mathbf{k}\right) \end{pmatrix} \begin{pmatrix} c_{\mathbf{k}\uparrow} \\ c^{\dagger}_{-\mathbf{k}\downarrow} \end{pmatrix}, \tag{2.3}$$

with $|u\left(\mathbf{k}\right)|^2 = \frac{1}{2}\left(1 + \frac{\xi(\mathbf{k})}{E(\mathbf{k})}\right)$ and $|v\left(\mathbf{k}\right)|^2 = \frac{1}{2}\left(1 - \frac{\xi(\mathbf{k})}{E(\mathbf{k})}\right)$ where $E\left(\mathbf{k}\right) = \sqrt{\xi^2\left(\mathbf{k}\right) + \Delta^2\left(\mathbf{k}\right)}$ is the quasiparticle energy. Due to the transformation above the BCS Hamiltonian (2.2) is diagonal and given by $H_{\mathrm{BCS}} - \mu N = E_{\mathrm{BCS}} + \sum_{\mathbf{k},s} E\left(\mathbf{k}\right) \gamma^{\dagger}_{\mathbf{k}s} \gamma_{\mathbf{k}s}$. It follows $u\left(\mathbf{k}\right) = u\left(-\mathbf{k}\right)$ and $v\left(\mathbf{k}\right) = v\left(-\mathbf{k}\right)$ for superconducting gaps with the property $\Delta\left(\mathbf{k}\right) = \Delta\left(-\mathbf{k}\right)$. Quasiparticles in superconductors, sometimes called Bogoliubiv quasiparticles, are a superposition of particle and hole states for energies nearby the Fermi energy.

A generalized formalism is the Bogoliubov - de Gennes (BdG) formalism [86], where the effects of disorder or magnetic fields are included. By doubling the terms in the BCS Hamiltonian (2.2) we can define the *Nambu spinor* $\Psi^{\dagger}_{\mathbf{k}} = \left(c^{\dagger}_{\mathbf{k}\uparrow}, c^{\dagger}_{\mathbf{k}\downarrow}, c_{-\mathbf{k}\uparrow}, c_{-\mathbf{k}\downarrow}\right)$ and the BCS Hamiltonian can be written as

[4] Very often many-body systems cannot be described without approximations. One simple approximation is the mean-field approximation where a Hamiltonian $H_{AB} = AB$ can be approximated to the form

$$H_{AB} \to H^{\mathrm{MF}}_{AB} = A\langle B\rangle + \langle A\rangle B - \langle A\rangle\langle B\rangle,$$

which is known as the mean-field approximation. One of the most famous mean-field theory is the Hartree approximations [87] with $A = c^{\dagger}_{\mathbf{k}\uparrow} c_{\mathbf{k}'\uparrow}$ and $B = c^{\dagger}_{\mathbf{k}\downarrow} c_{\mathbf{k}'\downarrow}$. In the case of the BCS theory the mean-field approximation is given by $A = c^{\dagger}_{\mathbf{k}\uparrow} c^{\dagger}_{-\mathbf{k}\downarrow}$ and $B = c_{-\mathbf{k}\downarrow} c_{\mathbf{k}\uparrow}$.

$$H_{\mathrm{BCS}} - \mu N = \frac{1}{2} \sum_{\mathbf{k}} \Psi_{\mathbf{k}}^{\dagger} \mathcal{H}_{\mathrm{BdG}} \Psi_{\mathbf{k}} + \text{const.}, \tag{2.4}$$

where $\mathcal{H}_{\mathrm{BdG}}$ is the BdG Hamiltonian, which has the form

$$\mathcal{H}_{\mathrm{BdG}}(\mathbf{k}) = \begin{pmatrix} \xi(\mathbf{k}) & 0 & 0 & -\Delta(\mathbf{k}) \\ 0 & \xi(\mathbf{k}) & \Delta(-\mathbf{k}) & 0 \\ 0 & \Delta^{\star}(-\mathbf{k}) & -\xi(-\mathbf{k}) & 0 \\ -\Delta^{\star}(\mathbf{k}) & 0 & 0 & -\xi(-\mathbf{k}) \end{pmatrix}. \tag{2.5}$$

With the Nambu construction we map the Schrödinger equation for the system specified by the second quantized Hamiltonian (2.2) to an eigenvalue problem

$$\mathcal{H}_{\mathrm{BdG}}(\mathbf{k}) \phi(\mathbf{k}) = E(\mathbf{k}) \phi(\mathbf{k}), \tag{2.6}$$

where $\phi(\mathbf{k}) = (u_{\uparrow}(\mathbf{k}), u_{\downarrow}(\mathbf{k}), v_{\uparrow}(-\mathbf{k}), v_{\downarrow}(-\mathbf{k}))^{T}$ is the eigenvector and $E(\mathbf{k})$ is the corresponding eigenvalue. This is the so-called *Bogoliubov - de Gennes equation*.

Finally, the BdG Hamiltonian satisfying the, in the previous chapter introduced, particle-hole symmetry $\mathcal{P}\mathcal{H}_{\mathrm{BdG}}(\mathbf{k})\mathcal{P}^{-1} = -\mathcal{H}_{\mathrm{BdG}}(-\mathbf{k})$ where the symmetry operator is defined as $\mathcal{P} = \tau_x K$ with $\mathcal{P}^2 = +1$. Therefore, if $\phi(\mathbf{k})$ is a solution of the BdG equation (2.6) with positive energy there exists a second solution $\phi^{P}(\mathbf{k}) = \mathcal{P}\phi(\mathbf{k})$ but with negative energy. We will call the solutions with positive energies quasiparticles and the solutions with negative energies holes. Thus, the particle-hole symmetry operator maps quasiparticles to holes.

In this thesis we consider systems that are not intrinsic superconductors. By coupling an s-wave superconductor to a normal conductor, the conductor becomes superconducting. This is the well-known *proximity effect* and can be described by Andreev reflections [90]. The microscopic model of the proximity effect is defined by the tunneling Hamiltonian

$$H_T = \sum_{s,\sigma} \sum_{\langle i_0, j_0 \rangle} \left(t_{m\sigma} c_{i_0 m}^{\dagger} d_{j_0,\sigma} + t_{m\sigma}^{\star} d_{j_0,\sigma}^{\dagger} c_{i_0 m} \right), \tag{2.7}$$

where $c_{is}^{\dagger}$ is the normal conductor creation operator at the lattice site i with spin quantum number s, $d_{j\sigma}$ the corresponding superonductor creation operator at the lattice site j with spin σ. By integrating out the superconductor operators, an effective model is derived for the normal conductor, including superconducting pairing and a renormalized chemical potential [91–95].

2.2. Majorana fermions, Majorana zero modes and Majorana bound states

In the year 1928 P. M. Dirac postulated a relativistic wave equation, the so-called *Dirac equation*, which combines the principles of quantum mechanics and special relativity [96]. In general, the Dirac equation is the equation of motion for spin-$\frac{1}{2}$ particles and the free form is given by

$$(i\gamma^\mu \partial_\mu - m)\,\Psi = (\gamma^\mu p_\mu - m)\,\Psi = 0, \tag{2.8}$$

where γ^μ are four 4×4 gamma matrices which satisfy the Clifford algebra $\{\gamma^\mu, \gamma^\nu\} = 2\eta^{\mu\nu}$ where $\eta^{\mu\nu} = \mathrm{diag}\,(1, -1, -1, -1)$ is the flat Minkowski metric, $p_\mu = (i\partial_t, \mathbf{p})$ and ∂_μ is defined as $\frac{\partial}{\partial x^\mu}$. The four-dimensional gamma matrices implies that solutions of the Dirac equation are four-component vectors. The Dirac equation (2.8) and the corresponding solution has many symmetries [97–99] and one of them is *charge conjugation*. The charge conjugation operator C maps a solution Ψ onto another solution $\Psi^C = C\Psi$. The charge conjugated solution Ψ^C, the so-called antiparticle, describes a fermion, in contrast to the solution Ψ, with opposite charge and negative energy. For clarification, it is defined that solutions with positive energies are particles while solutions with negative energies are antiparticles.

By definition, solutions of the Dirac equation (2.8) which are not eigenstates of the charge conjugation operator, i.e. $\Psi^C = C\Psi \neq \Psi$. are called *Dirac fermions*. In contrast, E. Majorana derived an alternative form of the Dirac equation [23] with the constraint that the solutions are eigenstates of the charge conjugation operator, i.e. $\Psi^C = C\Psi \stackrel{!}{=} \Psi$ which we will call the *Majorana condition*. Fermions with this property are called *Majorana fermions* and can not be differentiated from the antifermion.

Formally, it is possible to expand every second quantized operator in terms of the *Majorana basis* which is defined in the following way

$$c_j = \frac{1}{2}\left(\gamma_{j,1} + i\gamma_{j,2}\right) \text{ and } c_j^\dagger = \frac{1}{2}\left(\gamma_{j,1} - i\gamma_{j,2}\right), \tag{2.9}$$

where the new operators $\gamma_{j\alpha}$, which can be interpreted as real and imaginary parts of the fermion operator from a mathematical point of view, satisfy the anticommutator relation $\{\gamma_{i\alpha}, \gamma_{j\beta}\} = 2\delta_{ij}\delta_{\alpha\beta}$ and $\gamma_{i\alpha} = \gamma_{i\alpha}^\dagger$. The condition $\gamma_{i\alpha} = \gamma_{i\alpha}^\dagger$ is equivalent to the Majorana condition.

Since the theoretical prediction, it was not possible to measure a fundamental particle, in the standard model of particle physics, which is a Majorana fermion. Nowadays, new concepts were presented in condensed matter physics. Likewise in the particle physics, a positive energy solution ϕ of the BdG equation (2.6) can be transformed by the particle-hole symmetry to a negative energy solution $\phi^P = \mathcal{P}\phi$. This implies that the necessary condition of Majorana-like

excitations are solutions with zero energy. Then, the BdG equation is simplified

$$\mathcal{H}_{\mathrm{BdG}}\left(\mathbf{k}\right)\phi_0\left(\mathbf{k}\right)=0. \tag{2.10}$$

Now, like in the case with the Dirac equation, we will use the constraint that we search for a solution which is also an eigenstate of the particle-hole symmetry operator $\mathcal{P}\phi_0\left(\mathbf{k}\right)\overset{!}{=}\phi_0\left(\mathbf{k}\right)$. However, due to the fact that this kind of solution is not an elementary particle, we will call such solutions in superconductors not as Majorana fermions but as *Majorana zero modes*. Furthermore, localize Majorana zero modes are called *Majorana bound states*. The Majorana condition implies

$$\begin{pmatrix} u_\uparrow\left(\mathbf{k}\right) \\ u_\downarrow\left(\mathbf{k}\right) \\ v_\uparrow\left(-\mathbf{k}\right) \\ v_\downarrow\left(-\mathbf{k}\right) \end{pmatrix} \overset{!}{=} \begin{pmatrix} v_\uparrow^\star\left(-\mathbf{k}\right) \\ v_\downarrow^\star\left(-\mathbf{k}\right) \\ u_\uparrow^\star\left(\mathbf{k}\right) \\ u_\downarrow^\star\left(\mathbf{k}\right) \end{pmatrix}. \tag{2.11}$$

Superconductors with Majorana bound states are called *topological superconductors* and can be characterized by a topological invariant in the bulk. From the previous chapter, we know that a system, depending on the symmetries and spatial dimensions, can be described by a different kind of topological invariant. The relation between the bulk topological invariant and the emergence of boundary state is called *bulk-boundary correspondence* [1].

2.3. Topological superconductivity in p-wave superconductors

2.3.1. Kitaev chain

A. Kitaev introduced the first model of an one-dimensional topological superconductor and thus it is called the *Kitaev chain* [24]. The Kitaev chain is a very simple toy model that exhibits Majorana bound states at the ends of the chain. The Kitaev chain with N sites is a open chain and defined in terms of spinless fermions including a term for the chemical potential μ, a hopping term t and a nearest-neighbor superconducting pairing term Δ. Then, the Hamiltonian for the Kitaev chain is given by

$$H_K=-\mu\sum_{j=1}^{N}c_j^\dagger c_j+\sum_{j=1}^{N-1}\left[-t\left(c_j^\dagger c_{j+1}+c_{j+1}^\dagger c_j\right)+\Delta\left(c_j^\dagger c_{j+1}^\dagger+c_{j+1}c_j\right)\right], \tag{2.12}$$

The superconducting gap can transform into a real number by a gauge transformation. The energy spectrum of the Kitaev Hamiltonian (2.12) for $t=\Delta$ and a length of $N=50$ is shown in Fig. 2.1. Using the transformation (2.9) the Hamiltonian (2.12) becomes

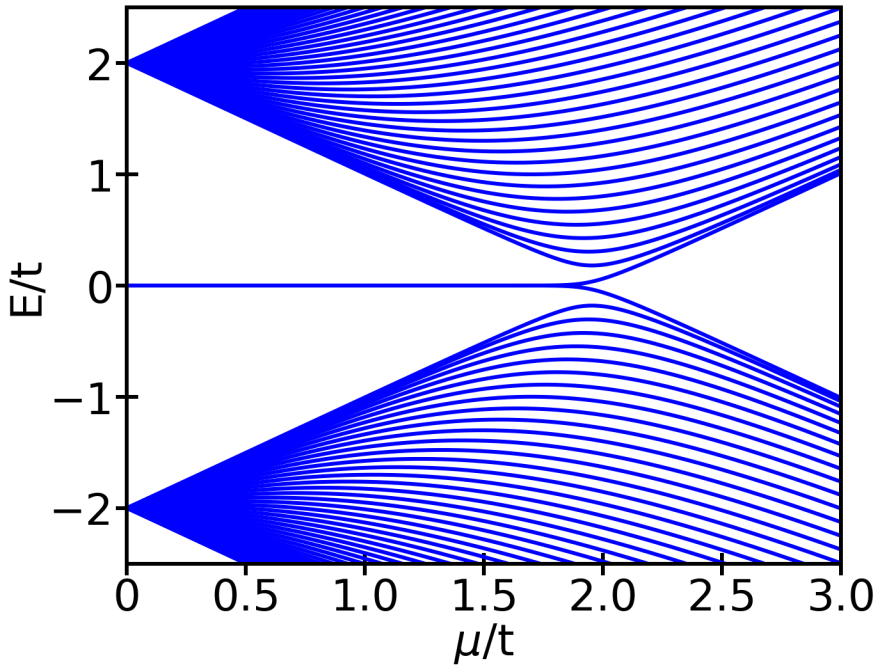

Figure 2.1: Energy spectrum of the clean Kitaev chain (2.12) as a function of the chemical potential μ with $N = 50$ lattice sites and $t = \Delta$.

$$H_K = -\frac{i\mu}{2}\sum_{j=1}^{N}\gamma_{j,1}\gamma_{j,2} + \frac{i}{2}\sum_{j=1}^{N-1}\left[(\Delta+t)\,\gamma_{j,2}\gamma_{j+1,1} + (\Delta-t)\,\gamma_{j,1}\gamma_{j+1,2}\right]. \tag{2.13}$$

In the case of $t = \Delta = 0$, the Hamiltonian is given by

$$H_K = -\frac{i\mu}{2}\sum_{j=1}^{N}\gamma_{j,1}\gamma_{j,2}. \tag{2.14}$$

Here, Majorana fermions are coupled together at the same site j and can be combined into a normal fermion, see Fig. 2.2(a). Therefore, this case corresponds to the trivial phase. Another case is given by the conditions $t = \Delta$ and $\mu = 0$ where the Hamiltonian reads

$$H_K = it\sum_{j=1}^{N-1}\gamma_{j,2}\gamma_{j+1,1}. \tag{2.15}$$

In this case, Majorana fermions are coupled at adjecent sites in the chain and the Majorana fermions at the first and last site is not included in the Hammiltonian, see Fig. 2.2(b). Therefore, at the ends are two decoupled Majorana fermions with zero energy, respectively.

For topological non-trivial case, the Kitaev Hamiltonian can be expressed in terms of new fermion operators. In the bulk, the new fermion operator is defined as $a_j = \frac{1}{2}\left(\gamma_{j,2} + i\gamma_{j+1,1}\right)$

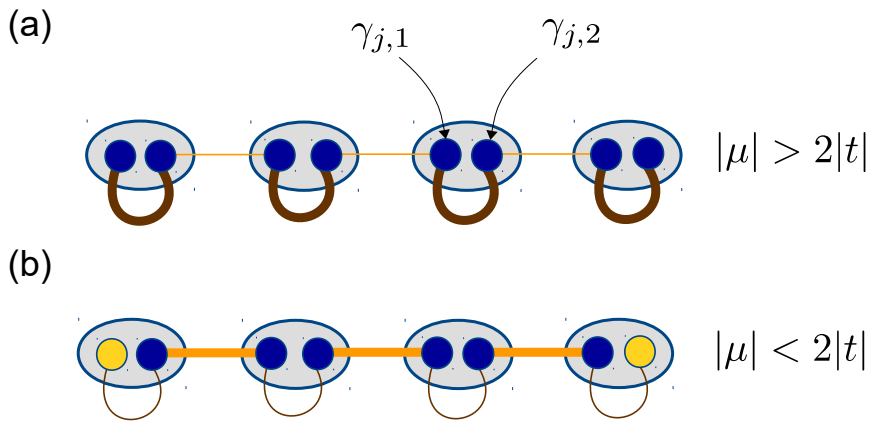

Figure 2.2: Kitaev chain in the two different topological phases. (a) In the trivial phase, Majorana fermions are paired at the same site and thus form a normal fermion. (b) While in the non-trivial phase implies that the Majorana fermions are paired on adjacent sites which yields two unpaired Majorana fermions at the boundaries.

with $j \in \{1, 2, \ldots, N-1\}$ and for the boundary states $f = \frac{1}{2}(\gamma_{1,1} + i\gamma_{N,2})$ which is delocalized. Then, the Kitaev Hamiltonian, in the new basis, becomes

$$H_K = 2t \sum_{j=1}^{N-1} \left(a_j^\dagger a_j - \frac{1}{2} \right) + 0 \cdot f^\dagger f. \tag{2.16}$$

The creation of a bulk fermion $a_j^\dagger |0\rangle$ from the groundstate $|0\rangle$ costs finite energy and thus the bulk is gapped. As a consequence of the zero energy Majorana fermions, the groundstate is two-fold degenerated because $|1\rangle = f^\dagger |0\rangle$ is a second groundstate with opposite fermion parity.

So far, the Kitaev chain is defined with open boundary conditions. In the case with periodic boundary condition, the Kitaev Hamiltonian can be transformed into a momentum representation by a Fourier transformation. Then, a BdG Hamiltonian can be defined $H_K = \frac{1}{2} \sum_k \Psi_k^\dagger \mathcal{H}_{\mathrm{BcG}}(k) \Psi_k$ which is given by

$$\mathcal{H}_{\mathrm{BdG}}(k) = \begin{pmatrix} -2t\cos(k) - \mu & -2i\Delta\sin(k) \\ 2i\Delta\sin(k) & 2t\cos(k) + \mu \end{pmatrix} = \xi(k)\tau_z + \Delta_p(k)\tau_y, \tag{2.17}$$

with the definitions $\xi(k) = -2t\cos(k) - \mu$ and $\Delta_p(k) = 2\Delta\sin(k)$. We see now the reason why the Kitaev chain is also called a toy model for a *p-wave superconductor*: firstly, the superconducting gap $\Delta_p(k)$ is an odd function of the momentum $\Delta_p(k) = -\Delta_p(-k)$; secondly, in the low-energy limit it follows that $\Delta(k) = 2\Delta k$, i.e. there is a linear dependence on the momentum.

The eigenvalues are $E(k) = \pm\sqrt{\xi^2(k) + \Delta_p^2(k)}$ and it is easy to see that the excitation spectrum remains fully gapped except when $2t = \pm\mu$. This condition defines the boundaries of the topological phase diagram. These distinct phases are distinguished by the presence or absence of unpaired Majorana states at the ends in the geometry with open boundary conditions.

2.3.2. Topological invariants

From the previous chapter we known that the topological phase diagram can be determined by a topological invariant which is defined by the symmetries of the system. Additionally to the particle-hole symmetry $\mathcal{P} = \tau_x K$ with $\mathcal{P}^2 = +1$, the BdG Hamiltonian (2.17) has time-reversal symmetry $\mathcal{T}\mathcal{H}_{\mathrm{BdG}}(k)\mathcal{T}^{-1} = \mathcal{H}_{\mathrm{BdG}}(-k)$ with $\mathcal{T} = K$ and $\mathcal{T}^2 = +1$. Therefore, the BdG Hamiltonian corresponds to the BDI symmetry class, see Table 1, and the topological properties can be identified by a winding number. The calculation of the winding number can be simplified by using the fact that a chiral symmetry can be defined by $C = \mathcal{T} \cdot \mathcal{P}$. Due to chiral symmetry we can transform (2.17) into a block off-diagonal form, where the blocks are defined as $q(k) = \frac{\xi(k) - i\Delta_p(k)}{E(k)}$. Then, we know that the winding is defined as

$$\nu = \frac{i}{2\pi}\int_{\pi}^{\pi} dk q^{-1}(k)\frac{d}{dk}q(k) = -\frac{1}{2\pi}\int_{\pi}^{\pi} dk \frac{\Delta(2t + \mu\cos(k))}{(2t\cos(k) + \mu)^2 + \Delta^2\sin^2(k)}. \tag{2.18}$$

The Kitaev chain has three different phases where $\nu = 0$ for $|\mu| > 2|t|$ is the trivial phase and depending of the superconducting gap sign two non-trivial phase $\nu = -\mathrm{sign}(\Delta)$ for $|\mu| < 2|t|$.

Furthermore, the corresponding Majorana number (1.28) for the Kitaev chain is given by

$$\mathcal{M} = \mathrm{sign}(-(2t + \mu)(2t - \mu)) = \begin{cases} +1 & \text{for } |\mu| > 2|t|, \\ -1 & \text{for } |\mu| < 2|t|, \end{cases}$$

where $|\mu| > 2|t|$ corresponds to the trivial phase with $\Rightarrow \mathcal{M} = +1$. Then, in the non-trivial phase $|\mu| < 2|t|$ the Majorana number is defined as $\Rightarrow \mathcal{M} = -1$. Thus, the results of both topological invariants are the same.

2.3.3. Stability of Majorana bound states

Real systems are never free from impurities and other defects causing disorder. We simulate disorder through a random on-site electrostatic potential, with varying concentration n, and potential strength chosen randomly from an interval $\left[-\frac{W_0}{2}; \frac{W_0}{2}\right]$. Then,

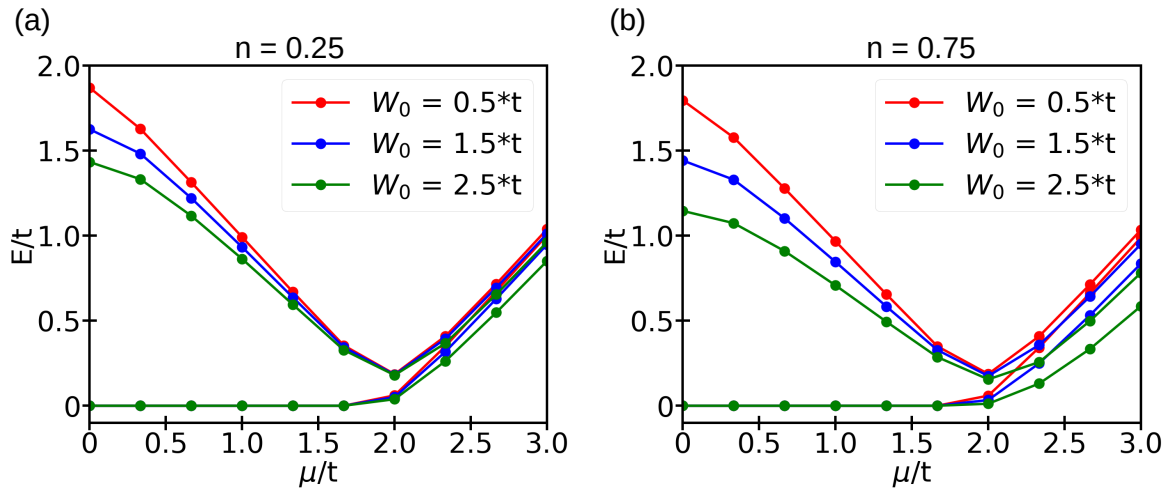

Figure 2.3: Mean value over $N_{\text{Disorder}} = 100$ disorder configurations of the lowest energy band E_0 and first excited state E_1 of the disordered Kitaev chain (in the same setup $N = 50$ and $t = \Delta$) with increasing disorder strength W_0 and two different concentrations of disorder. (a) System with a disorder concentration $n = 0.25$ and (b) with $n = 0.75$. In both cases, the disorder has the effect of decreasing E_1 with increasing W_0 and also with increasing the impurity concetration n. However, the zero energy state E_0 stays stable against the disorder

$$H_{\text{Disorder}} = \sum_{i,s} W_i c_{is}^{\dagger} c_{is}, \tag{2.19}$$

where $W_i \in \left[-\frac{W_0}{2}; \frac{W_0}{2}\right]$ is the strength of the disorder on lattice site i. The evolution of the lowest energy band E_0 which corresponds to the zero energy mode and the first excited state E_1 as a function the chemical potential μ for two impurity concentrations and increasing disorder strength W_0 is shown Fig. 2.3. Since disorder is distributed randomly, universal properties of the system are obtained after disorder average. In Fig. 2.3 we simulate $N_{\text{Disorder}} = 100$ disorder configurations and we see that the disorder has the effect of decreasing E_1 with increasing W_0 and also with increasing the impurity concetration n. However, the zero energy state E_0 stays stable against disorder because it is protected by particle-hole symmetry.

2.4. Topogical superconductivity in semiconductor-superconductor hybrid systems

From the beginning, the Kitaev chain has been viewed as an unphysical model. However, there are some materials which are suspected of having an intrinsic p-wave gap symmetry. Theoretically, in Sr_2RuO_4 a p-wave gap symmetry is expected [100, 101]. Due to the weak spin-orbit coupling, the boundary states in Sr_2RuO_4 are spin degenerated and thus Majorana bound states can be combined into a normal fermion [102]. More details about topological superconductivity can be found in the Ref. [103][5].

[5] Topological properties in superconductors and superfluids are well-known since the phases ^{3}He-B and ^{3}He-A are characterized by topological invariants [1].

Two breakthrough proposals by L. Fu and C. L. Kane has shown that an s-wave superconductor can effectively behave like a p-wave superconductor. If an s-wave superconductors is in contact with a topological insulators, then the emergence of p-wave pairing and Majorana bound states is demonstrated [25, 104]. Recently, a proposal has shown that in a chain of ferromagnetic atoms, for example Fe, on a superconducting substrates, such as Pb, can host Majorana bound states which can be measured by a scanning tunneling microscope [105].

In another realization the topological insulator is replaced by a semiconducting nanowire [26–29]. Semiconducting nanowires, like InAs and InSb, have two advantages. Firstly, the spin-orbit coupling is strong which implies that the energy bands are spin non-degenerated. Secondly, a smaller magnetic field is needed for the topological transition because the Landé g-factor is large.

2.4.1. Semiconductor model

The emergence of Majorana bound states in the Kitaev chain caused by the fact that it describes a p-wave superconductor of spinless fermions. However, the Kitaev chain is an unphysical toy model. In semiconductors it can be shown that electrons can effectively behave as spinless fermions due to a certain combination of strong spin-orbit coupling and an external magnetic field. Due to the superconducting proximity effect, the device may be driven in a topological superconducting state when the semiconductor is in contact with an s-wave superconductor. To understand the physical picture behind this idea we start from a Hamiltonian describing the low-energy behavior of electrons in a one-dimensional quantum wire along the x-direction includint a Rashba spin-orbit coupling that points perpendicularly to the quantum wire axis in z-direction

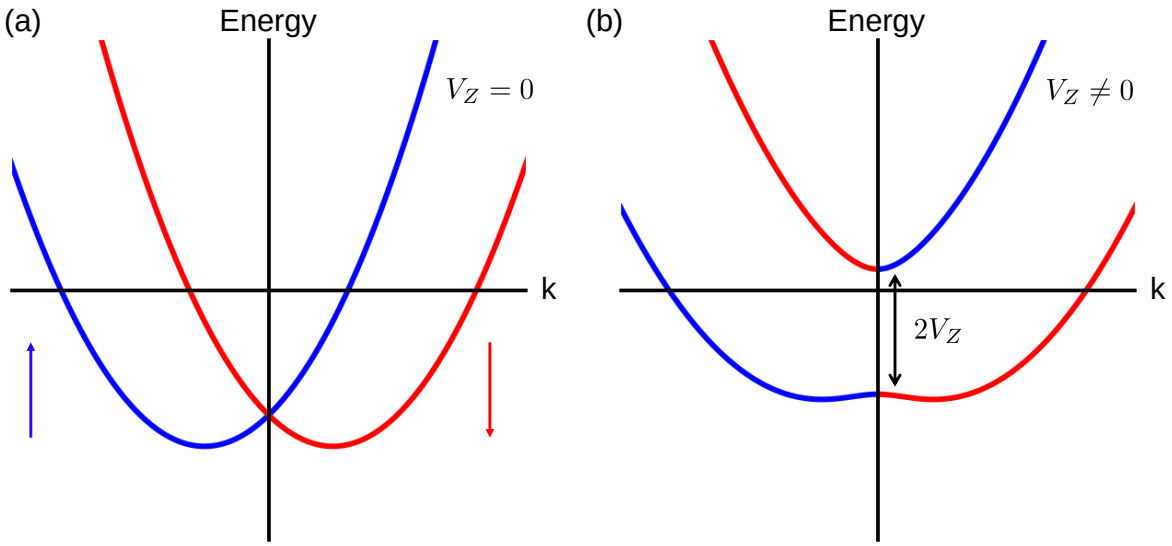

Figure 2.4: Energy spectrum of the Hamiltonian (2.21). (a) The spectrum in the case $V_Z = 0$. (b) For a finite magnetic field an energy gap $2V_Z$ opens at Γ-point. The color code corresponds to the expectation value $\langle\lambda|\, s_z \,|\lambda\rangle$ where red for spin down $\langle\lambda|\, s_z \,|\lambda\rangle = -1$ and blue for spin up $\langle\lambda|\, s_z \,|\lambda\rangle = +1$.

$$H_{\text{Semi}} - \mu N = \sum_k c_k^\dagger \left[\xi\left(k\right)\mathbb{1} + \alpha_R \hbar k s_z\right] c_k, \tag{2.20}$$

where the vector$c_k^\dagger$ is defined as $c_k^\dagger = \left(c_{k\uparrow}^\dagger,\, c_{k\downarrow}^\dagger\right)$, $\xi\left(k\right) = \frac{\hbar^2 k^2}{2m^\star} - \mu$ is the single particle energy, $m^\star$ is the effective electron mass and μ the chemical potential. The spin-orbit coupling is described by the coupling strength α_R. In general, in semiconductors the spin-orbit coupling caused by breaking the inversion symmetry of the lattice and it can be distinguished between two kinds of spin-orbit coupling [106]. The first kind of spin-orbit coupling is coming from a bulk inversion asymmetry and is called Dresselhaus spin-orbit coupling. Secondly, the Rashba spin-orbit coupling caused by breaking the structure inversion in epitaxially grown semiconductors. For simplification we will only consider a Hamiltonian with Rashba spin-orbit coupling. However, Majorana bound states are also possible with a combination of Dresselhaus and Rashba spin-orbit coupling [26].

The energy spectrum of (2.20) is comprised of two shifted parabolas $\epsilon_\pm\left(k\right) = \xi\left(k\right) \pm \alpha_R \hbar k$ and is depicted in Fig. 2.4(a). Due to the spin-orbit coupling, the spin degeneracy is broken, while at the Γ-point there is still a spin degeneracy because of the Kramers theorem which implies $\epsilon_+\left(k\right) = \epsilon_-\left(-k\right)$. By applying a magnetic field in direction perpendicular to z, the degeneracy at the Γ-point is also broken. The semiconductor Hamiltonian plus the Zeeman term induced by the magnetic field is given by

$$H_{\text{Semi}} - \mu N + H_Z = \sum_k c_k^\dagger \left[\xi\left(k\right)\mathbb{1} + \alpha_R \hbar k s_z + V_Z s_x\right] c_k, \tag{2.21}$$

where $V_Z = \frac{1}{2} g \mu_B B$ is the Zeeman energy, g is the Landé g-factor, μ_B is the Bohr magneton and B is the magnetic field which is applied parallel to the axis of the quantum wire. The large g-factor in the semiconductor allows one to achieve the opening of a large gap due to the Zeeman term. The Hamiltonian (2.21) can be diagonalized by the following unitary transformation

$$\begin{pmatrix} c_{k\uparrow} \\ c_{k\downarrow} \end{pmatrix} = \begin{pmatrix} a\left(k\right) & b\left(k\right) \\ -b\left(k\right) & a\left(k\right) \end{pmatrix} \begin{pmatrix} \alpha_{k+} \\ \alpha_{k-} \end{pmatrix}, \tag{2.22}$$

where $\alpha_\lambda^\dagger \left|0\right\rangle = \left|\lambda\right\rangle$, $\lambda = \pm$ and the coefficients are defined as

$$a^2(k) = \frac{1}{2}\left(1 - \frac{\alpha_R \hbar k}{\sqrt{(\alpha_R \hbar k)^2 + V_Z^2}}\right),$$
$$b^2(k) = \frac{1}{2}\left(1 + \frac{\alpha_R \hbar k}{\sqrt{(\alpha_R \hbar k)^2 + V_Z^2}}\right),$$

with $a^2(k) + b^2(k) = 1$ and $a(-k) = b(k)$. Then, the Hamiltonian (2.21) is transformed to

$$H_{\text{Semi}} - \mu N + H_Z = \sum_{k,\lambda} E_\lambda(k)\, \alpha_{k\lambda}^\dagger \alpha_{k\lambda} = \sum_{k,\lambda} \left(\xi(k) + \lambda\sqrt{(\alpha_R \hbar k)^2 + V_Z^2}\right) \alpha_{k\lambda}^\dagger \alpha_{k\lambda}, \quad (2.23)$$

where the single particle energy is invariant under $k \to -k$: $E_\lambda(k) = E_\lambda(-k)$ and $\lambda = \pm 1$ is the band index. The spin quantization axis is determined by the interaction between spin-orbit coupling and magnetic field, which are orthogonal to each other. In Fig. 2.4(a) the energy spectrum is shown in the case $V_Z = 0$. Then, the energy spectrum is given by two shifted parabolas, with the left corresponding to spin up projection and the right to spin down projection, and the spin quantization axis is fixed in z-direction. If a magnetic field is applied perpendicular to the spin-orbit coupling, a gap of the size $2V_z$ will open, since the spin degeneracy is lifted at the Γ-point, see Fig. 2.4(b). The magnetic field mixes the two spin projections and in the case where the chemical potential within the gap $2V_Z$ only the lowest energy band $\lambda = -1$ is occuped. The Fermi wave vector of the lowest energy band is defined by $E_-(k_F) = 0$ and given by $k_F = \sqrt{2k_R^2 + \sqrt{4k_R^4 + k_Z^4}}$ with $k_R = \frac{m^\star \alpha_R}{\hbar^2}$ and $k_Z = \frac{\sqrt{2V_Z m^\star}}{\hbar}$.

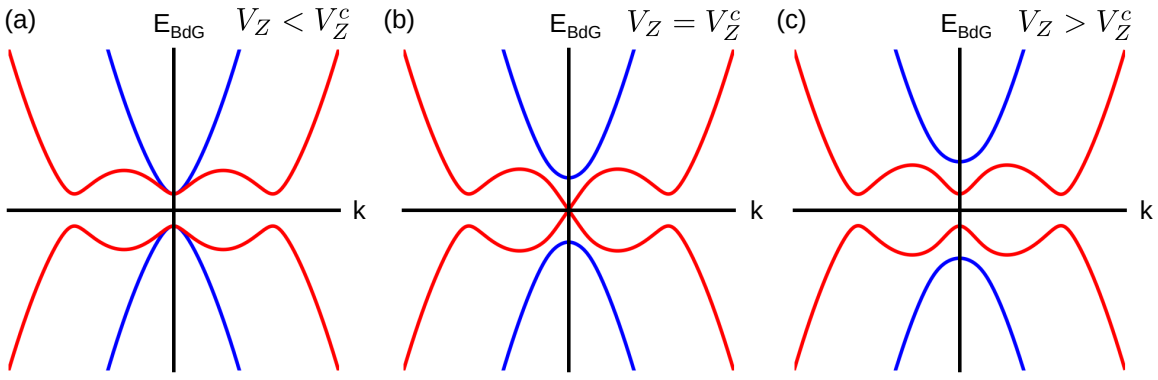

Figure 2.5: The energy spectrum of the BdG Hamiltonian (2.25) for three different values of the Zeeman energy V_Z. (a) $V_Z = 0$. (b) $V_Z = V_Z^c$. (c) $V_Z > V_Z^c$.

2.4.2. Superconducting bulk spectrum and topological phase diagram

Due to the proximity effect an additional pairing potential is generated which can be treated in the mean-field approximation as

$$H_{SC} = \sum_k \left(\Delta c^\dagger_{k\uparrow} c^\dagger_{-k\downarrow} + \Delta^\star c_{-k\downarrow} c_{k\uparrow} \right), \tag{2.24}$$

see also the discussion in 2.1. We can write down the BdG Hamiltonian by defining the Nambu spinor as $\Psi^\dagger_k = \left(c^\dagger_{k\uparrow}, c^\dagger_{k\downarrow}, c_{-k\uparrow}, c_{-k\downarrow} \right)$. Then, the full Hamiltonian is given by $H_{\text{Semi}} - \mu N + H_Z + H_{SC} = \frac{1}{2} \sum_k \Psi^\dagger_k \mathcal{H}_{\text{BdG}}(k) \Psi_k$ with the BdG Hamiltonian

$$\mathcal{H}_{\text{BdG}}(k) = \begin{pmatrix} \xi(k) + \alpha_R \hbar k & V_Z & 0 & \Delta \\ V_Z & \xi(k) - \alpha_R \hbar k & -\Delta & 0 \\ 0 & -\Delta & -\xi(k) + \alpha_R \hbar k & -V_Z \\ \Delta & 0 & -V_Z & -\xi(k) - \alpha_R \hbar k \end{pmatrix}. \tag{2.25}$$

We see that the BdG Hamiltonian for the nanowire is of the form of (1.9). The energy spectrum of the BdG Hamiltonian is given by

$$E^2_\pm(k) = \xi^2(k) + V_Z^2 + (\alpha_R \hbar k)^2 + \Delta^2 \pm 2\sqrt{V_Z^2 \Delta^2 + \xi^2(k) \left(V_Z^2 + (\alpha_R \hbar k)^2 \right)}, \tag{2.26}$$

and is depicted in Fig. 2.5. The energy gap at the Γ-point $\Delta_- = |E_-(k=0))|$ is defined as

$$\Delta_- = |E_-(k=0))| = \left| V_Z - \sqrt{\Delta^2 + \mu^2} \right| = |V_Z - V_Z^c|. \tag{2.27}$$

As shown in panel (b), the energy gap is closed at the Γ-point for a critical value of the magnetic field V_Z^c.

Now, we show the connection to the Kitaev chain and p-wave superconducitivity. For this we transform the superconducting pairing term in the eigenbasis of $H_{\text{Semi}} - \mu N + H_Z$ by using the unitary transformation (2.22). Then, the mean-field Hamiltonian describing the superconductivity becomes

$$H_{\text{SC}} = \sum_k \Delta_0 \left(b^2(k) \alpha^\dagger_{k-} \alpha^\dagger_{-k-} - a^2(k) \alpha^\dagger_{k+} \alpha^\dagger_{-k+} \right) + \Delta_0 a(k) b(k) \left(\alpha^\dagger_{k+} \alpha^\dagger_{-k-} - \alpha^\dagger_{k-} \alpha^\dagger_{-k+} \right) + \text{h.c.}$$

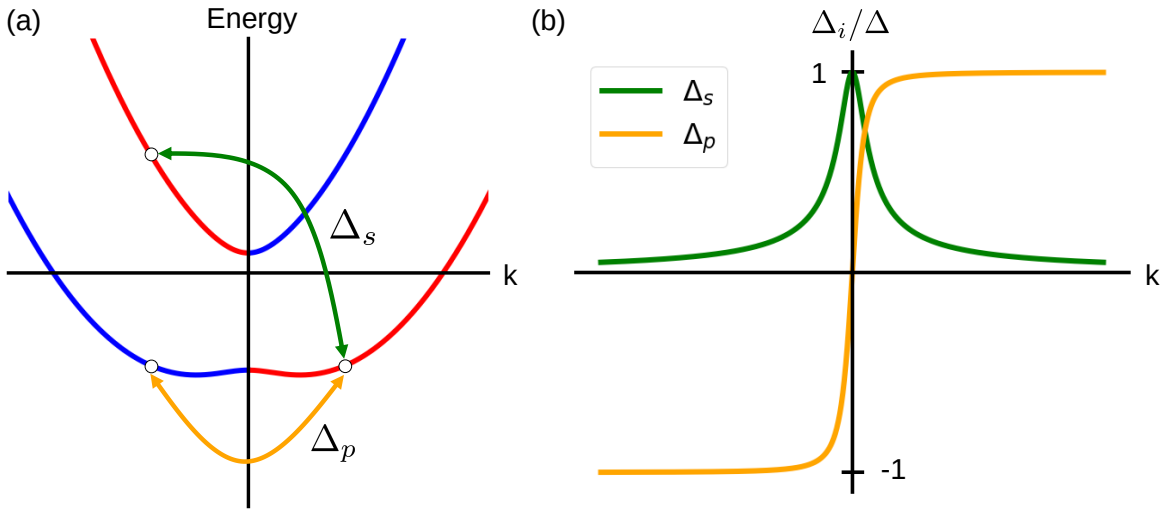

Figure 2.6: Superconducting gap in the nanowire with proximity-induced superconductivity. (a) In the eigenbasis of the Hamiltonian (2.21) there are two pairing mechanisms: the interband pairing $\Delta_s(k)$ and the intraband pairing $\Delta_p(k)$. The interband pairing $\Delta_s(k)$ couples electrons from both energy bands with opposite momentum k and the intraband pairing $\Delta_p(k)$ electrons with opposite momentum k in the same energy band. (b) The two superconducting gaps for a finite Zeeman energy V_Z as functions of k.

The interaction between spin-orbit coupling and magnetic field induces a non-trivial spin texture $s_\lambda^x(k) = \langle\lambda| s_x |\lambda\rangle = s_\lambda^x(-k)$ and $s_\lambda^z(k) = \langle\lambda| s_z |\lambda\rangle = -s_\lambda^z(-k)$. By coupling the semiconductor to an s-wave superconductor, the non-trivial spin-texture implies a mixture of s-wave and p-wave pairing terms. The BdG Hamiltonian with the Nambu spinor $\Psi_k^\dagger = \left(\alpha_{k+}^\dagger, \alpha_{k-}^\dagger, \alpha_{-k+}, \alpha_{-k-}\right)$ reads

$$\tilde{\mathcal{H}}_{\mathrm{BdG}}(k) = \begin{pmatrix} E_+(k) & 0 & \Delta_p(k) & \Delta_s(k) \\ 0 & E_-(k) & -\Delta_s(k) & \Delta_p(k) \\ \Delta_p(k) & -\Delta_s(k) & -E_+(k) & 0 \\ \Delta_s(k) & \Delta_p(k) & 0 & -E_-(k) \end{pmatrix}, \tag{2.28}$$

where we get two superconducting pairing terms $\Delta_s(k) = 2\Delta u(k) v(k)$ which is an interband pairing term and $\Delta_p(k) = \Delta\left(v^2(k) - u^2(k)\right)$ which is an intraband pairing term, see Fig. 2.6(a). The pairing $\Delta_s(k) = \Delta_s(-k)$ is an even function of k and $\Delta_p(k) = -\Delta_p(-k)$ is an odd function of k, see Fig. 2.6(b), and can be viewed as a p-wave gap like in the case of the Kitaev chain.

By definition the BdG Hamiltonian (2.25) has particle-hole symmetry $\mathcal{P} = \tau_x\mathcal{K}$, but the magnetic field breaks the time-reversal symmetry. Thus, the system is in class D which implies that the topological properties can be described by a $\mathbb{Z}_2$-invariant, see Tab. 3. However, it is possible to show that the BdG Hamiltonian has a hidden chiral symmetry [107, 108]. To understand this in more detail consider the unitary transformation

$$U = \begin{pmatrix} \mathbb{1} & 0 \\ 0 & s_x \end{pmatrix}. \tag{2.29}$$

Then, the Nambu spinor transforms as $U\Psi_k = \left(c_{k\uparrow},\, c_{k\downarrow},\, c^\dagger_{-k\downarrow},\, c^\dagger_{-k\uparrow}\right)^T$ and the BdG Hamiltonian takes the form

$$U\mathcal{H}_{\mathrm{BdG}}U^{-1} = \begin{pmatrix} \xi(k) + \alpha_R\hbar k & V_Z & \Delta & 0 \\ V_Z & \xi(k) - \alpha_R\hbar k & 0 & -\Delta \\ \Delta & 0 & -\xi(k) - \alpha_R\hbar k & -V_Z \\ 0 & -\Delta & -V_Z & -\xi(k) + \alpha_R\hbar k \end{pmatrix}, \tag{2.30}$$

which is of the form of (1.14). In this basis the particle-hole symmetry operator becomes $\bar{\mathcal{P}} = U\mathcal{P}U^{-1} = \tau_x \otimes s_x$ and the chiral symmetry operator is given by $C = \tau_y$. Then, we can define a pseudo time-reversal symmetry operator by $\tilde{\mathcal{T}} = C\bar{\mathcal{P}}^{-1} = -i\tau_z \otimes s_x\mathcal{K}$ with $\tilde{\mathcal{T}}^2 = +1$. Due to the presence of the chiral symmetry, the BdG Hamiltonian is an element of class BDI instead of class D and the topological properties can be determined by a $\mathbb{Z}$-invariant. However, the chiral symmetry is only exact in the effective model (2.25), since in the corresponding lattice Hamiltonian the chiral symmetry is broken by the interband spin-orbit coupling [107]. We will determine the topological properties of the system using the Majorana number (2.25)

$$\mathcal{M} = \mathrm{sign}\left(\Delta^2 + \mu^2 - V_Z^2\right) = \begin{cases} +1 & \text{for } V_Z < \sqrt{\Delta^2 + \mu^2}, \\ -1 & \text{for } V_Z > \sqrt{\Delta^2 + \mu^2}, \end{cases} \tag{2.31}$$

whose behavior is shown in Fig. 2.7. The topological phase transition occurs at the critical Zeeman energy $V_Z^c = \sqrt{\Delta^2 + \mu^2}$, for which in the BdG spectrum the energy gap at Γ-point is closed, see Fig. 2.5(b) and Fig. 2.7(a). For $V_Z < V_Z^c$ the spectrum is gapped and $\mathcal{M} = +1$, see Fig. 2.5. The energy gap is zero for $V_Z = V_Z^c$ (Fig. 2.5(b)), while for $V_Z > V_Z^c$ the energy gap opens again and $\mathcal{M} = -1$, see Fig. 2.5(c) and Fig. 2.7(a).

2.4.3. Zero energy modes

We will discuss the setup of the semiconductor-superconductor hybrid system in the article [109], where two regimes are considered. In the first regime the spin-orbit coupling at the chemical potential is larger than the Zeeman energy. In the second regime the spin-orbit coupling is weak. Here we will just discuss the strong spin-orbit coupling regime because it will show similarities to our case of the carbon nanotube setup.

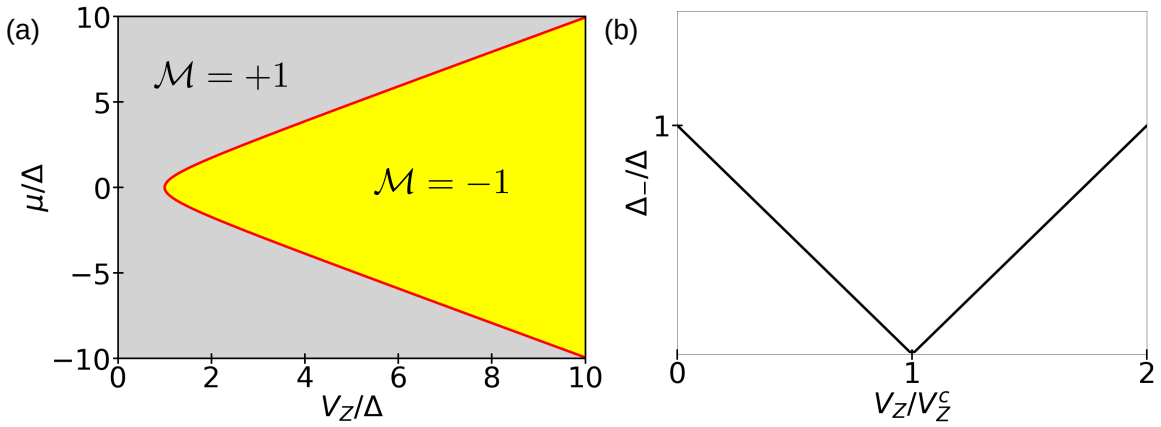

Figure 2.7: (a)The topological phase diagram obtained by the Majorana number (2.31). (b) The energy gap (2.27) as a function of the Zeeman energy V_Z. Both results are consistent with each other and predict the topological transition.

The first regime where the spin-orbit coupling is the largest energy scale is defined by $V_Z \ll \frac{m^\star \alpha_R^2}{\hbar^2}$ which leads to $k_F \approx 2k_R$ with k_R defined in section 2.4.1. In general, the superconducting gap is the smallest energy scale in the system and hence $\Delta \ll \frac{m^\star \alpha_R^2}{\hbar^2}$. Thus, the Zeeman energy and the superconducting gap can be considered as perturbations. The composition (spatial profile is also determined by the boundary condition and the length of the wire) of the Majorana bound states is determined by the BdG equation $\mathcal{H}_{\text{BdG}}\Psi = E\Psi$. For simplification, we work in the rotating frame by using a spin-dependent gauge transformation [110]. In real-space representation $k \to -i\partial_x$, the Hamiltonian for the quantum wire with Rashba spin-orbit coupling (2.20) is given by

$$H_{\text{Semi}} - \mu N = \int dx \Psi^\dagger(x) \left[\left(-\frac{\hbar^2 \partial_x^2}{2m^\star} - \mu \right) \mathbb{1} - i\alpha_R \hbar \partial_x s_z \right] \Psi(x), \tag{2.32}$$

with the spinor $\Psi^\dagger(x) = \left(\psi_\uparrow^\dagger(x), \psi_\downarrow^\dagger(x) \right)$ and the electron operator $\psi_s^\dagger(x)$ creating an electron with spin s at the position x. We will use the spin-dependent gauge transformation $\Psi^\dagger(x) = e^{ik_R s_z x} \tilde{\Psi}^\dagger(x)$ where $\tilde{\Psi}^\dagger(x)$ is the wave function in the rotating frame. Due to the gauge transformation the spin-orbit coupling is effectively eliminated

$$\tilde{H}_{\text{Semi}} - \mu \tilde{N} = \int dx \tilde{\Psi}^\dagger(x) \left(-\frac{\hbar^2 \partial_x^2}{2m^\star} - \mu \right) \mathbb{1} \tilde{\Psi}(x).$$

Moreover, the Zeeman term transforms as

$$H_Z = V_Z \int dx \Psi^\dagger(x) s_x \Psi(x) = V_Z \int dx \tilde{\Psi}^\dagger(x) \left(\cos(2k_R x) s_x - \sin(2k_R x) s_y \right) \tilde{\Psi}(x),$$

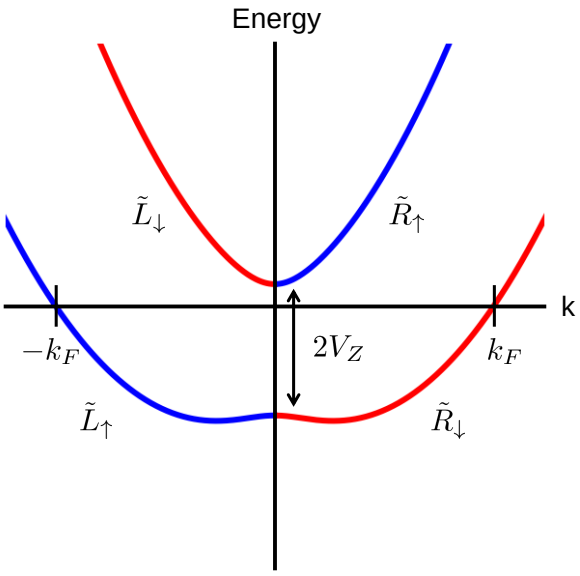

Figure 2.8: Energy spectrum and spin projection of the Hamiltonian (2.21). Eigenstates can classified into two branches: interior branches (states around $k = 0$) and exterior branches (states around $k = \pm k_F$). (Adapted from Ref. [109])

such that the magnetic field becomes a spiral $\mathbf{B} = B\left[\cos\left(2k_R x\right)\hat{\mathbf{x}} - \sin\left(2k_R x\right)\hat{\mathbf{y}}\right]$ where $\hat{\mathbf{x}}$ and $\hat{\mathbf{y}}$ are unit vectors in the corresponding directions, respectively. It follows that both Hamiltonians are equivalent. There are different methods to generate such a spatially rotating magnetic fields: by using nuclear spins [111], magnetic nanoparticles [112] or magnetic gates [113].

The BdG equation for zero energy solution can be solved by a linearization of the Hamiltonian around the Fermi points $\pm k_R$ and the electron operators $\tilde{\psi}_s(x) = e^{isk_R x}\psi_s(x)$ can be written in terms of right and left movers $\tilde{\psi}_s(x) = \tilde{R}_s(x)\, e^{ik_R x} + \tilde{L}_s(x)\, e^{-ik_R x}$, see Fig. 2.8. The linearized semiconductor Hamiltonian is given by

$$\tilde{H}_{\text{Semi}} = -i\hbar v_F \sum_s \int dx \left[\tilde{R}_s^\dagger(x)\,\partial_x \tilde{R}_s(x) - \tilde{L}_s^\dagger(x)\,\partial_x \tilde{L}_s(x)\right],$$

and the Zeeman Hamiltonian in the linearized basis is given by

$$\tilde{H}_Z = V_Z \sum_s \int dx \left[\tilde{\psi}_s^\dagger(x)\, e^{2isk_R x}\tilde{\psi}_{-s}(x)\right] \approx V_Z \int dx \left[\tilde{R}_\uparrow^\dagger(x)\,\tilde{L}_\downarrow(x) + \tilde{L}_\downarrow^\dagger(x)\,\tilde{R}_\uparrow(x)\right],$$

where we linearized the oscillating terms. The coupling of $\tilde{R}_\uparrow(x)$ and $\tilde{L}_\downarrow(x)$ leads to an energy gap at the Γ-point. Furthermore, the superconducting mean-field term becomes

$$\tilde{H}_{SC} = \Delta \sum_s \int dx \left[\tilde{R}_s^\dagger (x) \, \tilde{L}_{-s}^\dagger (x) + \tilde{L}_{-s} (x) \, \tilde{R}_s (x) \right].$$

The wave function of the Majorana bound state is determined by the zero energy solution of the BdG equation $\mathcal{H}_{\mathrm{BdG}} \varphi = 0$. Due to the linearization it is possible to define two Nambu spinors $\Psi_i (x) = \left(\tilde{R}_\uparrow (x) , \tilde{L}_\downarrow (x) , \tilde{R}_\uparrow^\dagger (x) , \tilde{L}_\uparrow^\dagger (x) \right)^T$ for the interior branch and $\Psi_e (x) = \left(\tilde{L}_\uparrow (x) , \tilde{R}_\downarrow (x) , \tilde{L}_\uparrow^\dagger (x) , \tilde{R}_\uparrow^\dagger (x) \right)^T$ for the exterior branch of the spectrum. Then, the two corresponding BdG Hamiltonians are given

$$\mathcal{H}_{\mathrm{BdG}}^{(i)} = -i\hbar v_F \partial_x s_z + V_Z s_x \tau_z + \Delta s_y \tau_y, \tag{2.33}$$

describing the interior branch, and for the exterior branch

$$\mathcal{H}_{\mathrm{BdG}}^{(e)} = -i\hbar v_F \partial_x s_z + \Delta s_y \tau_y, \tag{2.34}$$

where the Pauli matrices $s_{x,y,z}$ act on the spin space and $\tau_{x,y,z}$ in the Nambu space.

The zero energy solutions are two evanescent modes coming from the interior branch, where the decay wave vector is defined as $k_\pm^{(i)} = \frac{|\Delta_\pm|}{v_F \hbar}$ with $\Delta_\pm = \Delta \pm V_Z$, and two evanescent modes coming from the exterior branch with the decay wave vector $k^{(e)} = \frac{\Delta}{v_F \hbar}$. The corresponding four zero-energy eigenvectors are given by

$$\tilde{\varphi}_-^{(i)} (x) = \begin{pmatrix} -i \mathrm{sign} (\Delta_-) \, e^{-ik_R x} \\ e^{ik_R x} \\ i \mathrm{sign} (\Delta_-) \, e^{ik_R x} \\ e^{-ik_R x} \end{pmatrix} e^{-k_-^{(i)} x} \text{ and } \tilde{\varphi}_+^{(i)} (x) = \begin{pmatrix} e^{-ik_R x} \\ -ie^{ik_R x} \\ e^{ik_R x} \\ ie^{-ik_R x} \end{pmatrix} e^{-k_+^{(i)} x},$$

for the interior branch and for the exterior branch

$$\tilde{\varphi}_1^{(e)} (x) = \begin{pmatrix} ie^{ik_R x} \\ e^{-ik_R x} \\ -ie^{-ik_R x} \\ e^{ik_R x} \end{pmatrix} e^{-k^{(e)} x} \text{ and } \tilde{\varphi}_2^{(e)} (x) = \begin{pmatrix} e^{ik_R x} \\ ie^{-ik_R x} \\ e^{-ik_R x} \\ -ie^{ik_R x} \end{pmatrix} e^{-k^{(e)} x}.$$

By definition, this four solutions are Majorana solutions, i.e. the zero energy eigenstates of the BdG equation with the property to be also an eigenstate of the particle-hole symmetry operator. However, they do not fulfill the boundary condition and therefore they are not Majorana bound states. Thus, we need a superposition of the Majorana solutions, which we

will denote $\tilde{\varphi}_M(x)$, which fulfill the boundary condition $\tilde{\varphi}_M(x=0) \stackrel{!}{=} 0$. Here we neglect the overlap between the two Majorana bound states at each end because the length of the quantum wire L is large, such that we can assume a semi-infinite geometry with $\tilde{\varphi}_M(x=L)=0$. In the case of $V_Z > \Delta \Rightarrow \Delta_- < 0$, the two solutions $\tilde{\varphi}_-^{(i)}$ and $\tilde{\varphi}_1^{(e)}$ are linearly dependent at $x=0$. Thus, a Majorana bound state solution is given by $\tilde{\varphi}_M(x) = \tilde{\varphi}_-^{(i)}(x) - \tilde{\varphi}_1^{(e)}(x)$. By applying the inverse spin-dependent gauge transformation, the Majorana bound state has the form

$$\varphi_M(x) = \begin{pmatrix} i \\ 1 \\ -i \\ 1 \end{pmatrix} e^{-k_-^{(i)}x} - \begin{pmatrix} ie^{2ik_Rx} \\ e^{-2ik_Rx} \\ -ie^{-2ik_Rx} \\ e^{2ik_Rx} \end{pmatrix} e^{-k^{(e)}x}. \tag{2.35}$$

The boundary condition lifts the fourfold degeneracy of the Majorana solutions and thus we show the existence of a Majorana bound state solution at the left end of the nanowire. Furthermore, these two Majorana solutions have different localization lengths, $\xi^{(i)} = \frac{1}{k_-^{(i)}}$ and $\xi^{(e)} = \frac{1}{k^{(e)}}$ because the Majorana bound state is a superposition of two Majorana solutions coming from the two branches of the energy spectrum.

2.5. Experimental realization

Theoretically, we have shown the presence of Majorana states in nanowires with proximity-induced superconductivity. There are several experiments which probe by tunneling spectroscopy the Majorana states in the semiconductor-superconductor hybrid system [21, 33–36]. Tunnelling spectroscopy is measuring the local density of states and with this the the energy spectrum of the system. In general, if Majorana bound states exists in the system, then the differential conductance shows a zero-bias peak in the topological non-trivial phase [114]. Recently, a new experiment demonstrated high-quality contact between an InSb nanowire and Al superconductor [34]. Hence, the contact enable ballistic transport and thus the influence due to disorder can be neglected. Fig. 2.9(a) shows the device where the InSb nanowire (grey) is partially in contact with a thin Al superconductor (green). The tunnel gates (coral red) induces a tunnel barrier between the left contact (yellow) and the superconductor. The zero-bias peak is shown in Fig. 2.9(b) (experiment) and (d) (simulation) in a transport spectroscopy displaying $\frac{dI}{dV}$ as a function of voltage bias, V, and magnetic field, B (aligned with the nanowire axis). Figure 2.9(c) shows two cuts from Fig. 2.9(b) and (d) extracted at $B=0$ and 0.88T. In the measurement and the simulation, the zero-bias peak reaches the exptected value of $2\frac{e^2}{h}$.

In Tab. 4 properties of the semiconductors InAs and InSb are presented. Depending on the experiment, the Rashba spin-orbit coupling strength α_R and the Landé g-factor vary, but

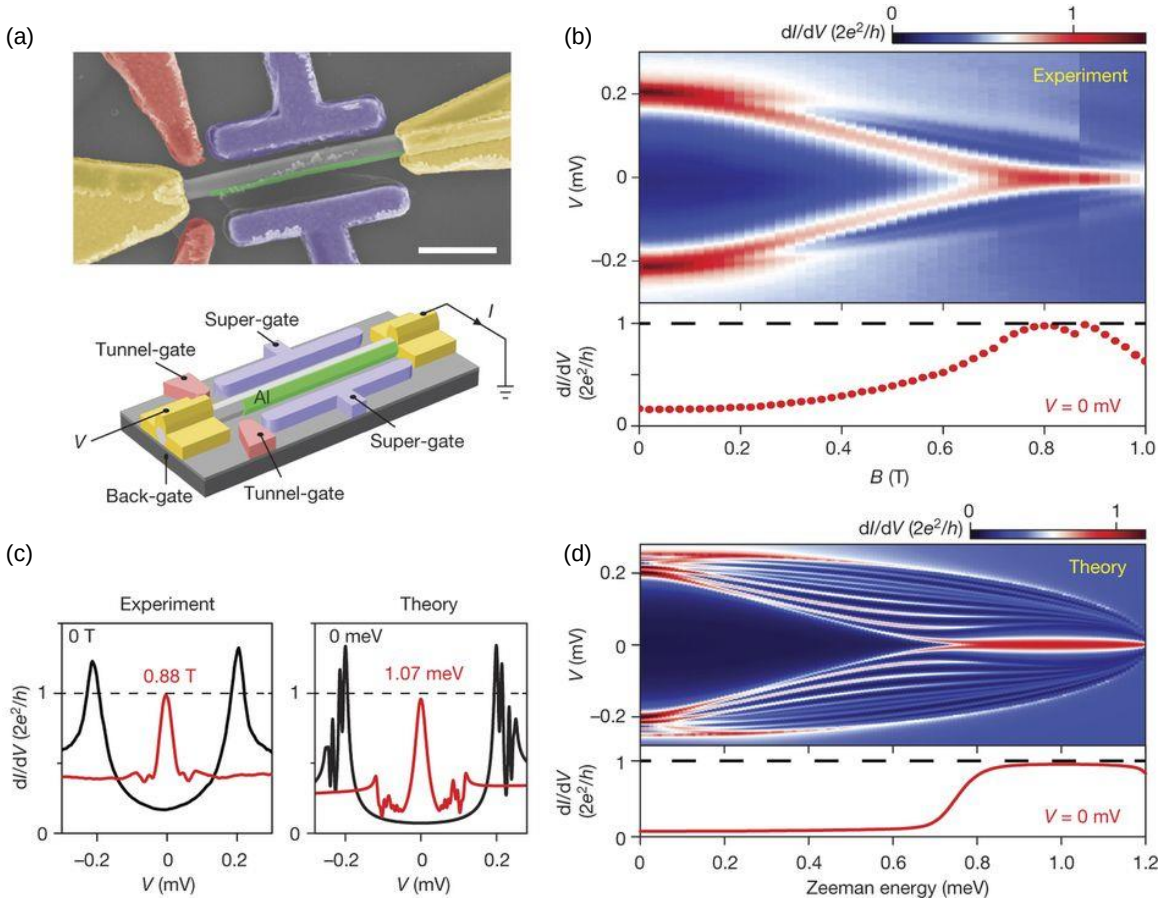

Figure 2.9: (a) Setup of the InSb nanowire and Al superconductor. (b) The result of the measurement as a function of the magnetic field. (c) Result of the measurement and the simulation at different magnetic fields $B = 0$T (black) and 0.88T (red). (d) Result of the corresponding simulation with a chemical potential $\mu = 0.3$meV. (Source: [34]).

Semiconductors	InAs	InSb
Effective mass $m^\star$	$0.023m_e$	$0.014m_e$
Spin-orbit coupling strength α_R	$0.2 - 0.8$eVÅ	$0.2 - 1$eVÅ
g-factor	$8 - 15$	$40 - 50$

Table 4: Properties of the semiconductors InAs and InSb for different experiments (Adapted from Ref. [32]).

Interface	InSb-NbTiN [21, 33]	InSb - Al [34]	InAs-Al [35, 36]
Induced gap Δ	$0.25 - 0.65$meV	$0.2 - 0.3$meV	$0.2 - 0.27$meV

Table 5: Proximity-induced superconducting gap for different configurations (Adapted from Ref. [32]).

are very strong. In the experiments with InSb nanowires, g-factor is much larger compared to experiments with InAs. This leads that in experiments with InSb a smaller external magnetic field is needed for the topological transition. In experiments Al and NbTiN have been primarily used for the superconducting materials. The induced superconducting gap can be determined by tunneling spectrospy in the case of zero magnetic field $V_Z = 0$. There are several measurements of the proximity-induced superconducting gap Δ for different setups, see Tab. 5.

In the experimental setup, signatures of Majorana states include e.g. a quantized zero-bias peak emerging in transport spectra while sweeping the magnetic field [114], see Fig. 2.9(b) and (d). Zero-bias peaks can however also emerge due to the coalescence of Andreev bound states [35, 115] - naturally occurring in confined normal conductor-superconductor systems - or due to the development of Kondo correlations [116].

An unambiguous theoretical confirmation of the experimental observation of Majorana bound states would require an accurate microscopic modeling of the nanowires. Diameters of many tens of nanometers and lengths of several micrometers hinder truly microscopic calculations of the electronic spectrum of finite systems. This is problematic since the real space models of semiconductor nanowires are usually constructed in a top-down approach, starting with an effective model and quantizing it on a chosen crystal lattice [39]. Without accurate modelling of experimental setups one can make only qualitative, rather than quantitative predictions of the properties of the system. This difficulty is strongly reduced if the host for topological features is a carbon nanotube. Due to their small diameter, they can be considered as truly one-dimensional conductors with one relevant transverse mode for each valley and spin. The low energy spectrum of the carbon nanotubes is well described in terms of tight-binding models for carbon atoms on a rolled graphene lattice [117]. Experimental advances in the preparation of ultraclean carbon nanotubes have allowed us to measure their transport spectra in various transport regimes [118], and hence to gain confidence in the accuracy of the theoretical modeling. The use of carbon nanotubes for topological superconductivity is the topic of the following chapters.

3. Carbon nanotubes

The discoveries of graphene and carbon nanotubes were breakthroughs for the material sciences and condensed matter physics. In the first part we introduce the atomic structure of graphene and carbon nanotubes. Then, we discuss three models of carbon nanotubes. The two first models are based on a translational construction of the carbon nanotube. In the first model built in the real space we include a perpendicular magnetic field and a valley mixing. From this model we derive an effective model in the reciprocal space, valid at low magnetic fields. The last model is based on the helical-angular construction of the carbon nanotube, again in the real space.

Finally, we discuss a microscopic model of superconducting correlations in carbon nanotubes based on lattice symmetry arguments, i.e. invariant under the D_{6h} lattice symmetry of the honeycomb lattice. We treat the superconducting correlations in the spirit of Ref. [119], admitting both the on-site and nearest-neighbor pairing Δ_0 and Δ_1. The results of this chapter have been published in Phys. Rev. B **96**, 125414 (2017) and Phys. Rev. B **97**, 075141 (2018).

3.1. Structure of graphene and carbon nanotubes

Graphene is a two-dimensional, monoatomic graphite structure where the lattice structure is given by a honeycomb lattice. The carbon atoms are correlated by a strong covalent bonds caused by the sp^2 hybridization of the orbitals $2s$, $2p_x$ and $2p_y$. The π bonds are defined by the $2p_z$ orbitals which are perpendicular to the lattice plane. While the σ bonds are defined by the in-plane orbitals [120]. The underlying Bravais lattice has a trigonal structure, where each unit cell contains the two basis atoms A and B, located at $\mathbf{R}+\mathbf{r}_\mathrm{A}$ and $\mathbf{R}+\mathbf{r}_\mathrm{B}$, see Fig. 3.1. The distance between two neighboring carbon atoms is approximately given by $a_c = 1.42\mathring{A}$ and the lattice constant is $a = \sqrt{3}a_c = 2.46\mathring{A}$. The basis vectors of lattice are defined as

$$\mathbf{a}_1 = \left(\sqrt{3}a_c,\, 0\right),\, \mathbf{a}_2 = \left(\frac{\sqrt{3}a_c}{2},\, \frac{3a_c}{2}\right).$$

The corressponding reciprocal lattice is defined by $\mathbf{a}_i\mathbf{b}_j = 2\pi\delta_{ij}$ and yields

$$\mathbf{b}_1 = \left(\frac{2\pi}{\sqrt{3}a_c},\, -\frac{2\pi}{3a_c}\right),\, \mathbf{b}_2 = \left(0,\, \frac{4\pi}{3a_c}\right).$$

Therefore, the reciprocal lattice constant is given by $\frac{4\pi}{\sqrt{3}a_c}$. The vectors connecting an atom of sublattice A with its nearest neighbors, the surrounding atoms of sublattice B, are given

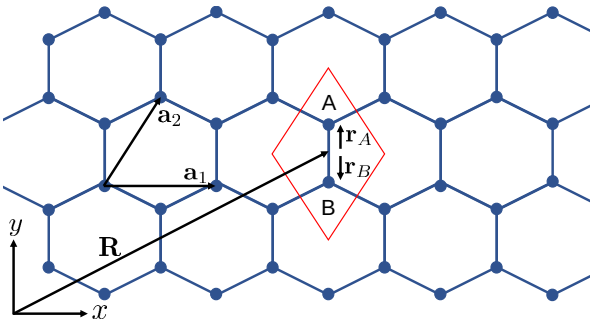

Figure 3.1: A segment of the graphene lattice including the unit cell (in red), the two sublattices, A and B and the two basis vector $\mathbf{a}_1$ and $\mathbf{a}_2$.

by

$$\mathbf{d}_1 = (0,\, a_c)\,,\, \mathbf{d}_2 = -\frac{a_c}{2}\left(\sqrt{3},\, 1\right),\, \mathbf{d}_3 = \frac{a_c}{2}\left(\sqrt{3},\, -1\right). \tag{3.1}$$

Singlewall carbon nanotubes are made out of a single graphene sheet rolled up into a nanotube [117][6]. Carbon nanotubes can be categorized in chiral and achiral tubes. The two achiral types of nanotubes are the so-called armchair and zigzag. Zigzag and armchair nanotubes are so called because of the shape of the edge formed by a cut perpendicular to the nanotube axis, see the red lines in Fig. 3.2. A carbon nanotube can be classified by the chiral vector $\mathbf{C}$ which can be expressed in terms of the basis of the graphene basis vectors as

$$\mathbf{C} = n\mathbf{a}_1 + m\mathbf{a}_2 := (n,\, m) \;\text{ with } n,\, m \in \mathbb{Z}. \tag{3.2}$$

The length of $\mathbf{C}$ defines the circumference of the nanotube. The radius of the carbon nanotube is given by

$$R = \frac{|\mathbf{C}|}{2\pi} = \frac{\sqrt{3}a_c\sqrt{n^2+m^2+nm}}{2\pi}. \tag{3.3}$$

The chiral angle θ is defined as the angle between the chiral vector and the x-axis

$$\theta = \arccos\left(\frac{\mathbf{C}\cdot\mathbf{a}_1}{|\mathbf{C}|\,|\mathbf{a}_1|}\right) = \arccos\left(\frac{2n+m}{2\sqrt{n^2+m^2+nm}}\right).$$

Furthermore, the chiral angle describes the rotation between carbon nanotube $\left(x_\perp,\, x_\parallel\right)$ and graphene coordinate system $(x,\, y)$. The value of θ is in the range $0 \le \theta \le \frac{\pi}{6}$, because of the hexagonal symmetry of the graphene sheet. Nanotubes with $\theta = 0$ are pure zigzag nanotubes and with $\theta = \frac{\pi}{6}$ are pure armchair. The unit cell of the carbon nanotube is spanned by the chiral vector $\mathbf{C}$ and the primitive translation $\mathbf{T}$ in $x_\parallel$ direction, see Fig. 3.2.

[6] Earlier, multiwall carbon nanotubes were discovered in 1991 by S. Iijima [121].

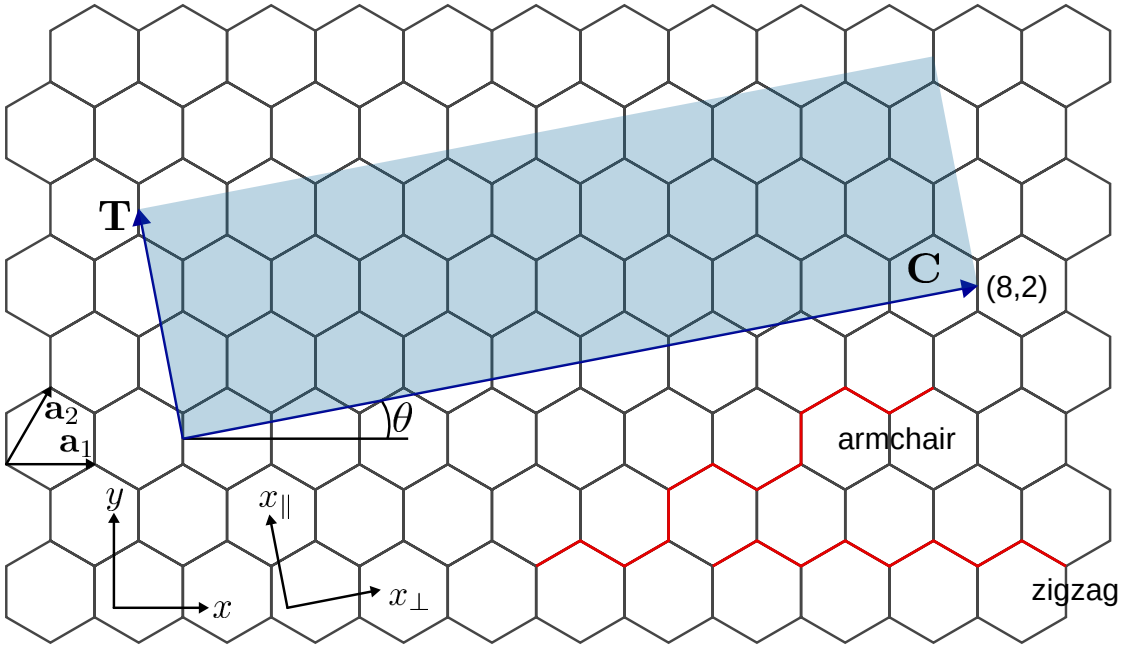

Figure 3.2: The translational unit cell (blue area) for a $\mathbf{C} = (8, 2)$ carbon nanotube. Moreover, the red lines corresponds to the edges of armchair and zigzag carbon nanotubes. (Source: [122])

3.2. Band structure of graphene

The band structure of graphene can be obtained using two different methods: the $\mathbf{k}\cdot\mathbf{p}$ method [123] or a tight binding calculation [124]. In this thesis, we will use the tight binding method to determine the electronic spectrum of graphene and later of carbon nanotubes. In the tight binding approach we assume that the only contribution to the energy comes from the nearest-neighbor hopping. Next-nearest neighbor contributions have a small effect on the electronic band structure and will not be discussed here. Furthermore, we set the energy of an isolated p_z orbital to zero. We define $t = V_{pp}^{\pi}$ as transfer integrals. Then, the Hamiltonian for graphene in real-space representation and in the notation of second quantization can be written as

$$H_0 = -t \sum_{\langle i,j\rangle,s} \left(a_{is}^{\dagger} b_{js} + b_{js}^{\dagger} a_{is} \right), \tag{3.4}$$

where a_{is} annihilates an electron on lattice site $\mathbf{R}_i$ on sublattice A with spin s, and b_{js} annihilates an electron on lattice site $\mathbf{R}_j$ on sublattice B with spin s. For obtaining the energy spectrum a Fourier transformation into reciprocal space must be done. The Fourier transformation is defined in the following way

$$a_{is} = \frac{1}{\sqrt{N}} \sum_{\mathbf{k}} e^{i\mathbf{k}\mathbf{R}_i} a_{\mathbf{k}s},$$
$$b_{is} = \frac{1}{\sqrt{N}} \sum_{\mathbf{k}} e^{i\mathbf{k}\mathbf{R}_i} b_{\mathbf{k}s}.$$

Then, the tight-binding Hamiltonian of graphene in reciprocal space and basis $\Psi_{\mathbf{k}} = (a_{\mathbf{k}s},\, b_{\mathbf{k}s})^T$ is given by

$$H_0(\mathbf{k}) = \begin{pmatrix} 0 & \gamma_0(\mathbf{k}) \\ \gamma_0^\star(\mathbf{k}) & 0 \end{pmatrix}, \tag{3.5}$$

where $\gamma_0(\mathbf{k}) = -t\left(1 + e^{i\mathbf{k}\mathbf{a}_1} + e^{-i\mathbf{k}\mathbf{a}_2}\right)$. The Hamiltonian can be diagonalized by the unitary transformation

$$\begin{pmatrix} a_{\mathbf{k}s} \\ b_{\mathbf{k}s} \end{pmatrix} = \frac{1}{\sqrt{2}} \begin{pmatrix} e^{i\eta(\mathbf{k})} & e^{i\eta(\mathbf{k})} \\ e^{-i\eta(\mathbf{k})} & -e^{-i\eta(\mathbf{k})} \end{pmatrix} \begin{pmatrix} c_{\mathbf{k}s} \\ d_{\mathbf{k}s} \end{pmatrix}, \tag{3.6}$$

where $c^\dagger_{\mathbf{k}s}$ creates an electron with the momentum $\mathbf{k}$ and spin s in the conduction band and $d^\dagger_{\mathbf{k}s}$ creates an electron in the valence band with the momentum $\mathbf{k}$ and spin s. The phase $\eta(\mathbf{k})$ is the phase of $\gamma(\mathbf{k})$, i.e. $\eta(\mathbf{k}) = \arg(\gamma(\mathbf{k}))$. The energy spectrum with a valence and a conduction band $E_{\mathbf{k}} = \pm|\gamma_0(\mathbf{k})|$ is

$$|\gamma_0(\mathbf{k})| = t\sqrt{1 + 4\cos^2\left(\frac{\sqrt{3}}{2}k_x a_c\right) + 4\cos\left(\frac{\sqrt{3}}{2}k_x a_c\right)\cos\left(\frac{3}{2}k_y a_c\right)}. \tag{3.7}$$

The Fermi surface is defined by six Fermi points, where only two of them are independent. The energy spectrum is shown in Fig. 3.3. Then, the low-energy spectrum is given by an expansion around the two Fermi points

$$\mathbf{K} = \left(-\frac{4\pi}{3\sqrt{3}a_c},\, 0\right)\ (\tau = +1),\ \mathbf{K}' = \left(\frac{4\pi}{3\sqrt{3}a_c},\, 0\right)\ (\tau = -1). \tag{3.8}$$

The Hamiltonian at low energies becomes

$$H_\tau(\boldsymbol{\kappa}) = v_F\hbar \begin{pmatrix} 0 & \tau\kappa_x + i\kappa_y \\ \tau\kappa_x - i\kappa_y & 0 \end{pmatrix}, \tag{3.9}$$

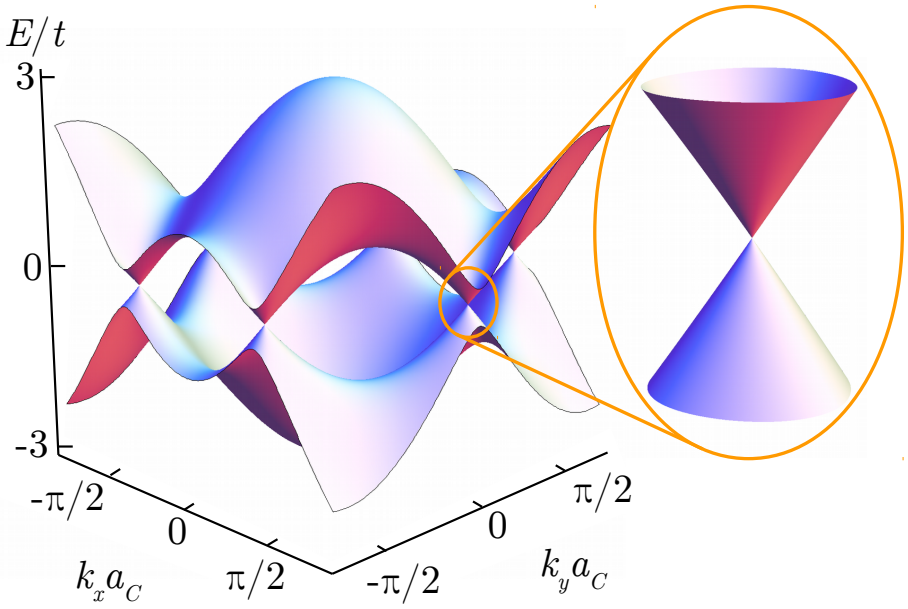

Figure 3.3: The energy spectrum of graphene as a function the momentum. A zoom of the spectrum around the Fermi points shows the linearity of the energy spectrum.

with $v_F = \frac{3}{2\hbar} a_c V_{pp}^{\pi}$, and $\boldsymbol{\kappa}$ defined via $\mathbf{k}_\tau = \tau \mathbf{K} + \boldsymbol{\kappa}$. Due to the fact that the remaining four Fermi points are the K, K' points shifted by reciprocal lattice vectors, it is enough to treat only two opposite Dirac cones. The two Dirac cones are called *valleys*. The resulting dispersion relation for low energies reads

$$E_{\pm}(\boldsymbol{\kappa}) = \pm v_F \hbar \sqrt{(\kappa_x)^2 + (\kappa_y)^2}. \tag{3.10}$$

We see in Eq. (3.10) and in the zoom of Fig. 3.3 that the low-energy excitations are described by a two-dimensional, massless Dirac equation. In contrast to the high-energey physic case, the electrons moves with a Fermi velocity given by $v_F \approx 10^6 \mathrm{m/s}$ [120]. A lot properties of graphene can be described by non-interacting fermions. However, interacting graphene can not be described by Landau Fermi liquid [125], because the density of states at the Dirac points vanishes in undoped graphene. However, this problem is well known from quantum electrodynamics and can be solved by using methods from quantum electrodynamics which renormalized the density of states and Fermi velocity v_F nearby the Dirac points. The resulting theory of interacting graphene is called *Dirac liquid* [126].

3.3. From graphene to carbon nanotubes - Curvature effects

Like in graphene, the energy spectrum in nanotubes shows the presence of two valleys K and K' which are characterized by the quantum number τ. However, the curvature of a carbon nanotube modifies the energy spectrum, leading a curvature induced band gap and an enhanced spin-orbit coupling [118, 127–130]. The tiny diameter of the nanotubes reduces the

number of relevant transverse modes to exactly one in the low-energy regime, with spin and valley degeneracy. A derivation of the effective low-energy Hamiltonian from the microscopic model can be found in Refs. [127, 131]. By using the chiral angle θ the graphene coordinate system can be rotated into the nanotube coordinate system by

$$\begin{pmatrix} e_x \\ e_y \end{pmatrix} = \begin{pmatrix} \cos(\theta) & -\sin(\theta) \\ \sin(\theta) & \cos(\theta) \end{pmatrix} \begin{pmatrix} e_\perp \\ e_\parallel \end{pmatrix}, \tag{3.11}$$

The low-energy Hamiltonian (3.9) is given in this basis by

$$H_\tau(\boldsymbol{\kappa}) = v_F \hbar \begin{pmatrix} 0 & e^{i\tau\theta}\left(\tau\kappa_\perp + i\kappa_\parallel\right) \\ e^{-i\tau\theta}\left(\tau\kappa_\perp - i\kappa_\parallel\right) & 0 \end{pmatrix}. \tag{3.12}$$

The Hamiltonian of a carbon nanotube in the reciprocal space is obtained using a zone folding technique [132, 133]. The spectrum of the carbon nanotube follows from that of graphene by imposing the periodic boundary conditions on the value of transverse momentum, which is then quantized, turning the two-dimensional dispersion of graphene into a series of one-dimensional cuts $E(k)$[7], which are the carbon nanotube's one-dimensional subbands [117]. The periodic boundary around the nanotube circumference leads to the quantization condition of the transverse momentum

$$k_\perp x_\perp + 2\pi R k_\perp = k_\perp x_\perp + 2\pi l_\perp, \tag{3.13}$$

which implies $k_\perp = \frac{l_\perp}{R}$ where $l_\perp$ is the angular momentum. A sketch is shown with the angular momentum states in Fig. 3.4. The index $l_\perp$ defines a discrete set of $\mathbf{k}$ vectors which are allowed in the reciprocal space. Figure 3.5(a)-(c) shows the Brillouin zones of different kinds of carbon nanotubes and the corresponding quantization lines. Further, in Fig. 3.5(d)-(f) are shown the corresponding one-dimensional energy spectrum. In the case of a metallic carbon nanotube, the quantization lines the quantization lines cross the Dirac points, resulting in a linear energy spectrum near the Dirac points, see Fig. 3.5(c) and (f) for the spectrum. However, in semiconducting carbon nanotube nanotube, the spetrum is gapped and the quantization lines do not cross the Dirac points, see Fig. 3.5(a) and (d) for the spectrum. In general, The conditon for the metallicity can be determined from the chiral index (m, n) and is given by

$$m - n \bmod 3 \begin{cases} = 0 & \text{metallic,} \\ \neq 0 & \text{semiconducting.} \end{cases} \tag{3.14}$$

[7] From now on we will use k instead of $k_\parallel$.

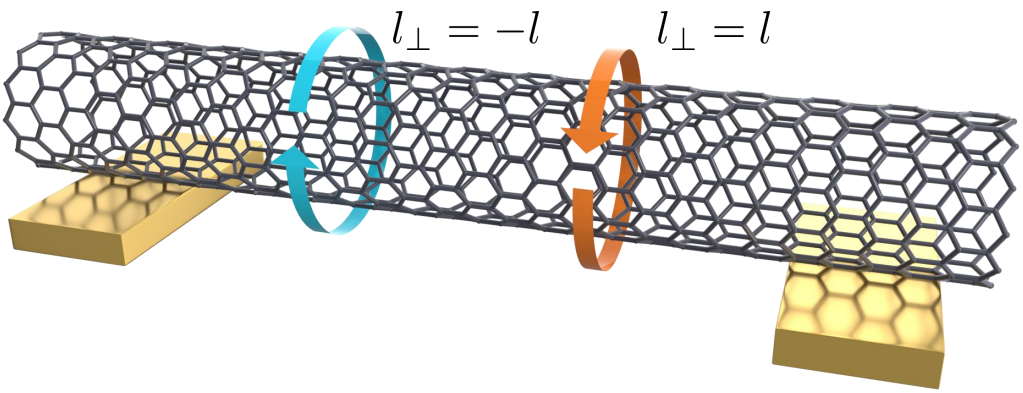

Figure 3.4: Schematic of a carbon nanotube device including the angular momentum states. (Source: [122])

The chiral index can also be used to classify nanotubes into zigzag and armchair class

$$m - n \bmod 3\text{d} \begin{cases} = 0 & \text{armchair class,} \\ \neq 0 & \text{zigzag class.} \end{cases} \tag{3.15}$$

In contrast to the condition for metallicity, the greatest common divisor $d = \gcd(m, n)$ of m and n is included in the condition. The difference between the zigzag and armchair class is the position of Fermi points k_F. In the case of a nanotube in zigzag class $k_F = 0$ and in armchair class k_F is finite. Zigzag and chiral nanotubes can be either metallic or semiconducting, but every armchair nanotube is metallic. In Fig. 3.5(a) we have a zigzag carbon nanotube, in 3.5(b) a chiral carbon nanotube and in 3.5(c) in the armchair class. In general, the energy spectrum of carbon nanotubes features two Fermi points at opposite k, see Fig. 3.5(e)-(f). However, in the case of zigzag class carbon nanotubes the Fermi points are at $k = 0$, see Fig. 3.5(d).

When the curvature of the carbon nanotube's lattice is included, it results in both spin-dependent and spin-independent modifications of graphene's dispersion, which can be treated in a perturbative way. They are most significant near the Dirac points of the spectrum. There are two spin-independent modifications of the energy spectrum. One modification is a negligible renormalization of the Fermi velocity [128]. Secondly, the C_3 rotational symmetry of the lattice is broken and the Dirac points are shifted by the vector $\Delta\mathbf{k}^c$ [128, 134]. Since states in the two valleys are time-reversed conjugates of each other the shift is opposite for K and K'. The components of the vector are given by

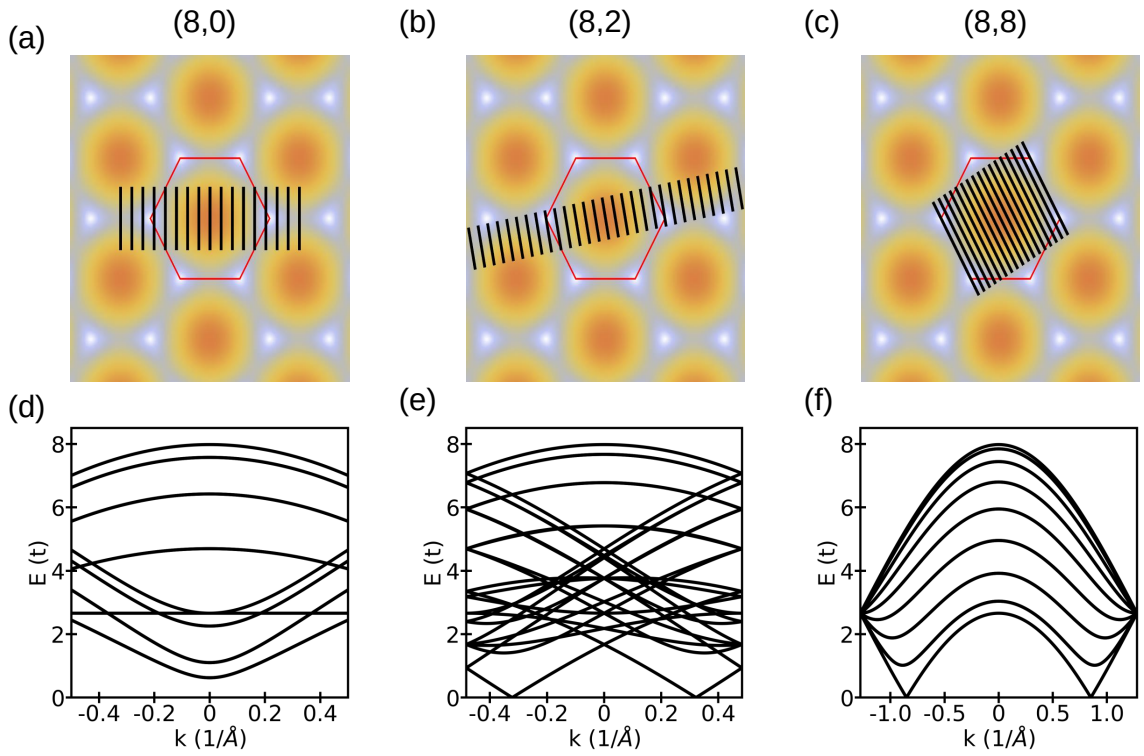

Figure 3.5: (a)-(c) The energy spectrum of graphene (color map), with the first Brillouin zone shown in red and transverse momentum quantization for a (a) (8, 0), (b) (8,2) and (c) (8,8) carbon nanotube shown in black. (d)-(f) One-dimensional cuts of the energy spectrum.

$$\Delta k_{\perp}^{c} = \frac{a_C}{4R^2}\left(1 + \frac{3}{8}\frac{V_{pp}^{\sigma} - V_{pp}^{\pi}}{V_{pp}^{\pi}}\right)\cos\left(3\theta\right), \tag{3.16}$$

$$\Delta k_{\parallel}^{c} = -\frac{a_C}{4R^2}\left(1 + \frac{5}{8}\frac{V_{pp}^{\sigma} - V_{pp}^{\pi}}{V_{pp}^{\pi}}\right)\sin\left(3\theta\right), \tag{3.17}$$

where $\Delta k_{\perp}^{c}$ is the component perpendicular and $\Delta k_{\perp}^{c}$ parallel to the nanotube axis. Both components depending on 3θ. Therefore, the influence of the shift $|\Delta\mathbf{k}^{c}|$ is different. For semiconducting carbon nanotubes the influence is small compared to $\kappa_{\perp}$. However, for metallic nanotubes, the shift opens a band gap $E_G = 2v_F\hbar\,|\Delta k_{\perp}^{c}|$. From the condition $\theta = \frac{\pi}{6}$ it follows that pure armchair carbon nanotubes are purely metallic nanotubes.

The tiny spin-orbit coupling of graphene becomes significantly enhanced in carbon nanotubes due to the curvature of their atomic lattice [127–130], leading to a spin-dependent hopping parameter

$$t \to \begin{pmatrix} t_{\uparrow\uparrow} & t_{\uparrow\downarrow} \\ t_{\downarrow\uparrow} & t_{\downarrow\downarrow} \end{pmatrix}, \tag{3.18}$$

where $t_{ss'}$ is the spin-dependent hopping matrix elements. This implies a spin-dependent

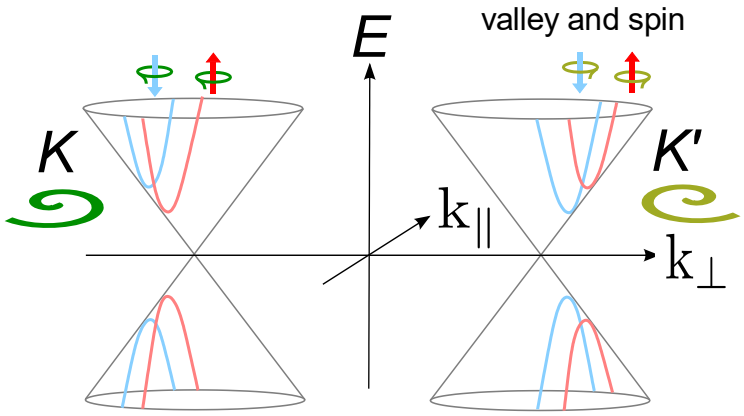

Figure 3.6: Sketch of the low energy spectrum of a carbon nanotube as a function of the parallel $k_\parallel$ and perpendicular $k_\perp$ momentum with respect to the CNT axis. In blue (spin down) and red (spin up) we show the hyperbolic one-dimensional spin-resolved energy cuts including curvature gaps and spin-orbit splitting.

modification of the $k_\perp$ momentum. The spin-dependent shift term becomes

$$\Delta k_\perp^{\mathrm{SO}} = \frac{2\delta}{R}\left(1 + \frac{3}{8}\frac{V_{pp}^{\sigma} - V_{pp}^{\pi}}{V_{pp}^{\pi}}\right). \tag{3.19}$$

More detailed calculations taking into account all four valence electrons show that there is actually a second type of spin-orbit coupling term $\Delta E_{\mathrm{SOC}} = \tau s \Delta_{\mathrm{SO}}^1$, corresponding to a Zeeman-like coupling [128]. The spin-orbit coupling shift $\Delta k_\perp^{\mathrm{SO}}$ corresponds to a Rashba spin-orbit coupling.

The low-energy spectrum of a carbon nanotube in the conduction band for given transverse momentum $k_\perp$ and longitudinal momentum k is then given by

$$\varepsilon_{\tau s}(k, k_\perp) = \hbar v_F \sqrt{\left(k - \tau K_\parallel + \tau \Delta k_\parallel^c\right)^2 + \left(k_\perp - \tau K_\perp + \tau \Delta k_\perp^c + s\Delta k_\perp^{\mathrm{SO}}\right)^2} + \tau s \Delta_{\mathrm{SO}}^1, \tag{3.20}$$

where $K_\perp$, $K_\parallel$ are the transverse and longitudinal component of momentum at the Dirac point K. The quantum numbers τ and s stand for the valley ($K: \ \tau = 1$, $K': \ \tau = -1$) and the spin component along the CNT axis $s = \pm 1$. A sketch of the low-energy spectrum including curvature effects is shown in Fig. 3.6. All quantities in this dispersion are directly related to the hopping integrals across π (V_{pp}^{π}) and σ bonds (V_{pp}^{σ}) in graphene, to nanotube geometry and to carbon's intrinsic spin-orbit coupling [127, 135]. Their values and signs may vary, depending on which set of tight-binding parameters is used. The spin-orbit coupling defines a quantization axis for the spin, along the CNT axis, and induces a band splitting $\Delta_{\mathrm{SO}}^0 = \varepsilon_{K\uparrow}(0) - \varepsilon_{K\downarrow}(0)$, which is reported to reach values larger than 3 meV [136]. Note that

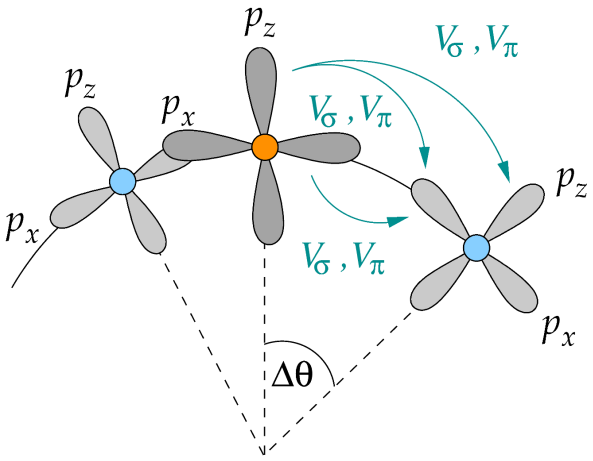

Figure 3.7: A sketch of a carbon nanotube and the corresponding orbitals to see the influence of the curvature. (Source: [135])

the single-particle energies satisfy the time-reversal conjugation $\varepsilon_{\tau s}(k) = \varepsilon_{-\tau -s}(-k)$.

3.4. Finite size carbon nanotubes

We have dealt so far with the properties of infinitely long carbon nanotubes. In reality, carbon nanotubes have a finite length. The wave functions have to obey open boundary conditions in longitudinal direction. Hence, the corresponding momentum $k' = k - \tau K_\parallel + \tau \Delta k_\parallel^c$ has to be quantized as a function of $k'_\perp = k_\perp - \tau K_\perp + \tau \Delta k_\perp^c + s\Delta k_\perp^{\mathrm{SO}}$. The full detailed calculation for both cases of zigzag and armchair class can be found in the Refs. [135, 137]. We will skip the case of armchair class carbon nanotubes. By considering the edge structure of zigzag-like carbon nanotube, the sublattice wave functions must satisfy the open boundary condition $\Psi_{A\tau s}(x = 0,\, x_\perp) \stackrel{!}{=} 0$ and $\Psi_{B\tau s}(x = L,\, x_\perp) \stackrel{!}{=} 0$. Then, the condition leads to the quantization condition for the longitudinal momentum component

$$\frac{\tau k'_\perp + ik'}{\tau k'_\perp - ik'} = e^{2ik'L}. \tag{3.21}$$

Another way of treating the finiteness of the carbon nanotubes is to simulate the system by a microscopic tight binding model in the real space. The microscopic model of the nanotube which we use, with one p_z orbital per atomic site, is shown schematically in Fig. 3.7. The hopping matrix elements, taking into account the hybridization between σ and π orbitals and the spin-orbit coupling induced by the curvature, are now spin-dependet and given by the formulae in Refs. [127, 135]. In our calculations we chose $V_{pp}^\sigma = 6.38$ eV and $V_{pp}^\pi = -2.66$ eV after Ref. [138], and we set the small parameter controlling nanotube's spin-orbit coupling to $\delta_{SO} = 3 \cdot 10^{-3}$, similar to $2.8 \cdot 10^{-3}$ measured in Ref. [139]. The real space carbon nanotube Hamiltonian is given by

$$H_{\mathrm{CNT}} = \sum_{\langle i,j\rangle, ss'} t_{ij,ss'} c_{is}^{\dagger} c_{js'}, \tag{3.22}$$

where i indexes the atomic positions, s is the spin, and $t_{ij,ss'}$ is the spin-dependent nearest neighbor hopping [127], $\langle i,j\rangle$ denotes a sum over the nearest neighbor atoms. Finite carbon nanotubes can host edge states whose energies lie in the bulk band gap and there is a one-to-one correspondence between the number of edge states and the winding number [140].

3.5. Four-band model: effects due to valley mixing and transverse magnetic fields

The energy spectrum of (3.12) is fourfold degenerate due to the valley and spin quantum numbers which has been confirmed by tunneling spectroscopy measurements [141, 142]. In ultraclean carbon nanotubes measurements show a lifting of the fourfold degeneracy caused by spin-orbit coupling and a mixing of the two valleys K and K' states [129, 136, 139]. Although the valley mixing indicates scattering between states in different valleys with the same spin, it does not reveal specific details of its microscopic origin. There are three mechanisms which can cause the valley mixing: i) scattering off impurities [129], ii) scattering off the nanotube ends [137, 140] or iii) breaking of the rotational symmetry e.g. by a substrate. In the microscopic simulation the valley mixing is due to the substrate and the tight binding Hamiltonian is given by

$$H_V = \sum_{i,s} V(\varphi_i) c_{is}^{\dagger} c_{is}, \tag{3.23}$$

where i indexes the atomic positions, s is the spin, and $V(\varphi_i)$ is the potential induced by the substrate at the i-th nanotube atom. It depends on the atom's height above the substrate, i.e. on its angular coordinate φ_i. Further details can be found in Appendix B.

The application of a uniform external magnetic field has profound consequences for the band structure of carbon nanotubes. When the magnetic field is applied, the electrons within the nanotube are influenced by the electromagnetic potential, whose effect is to add a phase factor to the hopping matrix element

$$t_{ij} \to t_{ij}(\mathbf{B}) = t \exp\left(i \frac{e}{\hbar} \int_{\mathbf{R}_i}^{\mathbf{R}_j} d\mathbf{r} \cdot \mathbf{A}(\mathbf{r}) \right), \tag{3.24}$$

where i and j are the lattice sites where the hopping occurs. The phase factor is known as the Peierls phase factor [143]. Furthermore, a Zeeman term $H_Z = \frac{g_s}{2} \mu_B \mathbf{B} \cdot \mathbf{s}$ must be included. In the parallel field the effect due to the Peierls phase is much stronger than the Zeeman

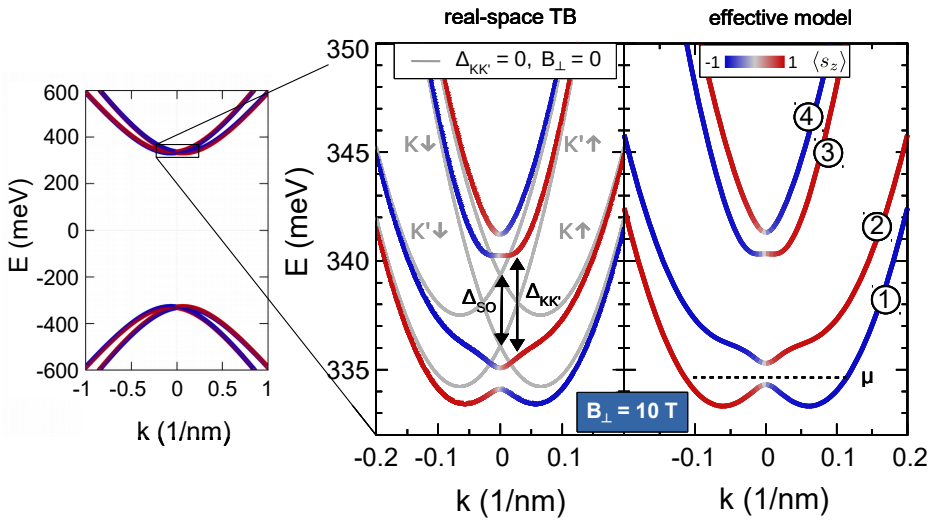

Figure 3.8: The energy bands of a (12,4) nanotube in the vicinity of the Dirac points are shown in the leftmost plot, with red/blue corresponding to spin up/down (quantized along the nanotube axis) bands. Our region of interest here is the neighborhood of the Γ point in the conduction band. The enlarged plots show the spectrum in this region, obtained both in the real-space tight-binding calculation and in an analytical effective model. The spin-orbit splitting between the Kramers doublets at $k = 0, B_\perp = 0$ is Δ_{SO} (here equal 2 meV), and the width of the anticrossing opening between different valley states is $\Delta_{KK'}$ (here 2.5 meV). Grey lines shown in the plot correspond to subbands without the valley mixing. There we can assign spin and valley quantum number to each band. With the valley mixing, $B_\perp$ is able to open a gap at $k = 0$.

term and leads to Aharonov-Bohm phenomena [144]. In the case where the magnetic field is applied perpendicular to the nanotube axis, the situation is changing completely. Now, the Peierls phase is much smaller than the Zeeman energy and can be neglected.

With added valley-mixing induced by the substrate and in an external perpendicular magnetic field, the CNT is described by the following effective Hamiltonian

$$H = H_{\mathrm{CNT}} + H_{\Delta_{KK'}} + H_{\mathrm{Z}}. \tag{3.25}$$

The effective Hamiltonian in second quantization for the CNT including a reference chemical potential μ is given by

$$H_{\mathrm{CNT}} - \mu N = \sum_{k,\tau,s} \xi_{\tau s}(k)\, c^{\dagger}_{k\tau s} c_{k\tau s}, \tag{3.26}$$

where $\xi_{\tau s}(k)$ is the single-particle energy measured with respect to the chemical potential, $\xi_{\tau s}(k) = \varepsilon_{\tau s}(k) - \mu$. We model the valley mixing potential by modifying the longitudinal curvature shift and fitting an appropriate constant $\Delta_{KK'}$ to the band structure obtained from the real space calculation. The valley-mixing term $H_{\Delta_{KK'}}$ coupling two electron states at opposite valleys but with the same spin s and momentum k. It reads

$$H_{\Delta_{KK'}} = \sum_{k,s} \left(\Delta_{KK'} c^\dagger_{kKs} c_{kK's} + \Delta^\star_{KK'} c^\dagger_{kK's} c_{kKs} \right), \tag{3.27}$$

with $\Delta_{KK'} \in \mathbb{C}$. In our calculations presented in chapter 5 $\Delta_{KK'}$ is real and equal to 2.5 meV. The Zeeman energy H_Z due to the perpendicular magnetic field $B_\perp$ induces a coupling of electrons with opposite spins and in the same valley

$$H_Z = \mu_B B_\perp \sum_{k,\tau} \left(c^\dagger_{k\tau\uparrow} c_{k\tau\downarrow} + c^\dagger_{k\tau\downarrow} c_{k\tau\uparrow} \right), \tag{3.28}$$

i.e. we assume $B_\perp$ to be applied in the x direction, while the z direction runs along the CNT axis. In principle both in (3.27) and (3.28) we should also have the valence band. Here we can however use the fact that due to the high chemical potential we are far away from the charge neutrality point and therefore the contribution from the valence band is negligible. The Bloch Hamiltonian in the basis $\{|kK\uparrow\rangle, |kK\downarrow\rangle, |kK'\uparrow\rangle, |kK'\downarrow\rangle\}$ at low energies is given by

$$H(k) = \begin{pmatrix} \xi_{K\uparrow}(k) & \mu_B B_\perp & \Delta_{KK'} & 0 \\ \mu_B B_\perp & \xi_{K\downarrow}(k) & 0 & \Delta_{KK'} \\ \Delta_{KK'} & 0 & \xi_{K'\uparrow}(k) & \mu_B B_\perp \\ 0 & \Delta_{KK'} & \mu_B B & \xi_{K'\downarrow}(k) \end{pmatrix}, \tag{3.29}$$

where $\xi_{\tau s}(k) = \varepsilon_{\tau s}(k) - \mu$ is the single-particle energy measured with respect to the chemical potential μ, $\varepsilon_{\tau s}(k)$ is the single-particle energy of the electrons (see Eq. (3.20)) and $c^\dagger_{k\tau s}|0\rangle = |k\tau s\rangle$ define the basis. Diagonalization of this Hamiltonian results in four spin- and valley-mixed bands shown in Fig. 3.8, featuring both the helical, spin-momentum locked modes and two energy ranges with odd number of Fermi surfaces. A very good agreement with the spectrum obtained from the full tight-binding calculation is achieved, which is crucial in the studies of topological matter. The eigenstates of the resulting Hamiltonian are then in general linear combinations of all τ, s eigenstates of the original H_CNT. We denote them by ①,②,③,④, shown in Fig. 3.8.

3.6. Two-band model

The four band model, while approximating very well the numerical results, is rather intractable analytically. We can simplify it, using the knowledge of the energy scales in our system. In the setup discussed in chapter 5 the largest relevant energy scales are Δ_SO and $\Delta_{KK'}$, similar in magnitude, with $\Delta_\mathrm{SO} = 2$ meV and $\Delta_{KK'} = 2.5$ meV. A smaller energy scale is the Zeeman energy $\mu_B B_\perp$, which can be tuned continuously. Our strategy is therefore to diagonalize the initial single-particle Hamiltonian of the CNT (3.26) together with the valley-mixing term

(3.27) exactly, express the Zeeman term (3.28) in this basis and omit the terms coupling the lower and upper band pairs. The two resulting subspaces contain only one band pair each, halving the dimensions of the Hamiltonians under our treatment.

The CNT Hamiltonian $H_{\mathrm{CNT}} - \mu N + H_{\Delta_{KK'}}$ can be brought to a diagonal form by employing the unitary transformation

$$\begin{pmatrix} c_{kKs} \\ c_{kK's} \end{pmatrix} = \begin{pmatrix} a_s(k) & b_s(k) \\ -b_s^\star(k) & a_s^\star(k) \end{pmatrix} \begin{pmatrix} \alpha_{ks} \\ \beta_{ks} \end{pmatrix}, \tag{3.30}$$

with $|a_s(k)|^2 + |b_s(k)|^2 = 1$. It is diagonalized by the following values of $a_s(k)$ and $b_s(k)$

$$\begin{aligned} |a_s(k)|^2 &= \frac{1}{2}\left(1 - \frac{\xi_{Ks}(k) - \xi_{K's}(k)}{\sqrt{(\xi_{Ks}(k) - \xi_{K's}(k))^2 + 4|\Delta_{KK'}|^2}}\right), \\ |b_s(k)|^2 &= \frac{1}{2}\left(1 + \frac{\xi_{Ks}(k) - \xi_{K's}(k)}{\sqrt{(\xi_{Ks}(k) - \xi_{K's}(ks))^2 + 4|\Delta_{KK'}|^2}}\right), \end{aligned} \tag{3.31}$$

and $\arg(a_s(k)) = \arg(b_s(k)) = \frac{\phi}{2}$ with $\phi = \arg(\Delta_{KK'})$. With these we obtain

$$H_{\mathrm{CNT}} - \mu N + H_{\Delta_{KK'}} = \sum_{k,s}\left(E_{+s}\beta_{ks}^\dagger\beta_{ks} + E_{-s}\alpha_{ks}^\dagger\alpha_{ks}\right), \tag{3.32}$$

where the eigenvalues are defined in the following way

$$E_{\pm s}(k) = \frac{1}{2}(\xi_{Ks}(k) + \xi_{K's}(k)) \pm \frac{1}{2}\sqrt{(\xi_{Ks}(k) - \xi_{K's}(k))^2 + 4|\Delta_{KK'}|^2}.$$

Due to the time-reversal conjugation of $\xi_{\tau s}(k) = \xi_{-\tau -s}(-k)$ it can be shown that $|a_s(k)| = |b_{-s}(-k)|$ and $E_{\pm s}(k) = E_{\pm -s}(-k)$. Now we will express the Zeeman term (3.28) in this basis:

$$H_Z = \sum_{ks}\mu_B\tilde{B}_\perp\left(\alpha_{ks}^\dagger\alpha_{k,-s} + \beta_{ks}^\dagger\beta_{k,-s}\right) + s\mu_B B_\perp^\star\left(\alpha_{ks}^\dagger\beta_{k,-s} - \beta_{ks}^\dagger\alpha_{k,-s}\right),$$

where $\tilde{B}_\perp$ and $B_\perp^\star$ are the renormalized magnetic field components. Using equations (3.31) we can express them as

$$\tilde{B}_{\perp} = B_{\perp}\left(|a_{\uparrow}(k)|\,|a_{\downarrow}(k)| + |b_{\uparrow}(k)|\,|b_{\downarrow}(k)|\right),$$
$$B^{\star}_{\perp} = B_{\perp}\left(|a_{\uparrow}(k)|\,|b_{\downarrow}(k)| - |b_{\uparrow}(k)|\,|a_{\downarrow}(k)|\right).$$

The magnetic field $\tilde{B}_{\perp}$ couples the spins within the lower and upper band pair, while $B^{\star}_{\perp}$ couples the spins between band pairs. As long as the energy difference between the lower and upper band pairs is larger than the Zeeman energy, $\Delta E = |E_{+s} - E_{-s}| > \mu_B B_{\perp}$, we can omit the terms with $B^{\star}_{\perp}$. The Hamiltonian for the two lowest energy bands is given by

$$\tilde{H} = \sum_{k,s}\left[E_{-s}\alpha^{\dagger}_{ks}\alpha_{ks} + E_{+s}\beta^{\dagger}_{ks}\beta_{ks} + \mu_B\tilde{B}_{\perp}\left(\alpha^{\dagger}_{ks}\alpha_{k,-s} + \beta^{\dagger}_{ks}\beta_{k,-s}\right)\right]. \tag{3.33}$$

This Hamiltonian can be diagonalized by the transformations

$$\begin{pmatrix}\alpha_{k\uparrow}\\ \alpha_{k\downarrow}\end{pmatrix} = \begin{pmatrix} g_{-}(k) & h_{-}(k)\\ -h_{-}(k) & g_{-}(k)\end{pmatrix}\begin{pmatrix} f_{k1-}\\ f_{k2-}\end{pmatrix}, \tag{3.34}$$

$$\begin{pmatrix}\beta_{k\uparrow}\\ \beta_{k\downarrow}\end{pmatrix} = \begin{pmatrix} g_{+}(k) & h_{+}(k)\\ -h_{+}(k) & g_{+}(k)\end{pmatrix}\begin{pmatrix} f_{k1+}\\ f_{k2+}\end{pmatrix}, \tag{3.35}$$

where the coefficients must satisfy $g^2_{\pm}(k) + h^2_{\pm}(k) = 1$. The new quantum number in (3.34) and (3.35) $i \in \{1,2\}$ just reflects the ordering of the energy bands $E^{\pm}_1 < E^{\pm}_2$. The coefficients s and t are defined as

$$g^2_{\pm}(k) = \frac{1}{2}\left(1 - \frac{E_{\pm\uparrow}(k) - E_{\pm\downarrow}(k)}{\sqrt{\left(E_{\pm\uparrow}(k) - E_{\pm\downarrow}(k)\right)^2 + 4\left(\mu_B\tilde{B}_{\perp}\right)^2}}\right), \tag{3.36}$$

$$h^2_{\pm}(k) = \frac{1}{2}\left(1 + \frac{E_{\pm\uparrow}(k) - E_{\pm\downarrow}(k)}{\sqrt{\left(E_{\pm\uparrow}(k) - E_{\pm\downarrow}(k)\right)^2 + 4\left(\mu_B\tilde{B}_{\perp}\right)^2}}\right). \tag{3.37}$$

The coefficients satisfy the following time-reversal conjugation $g_{\pm}(k) = h_{\pm}(-k)$. With this transformation we obtain the Hamiltonian in diagonal form (3.38) and the corresponding single-particle energies. The full Hamiltonian with decoupled band pairs in its diagonal basis is given by

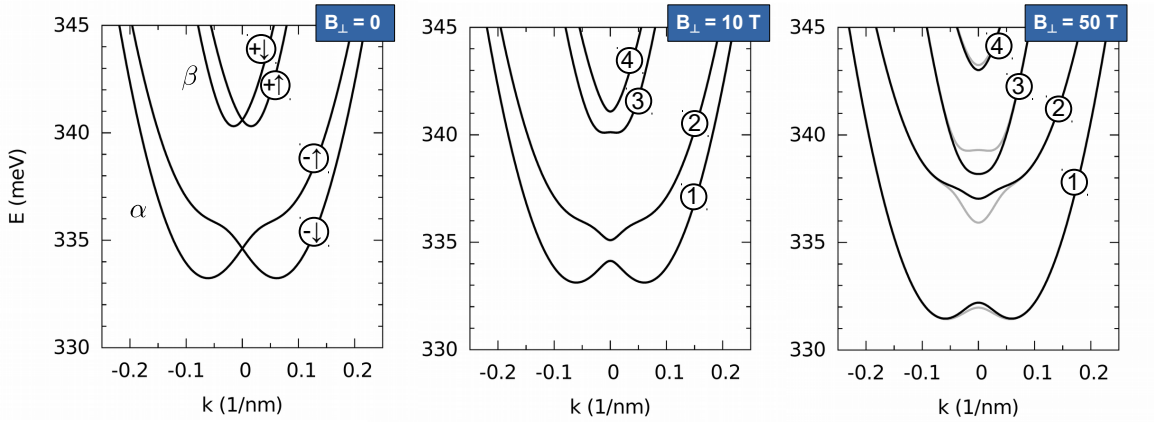

Figure 3.9: The two pairs of bands β and α with black lines showing the energies $E_{\pm s}$, respectively, at $B_\perp = 0$ and $\tilde{E}_{1/2/3/4}$ at $B_\perp = 10$ and 50T. The grey lines show the corresponding solutions of the four-band model. The approximation decoupling the upper pair from the lower holds at small fields, until $B_\perp^\star$ becomes too large to be neglected and the two-band model becomes unreliable.

$$\tilde{H}_{\mathrm{CNT}} = \sum_k \sum_{p=\pm} \sum_{i=1}^{2} \tilde{E}_i^p f_{kip}^\dagger f_{kip}, \tag{3.38}$$

with the corresponding single-particle energies

$$\tilde{E}_i^\pm(k) = \frac{1}{2}\left(E_{\pm\uparrow}(k) + E_{\pm\downarrow}(k)\right) + (-1)^i \frac{1}{2}\sqrt{\left(E_{\pm\uparrow}(k) - E_{\pm\downarrow}(k)\right)^2 + 4\left(\mu_B \tilde{B}_\perp\right)^2}.$$

The single-particle energies have the property $\tilde{E}_i^\pm(k) = \tilde{E}_i^\pm(-k)$ with $i \in \{1,2\}$ because $\tilde{B}_\perp(k) = \tilde{B}_\perp(-k)$. The renormalized magnetic field opens a band gap at the Γ-point. Figure 3.9 shows the four bands $\tilde{E}_{1/2/3/4}(k)$ for magnetic field strengths $B_\perp = 0, 10, 50$ T. At $B_\perp = 10$ T the energies obtained in the two-band model still agree very well with those of the full four-band model.

3.7. The lattice Hamiltonian in the helical-angular construction

Due to the C_d rotational symmetry of a CNT with respect to the tube axis, the orbital angular momentum $l_\perp = k_\perp R$ is a well-defined quantity which is characterized by the integer, $k_\perp = 0, 1, \cdots, d-1$. Recent studies [137, 145] have revealed that the carbon nanotubes can be divided into two classes according to the angular momentum of the Dirac subbands. In zigzag class the two valleys of the low energy subbands have different angular momenta $l_\perp \neq 0$ and in armchair class the low energy subbands in both valleys have the same angular momentum $l_\perp = 0$. Furthermore, also the spin component along the carbon nanotube axis is a conserved quantity, which allows us to decompose the Hamiltonian into $\boldsymbol{k}_\perp \equiv (k_\perp, s)$ subspaces. This approach will be used in chapter 4 to describe a carbon nanotube in a

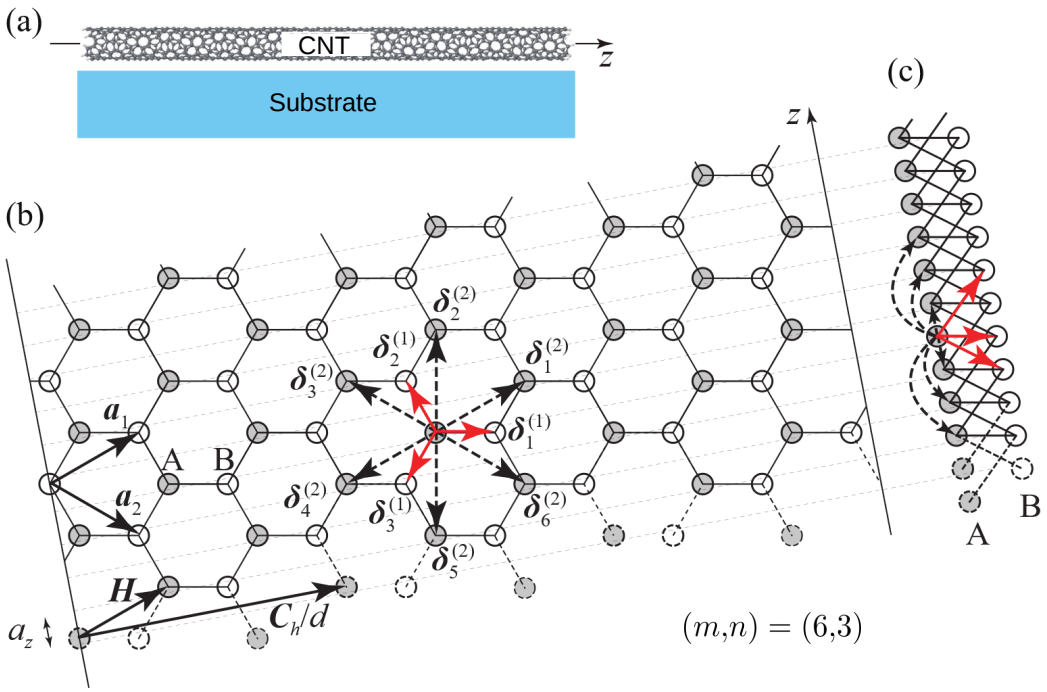

Figure 3.10: (a) Schematic figure of a CNT proximity coupled to a superconducting substrate. (b) Hexagonal lattice structure. Depicted are unit vectors $\boldsymbol{a}_1$, $\boldsymbol{a}_2$, alternative unit vectors $\boldsymbol{C}_h/d$, $\boldsymbol{H}$, and vectors to the nearest-neighbor and next-nearest-neighbor sites $\boldsymbol{\delta}_j^{(t)}$ for an unrolled $(n,m) = (6,3)$ CNT, where $d = \gcd(n,m) = 3$. A and B sublattices are denoted by gray and white circles, respectively. (c) An effective 1D lattice model, which is obtained by a partial Fourier transform in the circumferential direction, and is a projection of the 2D lattice structure onto the 1D nanotube axis z (see the dashed lines). Solid lines denote nearest-neighbor bond connections in the original lattice structure.

time-reversal invariant setup. The decomposition is performed by a partial Fourier transform in the circumference direction. To achieve this, it is convenient to use the helical-angular construction [146], i.e. the atomic position $\boldsymbol{r}$ is expressed by the alternative unit vectors $\boldsymbol{C}_h/d$ and $\boldsymbol{H}$, where $\boldsymbol{H} = p_s\boldsymbol{a}_1 + q_s\boldsymbol{a}_2$ with the integers p_s and q_s satisfying $mp_s - nq_s = d$. It holds $\boldsymbol{r} = \nu\,(\boldsymbol{C}_h/d) + \ell\boldsymbol{H} + \delta_{\sigma,\mathrm{B}}\boldsymbol{\delta}_1^{(1)}$ with the two integers $\nu = 0, 1, \cdots, d-1$ and ℓ. The integer ℓ indicates the lattice position in the axis direction in units of $a_z = \sqrt{3}ad/2\sqrt{n^2+m^2+nm}$, which is the shortest distance between same sublattice σ atoms in the axis direction [see Fig. 3.10(b)]. In this framework, the two-dimensional (2D) wave vector is expressed as $\boldsymbol{k} = k_\perp\boldsymbol{Q}_1/d + k\boldsymbol{Q}_2/(2\pi/a_z)$, where k is the wave number along the nanotube axis defined in the 1D Brillouin zone $-\pi/a_z \le k < \pi/a_z$, and $\boldsymbol{Q}_1$ and $\boldsymbol{Q}_2$ are the two reciprocal lattice vectors conjugated to $\boldsymbol{C}_h/d$ and $\boldsymbol{H}$, respectively. That is, the relations $\boldsymbol{Q}_1 \cdot \boldsymbol{C}_h/d = \boldsymbol{Q}_2 \cdot \boldsymbol{H} = 2\pi$ and $\boldsymbol{Q}_1 \cdot \boldsymbol{H} = \boldsymbol{Q}_2 \cdot \boldsymbol{C}_h/d = 0$ hold. The term H_0, which includes curvature-induced effects is explicitly given as follows:

$$H_{\mathrm{CNT}} = -\mu \sum_{\boldsymbol{r}\sigma s} c^\dagger_{\sigma\boldsymbol{r}s} c_{\sigma\boldsymbol{r}s} + \sum_{\boldsymbol{r}s}\sum_{j=1}^{3} \gamma^{(1)}_{s,j}\, c^\dagger_{\mathrm{A}\boldsymbol{r}s} c_{\mathrm{B}\boldsymbol{r}+\boldsymbol{\delta}_j^{(1)}s} + \sum_{\boldsymbol{r}\sigma s}\sum_{j=1}^{3} \gamma^{(2)}_{s,j}\, c^\dagger_{\sigma\boldsymbol{r}s} c_{\sigma\boldsymbol{r}+\boldsymbol{\delta}_j^{(2)}s} + \mathrm{h.c.},$$

where $c_{\sigma \boldsymbol{r} s}$ is the annihilation operator of one electron on sublattice σ (= A, B) at site $\boldsymbol{r}$ and with spin $s = \pm 1$. The spin quantization axis is chosen to be the nanotube axis, μ sets the CNT chemical potential and can be tuned, possibly, through external gate voltages. The vectors $\boldsymbol{\delta}_j^{(1)}$ $(j = 1, 2, 3)$ point to the three nearest-neighbor B sites from the A site, and the vectors $\boldsymbol{\delta}_j^{(2)}$ $(j = 1, \cdots, 6)$ point to the six next-nearest-neighbor sites [see Fig. 3.10(b)]. The vectors to the three nearest-neighbor B sites from the A site are given by $\boldsymbol{\delta}_1^{(1)} = (\boldsymbol{a}_1 + \boldsymbol{a}_2)/3$, $\boldsymbol{\delta}_2^{(1)} = (\boldsymbol{a}_1 - 2\boldsymbol{a}_2)/3$, and $\boldsymbol{\delta}_3^{(1)} = (-2\boldsymbol{a}_1 + \boldsymbol{a}_2)/3$. The vectors to the six next-nearest-neighbor sites are given by $\boldsymbol{\delta}_1^{(2)} = \boldsymbol{a}_1$, $\boldsymbol{\delta}_2^{(2)} = (\boldsymbol{a}_1 - \boldsymbol{a}_2)$, $\boldsymbol{\delta}_3^{(2)} = -\boldsymbol{a}_2$, and $\boldsymbol{\delta}_j^{(2)} = -\boldsymbol{\delta}_{j-3}^{(2)}$ for $j = 4, 5, 6$. A spin-independent shift of the Dirac points is included in the nearest-neighbor hopping, while spin-orbit effects influence both the nearest-neighbor and next-nearest-neighbor hoppings

$$\gamma_{s,j}^{(1)} = \gamma \left[1 + \Delta k_\perp^c \frac{a}{\sqrt{3}} \sin\phi_j - \left(\Delta k_\parallel^c + i s \Delta k_\perp^{SO} \right) \frac{a}{\sqrt{3}} \cos\phi_j \right],$$
$$\gamma_{s,j}^{(2)} = i \frac{(-1)^{j+1}}{3\sqrt{3}} s \varepsilon_{\rm so},$$

where $\phi_j = \theta - 5\pi/6 + 2\pi j/3$. Reflecting the time-reversal symmetry we have $(\gamma_{-s,j}^{(t)})^* = \gamma_{s,j}^{(t)}$. Then, the partial Fourier transform is expressed as

$$c_{\sigma \boldsymbol{r} s} = \frac{1}{\sqrt{d}} \sum_{k_\perp = 0}^{d-1} \exp\left(i \frac{2\pi}{d} \nu k_\perp \right) c_{\sigma \ell \boldsymbol{k}_\perp}. \tag{3.39}$$

The Hamiltonian of the normal term is rewritten as $H_{\rm CNT} = \sum_{\boldsymbol{k}_\perp} H_{\boldsymbol{k}_\perp}$, where [140, 145, 147],

$$H_{\boldsymbol{k}_\perp} = -\mu \sum_{\ell\sigma} c_{\sigma\ell\boldsymbol{k}_\perp}^\dagger c_{\sigma\ell\boldsymbol{k}_\perp} \sum_\ell \sum_{j=1}^{3} e^{i\frac{2\pi}{d}\delta\nu_j^{(1)} k_\perp} \gamma_{s,j}^{(1)} c_{{\rm A}\ell\boldsymbol{k}_\perp}^\dagger c_{{\rm B}\ell_j^{(1)}\boldsymbol{k}_\perp}$$
$$+ \sum_{\ell\sigma} \sum_{j=1}^{3} e^{i\frac{2\pi}{d}\delta\nu_j^{(2)} k_\perp} \gamma_{s,j}^{(2)} c_{\sigma\ell\boldsymbol{k}_\perp}^\dagger c_{\sigma\ell_j^{(2)}\boldsymbol{k}_\perp} + {\rm h.c.},$$

where

$$\ell_j^{(t)} = \ell + \delta\ell_j^{(t)}, \quad t = 1, 2.$$

The hopping distance $\delta\ell_j^{(t)}$ and the phase factor $\delta\nu_j^{(t)}$ are determined from $\boldsymbol{\delta}_j^{(t)} = \delta\nu_j^{(t)} \boldsymbol{C}_h/d + \delta\ell_j^{(t)} \boldsymbol{H}$. Their explicit expressions are given in Table 3.7. As schematically shown in Fig. 3.10(c), the Hamiltonian in each $\boldsymbol{k}_\perp$ subspace represents a ladder-type 1D lattice model [140, 146, 147].

In Fig. 3.11(a) we depict the energy bands of an $(n, m) = (6, 3)$ CNT which belongs to the

	$j=1$	$j=2$	$j=3$	$j=4$	$j=5$	$j=6$
$\delta\ell_j^{(1)}$	$-\frac{n-m}{3d}$	$\frac{2n+m}{3d}$	$-\frac{2m+n}{3d}$			
$\delta\nu_j^{(1)}$	$\frac{p_s-q_s}{3}$	$-\frac{2p_s+q_s}{3}$	$\frac{2q_s+p_s}{3}$			
$\delta\ell_j^{(2)}$	$\frac{m}{d}$	$\frac{n+m}{d}$	$\frac{n}{d}$	$-\frac{m}{d}$	$-\frac{n+m}{d}$	$-\frac{n}{d}$
$\delta\nu_j^{(2)}$	$-q_s$	$-(p_s+q_s)$	$-p_s$	q_s	p_s+q_s	p_s

Table 6: Hopping distance $\delta\ell_j^{(t)}$ and phase factor $\delta\nu_j^{(t)}$ in the 1D lattice model [140, 147]. The integers p_s and q_s satisfy $mp_s - nq_s = d$, where $d = \gcd(n, m)$.

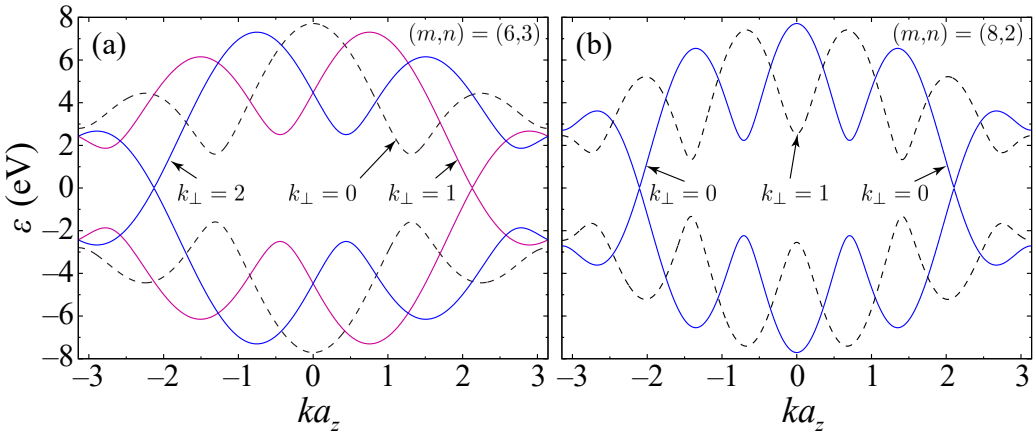

Figure 3.11: Conduction and valence bands of (a) $(n, m) = (6, 3)$ metal-1 CNT, classified into the zigzag class, and (b) $(n, m) = (8, 2)$ metal-2 CNT, classified into the armchair class. For both cases (a) and (b), $p_s = 1$ and $q_s = 0$. The angular momentum for each band is indicated, the blue curves show bands with $k_\perp = k_{\perp K}$, and the purple curves in (a) show bands with $k_\perp = k_{\perp K'}$. Curvature-induced energy gaps at zero energy and spin-orbit splitting are not seen on this energy scale.

zigzag class. The angular momentum $k_{\perp K} = 2$ of valley K is different from that of the K' valley which is $k_{\perp K'} = 1$. On the other hand, Fig. 3.11(b) shows the energy band of an $(n, m) = (8, 2)$ CNT, representative of the armchair class, where $k_{\perp K} = k_{\perp K'} = 0$.

3.8. Mean field approach of superconducting carbon nanotubes

Since in graphene the Coulomb potential can not be screened for small momenta, the electron-phonon coupling can not overcome the repulsive electron-electron interaction [125]. Thus, the electrons do not feel an attractive interaction potential and the formation of Cooper pairs can not occur. There are theoretical proposals where graphene is an intrinsic superconductor, but one has to shift the chemical potential far away from the Dirac point by doping graphene. The idea of doped graphene has been shown to be very interesting but doped graphene shows a d-wave gap symmetry instead of an s-wave gap symmetry [148]. Experiments shows proximity-induced superconductivity in graphene junctions [149] and proximity-induced superconductivity was also experimentally demonstrated in carbon nanotubes [150–152]. In confined nanoconductors such as quantum dots and wires [153], resonant Andreev processes at the superconductor–normal-metal interface cause the formation of bound states with excita-

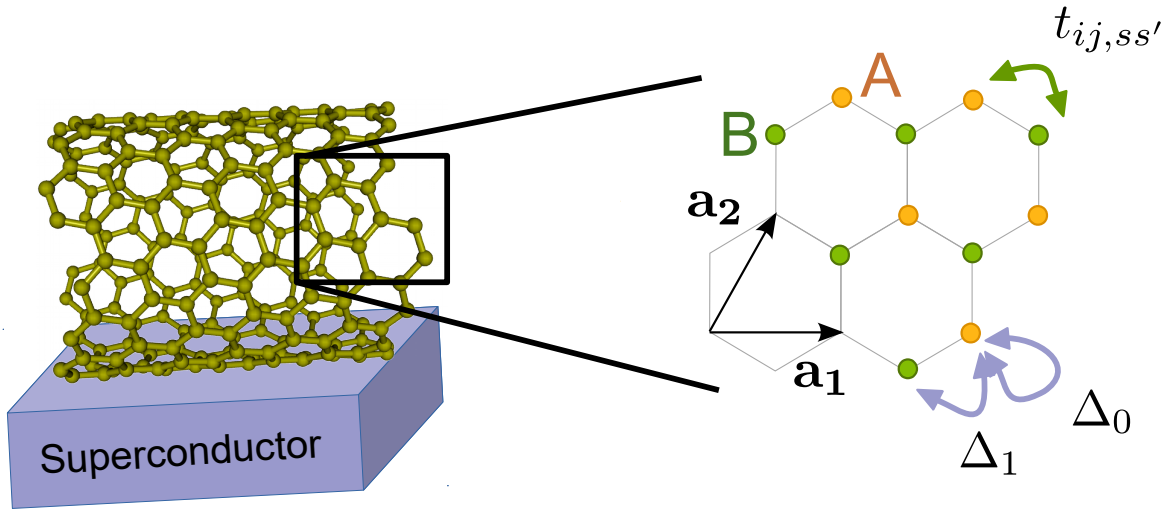

Figure 3.12: Schematic of the system including the CNT which lies on top of an s-wave superconductor. The nearest-neighbor hopping $t_{ij,ss'}$ is spin-dependent due to curvature. The superconducting substrate induces an on-site superconducting pairing term Δ_0 and nearest-neighbor pairing term Δ_1.

tion energies below the superconducting gap, referred to as Andreev bound states. Such bound states have also been observed in carbon nanotube - superconductor hybrid devices [154–159].

When setting up the effective pairing Hamiltonian H_{SC}, we notice that the diameter d of a carbon nanotube is much smaller than a typical superconducting penetration length $\lambda > 10$ nm [86]. Then, we can assume singlet superconducting pairing terms Δ_0, Δ_1 being constant on the whole lattice. Thus, the superconducting pairing is described by

$$H_{\mathrm{SC}} = \sum_i \Delta_0 \left(a^\dagger_{i\uparrow} a^\dagger_{i\downarrow} + b^\dagger_{i\uparrow} b^\dagger_{i\downarrow} \right) + \sum_{\langle i,j \rangle} \Delta_1 \left(b^\dagger_{j\downarrow} a^\dagger_{i\uparrow} - b^\dagger_{j\uparrow} a^\dagger_{i\downarrow} \right) + \mathrm{h.c.}. \tag{3.40}$$

The term proportional to Δ_0 represents the onsite pairing, and the term proportional to Δ_1 the pairing between the nearest-neighbor sites. The gauge freedom allows us to choose the coupling terms Δ_0, Δ_1 as real numbers. To determine the precise values of Δ_0 and Δ_1 for a given chirality of carbon nanotube contacted to a superconducting substrate, a microscopic analysis of the interactions between the superconducting substrate and the carbon nanotube would be needed [160], in principle including also pairing correlations between next-nearest and further neighbors. However, as will be discussed in the next chapter, the presence of nearest-neighbor pairing is the minimum requirement for the presence of nontrivial topological phases and time-reversal symmetry. Therefore, we shall treat both Δ_0 and Δ_1 as parameters in order to study their interplay.

We know that a carbon nanotube is rolled graphene and the curvature enhances the intrinsic spin-orbit coupling and induce energy gaps. Due to the enhanced spin-orbit coupling the spin rotation symmetry is broken and the kinetic energy depends on the spin. Since the nearest-neighbor pairing term is independent of the hopping integral the pairing term

depends on the momentum but is unaffected by the curvature effects. Thus, we introduce the parameter $f(\mathbf{k}) = 1 + e^{i\mathbf{k}\mathbf{a}_1} + e^{-i\mathbf{k}\mathbf{a}_2}$ which is different from the kinetic energy term $\gamma_s(\mathbf{k}) = -\left(t_1 + t_{2s}e^{i\mathbf{k}\mathbf{a}_1} + t_{3s}e^{-i\mathbf{k}\mathbf{a}_2}\right)$.

$$
\begin{aligned}
H_{\mathrm{SC}} = &\sum_{\mathbf{k}} \left(\Delta_0 \left(a^{\dagger}_{\mathbf{k}\uparrow} a^{\dagger}_{-\mathbf{k}\downarrow} + b^{\dagger}_{\mathbf{k}\uparrow} b^{\dagger}_{-\mathbf{k}\downarrow} \right) + \Delta_0^{\star} \left(a_{-\mathbf{k}\downarrow} a_{\mathbf{k}\uparrow} + b_{-\mathbf{k}\downarrow} b_{\mathbf{k}\uparrow} \right) \right) \\
&+ \sum_{\mathbf{k}} \left(\Delta_1 \left(f(\mathbf{k})\, a^{\dagger}_{\mathbf{k}\uparrow} b^{\dagger}_{-\mathbf{k}\downarrow} + f^{\star}(\mathbf{k})\, b^{\dagger}_{\mathbf{k}\uparrow} a^{\dagger}_{-\mathbf{k}\downarrow} \right) + \Delta_1^{\star} \left(f^{\star}(\mathbf{k})\, b_{-\mathbf{k}\downarrow} a_{\mathbf{k}\uparrow} + f(\mathbf{k})\, a^{\dagger}_{-\mathbf{k}\downarrow} b_{\mathbf{k}\uparrow} \right) \right).
\end{aligned}
$$

We see that for the on-site pairing terms the superconducting gap is isotropic in momentum space representation $\Delta_0(\mathbf{k}) = \Delta_0$ and hence this is an s-wave pairing term. The nearest-neighbor superconducting gap in the momentum space representation is $\Delta_1(\mathbf{k}) = \Delta\gamma(\mathbf{k})$. In the low-energy limit it follows $\Delta_1(\mathbf{k}) \sim \Delta_1(k_x + ik_y)$. Thus, the nearest-neighbor pairing term is of $p + ip$-wave nature.

Under the partial Fourier transform of Eq. (3.39), the superconducting term of the Hamiltonian takes the form,

$$
H_{\mathrm{SC}} = \sum_{\boldsymbol{k}_\perp} \left[\frac{\Delta_0}{2} \sum_{\ell\sigma} s c^{\dagger}_{\sigma\ell\boldsymbol{k}_\perp} c^{\dagger}_{\sigma\ell-\boldsymbol{k}_\perp} + \mathrm{H.c.} + \Delta_1 \sum_{\ell} \sum_{j=1}^{3} e^{i\frac{2\pi}{d}\delta\nu_j^{(1)}\mu} s c^{\dagger}_{\mathrm{A}\ell\boldsymbol{k}_\perp} c^{\dagger}_{\mathrm{B}\ell_j^{(1)}-\boldsymbol{k}_\perp} + \mathrm{h.c.} \right].
$$

The pair $\boldsymbol{k}_\perp$ and $-\boldsymbol{k}_\perp$ in the superconducting term reflects the conservation of angular momentum and spin.

With this we finish the introductory part of thesis the. In the next chapter we will demostrate by using the helicular-angular model that without breaking the time-reversal symmetry the presence of nearest-neighbor pairing is the minimum requirement for the presence of nontrivial phases. Thus, we have a minimal model of topological superconductivity in the carbon nanotubes. Then, in chapter 5 we show that due to the presence of a perpendicular magnetic field and valley mixing we will have edge states with Majorana nature. Contrary to the time-reversal symmetric case, for the appearance of Majorana bound states the Δ_1 contribution is not necessary.

4. Topological superconductivity in superconducting carbon nanotubes with time-reversal symmetry

In this chapter we address theoretically the topological origin of zero energy bound states localized at the edges of a carbon nanotube proximity coupled to a superconductor. We investigate the spectrum of finite-length carbon nanotubes in the presence of onsite and nearest-neighbor superconducting pairing terms. We find that zero energy edge states can emerge in zigzag class carbon nanotubes as a combined effect of curvature-induced Dirac point shift and strong superconducting coupling between nearest-neighbor sites. The chiral symmetry of the system is exploited to define a winding number topological invariant. The associated topological phase diagram shows regions with nontrivial winding number in the plane of chemical potential and superconducting nearest-neighbor pair potential (relative to the onsite pair potential). A one-dimensional continuum model reveals the topological origin of the zero energy edge states: A bulk-edge correspondence is proven, which shows that the condition for nontrivial winding number and that for the emergence of edge states are identical. For armchair class nanotubes, the presence of edge states in the superconducting gap depends on the nanotube's boundary shape. For the minimal boundary condition, the emergence of the subgap states can also be deduced from the winding number. The results of this chapter have been published in Phys. Rev. B **96**, 125414 (2017).

4.1. Bulk spectrum of superconducting carbon nanotubes

We discuss the bulk energy spectrum of zigzag-class carbon nanotubes with superconducting correlations. The Hamiltonian of the superconducting carbon nanotube obeys the same lattice symmetries like the normal conducting carbon nanotube. The reason is that the superconducting correlations do not perturb the lattice of the carbon nanotube and change only the energy spectrum of the system. Since the mean-field Hamiltonian $H_{\mathrm{CNT}} + H_{\mathrm{SC}}$ has a bilinear form in the fermionic operators, the quasiparticle spectrum can be again calculated by a Bogoliubov transformation. However, this time we will introduce the Bogoliubov - de Gennes (BdG) formalism [86]. The BdG Hamiltonian $\mathcal{H}$ is given by doubling the fermionic operators upon introduction of the Nambu spinor $\Psi^{\dagger}_{\mathbf{k},s} = \left(a^{\dagger}_{\mathbf{k}s},\, b^{\dagger}_{\mathbf{k}s},\, a_{-\mathbf{k}-s},\, b_{\mathbf{k}-s}\right)$. Then, the Hamiltonian of the bulk system can be written as

$$H - \mu N = \frac{1}{2} \sum_{\mathbf{k},s} \Psi^{\dagger}_{\mathbf{k},s} \mathcal{H}^{(s)}_{\mathrm{BdG}}\left(\mathbf{k}\right) \Psi_{\mathbf{k},s}, \tag{4.1}$$

where the BdG Hamiltonian $\mathcal{H}^{(s)}_{\mathrm{BdG}}\left(\mathbf{k}\right)$ is defined as

$$\mathcal{H}_{\mathrm{BdG}}^{(s)}(\mathbf{k}) = \begin{pmatrix} \tilde{\varepsilon}(\mathbf{k}) & \gamma_s(\mathbf{k}) & -s\Delta_0 & -s\Delta_1 f(\mathbf{k}) \\ \gamma_s^\star(\mathbf{k}) & \tilde{\varepsilon}(\mathbf{k}) & -s\Delta_1 f^\star(\mathbf{k}) & -s\Delta_0 \\ -s\Delta_0^\star & -s\Delta_1^\star f(\mathbf{k}) & -\tilde{\varepsilon}(\mathbf{k}) & -\gamma_{-s}^\star(-\mathbf{k}) \\ -s\Delta_1^\star f^\star(\mathbf{k}) & -s\Delta_0^\star & -\gamma_{-s}(-\mathbf{k}) & -\tilde{\varepsilon}(\mathbf{k}) \end{pmatrix}, \tag{4.2}$$

with $\tilde{\varepsilon}(\mathbf{k}) = -\mu + \varepsilon_{SO}(\mathbf{k})$ and $\varepsilon_{SO}(\mathbf{k})$ is the Zeeman-like spin-orbit coupling. Due to the doubling the BdG Hamiltonian has the particle-hole symmetry and since the time-reversal symmetry is present, the BdG Hamiltonian has the chiral symmetry as well. The BdG Hamiltonian (4.2) can be written in terms of Pauli matrices by using time-reversal conjugation $\gamma_s(\mathbf{k}) = \gamma_{-s}^\star(-\mathbf{k})$ and the superconducting gaps are fixed to be real $\Delta_0 \in \mathbb{R}$ and $\Delta_1 \in \mathbb{R}$ due to a gauge transformation. Then, the BdG Hamiltonian (4.2) can be written in a compact way

$$\mathcal{H}_{\mathrm{BdG}}^{(s)}(\mathbf{k}) = \begin{pmatrix} \tilde{\varepsilon}(\mathbf{k}) & \gamma_s(\mathbf{k}) \\ \gamma_s^\star(\mathbf{k}) & \tilde{\varepsilon}(\mathbf{k}) \end{pmatrix} \tau_z + s \begin{pmatrix} \Delta_0 & \Delta_1 f(\mathbf{k}) \\ \Delta_1 f^\star(\mathbf{k}) & \Delta_0 \end{pmatrix} \tau_x. \tag{4.3}$$

The BdG spectrum of the bulk system is obtained by diagonalizing the Hamiltonian matrix (4.3), which is of the form (1.14). It follows from the chiral symmetry that $\mathcal{H}_{\mathrm{BdG}}^{(s)}$ has block-diagonal form, see chapter 1.2.3, with the blocks $D_s^\dagger(\mathbf{k}) D_s(\mathbf{k})$ and $D_s(\mathbf{k}) D_s^\dagger(\mathbf{k})$. Then, due to the transformation (1.15) the BdG Hamiltonian becomes off-diagonal

$$\tilde{\mathcal{H}}_{\mathrm{BdG}}^{(s)}(\mathbf{k}) = \begin{pmatrix} \tilde{\varepsilon}(\mathbf{k}) & \gamma_s(\mathbf{k}) \\ \gamma_s^\star(\mathbf{k}) & \tilde{\varepsilon}(\mathbf{k}) \end{pmatrix} \tau_x + s \begin{pmatrix} \Delta_0 & \Delta_1 f(\mathbf{k}) \\ \Delta_1 f^\star(\mathbf{k}) & \Delta_0 \end{pmatrix} \tau_y = \begin{pmatrix} 0 & D_s(\mathbf{k}) \\ D_s^\dagger(\mathbf{k}) & 0 \end{pmatrix}, \tag{4.4}$$

where

$$D_s(\mathbf{k}) = \begin{pmatrix} \tilde{\varepsilon}(\mathbf{k}) - is\Delta_0 & \gamma_s(\mathbf{k}) - is\Delta_1 f(\mathbf{k}) \\ \gamma_s^\star(\mathbf{k}) - is\Delta_1 f^\star(\mathbf{k}) & \tilde{\varepsilon}(\mathbf{k}) - is\Delta_0 \end{pmatrix}. \tag{4.5}$$

Thus, the eigenvalue problem can be reduced, see section 1.2.3, to solving the equation

$$\det\left(D_s(\mathbf{k}) D_s^\dagger(\mathbf{k})^\dagger - E_s(\mathbf{k}) \mathbb{1} \right) = 0,$$

which gives

$$E_s^4(\mathbf{k}) - 2E_s^2(\mathbf{k})\left[\tilde{\varepsilon}(\mathbf{k})^2 + |\gamma_s(\mathbf{k})|^2 + \Delta_0^2 + \Delta_1^2|f(\mathbf{k})|^2\right] + \left[\tilde{\varepsilon}(\mathbf{k})^2 - \Delta_0^2 - \left(|\gamma_s(\mathbf{k})|^2 - \Delta_1^2|f(\mathbf{k})|^2\right)\right]^2$$
$$+ \left[2\tilde{\varepsilon}(\mathbf{k})\Delta_0 + \Delta_1\left(\gamma_s(\mathbf{k})f^\star(\mathbf{k}) + \gamma_s^\star(\mathbf{k})f(\mathbf{k})\right)\right]^2 = 0.$$

Since the characteristic polynomial is biquadratic we can solve it very easily. The solution can be written as $E_s^2(\mathbf{k}) = A_s \pm 2\sqrt{B_s}$ with the definitions

$$\begin{aligned}
A_s &= \tilde{\varepsilon}^2(\mathbf{k}) + |\gamma_s(\mathbf{k})|^2 + \Delta_0^2 + \Delta_1^2|f(\mathbf{k})|^2, \\
B_s &= \left(\Delta_0^2 + |\gamma_s(\mathbf{k})|^2\right)\left(\tilde{\varepsilon}^2(\mathbf{k}) + \Delta_1^2|f(\mathbf{k})|^2\right) \\
&\quad - \left(\tilde{\varepsilon}(\mathbf{k})\Delta_0 + \frac{\Delta_1}{2}\left(\gamma_s(\mathbf{k})f^\star(\mathbf{k}) + \gamma_s^\star(\mathbf{k})f(\mathbf{k})\right)\right)^2.
\end{aligned}$$

The condition of the gap closing is expressed as $A_s^2 - 4B_s = 0$.

In the following, consider the BdG spectrum around the Fermi points of the single-particle energy. Especially, we focus on the zigzag class class carbon nanotube where two valleys are well decoupled and we analyze the behavior of the superconducting gap.

Since our interest is on the impact of superconductivity on the conducting electrons, the chemical potential will be set in the energy region corresponding to electron transport. Fig. 4.1(a) shows the energy bands near the K point for an $(m,n) = (6,3)$ carbon nanotube. The dashed line indicates the chemical potential. Fig. 4.1(b) shows the corresponding BdG spectrum. As shown in the two insets, the BdG spectrum exhibits small superconducting gaps of the order of the superconducting couplings near the two Fermi points $k = k_-^{(\tau,s)}$ and $k = k_+^{(\tau,s)} (> k_-^{(\tau,s)})$, at which

$$\xi_{\tau s}\left(k_r^{(\tau,s)}\right) = \varepsilon_{\tau s}\left(k_r^{(\tau,s)}\right) - \mu \stackrel{!}{=} 0 \quad (r = \pm 1), \tag{4.6}$$

is satisfied in the τ valley, s is the spin and $\varepsilon_{\tau s}(k_r^{(\tau,s)})$ is the single-particle energy at $k_r^{(\tau,s)}$ given by Eq. (3.20). Then, the two Fermi points measured from the τ point are given by

$$k_r^{(\tau,s)} = -\tau\Delta k_\parallel^c + \tau K_\parallel + r\sqrt{\left(\frac{\tilde{\mu}_{\tau s}}{v_F\hbar}\right)^2 - \left(k_\perp - \tau K_\perp + \tau\Delta k_\perp^c + s\Delta k_\perp^{SO}\right)^2}, \tag{4.7}$$

with $\tilde{\mu}_{\tau s} = \mu - \tau s\Delta_{SO}^1$. Here, $\Delta k_\parallel^c$, $\Delta k_\perp^c$ are the curvature-induced shifts of the Dirac point from the τ point in the circumferential and the axial directions, respectively. $\Delta k_\perp^{SO}$ and Δ_{SO}^1 are the spin-dependent Dirac point shift in the circumferential direction and the Zeeman-type

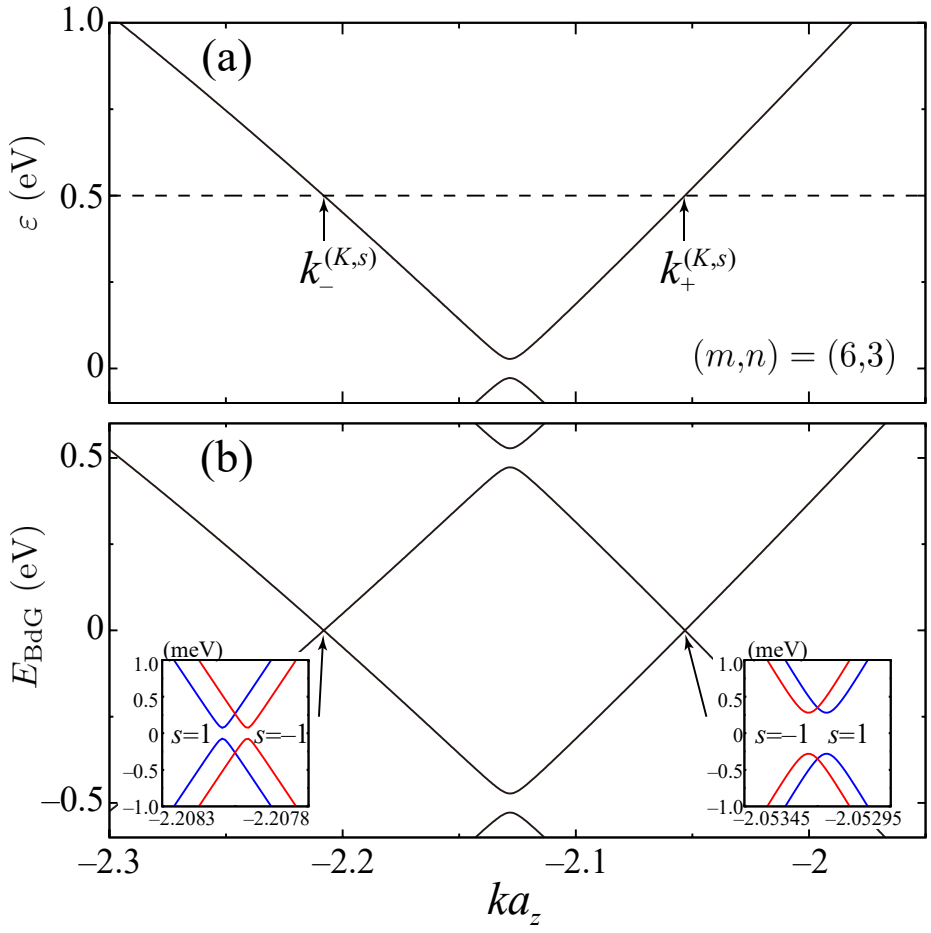

Figure 4.1: (a) Energy band, and (b) BdG excitation spectrum near the K point for an $(m, n) = (6, 3)$ carbon nanotube. The chemical potential is set to be $\mu = 500$ meV. The two arrows with $k_{\pm}^{(K,s)}$ in (a) indicate the two Fermi points. In (b) the superconducting coupling parameters are chosen to be $\Delta_0 = 0.5$ meV and $\Delta_1 = 2$ meV. Each inset in (b) shows the enlarged BdG spectrum near the two Fermi points. The blue and red curves show the BdG spectra for the spin-up and -down components, respectively.

energy shift, respectively, induced by the spin-orbit interaction.

We shall now derive the formula for the superconducting near the Fermi points. Thus, let us focus on the BdG spectrum near the superconducting gap by expanding $E_s = \pm\sqrt{A_s - 2\sqrt{B_s}}$ near the Fermi points. For a moderate chemical potential $|\mu| \lesssim 1$ eV, the $\boldsymbol{k}\cdot\boldsymbol{p}$ scheme can be used. The hopping functions $\gamma_s(\mathbf{k})$ and $f(\mathbf{k})$ are expanded around the τ point as [128]

$$\gamma_{\tau s}(k) \simeq v_F\hbar\left[\left(k - \tau K_{\parallel} + \tau\Delta k_{\parallel}^{c}\right) + i\left(k_{\perp} - \tau K_{\perp} + \tau\Delta k_{\perp}^{c} + s\Delta k_{\perp}^{SO}\right)\right], \tag{4.8}$$

$$\Delta_1 f(k) \simeq c\Delta_1\left(k - \tau K_{\parallel} + i\left(k_{\perp} - \tau K_{\perp}\right)\right), \tag{4.9}$$

where $c = \sqrt{3}a_c/2 = v_F\hbar/t$. Near the two Fermi points $k = k_r^{(\tau,s)}$ $(r = \pm 1)$ it holds

$$\gamma_{\tau s}\left(k_r^{(\tau,s)}\right) \simeq \gamma_{\tau sr} + v_F\hbar k', \quad \Delta_1 f\left(k_r^{(\tau,s)}\right) \simeq f_r = \frac{\Delta_1}{t}\gamma_{\tau sr} + C, \tag{4.10}$$

where k' is the 1D wave number measured from $k = k_r^{(\tau,s)}$. Furthermore, $\gamma_{\tau sr}$ and f_r are $\gamma_{\tau s}$ and f at the Fermi point, respectively,

$$\gamma_{\tau sr} = v_F\hbar\left[\left(k_r^{(\tau,s)} - \tau K_\parallel + \tau\Delta k_\parallel^c\right) + i\left(k_\perp - \tau K_\perp + \tau\Delta k_\perp^c + s\Delta k_\perp^{SO}\right)\right], \tag{4.11}$$

$$C = -c\Delta_1\left(\tau\Delta k_\parallel^c + i\left(\tau\Delta k_\perp^c + s\Delta k_\perp^{SO}\right)\right), \tag{4.12}$$

and we have discarded the weak k' dependence of $\gamma_{\tau s}$. Then, A and B are expanded near each Fermi point as $A_{\tau s} = A_0^{(\tau,s)} + A_1^{(\tau,s)}k' + A_2^{(\tau,s)}k'^2 + \cdots$ and $B_{\tau s} = B_0^{(\tau,s)} + B_1^{(\tau,s)}k' + B_2^{(\tau,s)}k'^2 + \cdots$ where $A_0^{(\tau,s)} = 2\tilde{\mu}_{\tau s}^2 + \Delta_0^2 + |f_r|^2$, $A_1^{(\tau,s)} = v_F\hbar\left(\gamma_{\tau sr} + \gamma_{\tau sr}^*\right)$ and

$$\begin{aligned}
B_0^{(\tau,s)} &= \tilde{\mu}_{\tau s}^4 + \tilde{\mu}_{\tau s}^2|\gamma_{\tau sr}|^2 - \frac{1}{4}\left(f_r\gamma_{\tau sr}^* + f_r^*\gamma_{\tau sr}\right)^2 - \left(f_r\gamma_{\tau sr}^* + f_r^*\gamma_{\tau sr}\right)\tilde{\mu}_{\tau s}\Delta_0, \\
B_1^{(\tau,s)} &= \tilde{\mu}_{\tau s}^2 v_F\hbar\left(f_r + f_r^*\right) + cv_F\hbar\left(f_r + f_r^*\right)|\gamma_{\tau sr}|^2 \\
&\quad - \frac{1}{2}v_F\hbar\left(f_r\gamma_{\tau sr}^* + f_r^*\gamma_{\tau sr}\right)\left(\gamma_{\tau sr} + \gamma_{\tau sr}^*\right) - v_F\hbar\left(\gamma_{\tau sr} + \gamma_{\tau sr}^*\right)\tilde{\mu}_{\tau s}\Delta_0.
\end{aligned}$$

Near the gap region, we have

$$E_{\tau s}^2 = A_{\tau s} - 2\sqrt{B_{\tau s}} = \left(A_0^{(\tau,s)} - 2\sqrt{B_0^{(\tau,s)}}\right) + \left(A_1^{(\tau,s)} - \frac{B_1^{(\tau,s)}}{\sqrt{B_0^{(\tau,s)}}}\right)k' + \cdots. \tag{4.13}$$

Using

$$\sqrt{B_0^{(\tau,s)}} \simeq \tilde{\mu}_{\tau s}^2\left[1 + \frac{1}{2}\left(\frac{|\gamma_{\tau sr}|^2}{\tilde{\mu}_{\tau s}^2} - \frac{\left(f_r\gamma_{\tau sr}^* + f_r^*\gamma_{\tau sr}\right)^2}{4\tilde{\mu}_{\tau s}^4} - \frac{\left(f_r\gamma_{\tau sr}^* + f_r^*\gamma_{\tau sr}\right)\Delta_0}{\tilde{\mu}_{\tau s}^3}\right)\right],$$

each coefficient in Eq. (4.13) is expressed as

$$A_0^{(\tau,s)} - 2\sqrt{B_0^{(\tau,s)}} = \left(\frac{\varepsilon_{\mathrm{g},r}^{(\tau,s)}}{2}\right)^2, \quad A_1^{(\tau,s)} - \frac{B_1^{(\tau,s)}}{\sqrt{B_0^{(\tau,s)}}} \simeq 0,$$

where

$$\varepsilon_{\mathrm{g},r}^{(\tau,s)} \equiv \frac{f_r \gamma_{\tau s r}^* + f_r^* \gamma_{\tau s r}}{\tilde{\mu}_{\tau s}} + 2\Delta_0, \tag{4.14}$$

and we have discarded the higher order of $\Delta_{0/1}/\tilde{\mu}_{\tau s}$ and $\Delta_{0/1}/t$ in each contribution. The coefficient of k' in Eq. (4.13) being zero means that the gap position is at $k = k_r^{(\tau,s)}$ within this approximation. Therefore, $\varepsilon_{g,r}^{(\tau,s)}$ represents the superconducting gap at $k = k_r^{(\tau,s)}$. By using Eqs. (4.10)–(4.12), we finally get the expression of the superconducting gap near $k_r^{(\tau,s)}$

$$\varepsilon_{g,r}^{(\tau,s)} = 2\Delta_0 + 2\Delta_1 \frac{\tilde{\mu}_{\tau s}}{t} \left[1 + \varepsilon_{\perp}^{(\tau,s)} E_{\perp}^{(\tau,s)} - r\tau \mathrm{sgn}\left(\tilde{\mu}_{\tau s}\right) \varepsilon_{\parallel}^{(\tau,s)} \sqrt{1 - \left(E_{\perp}^{(\tau,s)}\right)^2} \right], \tag{4.15}$$

where $E_{\perp}^{(\tau,s)} = \frac{v_F \hbar \left(k_\perp - \tau K_\perp + \tau \Delta k_\perp^c + s \Delta k_\perp^{SO}\right)}{\tilde{\mu}_{\tau s}}$, $\varepsilon_{\perp}^{(\tau,s)} = -\frac{v_F \hbar \left(\tau \Delta k_\perp^c + s \Delta k_\perp^{SO}\right)}{\tilde{\mu}_{\tau s}}$ and $\varepsilon_{\parallel}^{(\tau,s)} = \frac{v_F \hbar \Delta \left(k_\parallel^c - K_\parallel\right)}{\tilde{\mu}_{\tau s}}$. Since the absolute value of the numerator of $E_{\perp}^{(\tau,s)}$ expresses half of the bulk band gap, the relation $|E_{\perp}^{(\tau,s)}| < 1$ holds when the chemical potential is in the energy band regions. It should be noted that the superconducting gaps at the two Fermi points $k_r^{(\tau,s)}$ ($r = \pm 1$) are different as shown in the inset of Fig. 4.1(b) as well as expressed in Eq. (4.15). This is because the contribution of Δ_1 to the superconducting gap is k dependent and the contribution at the two Fermi points is different, reflecting the shift $\Delta k_\parallel^c$ of the Dirac point. The two different superconducting gaps at the two Fermi points play an important role in the emergence of edge states, as it will be discussed in the next chapter.

4.2. BdG spectrum in finite-length zigzag class carbon nanotubes

We perform numerical calculations of the spectrum of CNTs with length of a few micrometers which show that zero energy edge states emerge in some regions of chemical potential and proximity pairing strengths. These calculations are based on a 1D lattice model which includes the effects of curvature and superconductivity, and uses the helical-angular symmetry of the system [146]. It extends the 1D lattice model of Refs. [140, 145, 147] to the superconducting case and is introduced in section 3.7. The eigenvalue solver FEAST [161] of the Intel Math Kernel Library was used for the numerical calculation.

We focus on a (6,3) carbon nanotube with $N_L = 2 \cdot 10^5$ unit cells, which corresponds to a length of 16.1 μm, as an example for the zigzag class CNTs. The BdG Hamiltonian is diagonalized as

$$\mathcal{H}_{\boldsymbol{\mu}} = \sum_{l_v} \varepsilon_{\mathrm{BdG}}^{(\boldsymbol{k}_\perp l_v)} b_{\boldsymbol{k}_\perp l_v}^\dagger b_{\boldsymbol{k}_\perp l_v}, \tag{4.16}$$

where l_v enumerates the quasiparticle energy levels, and

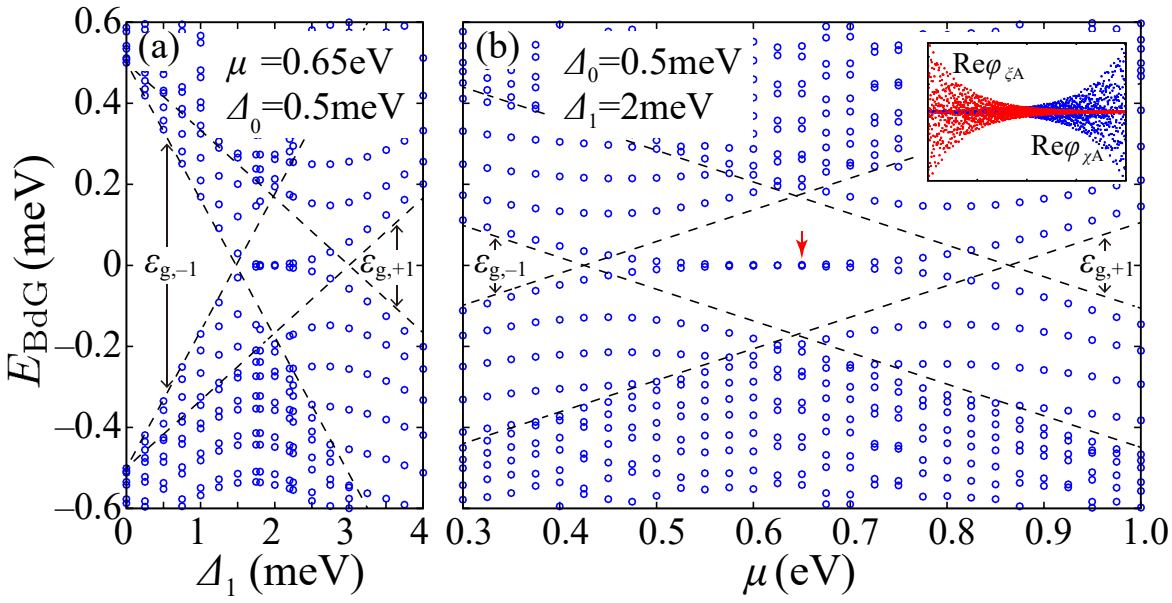

Figure 4.2: BdG spectrum of a $(6,3)$ nanotube with a length of 16.1 μm in the $(K,1)$ subspace. (a) Spectrum as a function of the superconducting pairing Δ_1, and (b) as a function of the chemical potential μ. Blue circles show the calculated spectrum and the dashed lines show the superconducting gaps $\varepsilon_{\mathrm{g},r}^{(K,s=1)}$ of the bulk system given in Eq. (4.15). The inset in (b) shows the real part components $\phi_{\chi\mathrm{A}}$ (blue) and $\phi_{\xi\mathrm{A}}$ (red) in arbitrary units as a function of lattice site ℓ for the calculated eigenfunction at $\varepsilon_{\mathrm{BdG}}=0$ with $\Delta_0=0.5$ meV, $\Delta_1=2$ meV and $\mu=650$ meV [indicated by the red arrow in (b)]. The definition of $\phi_{p\sigma}$ $(p=\chi,\xi)$ is given in Eq. (4.18).

$$b^{\dagger}_{\boldsymbol{k}_\perp l_v}=\sum_{\ell\sigma}\left(\phi^{(\boldsymbol{k}_\perp l_v)}_{\mathrm{p}\sigma}(\ell)c^{\dagger}_{\sigma\ell\boldsymbol{k}_\perp}+\phi^{(\boldsymbol{k}_\perp l_v)}_{\mathrm{h}\sigma}(\ell)c_{\sigma\ell-\boldsymbol{k}_\perp}\right). \tag{4.17}$$

Figure 4.2 shows the calculated spectrum in the energy region of the order of the superconducting gaps in the subspace $(K,1)$. The boundary shape is depicted in Fig. 3.10(c), which belongs to the class of so-called minimal boundaries. The dashed lines show the evolution of the superconducting gaps $\varepsilon_{\mathrm{g},r}^{(\tau,s)}$ given in Eq. (4.15) with Δ_1 [Fig. 4.2(a)] and μ [Fig. 4.2(b)]. The functions $\phi_{\chi\mathrm{A}}$, $\phi_{\xi\mathrm{A}}$ shown in the inset of Fig. 4.2(b) are connected to ϕ_{pA}, ϕ_{hA} by a unitary transformation

$$\begin{pmatrix}\phi_{\chi\sigma}\\ \phi_{\xi\sigma}\end{pmatrix}=U_C^{-1}\begin{pmatrix}\phi_{\mathrm{p}\sigma}\\ \phi_{\mathrm{h}\sigma}\end{pmatrix}, \tag{4.18}$$

where U_C is the chiral transformation (1.15). In the region $1.5\lesssim\Delta_1\lesssim 3$ meV in Fig. 4.2(a) and $400\lesssim\mu\lesssim 900$ meV in Fig. 4.2(b), states near zero energy exist inside the gap region. As shown in the inset in Fig. 4.2(b), these states are localized at the edges and their nature will be discussed in the coming sections. Calculations for the other three subspaces, $(K,-1)$ and $(K',\pm1)$, exhibit an almost identical behavior (not shown) as the one seen in Fig. 4.2. Emergence of the zero energy states in these region is also seen (not shown) for other boundary

shapes, e.g., when removing or adding a A sublattice atom at the end of the boundary shown in Fig. 3.10(c). The numerical result in Fig. 4.2 clearly shows that there exist edge states at zero energy in some parameter regions. To explore the condition for the emergence of the edge states, we will analyze the bulk system from a topological viewpoint.

4.3. Topological phase diagram

We consider the bulk Hamiltonian given in Eq. (4.3). Let us comment on the symmetry class to which our 1D model belongs according to the topological classification in Ref. [75]. Since we have only the chiral symmetry in each (τ,s) subspace, the 1D model in that space belongs to the AIII class. The total Hamiltonian has time-reversal symmetry, and belongs to class DIII. Further discussion on the different topological invariants in our system can be found in chapter 4.3.2. Since the Hamiltonian has the chiral symmetry $\{C,\mathcal{H}_{\rm BdG}\}=0$, where $C=\tau_y$ acting in the Nambu space. We will now use the Hamiltonian in Eq. (4.3) in its off-diagonal form (4.4).

4.3.1. Winding number

Due to the chiral symmetry, one can introduce the winding number (1.21)

$$\nu=-\frac{1}{4\pi i}\int_{-\pi/a_z}^{\pi/a_z}dk{\rm Tr}\left[C\mathcal{H}_{\rm BdG}^{-1}(k)\partial_k\mathcal{H}_{\rm BdG}(k)\right]$$

as a 1D topological invariant [81, 82]. Because the chiral operator is transformed as $\tilde{C}=U_C^\dagger C U_C=\tau_z$, the winding number is written as

$$\begin{aligned}\nu_s&=-\frac{1}{4\pi i}\int dk{\rm Tr}\left[\tilde{C}\tilde{\mathcal{H}}_s^{-1}\partial_k\tilde{\mathcal{H}}_s\right]=\frac{1}{4\pi i}\int dk{\rm Tr}\left[D_s^{-1}\partial_k D_s-D_s^{\dagger-1}\partial_k D_s^\dagger\right]\\&=\frac{1}{4\pi i}\int dk\left(\partial_k\log\det D_s-\partial_k\log\det D_s^\dagger\right)=\frac{1}{2\pi}{\rm Im}\int dk\partial_k\log\det D_s\\&=\frac{1}{2\pi}\int dk\partial_k\arg\det D_s,\end{aligned}\tag{4.19}$$

where we have used the formulas

$$\begin{aligned}&{\rm Tr}\left[D^{-1}\partial_k D\right]=\partial_k\log\det D,\\&\log\det D^\dagger={\rm Re}\left(\log\det D\right)-i{\rm Im}\left(\log\det D\right),\end{aligned}$$

the determinant of $D_s(\mathbf{k})$ being

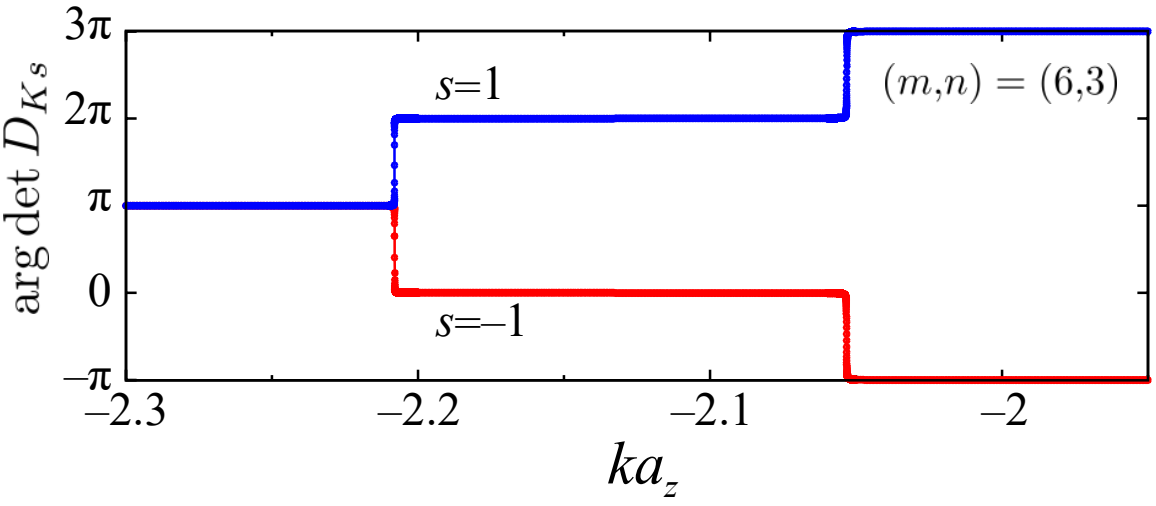

Figure 4.3: Phase of $\det D_{\tau s}$, $\arg\det D_{\tau s}$, appearing in the integrand of the winding number in Eq. (4.19), for an $(6,3)$ nanotube near the K point for which the angular momentum is $k_\perp = 2$. The parameters are the same as those in Fig. 4.1(b). The continuous change of the function in the interval $-\pi \leq \arg\det D_{\tau s} \leq 3\pi$ is clearly seen. The blue and red curves show the spin components $s = 1$ and -1, respectively. Note that both of them are almost equal π in the regions of $ka_z \lesssim -2.21$. For this case, the integrand gives contribution $+1$ (-1) to the winding number for $s = 1$ $(s = -1)$.

$$\det D_s(\mathbf{k}) = \tilde{\varepsilon}^2(\mathbf{k}) - \Delta_0^2 - |\gamma_s(\mathbf{k})|^2 + \Delta_1^2 |f(\mathbf{k})|^2 + 2is\left(\tilde{\varepsilon}(\mathbf{k})\Delta_0 + \Delta_1 \frac{\gamma_s(\mathbf{k}) f(\mathbf{k})^* + \gamma_s(\mathbf{k})^* f(\mathbf{k})}{2}\right) \tag{4.20}$$

For the case of $|\Delta_0|, |\Delta_1| \ll |\mu|, |t|$, on which we are focusing, the real part of $\det D_s(\mathbf{k})$ is expressed as

$$\mathrm{Re}\left(\det D_s(\mathbf{k})\right) \simeq \tilde{\varepsilon}^2(\mathbf{k}) - |\gamma_s(\mathbf{k})|^2.$$

Except near the Fermi points, we have

$$|\mathrm{Re}\left(\det D_s(\mathbf{k})\right)| \gg |\mathrm{Im}\left(\det D_s(\mathbf{k})\right)|$$

since the imaginary part of $\det D_s(\mathbf{k})$ is proportional to the superconducting pairing potentials Δ_0 and Δ_1. Therefore, Eq. (4.20) is approximated as a positive or negative real number, and then the phase of $\det D_s(k)$ is almost constant and equal to 0 or π. This feature is clearly observed in Fig. 4.3, which shows the phase of the determinant of $D_{Ks}(k)$ near the K point.

Let us focus on the regions near the Fermi points at the τ valley, which are the only ones where the phase of $\det D_s$ changes and a finite contribution to the integral in Eq. (4.19) is expected, as can be seen in Fig. 4.3. As seen in the $\boldsymbol{k}\cdot\boldsymbol{p}$ scheme, in which the functions $\gamma_s(\mathbf{k})$ and $f(\mathbf{k})$ have the form in Eqs. (4.8) and (4.9), $\mathrm{Re}\left(\det D_{\tau s}\right)$ behaves quadratically in k near

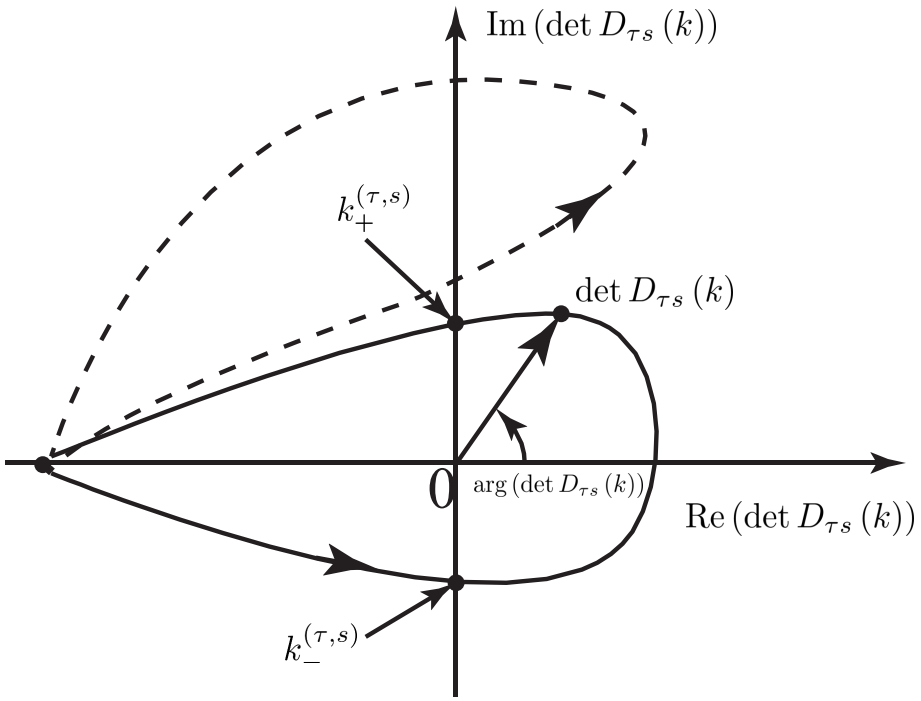

Figure 4.4: Schematics of the trajectories of the complex function $\det D_{\tau s}$ in the complex plane when k changes from $k \ll k_-^{(\tau,s)}$ to $k \gg k_+^{(\tau,s)}$. The solid curve shows an example for a nontrivial winding number $\nu_{\tau s} = 1$ and the dashed curve shows a case for a trivial winding number $\nu_{\tau s} = 0$.

the τ point. That is, $\mathrm{Re}\,(\det D_{\tau s})$ is negative for $k < k_-^{(\tau,s)}$ and $k > k_+^{(\tau,s)}$, and is positive for $k_-^{(\tau,s)} < k < k_+^{(\tau,s)}$. Note that the two roots of $\mathrm{Re}\,(\det D_{\tau s})$ are regarded as the two Fermi points in our approximation of small superconducting couplings.

Let us define $D_r^{(\tau,s)} \equiv D_{\tau s}\left(k_r^{(\tau,s)}\right)$, the function $D_{\tau s}$ at the Fermi point for the τ valley. When $\mathrm{Im}(D_+^{(\tau,s)})$ has the opposite sign of $\mathrm{Im}(D_-^{(\tau,s)})$,

$$\mathrm{Im}\left(\det D_+^{(\tau,s)}\right)\mathrm{Im}\left(D_-^{(\tau,s)}\right) < 0, \tag{4.21}$$

then $\det D_{\tau s}$ near the Dirac point contributes to a nontrivial winding number (see the schematics in Fig. 4.4). Note that the maximum contribution to the winding number per Dirac point is $|\nu_{\tau s}| = 1$ because of the above discussion. The sign of the winding number is given by the sign of $\mathrm{Im}(\det D_+^{(\tau,s)})$, that is, the winding number is

$$\nu_{\tau s} = \mathrm{sgn}\left[\mathrm{Im}(\det D_+^{(\tau,s)})\right]\nu_{\tau s}|.$$

Figure 4.5 shows the topological phase diagram for an (6,3) nanotube calculated from Eq. (4.21) for $(\tau, s) = (K, 1)$. Within the $\boldsymbol{k}\cdot\boldsymbol{p}$ approximation, near the τ point the imaginary part of $\det D_{\tau s}$ is given by

$$\frac{\mathrm{Im}\left(\det D_r^{(\tau,s)}\right)}{2s} = \tilde{\mu}_{\tau s}\Delta_0 + cv_F\hbar\Delta_1\left[k\left(k+\tau\Delta k_\parallel^c\right) + k_\perp\left(k_\perp + \tau\Delta k_\perp^c + s\Delta k_\perp^{SO}\right)\right].$$

At the Fermi points $k = k_r^{(\tau,s)}$ the imaginary part is calculated as

$$\frac{\mathrm{Im}\left(\det D_r^{(\tau,s)}\right)}{2s}\frac{t}{\tilde{\mu}_{\tau s}^2\Delta_0} = \frac{t}{\tilde{\mu}_{\tau s}} + \frac{\Delta_1}{\Delta_0}\left(1+\varepsilon_\perp^{(\tau,s)}E_\perp^{(\tau,s)}\right) - r\frac{\Delta_1}{\Delta_0}\tau\varepsilon_\parallel^{(\tau,s)}\mathrm{sgn}(\tilde{\mu}_{\tau s})\sqrt{1-\left(E_\perp^{(\tau,s)}\right)^2}.$$

Then, the condition (4.21) is summarized as

$$\left[\frac{t}{\tilde{\mu}_{\tau s}} + \left(\frac{\Delta_1}{\Delta_0}\right)\left(1+\varepsilon_\perp^{(\tau,s)}E_\perp^{(\tau,s)}\right)\right]^2 - \left(\varepsilon_\parallel^{(\tau,s)}\right)^2\left(\frac{\Delta_1}{\Delta_0}\right)^2\left(1-\left(E_\perp^{(\tau,s)}\right)^2\right) < 0. \tag{4.22}$$

Using the relation

$$\mathrm{Im}\left(\det D_r^{(\tau,s)}\right) = s\tilde{\mu}_{\tau s}\varepsilon_{\mathrm{g},r}^{(\tau,s)}, \tag{4.23}$$

which comes from Eq. (4.14), the sign of the winding number can also be evaluated. As seen in Eq. (4.22), the condition holds only when $\varepsilon_\parallel^{(\tau,s)} \neq 0$, that is, $\Delta k_\parallel^c \neq 0$, the case of a finite shift of the Dirac point in the axial direction, and $\Delta_1 \neq 0$. Note that $\left(E_\perp^{(\tau,s)}\right)^2 < 1$ holds outside the energy gap of the nanotubes. As shown in Eq. (3.17), we have a finite $\Delta k_\parallel^c$ except for the pure zigzag CNTs, for which the chiral angle is $\theta = 0$. We also notice that the condition (4.22) depends on the ratio of Δ_0 and Δ_1 but not on their absolute values.

At the border between different topological phases, one of the two superconducting gaps $\varepsilon_{\mathrm{g},r}^{(\tau,s)}$ ($r = \pm 1$) becomes zero. Then, from the condition $\varepsilon_{\mathrm{g},r}^{(\tau,s)} = 0$ and Eq. (4.15), the border is determined by

$$\frac{\Delta_1}{\Delta_0} = -\frac{t}{\tilde{\mu}_{\tau s}}\frac{\left(1+\varepsilon_\perp^{(\tau,s)}E_\perp^{(\tau,s)}\right) + r\tau\mathrm{sgn}(\tilde{\mu}_{\tau s})\varepsilon_\parallel^{(\tau,s)}\sqrt{1-\left(E_\perp^{(\tau,s)}\right)^2}}{\left(1+\varepsilon_\perp^{(\tau,s)}E_\perp^{(\tau,s)}\right)^2 - \left(\varepsilon_\parallel^{(\tau,s)}\right)^2\left(1-\left(E_\perp^{(\tau,s)}\right)^2\right)}. \tag{4.24}$$

Note that the border is also given by the roots of the left-hand side of Eq. (4.22). By comparing with the numerical calculation in Fig. 4.2, we confirm that the zero energy edge states appear in the region where the winding number has a nonzero value. The region becomes narrower and the borders asymptotically behave as $\Delta_1/\Delta_0 \simeq -t/\mu$ for a large μ. This implies that to

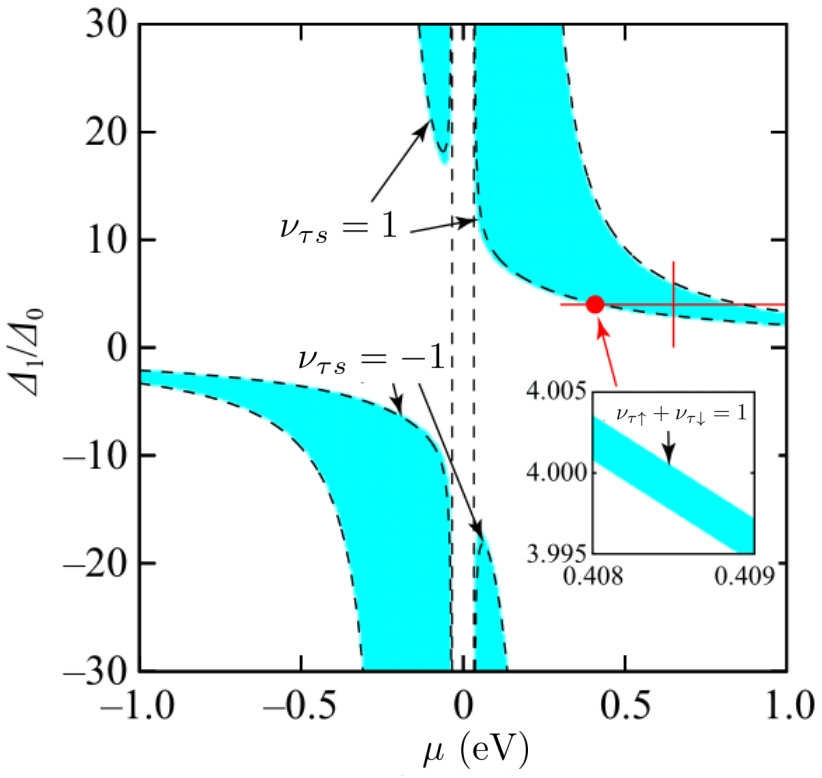

Figure 4.5: Topological phase diagram for an (6, 3) nanotube estimated from Eq. (4.21) for $(\tau, s) = (K,1)$ in μ and Δ_1/Δ_0 plane, where $\Delta_0 = 0.5$meV. The light blue areas show the region of nontrivial winding number, $|\nu_{\tau s} = 1|$. The dashed curves show Eq. (4.24), the analytical expression for the border of the topological phases. The region between the dashed vertical lines is the band-gap region of the normal state. The red lines indicate the parameter of Fig. 4.2. The inset shows the phase diagram for the value $\nu_{\tau+1} + \nu_{\tau-1}$ near the region marked by the red point, which has a nontrivial value only near the border of the main figure.

have nontrivial winding number, the ratio $\delta = \Delta_1/\Delta_0$ becomes smaller and comparable to 1 for $|\mu| \sim |t|$, as shown in Fig. 4.5. However, such a chemical potential might be unrealistically large.

Let us comment on the effect of the spin-orbit interaction. As shown in Eq. (3.19), the spin-orbit interaction gives the spin dependence in the phase diagram. Since we are focusing on the conducting region for the normal state, we have $|\mu| \gg |\Delta^1_{SO}|$. Furthermore, we also have the relation $|\Delta k^c_\perp| \gg |\Delta k^{SO}_\perp|$ except for the armchair CNTs. For the armchair CNTs, the spin-orbit interaction opens a small gap at $\mu = 0$, as already pointed out in previous studies [127, 128, 162, 163]. Therefore, we have an almost identical phase diagram for the (τ, s) and $(\tau, -s)$ subspaces except for the sign difference reflecting the opposite winding direction between s and $-s$, as seen in the relation (4.23). A small difference between the opposite spins, shown as the finite value of $\nu_{K\uparrow} + \nu_{K\downarrow}$ in the inset of Fig. 4.5, appears at the border region scaled by the spin-orbit interaction. Note that the phase diagrams for (τ, s) and $(-\tau, -s)$ are the same including the sign. Therefore, the total winding number, $\sum_{\tau,s} \nu_{\tau s} = 2(\nu_{K\uparrow} + \nu_{K\downarrow})$, shows the same diagram as $\nu_{K\uparrow} + \nu_{K\downarrow}$. As a result, the *total* winding number is nonzero only in very narrow regions of the parameter space. Nevertheless, several

edge states are present in the nanotube even when the total winding number is zero, which proves that the total topological invariant may miss a rich part of the physics of the system.

As a further example, it should be noted that in the armchair class the winding number becomes zero even when the condition (4.22) is satisfied for both valleys. This is because the winding directions for the τ and $-\tau$ valley are opposite, which can be seen from the relation Eq. (4.23). However, this does not mean that there is no edge state for the armchair class, as discussed in Sec. 4.5.

It should be noted that the nontrivial topological phase obtained in our work does not contradict a previous study [164], which predicts only a trivial topological phase if the induced superconducting correlation is s-wave. This correlation appears in our Hamiltonian as the onsite pairing. As already mentioned, the Δ_1 term, which is the coupling constant for the k-linear term in Eq. (4.9), and thus acts as the p-wave superconducting coupling [119], is needed to have the nontrivial topological phases.

4.3.2. Relation between $\mathbb{Z}$ and $\mathbb{Z}_2$ invariants

We have shown that an integer ($\mathbb{Z}$) topological invariant, the winding number, can be defined for our system. The periodic table of topological invariants [22] nevertheless states that a DIII class Hamiltonian has a parity like $\mathbb{Z}_2$ invariant. These two facts appear contradictory, but are not, as we will now clarify. The discussion is based on the approach to topological invariants presented in the review by Chiu *et al* [22]. In systems with chiral symmetry, in the gauge given by the chiral basis the winding number can be shown to be $\mathbb{Z} \ni \nu_l = 2\gamma_l$ with γ_l defined in Eq. (1.19), therefore $\mathcal{M} = \exp(i\pi \sum_l \nu_l) = \pm 1$. In systems with particle-hole symmetry the topological invariant $\mathcal{M}$ can be evaluated using the representation of the Hamiltonian in the Majorana basis,

$$\mathcal{H}(k) = U_{\mathrm{M}}^{\dagger}[iX(k)]U_{\mathrm{M}}.$$

The topological invariant $\mathcal{M}$ can then be expressed through the Pfaffian of X (1.28),

$$\mathcal{M} = \mathrm{sgn}\left\{\mathrm{Pf}[X(\pi)]\ \mathrm{Pf}[X(0)]\right\} = \pm 1,$$

In our system the Hamiltonian $\mathcal{H}(\mathbf{k})$ has the block-diagonal form,

$$\mathcal{H}(\mathbf{k}) = \mathrm{diag}\left[H_{\uparrow}(\mathbf{k}), H_{\downarrow}(\mathbf{k})\right],$$

where $H_s(\mathbf{k})$ are defined in Eq. (4.3). The transformation U_{M} is defined as

$$U_{\mathrm{M}} = \frac{1}{\sqrt{2}} \begin{pmatrix} 1 & 0 & 0 & 0 & 0 & 0 & 1 & 0 \\ i & 0 & 0 & 0 & 0 & 0 & -i & 0 \\ 0 & 1 & 0 & 0 & 0 & 0 & 0 & 1 \\ 0 & i & 0 & 0 & 0 & 0 & 0 & -i \\ 0 & 0 & 1 & 0 & 1 & 0 & 0 & 0 \\ 0 & 0 & i & 0 & -i & 0 & 0 & 0 \\ 0 & 0 & 0 & 1 & 0 & 1 & 0 & 0 \\ 0 & 0 & 0 & i & 0 & -i & 0 & 0 \end{pmatrix},$$

resulting in $X(\mathbf{k}) = \mathrm{diag}\left[X_{\uparrow}(\mathbf{k}), X_{\downarrow}(\mathbf{k})\right]$. Then, the Pfaffian is given by

$$\mathrm{Pf}[X\left(\mathbf{k}\right)] = \mathrm{Pf}[X_{\uparrow}\left(\mathbf{k}\right)]\,\mathrm{Pf}[X_{\downarrow}\left(\mathbf{k}\right)]$$

where

$$\begin{aligned} \mathrm{Pf}[X_s\left(\mathbf{k}\right)] = & \left[\left(\tilde{\varepsilon}^2\left(\mathbf{k}\right) - \Delta_0^2\right) - \left(\left|\gamma_s\left(\mathbf{k}\right)\right|^2 - \Delta_1^2 \left|f\left(\mathbf{k}\right)\right|^2\right)\right]^2 \\ & + \left[2\tilde{\varepsilon}\left(\mathbf{k}\right)\Delta_0 + \Delta_1\left(\gamma_s\left(\mathbf{k}\right) f^*\left(\mathbf{k}\right) + \gamma_s^*\left(\mathbf{k}\right) f\left(\mathbf{k}\right)\right)\right]^2. \end{aligned}$$

Since the Pfaffian is always non-negative, the topological invariant $\mathcal{M}$ is also trivial. Indeed, our total winding number is always even, $\nu = \sum_{\tau,s} \nu_{\tau s} = 0, \pm 2$, therefore, the corresponding $\mathcal{M} = +1$. Our nanotube from the $\mathbb{Z}_2$ point of view is always in the trivial phase. Nevertheless, a total invariant does not give the full information about the system. It is especially clear in quantum spin Hall insulators, where the total Chern number, summed over two spin directions, vanishes but the edge states exist for both spins and even are topologically protected [165]. The information carried by the partial invariants is therefore more useful.

As a last remark, in contrast to the topological insulators, the edge states generated by the four (τ,s) subspaces of our system are not topologically protected, as can be seen from Figs. 4.6(d) and 4.6(e), where the valley mixing clearly gaps them. Our system is then more similar to a weak topological insulator, where the states generated by the nontrivial weak partial invariant can be gapped by disorder, i.e., a breaking of translational invariance [166].

4.4. Bulk-edge correspondence

In this section we shall reveal the deep physical meaning of the condition constituting Eq. (4.21). As mentioned in the Introduction, it has been shown [140] for the CNTs in the normal state that the winding number per (τ,s) space $\nu_{\tau s}$ is equal to the number of edge states in this

space. The latter are given by the difference between the number of evanescent modes, being the solutions of the mode equation at zero energy, and the number of boundary conditions for given sublattice. This gives a one-to-one correspondence between the winding number as a topological invariant and the number of physical edge states. This kind of relation is called a bulk-edge correspondence. Let us discuss the bulk-edge correspondence for the present system by including the finite length of the CNT in our description.

Since the relevant contribution to the winding number comes from the neighborhood of the τ point, we shall consider an effective 1D continuum model obtained by expanding around the τ point. The envelope function,

$$\Psi_{\tau s} = \begin{pmatrix} \Psi_{\chi\tau s} \\ \Psi_{\xi\tau s} \end{pmatrix}, \quad \Psi_{p\tau s} = \begin{pmatrix} \Psi_{p\mathrm{A}\tau s} \\ \Psi_{p\mathrm{B}\tau s} \end{pmatrix},$$

obeys the equation,

$$\hat{\tilde{H}}_{\tau s}(\hat{k})\Psi_{\tau s} = E\Psi_{\tau s},$$

where $p = \chi, \xi$, and $\hat{\tilde{H}}_{\tau s}(\hat{k})$ has the same functional form of Eq. (4.4) with Eqs. (4.8) and (4.9). However, the wave number k is now regarded as the operator

$$\hat{k} = -i\frac{\partial}{\partial z}$$

in the continuum model. At zero energy, $E = 0$, the equation can be divided into two sets of equations with 2×2 matrix forms:

$$\hat{D}_{p\tau s}(\hat{k})\Psi_{p\tau s} = 0,$$

where $\hat{D}_{\chi\tau s}(\hat{k})$ and $\hat{D}_{\xi\tau s}(\hat{k})$ are given by changing $k \to \hat{k}$ in $D^{\dagger}_{\tau s}(k)$ and $D_{\tau s}(k)$, respectively. Let us consider the modes with the following form:

$$\Psi_{p\tau s} = e^{iqz} \begin{pmatrix} 1 \\ \eta_p \end{pmatrix}. \tag{4.25}$$

In each p block, the modes obey the following equation:

$$\begin{pmatrix} -\tilde{\mu}_{\tau s} + ips\Delta_0 & v_F\hbar\left(q + \tau\Delta k_{\parallel}^c\right) + ipcs\Delta_1 q + iv_F\hbar\left(k_\perp + \tau\Delta k_\perp^c + s\Delta k_\perp^{SO}\right) - pcs\Delta_1 k_\perp \\ v_F\hbar\left(q + \tau\Delta k_{\parallel}^c\right) + ipcs\Delta_1 q - iv_F\hbar\left(k_\perp + \tau\Delta k_\perp^c + s\Delta k_\perp^{SO}\right) - pcs\Delta_1 k_\perp & -\tilde{\mu}_{\tau s} + ips\Delta_0 \end{pmatrix} \times \begin{pmatrix} 1 \\ \eta_p \end{pmatrix} = 0, \tag{4.26}$$

where we have alternatively used the index $p = 1$ and -1 for $p = \chi$ and ξ, respectively. To have nontrivial solutions, the determinant of the matrix in Eq. (4.26) should be zero. Since this gives a second-order equation in q, there exist two modes corresponding to the solutions $q_r^{(\tau,s)}$. A relation between $q_r^{(\tau,s)}$ and the Fermi point $k_r^{(\tau,s)}$ will be shown in Eq. (4.28).

Within the continuum model, the microscopic boundary condition is implicitly taken into account in order to form eigenstates. They are constructed as linear combinations of two independent modes, a leftgoing and a rightgoing one, subject to boundary conditions at each end. Note that in the superconducting gap region the two modes are two decaying modes, that is, $|\kappa_r^{(\tau,s)}| < 1$ or $|\kappa_r^{(\tau,s)}| > 1$, where $\kappa_r^{(\tau,s)} \equiv \mathrm{Im}(q_r^{(\tau,s)})$. If the two modes have the same decaying direction, that is,

$$\kappa_+^{(\tau,s)}\kappa_-^{(\tau,s)} > 0, \tag{4.27}$$

then an edge state given by the linear combination of the two modes appears at an end. In the following we explicitly show that this condition is identical to the condition (4.21) for nontrivial winding number.

As shown in Appendix C, we arrive after some algebra to the two solutions

$$\mathrm{Re}\left(q_r^{(\tau,s)}\right) \simeq k_r^{(\tau,s)}, \quad \kappa_r^{(\tau,s)} \simeq -\frac{rps\,\mathrm{sgn}(\tilde{\mu}_{\tau s})}{v_F\hbar\sqrt{1 - \left(E_\perp^{(\tau,s)}\right)^2}} \frac{\varepsilon_{\mathrm{g},r}^{(\tau,s)}}{2}. \tag{4.28}$$

Since we have the relation (4.23), we get

$$\kappa_r^{(\tau,s)} = -\frac{rp\ \mathrm{Im}\left(\det D_r^{(\tau,s)}\right)}{4|\tilde{\mu}_{\tau s}|v_F\hbar\sqrt{1 - \left(E_\perp^{(\tau,s)}\right)^2}}. \tag{4.29}$$

Combining Eqs. (4.27) and (4.29), it is immediately clear that the condition for emergence of an edge state is identical to the condition for a nontrivial winding number expressed by Eq. (4.21).

It is worth noting that, from Eq. (4.28), the decay length of the edge state is proportional to the Fermi velocity, $-v_F\hbar\sqrt{1-\left(E_\perp^{(\tau,s)}\right)^2}/\hbar$, of the normal states at the given chemical potential and is inversely proportional to the superconducting gap. This implies the shortest decay length to be near the bottom of the conduction or top of the valence bands for the semiconducting CNTs.

4.5. Armchair class

Let us discuss the effect of valley coupling by considering the armchair class CNTs, in which the two valleys have the same angular momentum. In previous studies [137, 145], it has been shown that the nature of the valley coupling depends on the boundary conditions. Here we consider two types of boundaries. One is the minimal boundary, in which the edge has minimum number of dangling bonds [see Figs. 4.6(a) and 4.6(b)]. Another is the orthogonal boundary formed by a simple cut of the lattice in the plane orthogonal to the nanotube axis [see Figs. 4.6(a) and 4.6(c)]. The two valleys are nearly decoupled for the former case, while they strongly couple for the latter case, where each eigenstate is formed from a leftgoing mode at one valley and a rightgoing mode at another valley [145].

Figure 4.6 shows the calculated spectrum for an (5,2) nanotube with $N_L = 4 \cdot 10^5$ unit cells, which corresponds to the nanotube length of 13.6 μm, in the subspace of $(k_{\perp K}, 1)$, where now K K' correspond to the same $l_\perp = 0$. Figures 4.6(d) and 4.6(e), which show the case of the minimal boundary, exhibit a spectrum similar to that in Fig. 4.2. Edge states near zero energy are seen inside the gap region for $1 \lesssim \Delta_1 \lesssim 4$ meV in Fig. 4.6(d), and for $350 \lesssim \mu \lesssim 950$ meV in Fig. 4.6(e). A small deviation from zero energy is observed because of weak valley coupling. On the other hand, Figs. 4.6(f) and 4.6(g), which show the case of the orthogonal boundary, do not support zero energy states in the same region of superconducting pairing and chemical potential as in Figs. 4.6(d) and 4.6(e). This is in contrast to the zigzag class CNTs, in which the shape of the boundary does not affect the number of edge states if $k_\perp$ remains a good quantum number since the two valleys have different $k_\perp$ and they are decoupled.

The absence of zero energy states for the case of strong valley coupling in Figs. 4.6(f) and 4.6(g) can be captured by the expressions we have obtained in Sec. 4.4. Between the two states specified by (τ, s, r) and $(-\tau, s, -r)$, which form a pair for an eigenstate under the boundary condition, we always have the relation $\kappa_r^{(\tau,s)} \simeq -\kappa_{-r}^{(-\tau,s)}$ because $\varepsilon_{\mathrm{g},r}^{(\tau,s)} \simeq \varepsilon_{\mathrm{g},r}^{(-\tau,s)}$. Therefore, the condition (4.27) of emergence of edge states is never satisfied for this case.

4.6. Conclusion

We have studied the edge states in the proximity-induced superconducting gap of finite-length CNTs from the topological viewpoint. Our analysis shows that the numerically observed edge states are due to the combined effect of curvature-induced Dirac point shifting and strong

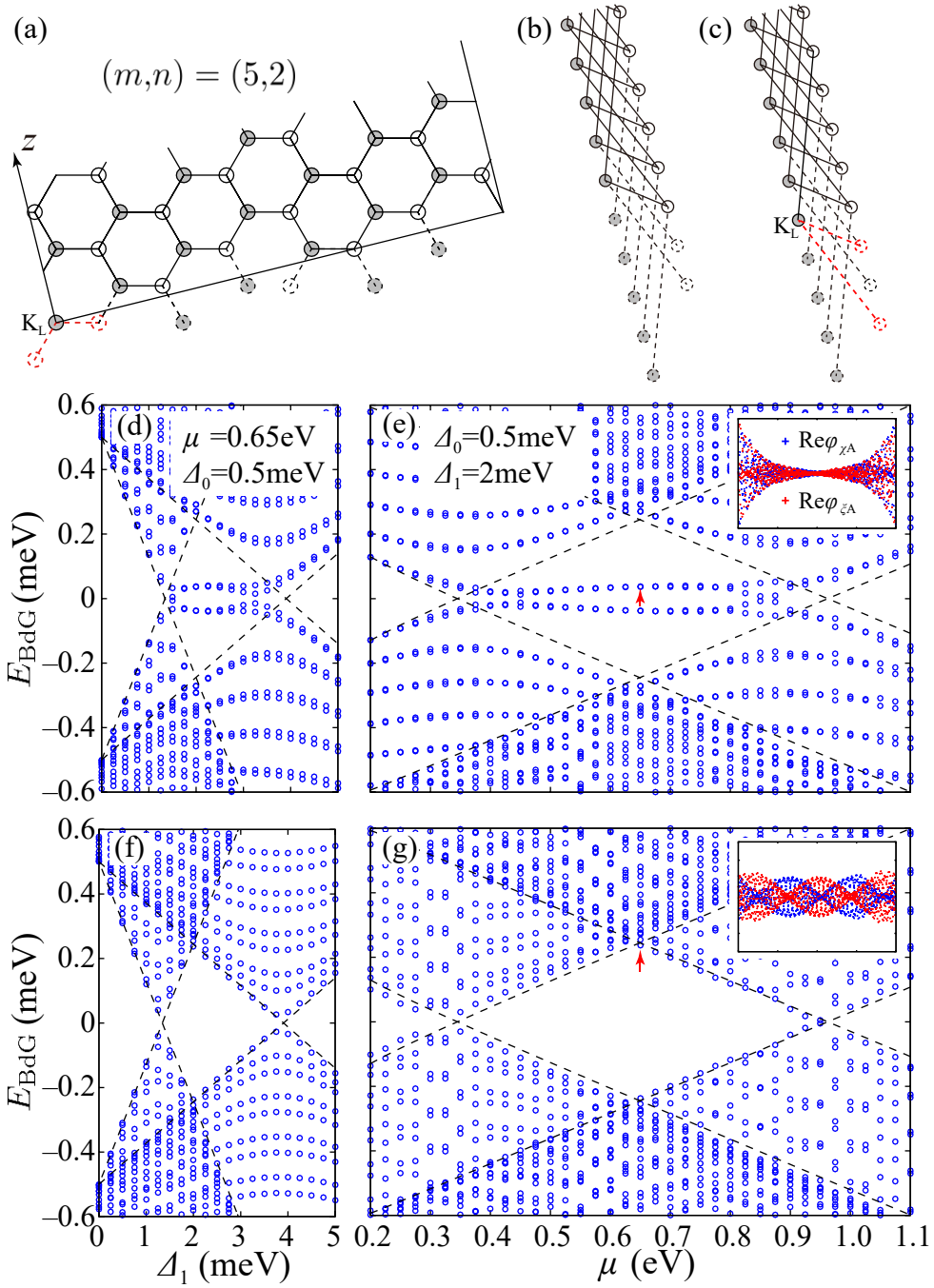

Figure 4.6: BdG spectrum of an armchair class $(5,2)$ nanotube with length of 13.6 μm in the $(K,+1)$ subspace. (a) Unrolled tube near the left end. The boundary is formed by a simple cut of the lattice in the plane orthogonal to the nanotube axis, represented by the solid line perpendicular to the z axis. Removed lattice sites adjacent to the boundary sites are represented by dashed circles, and the dangling bonds are represented by the dashed lines. The orthogonal boundary is given by keeping the Klein site indicated by $\mathrm{K_L}$, and the minimal boundary is given by removing the Klein site. (b) Minimal and (c) orthogonal boundaries, respectively, in the 1D model. (d) BdG spectrum as a function of the superconducting pairing Δ_1, and, (e) as a function of the chemical potential μ, respectively, for the minimal boundary, and in (f) and (g) for the orthogonal boundary. Each inset in (e) and (g) shows the real part components $\phi_{\chi\mathrm{A}}$ (blue) and $\phi_{\xi\mathrm{A}}$ (red) in arbitrary units as a function of lattice site ℓ for the calculated eigenfunction at the state indicated by the red arrow.

superconducting coupling between nearest-neighbor sites. A 1D continuum model reveals that the condition for nontrivial winding number coincides with the condition for emergence of edge states in the finite length case.

We have seen that in our setup the edge states of zigzag and armchair classes with the minimal boundary are formed not by time-reversal symmetric partners, but by the (τ, s, r) and $(\tau, s, -r)$ states. Here, τ is the index of the two valleys K and K', s is that of spin direction $\uparrow$ and $\downarrow$, and r is that of left and right branch of the energy bands. In armchair class with the orthogonal boundary it was impossible to construct an edge mode, because that required combining (τ, s, r) and $(-\tau, s, -r)$ states, which always decay in the opposite directions.

The zero energy edge states studied in this paper appear in pairs because of the unbroken time-reversal symmetry as well as the decoupling of two valleys. As seen in Fig. 4.6, mixings of subspaces such as spin mixing induced, e.g., by an external magnetic field or valley mixing induced, e.g., by broken rotational symmetry would couple the two pair members and they would deviate from the zero energy. These properties would be in contrast to those of the Majorana bound states, which emerge under breaking of the time-reversal symmetry and might further necessitate valley mixing, as shown, e.g., in the previous study [167]. Therefore, the control of the magnetic field as well as the rotational symmetry provides us with a tool for discriminating between the zero energy edge states discussed in this paper and the Majorana bound states.

Finally, it is interesting to comment on the possibility of Majorana bound states in the CNTs. If the parameters of the system can be tuned in such a way that the bound states combine two time-reversal partners (τ, s, r) and $(-\tau, -s, -r)$, the requirement of the same decay direction $\kappa_r^{(\tau,s)}\kappa_{-r}^{(-\tau,-s)} > 0$ follows automatically from Eq. (4.28). This can be achieved in the presence of the spin mixing and the valley mixing induced by, e.g., an external magnetic field and a potential scattering. This we will discuss in the next chapter.

5. Topological superconductivity in superconducting carbon nanotubes without time-reversal symmetry

In this chapter we demonstrate that semiconducting carbon nanotubes in proximity with ultrathin s-wave superconductors, e.g. exfoliated $NbSe_2$, can host Majorana states. By precise numerical tight-binding calculations in the real space we show the emergence of localized zero-energy states at the CNT ends above a critical value of the applied magnetic field. Knowing the microscopic wave functions, we unequivocally demonstrate the Majorana nature of the localized states. An effective four-band model in the k-space, with parameters determined from the numerical spectrum is used to calculate the topological phase diagram and its phase boundaries in analytic form. Finally, the impact of symmetry breaking contributions, like disorder and an axial component of the magnetic field, is investigated. The results of this chapter have been published in Phys. Rev. B **97**, 075141 (2018).

5.1. Microscopic model

The setup which we describe here is, similar to [167], based solely on the intrinsic curvature-induced spin-orbit coupling of CNTs. The physical setup is shown in Fig. 5.1(a) and consists of a CNT placed on an ultrathin superconducting film, with a gating layer beneath and the magnetic field applied parallel to the film and perpendicular to the nanotube. The subband degeneracies at $k = 0$ are broken by the valley mixing, caused by the interaction with the substrate, and a magnetic field applied perpendicular to the CNT axis, see Fig. 3.8. In contrast to [167], we consider semiconducting rather than metallic CNTs, since the Fermi velocity in the former is lower by a factor of $\sim 10^{-3}$ than in the latter. Because the Fermi velocity controls the localization properties of Majorana bound states, semiconducting CNTs can host Majorana end states at a thousand times smaller length than metallic ones. The presence of a superconducting substrate plays here a double role. On the one hand it serves as a source of superconducting correlations in the nanotube, acquired by the proximity effect. On the other hand it breaks the rotational symmetry of the nanotube and is the cause of valley mixing $\Delta_{KK'}$. In combination with the perpendicular magnetic field $B_\perp$, this allows the bands at the Γ point to hybridize. The increased electrostatic potential in the vicinity of the substrate atoms is shown as a darker stripe across the inset in Fig. 5.1(a).

We propose to use the two-dimensional (2D) gate-tunable superconductor $NbSe_2$, where superconductivity can survive up to 30 T in magnetic fields applied in-plane [168]. Hence in our set-up the magnetic field is applied in the direction perpendicular to the nanotube axis but, crucially, parallel to the substrate. Contrary to the previous chapter, here the Δ_1 contribution is not necessary for the MBSs to arise and we shall discuss its effects further only in the chapter 5.5, here assuming $\Delta_0 \in \mathbb{R}$ and $\Delta_1 = 0$. In our calculation $\Delta_0 = 0.4$ meV, consistent with the value of the gap reported in proximitized CNT quantum dots [169]. In order to find the spectrum of a superconducting CNT, we express the Hamiltonian

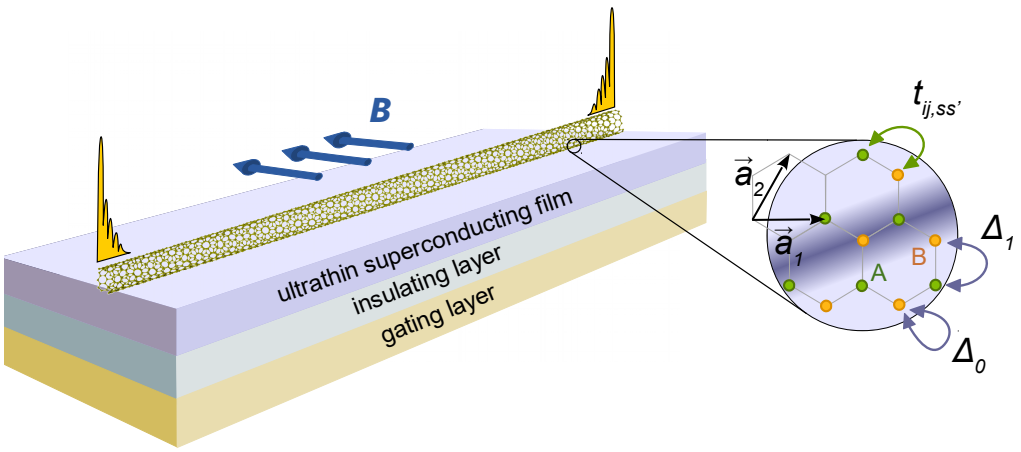

Figure 5.1: Schematic of the system, the CNT with its proximal superconductor and a gating layer. A magnetic field is applied in parallel to the substrate and perpendicular to the nanotube. We find Majorana quasiparticles at the ends of the CNT/superconductor hybrid. The ingredients of our model are shown in the inset. The nearest neighbor hopping $t_{ij,ss'}$ is spin-dependent because of spin-orbit coupling. The superconducting substrate (i) breaks the rotational symmetry of the nanotube, as shown by the darker strip with finite electrostatic on-site potential, and (ii) induces superconducting pairing in the nanotube, with on-site (Δ_0) and nearest-neighbor (Δ_1) pairing correlations.

$$H = \sum_{\langle i,j\rangle,ss'} t_{i,j,ss'} c_{is}^\dagger c_{js'} + \sum_{i,s} V(\varphi_i)\, c_{is}^\dagger c_{is} + \mu_B B_\perp \sum_{i,s} c_{is}^\dagger c_{i-s} + \sum_i \Delta_0 \left(a_{i\uparrow}^\dagger a_{i\downarrow}^\dagger + b_{i\uparrow}^\dagger b_{i\downarrow}^\dagger \right) + \text{h.c.}$$

in a particle-hole symmetric form by introducing a Nambu spinor, $\Psi = \oplus_{i=1}^N \Psi_i$ with $\Psi_i^\dagger = (c_{i\uparrow}^\dagger, c_{i\downarrow}^\dagger, c_{i\uparrow}, c_{i\downarrow})$, where $\oplus$ is the direct sum over the N atomic positions[8]. This procedure effectively doubles the number of degrees of freedom of the system. The full Hamiltonian becomes $H = \frac{1}{2}\Psi^\dagger H_{\text{BdG}} \Psi$, where the field operators are contained in $\Psi, \Psi^\dagger$ and H_{BdG} is an ordinary matrix, the Bogoliubov-de Gennes Hamiltonian of our system. Its eigenvectors, defining the quasiparticle eigenstates with a set of quantum numbers n, have the structure

$$\boldsymbol{\chi}^n = \oplus_{i=1}^N \boldsymbol{\chi}_i^n, \quad (\boldsymbol{\chi}_i^n)^T = (u_{i\uparrow}^n, u_{i\downarrow}^n, v_{i\uparrow}^n, v_{i\downarrow}^n), \tag{5.1}$$

where n is a generic collective index which may contain e.g. the valley and, in a system with translational invariance, k quantum numbers. The particle components with spin s on atom i are denoted by u_{is}^n and the corresponding hole components by v_{is}^n. The quantum eigenstates of the system have the form $|\psi^n\rangle = \oplus_{i=1}^N \Psi_i^\dagger \cdot \chi_i^n \; |0\rangle_{\text{BCS}}$, where $|0\rangle_{\text{BCS}}$ is the BCS ground state in the CNT. The low energy bands obtained for our proximitized infinite (12,4) nanotube

[8] A direct sum $\mathbf{A} \oplus \mathbf{B}$ of a p-component vector $\mathbf{A}$ and an q-component vector $\mathbf{B}$ is a $p+q$-dimensional vector whose first p components are those of $\mathbf{A}$ and the last q are those of $\mathbf{B}$. Our Ψ and $\boldsymbol{\chi}^n$ are both $4N$-dimensional vectors. The components of Ψ are operators, while those of $\boldsymbol{\chi}^n$ are complex numbers.

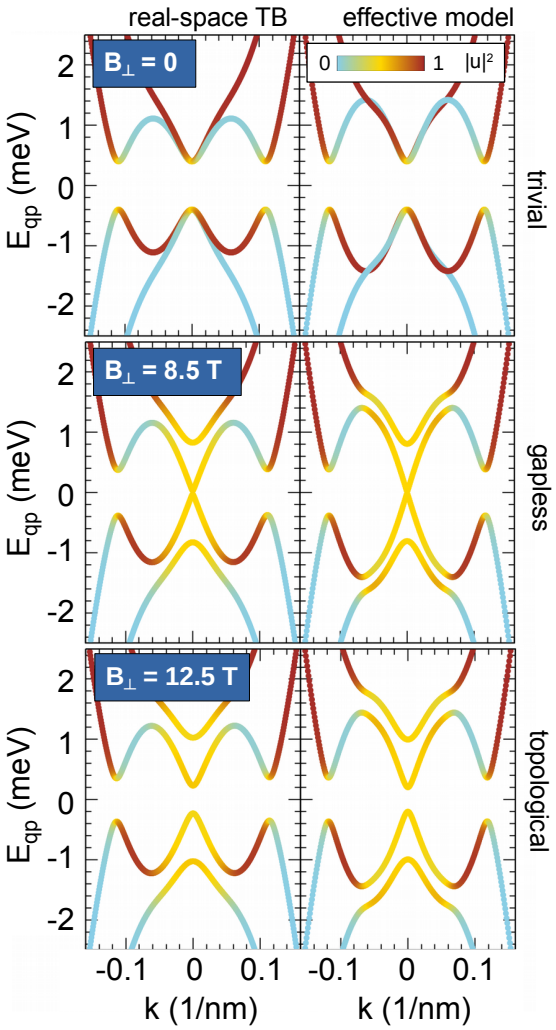

Figure 5.2: The Bogoliubov-de Gennes spectra of the superconducting nanotube in three different topological phases which can be accessed by tuning $B_\perp$ for the chemical potential $\mu = 334.6$ meV. The color scale shows the weight of the particle part of the corresponding CNT's eigenstate; gold color indicates equal particle and hole contributions. The superconducting pairing is $\Delta_0 = 0.4$ meV, $\Delta_1 = 0$.

are shown in Fig. 5.2, for the three topologically distinct phases encountered by increasing the magnetic field. The color scale shows the overall weight of particle component in the given energy eigenstate, $|u|^2 = \sum_{is} |u_{is}|^2$. The solutions which have a predominantly particle character trace the original single-particle bands, while the predominantly hole-type solutions are mirror-reflected around the chemical potential.

5.2. Bulk properties

5.2.1. Superconducting pairing in four-band model

The superconducting correlations induced by proximity are treated in a mean-field approximation according to Eq. (3.40). We only consider the case of an on-site pairing potential

which is described by the superconducting gap Δ_0. Since Δ_0 is isotropic in momentum space, our mean-field pairing Hamiltonian has an s-wave gap symmetry. The mean-field Hamiltonian reads

$$H_{\mathrm{SC}} = \sum_k \Delta_0 \left(c^\dagger_{kK\uparrow} c^\dagger_{-kK'\downarrow} + c^\dagger_{kK'\uparrow} c^\dagger_{-kK\downarrow} + \mathrm{h.c.} \right), \tag{5.2}$$

where we are coupling the corresponding Kramers partners. Introducing the Nambu spinor defined as

$$\Psi^\dagger = (c^\dagger_{kK\uparrow}, c^\dagger_{kK\downarrow}, c^\dagger_{kK'\uparrow}, c^\dagger_{kK'\downarrow}, c_{-kK'\downarrow}, c_{-kK'\uparrow}, c_{-kK\downarrow}, c_{-kK\uparrow}),$$

we obtain the Bogoliubov-de Gennes (BdG) Hamiltonian

$$\mathcal{H}_{\mathrm{BdG}}(k) = \begin{pmatrix} H(k) & \Delta \\ \Delta & -H(k) \end{pmatrix}, \tag{5.3}$$

with

$$H(k) = \begin{pmatrix} \xi_{K\uparrow}(k) & \mu_B B_\perp & \Delta_{KK'} & 0 \\ \mu_B B_\perp & \xi_{K\downarrow}(k) & 0 & \Delta_{KK'} \\ \Delta_{KK'} & 0 & \xi_{K'\uparrow}(k) & \mu_B B_\perp \\ 0 & \Delta_{KK'} & \mu_B B & \xi_{K'\downarrow}(k) \end{pmatrix}, \tag{5.4}$$

and

$$\Delta = \begin{pmatrix} \Delta_0 & & & \\ & -\Delta_0 & & \\ & & \Delta_0 & \\ & & & -\Delta_0 \end{pmatrix}.$$

The single particle energies are defined with respect to the chemical potential μ, as in (3.26). When expressed in the eigenbasis of the single particle Hamiltonian (3.25), the superconducting pairing couples all four bands, though not with equal strength. The most important are the intraband pairing and interband pairing within the same pair. Reflecting the same spin direction s_x between k and $-k$ states in the same band, the intraband pairing is odd in k, thus we call it Δ_p. The interband pairing is even in k and we call it Δ_s. Analytical expressions for Δ_s and Δ_p, derived with the assumption that the two band pairs are decoupled (valid in low fields), are given in section 5.2.2. The pairings with the members of the other band pair are

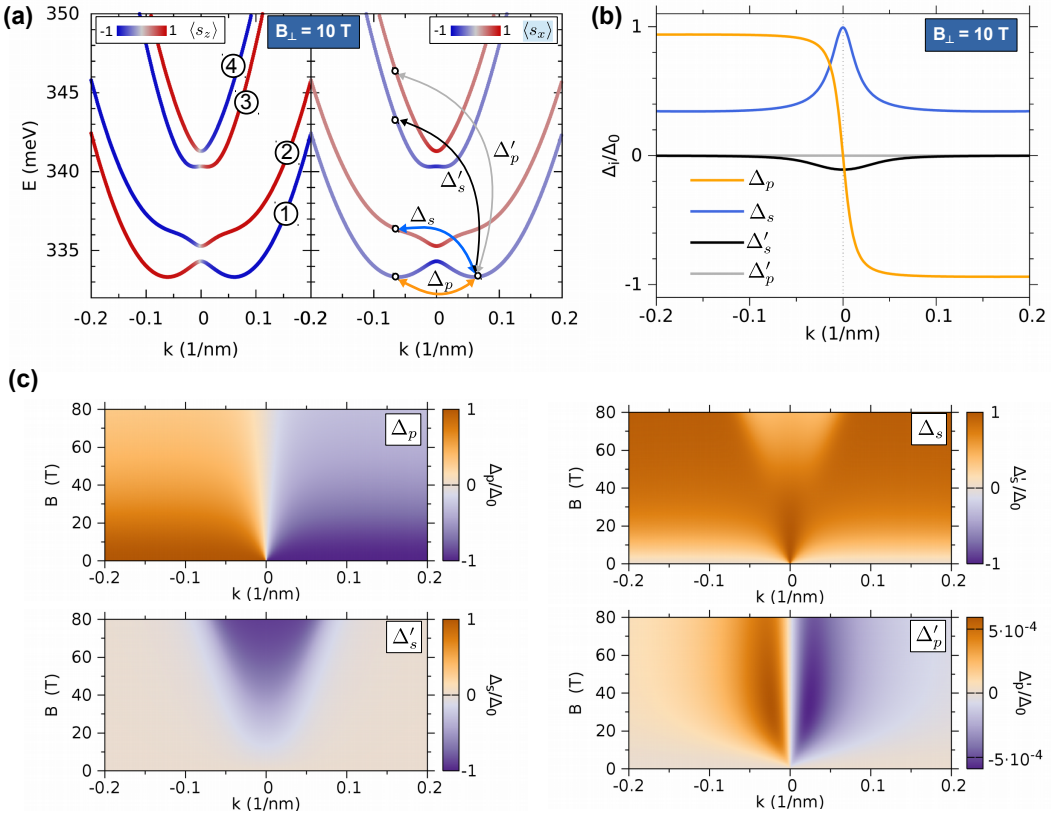

Figure 5.3: (a) The lowest four bands of a (12,4) semiconducting CNT with valley mixing and in $B_\perp = 10$ T, obtained with the effective four-band model. The color scale shows the expectation value of the s_z (left panel) or s_x (right panel) component of an eigenstate's spin. The pairings between a positive k state in band ① and the four states with opposite k are indicated in the right panel. (b) Pairing strength as a function of k for $B_\perp$, in Δ_0 units. (c) The four pairing terms as functions of k and $B_\perp$, in Δ_0 units. Note the increase in Δ'_s, which couples the upper and lower band pairs, beyond ∼20 T.

weaker, and we call them Δ'_p and Δ'_s. The different pairings coupling a band ① state with positive k to the states with negative k are illustrated in Fig. 5.3(a), and their k dependence at $B_\perp = 10$ T is plotted in Fig. 5.3(b). The dependence of those different pairings on k and $B_\perp$ is plotted in Fig. 5.3(c). Initially with increasing field strength the spins become polarized in the x direction, thus the terms Δ_p, Δ'_s pairing the same s_x spin states become on average weaker, while Δ_s pairing opposite s_x states gain in strength. Beyond the field strength of ∼20 T the amplitude of the Zeeman term $\mu_B B_\perp$ becomes comparable to that of the spin-orbit splitting and the pairing Δ'_s mixes the two band pairs. This effect will be visible in the topological phase diagram discussed later. The region which holds greatest interest for the experimental realizations is that of lower magnetic fields, in the neighborhood of B_c, i.e. the lowest field for which the energy gap closes at the Γ point. In this regime the two band pairs can be considered independent, and we show that near the critical field they give the largest contribution to the topological phase. The construction of this further simplified model is described in the next section, allowing us to find the energy spectrum analytically.

5.2.2. Superconducting pairings in two-band model

The pairing Hamiltonian (5.2) with the two-band approximation, which is described in section 3.6, by using the transformation (3.30) becomes

$$H_{\mathrm{SC}} = \sum_k \Delta_+(k)\left(\beta^\dagger_{k\uparrow}\beta^\dagger_{-k\downarrow} - \alpha^\dagger_{k\uparrow}\alpha^\dagger_{-k\downarrow} + \mathrm{h.c.}\right) + \Delta_-(k)\left(\beta^\dagger_{k\uparrow}\alpha^\dagger_{-k\downarrow} + \alpha^\dagger_{k\uparrow}\beta^\dagger_{-k\downarrow} + \mathrm{h.c.}\right),$$

where we introduce the following definition

$$\Delta_+(k) = \Delta_0\left(|a_\uparrow(k)|\,|b_\downarrow(-k)| + |b_\uparrow(k)|\,|a_\downarrow(-k)|\right), \tag{5.5}$$

$$\Delta_-(k) = \Delta_0\left(|a_\uparrow(k)|\,|a_\downarrow(-k)| - |b_\uparrow(k)|\,|b_\downarrow(-k)|\right). \tag{5.6}$$

For simplifications we can use the time-reversal conjugation $|a_s(k)| = |b_{-s}(-k)|$ and by using the condition $|a_s(k)|^2 + |b_s(k)|^2 = 1$ we obtain that $\Delta_+(k) = \Delta_0$ and $\Delta_-(k) = 0$, also if $\tilde{B}_\perp \neq 0$. Only $B^\star_\perp \neq 0$ would induce a finite $\Delta_-(k)$. Since we omit $B^\star_\perp$, $\Delta_-(k)$ is vanishing and we have again two separate pairings in the Hamiltonian. We can express the pairing Hamiltonian in the eigenbasis of the carbon nanotube (5.4) with the transformation (3.34) and omitting the pairing with the upper bands we obtain

$$\tilde{H}_{\mathrm{SC}} = \sum_k \Delta_0 \left(g^2(k) f^\dagger_{k1} f^\dagger_{-k1} - h^2(k) f^\dagger_{k2} f^\dagger_{-k2} \right) + \Delta_0 g(k) h(k) \left(f^\dagger_{k2} f^\dagger_{-k1} - f^\dagger_{k1} f^\dagger_{-k2} \right) + \mathrm{h.c.}$$

The BdG Hamiltonian can be defined by $\tilde{H}_{12} = \frac{1}{2} \sum_k \Psi^\dagger \tilde{\mathcal{H}}_{\mathrm{BdG}} \Psi$ with the Nambu spinor $\Psi^\dagger = \left(f^\dagger_{k1}, f^\dagger_{k2}, f_{-k1}, f_{-k2} \right)$. The corresponding BdG Hamiltonian for our system is given by

$$\tilde{\mathcal{H}}_{\mathrm{BdG}} = \begin{pmatrix} \tilde{E}_1(k) & 0 & \tilde{\Delta}_p(k) & -\tilde{\Delta}_s(k) \\ 0 & \tilde{E}_2(k) & \tilde{\Delta}_s(k) & \tilde{\Delta}_p(k) \\ \tilde{\Delta}_p(k) & \tilde{\Delta}_s(k) & -\tilde{E}_1(k) & 0 \\ -\tilde{\Delta}_s(k) & \tilde{\Delta}_p(k) & 0 & -\tilde{E}_2(k) \end{pmatrix}, \tag{5.7}$$

with the pairing terms

$$\tilde{\Delta}_p(k) = \Delta_0 \left(g^2(k) - h^2(k) \right) = -\tilde{\Delta}_p(-k), \tag{5.8}$$

$$\tilde{\Delta}_s(k) = 2\Delta_0 g(k) h(k) = \tilde{\Delta}_s(-k). \tag{5.9}$$

The eigenvalues are shown in Fig. 5.4(a), including the spin density $\langle s_z \rangle$ which shows the spin-momentum locking due to interplay of spin-orbit coupling, valley mixing and perpendicular magnetic field. Further, the allowed pairing of the energy bands is shown. We see that the pairing term $\tilde{\Delta}_s(k)$ has an even and $\tilde{\Delta}_p(k)$ an odd parity, as shown in Fig. 5.4(b). From the conservation of energy it follows that $\tilde{\Delta}^2_p(k) + \tilde{\Delta}^2_s(k) = \Delta^2_0$.

The BdG Hamiltonian (5.7) can be partly diagonalized, taking into account the blocks with the single particle energies $\tilde{E}_1(k)$, $\tilde{E}_2(k)$ and the superconducting gap $\tilde{\Delta}_s(k)$. The transformation is given by

$$\begin{pmatrix} f_{k1} \\ f^\dagger_{-k2} \end{pmatrix} = \begin{pmatrix} m(k) & n(k) \\ -n(k) & m(k) \end{pmatrix} \begin{pmatrix} d_{k+} \\ d^\dagger_{-k-} \end{pmatrix}, \tag{5.10}$$

with the normalization condition $m^2(k) + n^2(k) = 1$ and the coefficients defined in the following way:

$$m^2(k) = \frac{1}{2} \left(1 + \frac{E_1(k) + E_2(k)}{\sqrt{\left(E_1(k) + E_2(k) \right)^2 + \left(2\tilde{\Delta}_s(k) \right)^2}} \right),$$

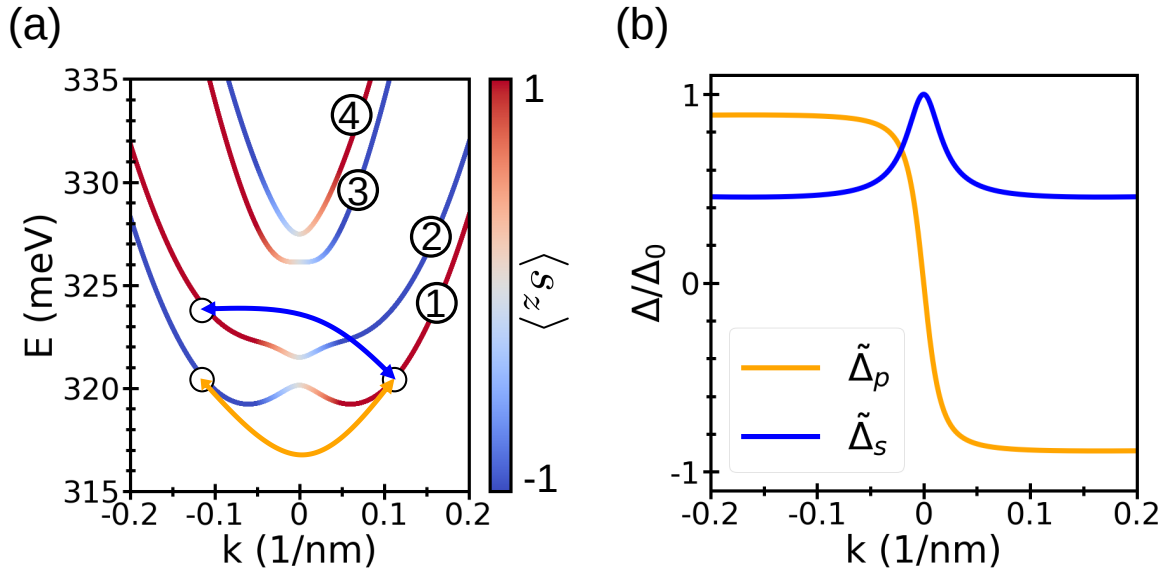

Figure 5.4: (a) The single particle energy spectrum of a (12,4) nanotube in the vicinity of the Γ-point for a magnetic field of $B_\perp = 14$T. Only the superconducting pairings in the same band pair are retained, with $\tilde{\Delta}_p(k)$ acting within band and $\tilde{\Delta}_s(k)$ pairing each member of the pair with its partner. Color scale shows the expectation value of $\langle s_z \rangle$ for the corresponding energy state. (b) The two superconducting pairing terms $\tilde{\Delta}_s(k)$ (interband), and $\tilde{\Delta}_p(k)$ (intraband), as functions of k.

$$n^2(k) = \frac{1}{2}\left(1 - \frac{E_1(k) + E_2(k)}{\sqrt{(E_1(k) + E_2(k))^2 + \left(2\tilde{\Delta}_s(k)\right)^2}}\right).$$

Then, the rotated BdG Hamiltonian is block-diagonal and the blocks are given by

$$\hat{\mathcal{H}}^{\pm}_{\mathrm{BdG}} = \begin{pmatrix} \tilde{\xi}_{\pm}(k) & \tilde{\Delta}_p(k) \\ \tilde{\Delta}_p(k) & -\tilde{\xi}_{\pm}(k) \end{pmatrix}. \tag{5.11}$$

The quasiparticle energy $\tilde{\xi}_{\pm}(k)$ is given by

$$\tilde{\xi}_{\pm}(k) = \frac{1}{2}\left(\tilde{E}_1(k) - \tilde{E}_2(k)\right) \pm \frac{1}{2}\sqrt{\left(\tilde{E}_1(k) + \tilde{E}_2(k)\right)^2 + 4\tilde{\Delta}_s^2(k)}.$$

The Hamiltonian (5.11) is an usual BCS BdG Hamiltonian with the the quasiparticle energy $E_{\pm} = \sqrt{\tilde{\xi}_{\pm}^2(k) + \tilde{\Delta}_p^2(k)}$ [86]. Since $\tilde{\Delta}_p(k=0) = 0$, the gap closing condition can be expressed directly as

$$\tilde{\xi}_{\pm}(k=0) = 0, \tag{5.12}$$

This condition, neglecting the mixing between the band pairs, is shown with dashed lines in Fig. 5.5(b),(d).

5.2.3. Symmetries and topological invariants

The Hamiltonian H_{BdG}, like all Bogoliubov-de Gennes Hamiltonians, is by construction invariant under a particle-hole operation. That is, we can define an antiunitary operator $\mathcal{P}$, such that $\mathcal{P}H_{\mathrm{BdG}}\mathcal{P}^{-1} = -H_{\mathrm{BdG}}$. The action of $\mathcal{P}$ on the original electron operators and on doubled Hilbert space states is

$$\mathcal{P}c_{is} = c_{is}^{\dagger}, \quad \mathcal{P}\boldsymbol{\chi}_i = (v_{i\uparrow}^*, v_{i\downarrow}^*, u_{i\uparrow}^*, u_{i\downarrow}^*)^T. \tag{5.13}$$

The particle-hole operation maps the positive energy solutions onto their Nambu partners with negative energy. If the particle-hole symmetric Hamiltonian of a finite system has zero energy modes, they can be cast in the form of eigenstates of $\mathcal{P}$,

$$\mathcal{P}\psi = \psi. \tag{5.14}$$

Inspecting the first relation of (5.13) shows that (5.14) is only an equivalent definition of the Majorana property, usually stated as $\gamma_\sigma(\mathbf{r}) = \gamma_\sigma^\dagger(\mathbf{r})$, where $\gamma^\dagger$ is the operator creating a particle with spin σ at position $\mathbf{r}$.

The presence or absence of Majorana solutions can be predicted from a topological phase diagram, where different phases correspond to different values of a topological invariant. In a system with translational symmetry, such as the bulk of the CNT, the basic quantity determining the topological invariant in 1D is γ^-, the sum of the Berry phases carried by all occupied (negative energy) bands, integrated over the Brillouin zone. Since γ^- is gauge-dependent and defined only up to an integer, another invariant is commonly used, $W = \exp(i2\pi\gamma^-)$, which is gauge-independent. The particle-hole symmetry in a system with translational invariance is expressed as $\mathcal{P}H_{\mathrm{BdG}}(k)\mathcal{P}^{-1} = -H_{\mathrm{BdG}}(-k)$, i.e. the positive energy solutions at momentum k are related to negative energy solutions at momentum $-k$, as sketched in Fig. 5.5(a). This constrains the values which W can take to ± 1, i.e. W is of a $\mathbb{Z}_2$ type, associated with the class D systems. $W = +1$ corresponds to the trivial topological phase, while $W = -1$ implies the presence of MBSs at the system boundaries. The phase diagram calculated for our model nanotube, using the standard Pfaffian technique and the effective model for the bulk bands, is shown in Fig. 5.5(b). The borders between different phases in the diagram correspond to $(B_\perp, \mu)$ such that the gap is closed at $k = 0$. From our effective four-band model we find that this occurs at

$$\tilde{\mu}^2 = \frac{\Delta_{\mathrm{SO}}^2}{4} + (\Delta_{KK'}^2 + (\mu_B B_\perp)^2 - \Delta_0^2) \pm \sqrt{4\Delta_{KK'}^2((\mu_B B_\perp)^2 - \Delta_0^2) - \Delta_0^2\Delta_{\mathrm{SO}}^2}, \qquad (5.15)$$

where $\tilde{\mu}$ is the chemical potential measured from the center of either the ①,② or ③,④ pair in Fig. 5.1(b). The critical magnetic field is given by $\mu_B B_c = \Delta_0\sqrt{\Delta_{SO}^2 + 4\Delta_{KK'}^2}/(2\Delta_{KK'})$. If we assume that the band pair ①,② is independent of ③,④ (i.e. Δ_s' can be neglected), we can expand (5.15) around B_c, obtaining a simpler formula $\tilde{\mu}^2 = \Delta_0^2((B_\perp/B_c)^2 - 1)$. The red lines in Fig. 5.5(b) follow (5.15), the dashed lines mark the borders of the non-trivial phase obtained with the simpler approximated formula. The coupling between the band pairs changes visibly the phase diagram – when the Zeeman energy reaches the magnitude of the original spin-orbit splitting, it destroys the topological phase. The same phenomenon occurs in multiband semiconducting nanowires, where the mixing between various transverse modes caused by the Rashba spin-orbit coupling strongly reduces the non-trivial topological regions in the phase diagram, as demostrated in Ref [107].

As can be seen in Fig. 5.2, the Hamiltonian H_{BdG} is highly symmetric. In particular, a unitary operation C can be defined, such that $CH_{\mathrm{BdG}}(k)C^{-1} = -H_{\mathrm{BdG}}(k)$. The operation C is the chiral symmetry, connecting positive and negative energy solutions at the same momentum k, as sketched in Fig. 5.5(c). The MBSs in our system are also eigenstates of C. In systems with this symmetry, the topological invariant γ^- has a clear interpretation as a winding number, $\gamma^- = \nu/2$, see the previous chapter 1.3. The winding number is an integer, i.e. it belongs to $\mathbb{Z}$. That apparent contradiction with $W \in \mathbb{Z}_2$ is solved when we recall that W was constructed with an extra exponentiation step, which obliterates the difference between the phases with $\nu = \pm 1$. The phase diagram calculated using the winding number is shown in Fig. 5.5(d), with exactly the same phase boundaries, but showing clearly that the lower non-trivial region and the upper non-trivial region in fact correspond to different non-trivial phases.

The symmetries of the BdG Hamiltonian (5.3) can be expressed in terms of Pauli matrices, denoted by π in the particle-hole (Nambu) subspace, by τ in the valley subspace and by s in the spin subspace. The particle-hole symmetry operator $\mathcal{P}$, such that $\mathcal{P}\mathcal{H}_{\mathrm{BdG}}(k)\mathcal{P}^{-1} = -\mathcal{H}_{\mathrm{BdG}}(-k)$, is given by $\mathcal{P} = \pi_x \otimes \tau_x \otimes s_x \mathcal{K}$, where τ_0 and s_0 are the identities in their respective subspaces and $\mathcal{K}$ denotes the operator of the complex conjugation. The Hamiltonian H_{BdG} has also a chiral symmetry, i.e. it fulfills $C\mathcal{H}_{\mathrm{BdG}}(k)C^{-1} = -\mathcal{H}_{\mathrm{BdG}}(k)$ with a unitary operator C. The operator is given by $C = \pi_y \otimes \tau_0 \otimes s_0$. The presence of those two symmetries implies that there exists a third one, which we call $\tilde{\mathcal{T}} = C\mathcal{P}^{-1}$ and which fulfills $\tilde{\mathcal{T}}\mathcal{H}_{\mathrm{BdG}}(k)\tilde{\mathcal{T}}^{-1} = \mathcal{H}_{\mathrm{BdG}}(-k)$. Its expression in this basis is $\tilde{\mathcal{T}} = -i\pi_z \otimes \tau_x \otimes s_x \mathcal{K}$. The operation $\tilde{\mathcal{T}}$ squares to $+1$, hence it is clear that it is not the time reversal symmetry of a spin-1/2 system. The fact that it is diagonal in the Nambu space implies that already the non-superconducting Hamiltonian $H(k)$ (5.4) is invariant under a restricted $\tilde{\mathcal{T}}_{\mathrm{red}} = \tau_x \otimes s_x \mathcal{K}$, which is indeed the case and reflects a physical symmetry of the system. It is the symmetry of rotation with respect to an axis *perpendicular* to the CNT, which exchanges both the valley, longitudinal momentum and spin. It also exchanges the sublattices, which accounts for its $\mathcal{K}$

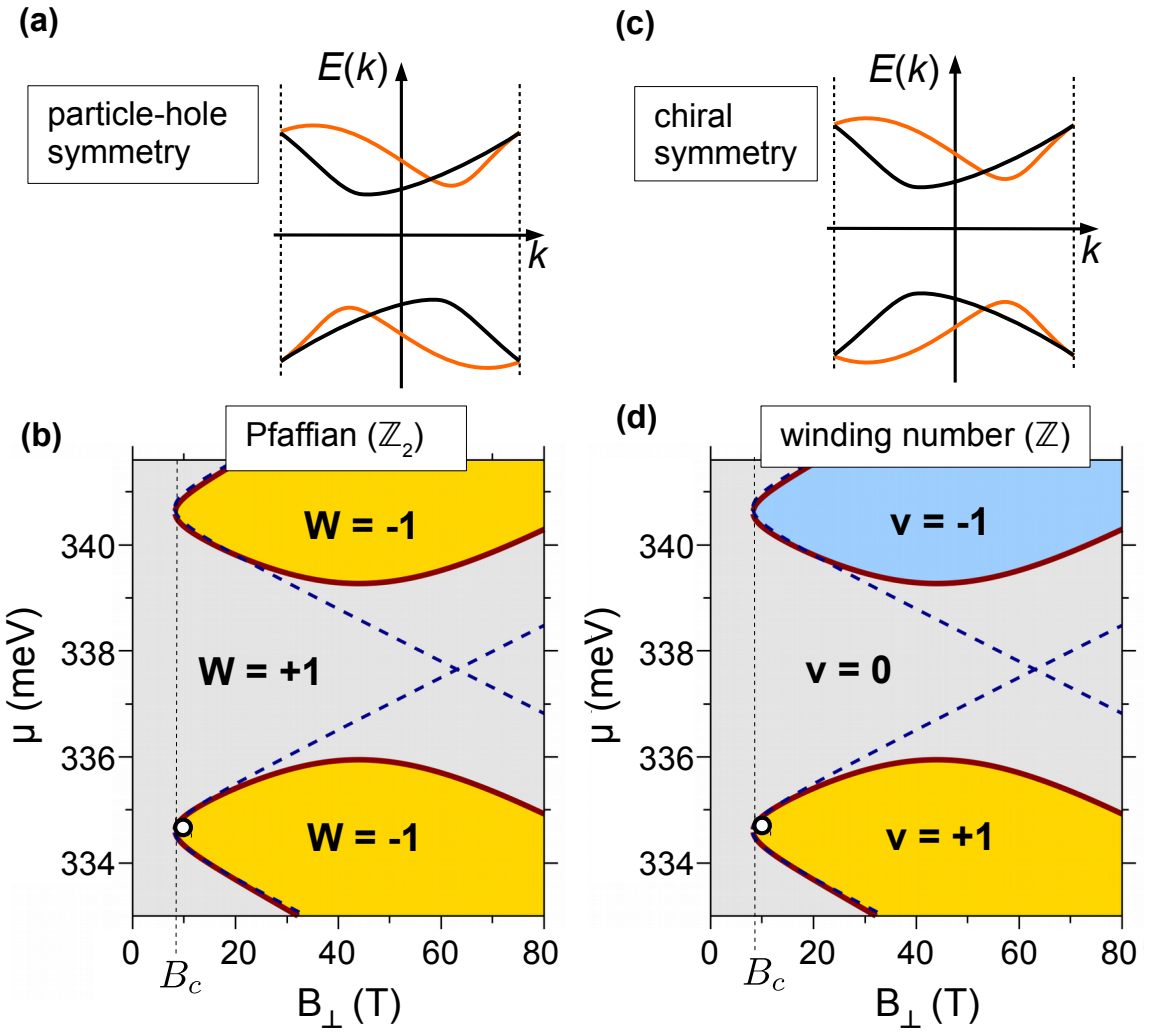

Figure 5.5: Symmetries and topological invariants. (a) Sketch of a spectrum with particle-hole symmetry. Bands of the same color are related by the symmetry. (b) The phase diagram calculated using the effective model and the Pfaffian formulation of the topological invariant, typical for particle-hole symmetric systems. The topologically non-trivial regions are shown in yellow, the red line at the border between the phases is the contour of $E = 0$ at the Γ point. The dot in the lower $W = -1$ area marks the μ and $B_\perp$ used in Fig. 5.7. The dashed lines trace the borders of non-trivial phase calculated from a model which contains only one single-particle band pair, either ① and ② (lower region) or ③ and ④ (higher region) from Fig. 5.1(b). (c) Sketch of a spectrum with chiral symmetry. The Bogoliubov-de Gennes spectrum in Fig. 5.2 has both particle-hole and chiral symmetry. (d) The phase diagram calculated using the winding number invariant, defined for chiral-symmetric systems. The values $\nu = \pm 1$ in the lower and upper non-trivial area indicate that these regions correspond to different topological phases, with one zero energy mode in each.

component. If, and only if, the magnetic field is also applied perpendicular to the CNT axis, the non-superconducting Hamiltonian is invariant under $\tilde{\mathcal{T}}_{\text{red}}$.

5.3. Emergence of MBSs in finite nanotubes

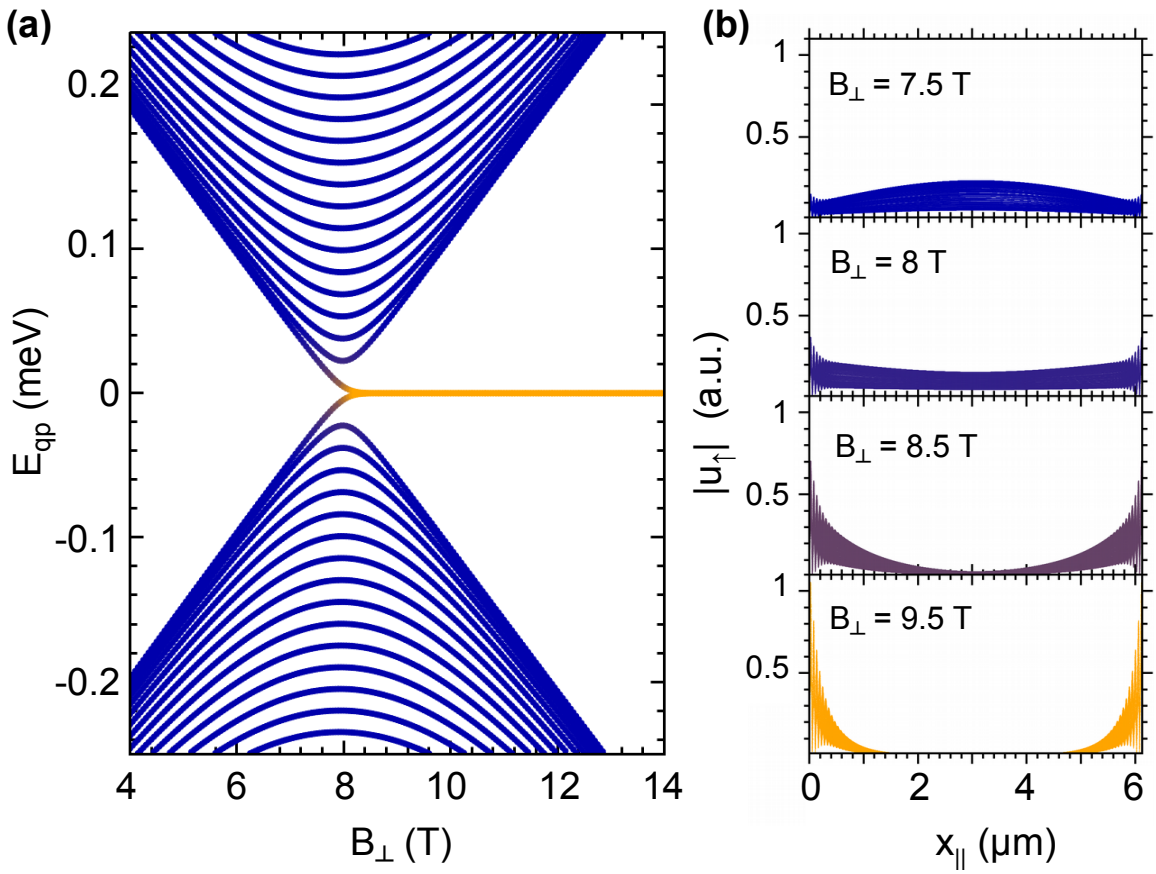

Figure 5.6: Topological phase transition. (a) The quasiparticle spectrum of a finite (12,4) nanotube with 4000 unit cells ($L = 6.03\,\mu$m), at the chemical potential $\mu = 334.6$ meV for varying magnetic field. The topological phase transition occurs at $B_c = 8.5$ T, beyond which the lowest energy eigenstate becomes a zero energy mode. (b) The wave function of the lowest energy mode undergoes a gradual localization with increasing magnetic field. Here only the amplitude $|u_\uparrow(x_\parallel)|$ of the spin up particle component, projected onto the direction along the CNT's axis, is shown. The shape of the remaining components is indistinguishable from that of $|u_\uparrow(x_\parallel)|$ at this scale, which comprises the data points from $N = 8.32 \cdot 10^5$ atoms. The units are arbitrary and the same for all wave function plots in this figure.

Changing the chemical potential or the strength of the magnetic field can drive the proximitized nanotube across a topological phase transition, into a regime in which it becomes a topological superconductor. An example of the changes in the Bogoliubov-de Gennes spectrum during such a transition is shown in Fig. 5.6(a), for a 6 μm long (12,4) CNT at a fixed chemical potential $\mu = 334.6$ meV and varying magnetic field $B_\perp$. The energy of the lowest quasiparticle states is further lowered with increasing $B_\perp$, until they become a doubly degenerate zero energy mode. The degeneracy is artificial, caused by the doubling of degrees of freedom introduced with the Nambu spinor, and the nanotube de facto hosts only one eigen-

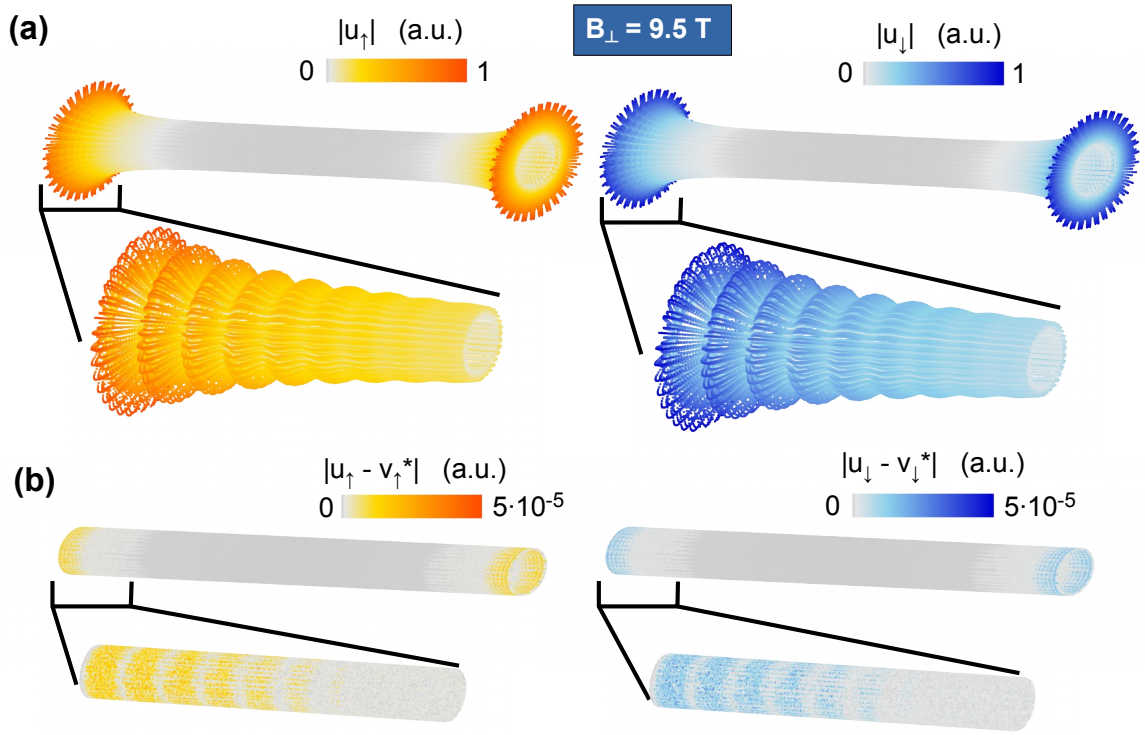

Figure 5.7: Majorana bound states. (a), The full spatial profile of the the spin up and spin down particle components, $|u_\uparrow(\mathbf{r})|$ and $|u_\downarrow(\mathbf{r})|$. The amplitude of the electronic wave function is shown through both the distance from the nanotube's surface (light grey) and through the color scale. The wavelength of the oscillations is given by the value of k_F at the chosen chemical potential. (b), Spatially resolved amplitude of the *difference* between the particle and conjugated hole components for the same spin, $|u_\uparrow(\mathbf{r}) - v_\uparrow^*(\mathbf{r})|$ and $|u_\downarrow(\mathbf{r}) - v_\downarrow^*(\mathbf{r})|$. The distance from the CNT's surface is scaled in the same way as in **c**, and the color scale is greatly enhanced. Only faint differences are visible, of the order of 10^{-5}, which shows the Majorana nature of the zero energy mode.

state at zero energy. The change in the shape of the quasiparticle wave function associated with the lowest energy eigenstate is illustrated in Fig. 5.6(b), showing clearly its increasing localization at the ends of the proximitized CNT. In the figure only the amplitude $|u_\uparrow(\mathbf{r})|$ of the particle component with spin up is shown, the remaining components $u_\downarrow(\mathbf{r}), v_\uparrow(\mathbf{r}), v_\downarrow(\mathbf{r})$ have profiles which are indistinguishable from $|u_\uparrow(\mathbf{r})|$ at this scale. Having a direct access to the particle and hole components of the zero energy mode, we can prove that it indeed has Majorana nature according to (5.14).

The spatially resolved wave function of the zero energy mode at $B_\perp = 9.5$ T is shown in Fig. 5.7(a). The amplitude of spin up and down particle components, $|u_\uparrow(\mathbf{r})|$ and $|u_\downarrow(\mathbf{r})|$, is shown both as the distance from the CNT's surface (grey) at each atomic position and via the color scale. The wavelength of the oscillations is set by the value of k_F at the chosen chemical potential. The decay length is field-dependent and at $B_\perp = 9.5$ it is $\sim 0.4\,\mu$m. The Majorana nature of the zero energy mode becomes evident in the Fig. 5.7(b), where the differences between particle and (complex conjugated) hole component of the wave function for each spin, $|u_\uparrow(\mathbf{r}) - v_\uparrow^*(\mathbf{r})|$ and $|u_\downarrow(\mathbf{r}) - v_\downarrow^*(\mathbf{r})|$ are shown. They are identical up to the order of 10^{-5} of the maximum amplitude, which constitutes a numerical proof that the zero energy mode fulfills the Majorana condition (5.14).

5.4. MBS stability

5.4.1. Disorder

The stability of the MBSs against perturbations is crucial for their experimental realization. The techniques for growing carbon nanotubes are now so advanced that their atomic lattices are nearly perfect [170, 171]. Nevertheless, some atoms may be adsorbed on the nanotube during the device production. We simulate their effect through a random on-site electrostatic potential, with varying concentration of impurities $n_0 = N_{\text{imp}}/N$, and potential strength chosen randomly from a range $[-W_0, W_0]$. The evolution of the quasiparticle spectra with magnetic field for two impurity concentrations and varying disorder strength is shown in Fig. 5.8. The nanotube and other parameters $(\Delta_0, V(\varphi_i))$ remain unchanged.

At realistically low concentrations increasing W_0 delays the onset of the zero energy mode, as can be seen from Fig. 5.8(a),(c), and perturbs the bulk bands (cf. Fig. 5.8(c) at $W_0 = 0.6, 0.9$ eV). It also decreases the gap between the zero energy mode and the bulk states (cf. Fig 5.8b), but the Majorana mode is clearly present and protected, albeit it forms at higher $B_\perp$ than in the clean system.

Increasing the impurity concentration beyond the realistic values, to $n_0 = 1\%$, as illustrated in Fig. 5.8(d)-(f), is more effective at destroying the non-trivial topological phase than the increase in the disorder strength. For intermediate and large disorder strength $W_0 \geq 0.5$ eV the formation of the zero mode occurs at much higher $B_\perp$, as can be seen from Fig. 5.8(d),(f).

Even when the zero energy mode forms, it is mixed with the bulk bands (cf. Fig. 5.8(e),(f)), resulting in several ordinary localized states.

5.4.2. Magnetic field misalignment

Another factor which has to be taken into account is the precision of alignment of the magnetic field. The presence of a field component parallel to the nanotube axis gives rise to the Aharonov-Bohm effect. In nanotubes this causes a different orbital response in the two valleys, resulting in a removal of the valley degeneracy [172] and breaking of the chiral symmetry. When the parallel component of the magnetic field reaches a threshold value, the electrons on opposite sides of the Γ point no longer have matching momenta and the superconducting correlations become ineffective, yielding a gapless spectrum. The lowest thirty two eigenvalues of the Bogoliubov-de Gennes spectrum in magnetic field of 12 T amplitude and varying angle θ with respect to the nanotube axis are plotted in Fig. 5.9. At this chosen field amplitude the finite system supports a Majorana mode within a range of $\pm 5^\circ$ deviation of the field from the perpendicular. Increasing the field amplitude widens the maximum gap at 90°, but the higher value of the parallel component decreases the θ range in which the spectrum is gapped. Maximizing the stability of the MBS in the experiment will then necessarily involve a trade-off between protection against angle fluctuations and protection against scattering into the bulk.

The two major experimental challenges in achieving the formation of MBSs in this setup are the necessity of controlling the chemical potential of the CNT and of applying a large magnetic field without destroying superconducting correlations. Both may be accomplished with the use of 2D transition metal dichalcogenide (TMDC) superconductors, such as $NbSe_2$, with its larger superconducting gap of 1.26 meV [173]. The superconducting pairing was demonstrated to survive in fields up to 30 T [168], and the thinness of the 2D layer allows the superconductor itself to be gated, together with the CNT in its proximity.

5.5. Influence of the nearest-neighbor pairing Δ_1

The spin-singlet superconducting correlations can act both on-site and between nearest neighbor sites [119]. When the nearest-neighbor pairing is stronger than the on-site pairing, $\Delta_1 > \Delta_0$, a CNT can enter a non-trivial topological phase even in the absence of magnetic field, as discussed in the previous chapter, although the presence of time-reversal symmetry causes the zero energy modes to be Dirac, rather than Majorana fermions [164]. We present here the topological phase diagrams obtained with the Pfaffian technique, for the range of $\Delta_1/\Delta_0 \leq 10$. We keep the overall superconducting gap constant, $\sqrt{\Delta_0^2 + \Delta_1^2} = 0.4$ meV.

In the basis of Bloch states the pairing Δ_1 becomes dependent on k in a way similar to $\Delta_{KK'}$ (cf. Appendix B), i.e. it becomes modulated by $|\sum_{j=1}^{3} \exp(i\mathbf{k}\cdot\Delta\mathbf{R}_j)|$, where $\Delta\mathbf{R}_j$ are lattice vectors between unit cells to which those nearest neighbors belong. That modulation for our

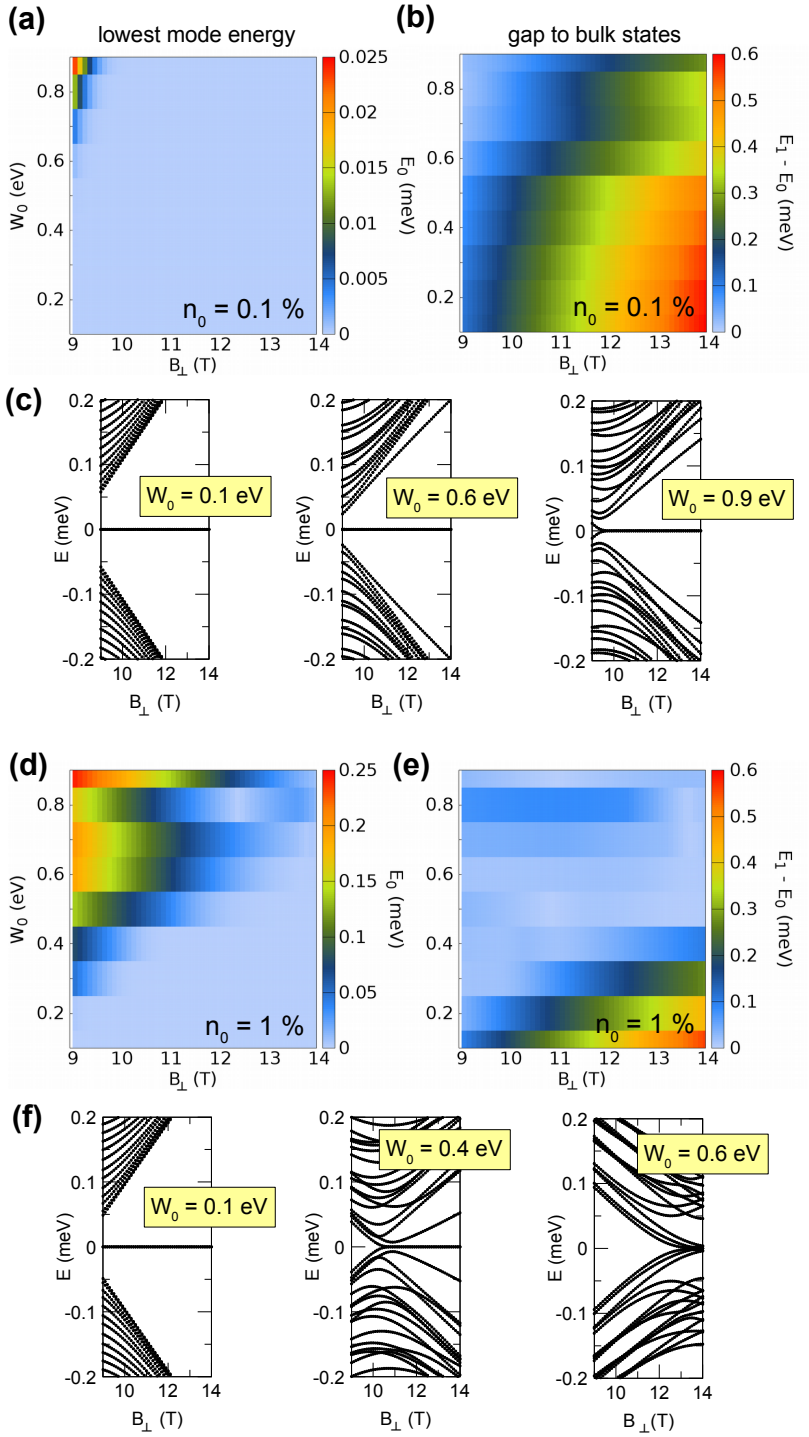

Figure 5.8: (a) The energy of the lowest positive mode E_0 of the (12,4) nanotube with $L \simeq 6\,\mu$m discussed in the main text. The chemical potential is fixed at $\mu = 334.6$ meV, both the magnetic field $B_\perp$ and the maximum disorder strength W_0 vary. The latter increases in steps of 0.1 eV. In this magnetic field range the clean system is in the non-trivial topological phase. The concentration of impurities in (a)-(c) is 0.1%, which corresponds to 832 impurities. In all plots of this figure each value of W_0 corresponds to one realization of disorder. (b) The gap between the lowest energy mode E_0 and the next, E_1. For $E_0 \approx 0$ a large value of $E_1 - E_0$ means wide gap between the MBS and the bulk states, indicating a stable MBS mode. (c) Three examples of the quasiparticle spectra near $E = 0$. (d) Similar to (a), with a tenfold increase in the impurity concentration, i.e. 8320 impurities in the CNT. The concentration is the same in (d)-(f). (e) Similar to (b). (f) Similar to (c).

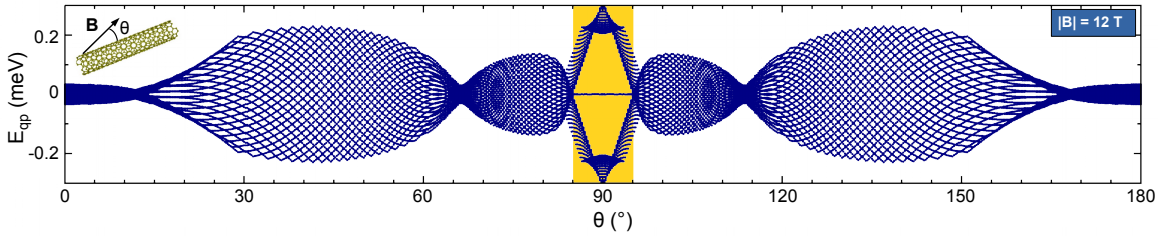

Figure 5.9: Stability of MBSs with respect to magnetic field alignment. The thirty two lowest quasiparticle energies as a function of varying angle of the magnetic field, with its amplitude fixed at $B = 12$ T. The bulk Hamiltonian is gapped only within the area marked in yellow, $85° \leq \theta \leq 95°$. In a finite system a zero energy mode appears throughout this range of θ, with maximum distance to the other eigenstates at $\theta = 90°$.

(12,4) CNT is plotted in Fig. 5.10(a). The Δ_0 term remains constant in the momentum space, with its relative strength of 1 also plotted for comparison. The topological phase diagram with $\Delta_1 = 2\Delta_0$ is shown in Fig. 5.10(b). The non-trivial regions are extended farther towards low magnetic field, but at high $B_\perp$ the presence of Δ_1 has no discernible influence. The topological phase diagram in the $B_\perp, \Delta_1/\Delta_0$ plane at constant $\mu = 334.6$ meV is shown in Fig. 5.10(c). Again, the visible variations occur only in the low field ranges, and for low Δ_1/Δ_0 ratios. Beyond $\Delta_1/\Delta_0 \approx 4$ the low field boundary of the topological phase does not extend any further. Also when $B_\perp$ is kept constant, as shown in Fig. 5.10(d) at $B_\perp = 12$ T, the boundaries of non-trivial phase vary only slightly and mostly for $\Delta_1/\Delta_0 < 2$. In conclusion, the only relevant effect of Δ_1 is that it allows the MBS to form at lower magnetic field, which is a bonus for experimentalists.

5.6. Majorana states at a phase boundary

Both the Pfaffian and the winding number invariants predict correctly whether the system is in a trivial or non-trivial topological phase, but the winding number also distinguishes between different non-trivial phases. This could be seen from Fig. 5.5(d), where the upper and lower non-trivial regions are characterized by different values of the winding number. In consequence, if the chemical potential of the CNT is tuned in such a way that a part of the tube resides in the phase with $\nu = -1$ and another in the $\nu = +1$ phase, two MBS modes arise, localized at the ends of the CNT and back-to-back at the boundary between the two phases. This situation is shown in Fig. 5.11(a),(b), where the left half of the CNT is at $\mu_L = 334.6$ meV, the right half at $\mu_R = 340.7$ meV, the crossover region where the potential varies smoothly from μ_L to μ_R has the length of ∼20 Å and the magnetic field is $B_\perp = 14$ T.

The lowest energy mode, localized at the CNT ends, is a true Majorana mode with the energy equal zero within the machine precision. Since it is composed of two parts from different topological phases, its wave function has different profile at the left and at the right end. Its left part is characterized by a single characteristic oscillation period, corresponding to the k_F of band ①, which is the single one contributing to the zero energy mode in the lower

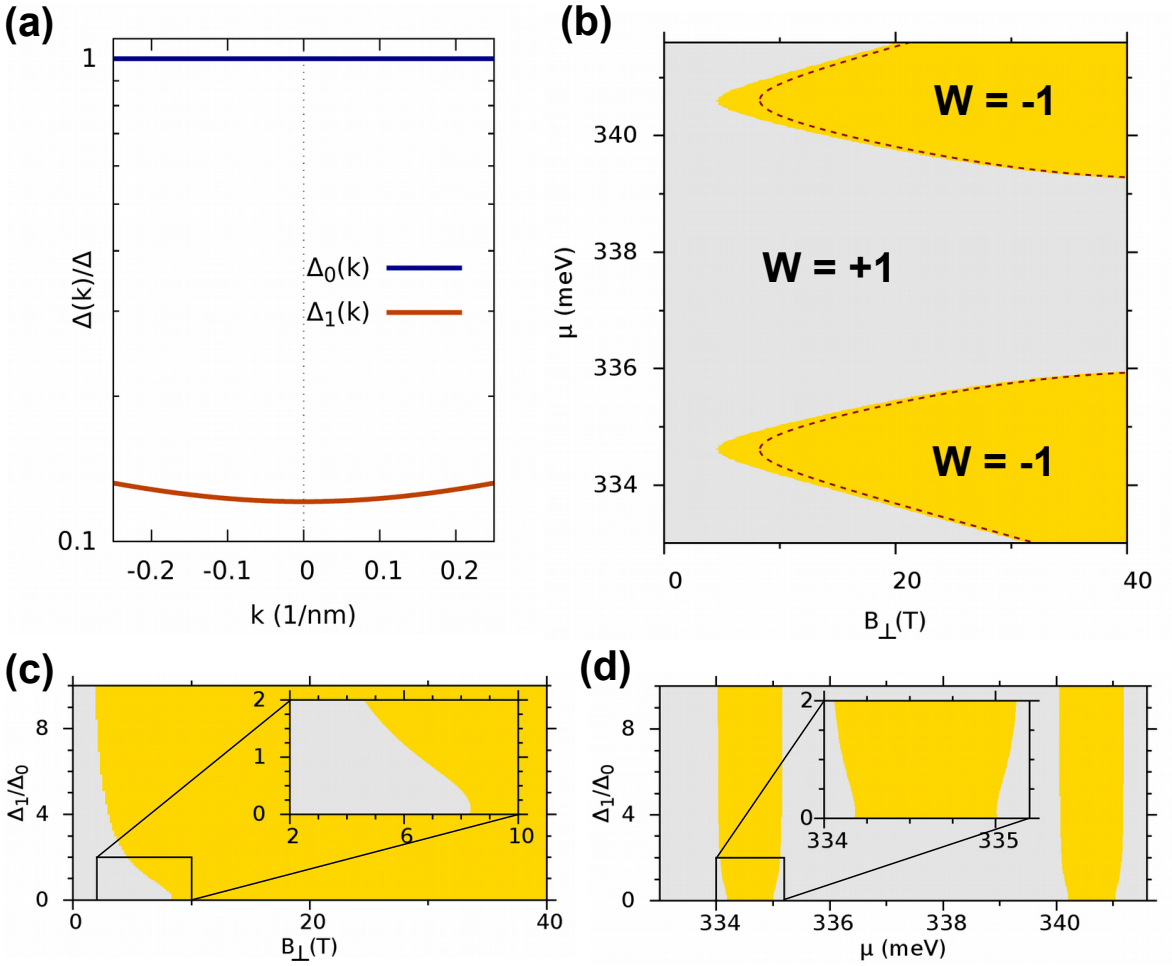

Figure 5.10: (a) The Δ_0 and $\Delta_1(k)$ pairing strength, in the units of the appropriate pairing type, bare Δ_0 and bare Δ_1, respectively. (b) Topological phase diagram constructed with the Pfaffian invariant, with bare $\Delta_1 = 2\Delta_0$. Here and in **c,d** the value of $\sqrt{\Delta_0^2 + \Delta_1^2}$ is kept constant and equal 0.4 meV. The red lines show the phase boundaries with $\Delta_1 = 0$. The inclusion of nearest neighbor pairing has extended the non-trivial region towards lower magnetic field, but otherwise its influence is invisible. (c) Topological phase diagram at constant $\mu = 334.6$ meV. Here too the increasing contribution of Δ_1 with respect to Δ_0 extends the lower border of the non-trivial phase. (d) Topological phase diagram at $B_\perp = 12$ T. Again, the inclusion of Δ_1 slightly extends the borders of the non-trivial phase.

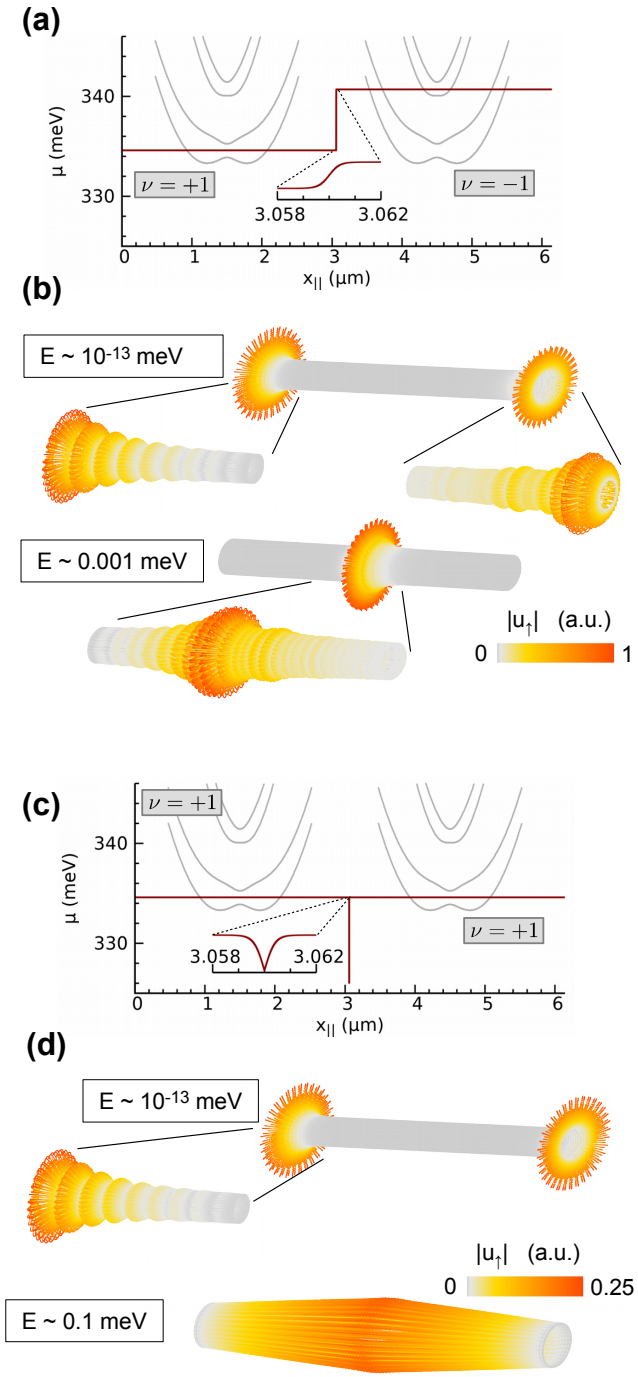

Figure 5.11: (a) The profile of the chemical potential where the left and right half of the CNT are in different non-trivial topological phases. The magnetic field is $B_\perp = 14$ T and the length of the crossover region is ~ 20 Å. The grey lines show for reference the energy bands. (b) The amplitude $|u_\uparrow(\mathbf{r})|$ of spin up component of the two lowest energy eigenstates. Remaining components have almost identical profiles. The state localized at the ends is a true MBS. Note different wave function profile at the left and right end, which are in different phases. The eigenstate in the center is composed of the partners of the left and right parts of the Majorana mode, which overlap and slightly hybridize, pushing the state's energy to roughly 1% of the bulk gap. (c) The chemical potential profile for a CNT whose two halves are in the same phase, but separated by a narrow region of the trivial phase, also with the length of ~ 20 Å. (d) The amplitude $|u_\uparrow(\mathbf{r})|$ of spin up component of the two lowest energy eigenstates. Remaining components have almost identical profiles. The lower energy eigenstate is a Majorana mode, the next one belongs already to the bulk, extending over the whole CNT.

non-trivial region. The right part of the Majorana mode shows clear beating behaviour, due to the interference of contributions from ①,② and ③ bands. The other low energy state is composed of the partners of the left and right part, located at the phase boundary. There the two modes overlap and slightly hybridize, moving the energy of the resulting state to $\sim 1\%$ of the band gap, and skewing them from the true Majorana nature. The overlap between the two modes has however much more dramatic consequences if the two halves of the CNT are in the same phase, with an equally narrow region of trivial phase in the center, as shown in Fig. 5.11(c),(d). There the end state remains a Majorana state, but the center state hybridizes fully and moves into the bulk.

5.7. Conclusion

In this chapter, we have shown in a combination of numerical modeling and analytical calculations that proximitized semiconducting carbon nanotubes are predestined hosts for Majorana bound states. While the numerical approach has allowed us to test the robustness of the topological phase against disorder or field misalignement, the analytical model has given us the possibility to clearly identify the phase boundaries of the topological phase transition, all issues crucial for an experimental observation. The use of semiconducting nanotubes instead of metallic ones as proposed in Ref. [167] has the crucial advantage that - due to the much smaller Fermi velocity - the Majorana modes already emerge in carbon nanotubes of few micrometers in length, routinely accessible in experiments. In our setup, perpendicular magnetic fields of around 10T are required to reach the topological phase. Thus, besides involving semiconducting carbon nanotubes, we propose the use of a thin layer of superconducting $NbSe_2$ to induce the proximity effect. In fact, this material is known to sustain very large in plane magnetic fields before superconductivity is destroyed. With all experimental requiements being in the reach of state-of-the-art technology, we are confident that our work will stimulate experimental research to engineer Majorana modes in carbon nanotubes.

6. Transverse profile and 3D spin canting of a Majorana state in carbon nanotubes

In this chapter we analytically obtain the full 3D spatial profile of the Majorana wave function. First, we exploit our knowledge of the three symmetries of the BdG Hamiltonian in order to derive the relations between the four components of the Majorana spinor (see Fig. 6.1), thus reducing the number of independent components to one. Second, we find that the presence of two angular momentum contributions (valleys) and the spin degree of freedom results in the formation of a composite, three-piece MBS whose 3D wave function has a distinctive spiral pattern with a C_2 symmetry, impossible to factorize into separate transverse and longitudinal profiles. Equally non-isotropic is the spin canting angle (a quantity encoding the relative phase of the spin up and spin down particle components of the Majorana wave function) which plays an important role in determining the probability of electrons tunneling into the Majorana wire [41] or CNT. This is in contrast with the nanowire, where the spatial profile is obtained with simple one-dimensional models which do not have a microscopic counterpart [109]. The transverse profile has so far been obtained only numerically for effective models of core-shell nanowires in cylindrical [174, 175] and prismatic [176] geometries. The results of this chapter have been published in Phys. Rev. B **100**, 155417 (2019).

6.1. Symmetries of the Majorana spinor

We use the same model as in chapter 5 to analytically obtain the full spatial profile $\langle \mathbf{r} \,|\, \Psi_M \rangle = \Psi_M(\mathbf{r})$. $|\Psi_M\rangle = \gamma_M |0\rangle$ where $\gamma_M^\dagger = \gamma_M$ is the Majorana creation operator. Here $\mathbf{r} = (z, r_\perp)$, where z and $r_\perp$ denote the longitudinal and the transverse components, respectively. The MBS is described by a spinor, $\Psi_M(\mathbf{r}) = (u_\uparrow(\mathbf{r}), u_\downarrow(\mathbf{r}), v_\uparrow(\mathbf{r}), v_\downarrow(\mathbf{r}))^T$, with $u_s(\mathbf{r})$ and $v_s(\mathbf{r})$ the electron and hole components, respectively, and s indicating the spin degree of freedom. As detailed below, it is enough to find the $u_\uparrow(\mathbf{r})$ components and use the symmetries of the underlying BdG Hamiltonian to determine the rest, see Fig. 6.1.

The first symmetry is inherent in the fundamental property $\mathcal{P}\Psi_M(\mathbf{r}) \stackrel{!}{=} \Psi_M(\mathbf{r})$ of a Majorana state, where $\mathcal{P}$ is the antiunitary particle-hole operator. As a consequence $u_s(\mathbf{r}) = v_s^\star(\mathbf{r})$ as illustrated in Fig. 6.1. A pseudo time-reversal symmetry $\tilde{\mathcal{T}}$ can be defined, which has bosonic nature $\tilde{\mathcal{T}}^2 = 1$ and implies $u_s(\mathbf{r}) = -iu_{-s}^\star(\mathbf{r})$. The pseudo-time reversal represents the physical invariance of the CNT under C_2' symmetry - a rotation by π with respect to an axis perpendicular to the CNT. This rotation maps the $\mathbf{k}, s$ quantum states onto $-\mathbf{k}, -s$ and exchanges the sublattice. For conduction band states this results in the relation depicted in Fig. 6.4. Since the single-particle states of a finite CNT in our setup contain both $\mathbf{k}, s$ and $-\mathbf{k}, -s$ contributions with equal weights, their spin components in the real space must also obey the relation shown in Fig. 6.1.

As a side note, the choice of the C_2' axis is not free, but must agree with the lattice structure.

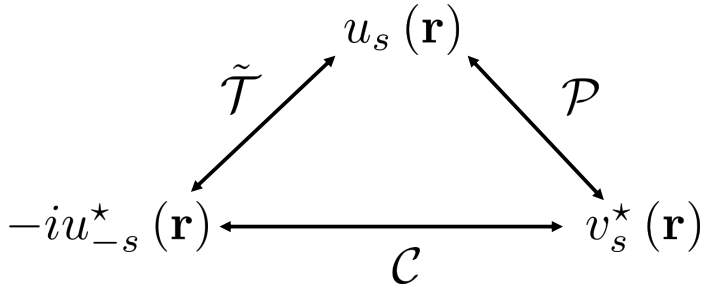

Figure 6.1: Relation between the electron and hole components of a Majorana spinor under $\mathcal{P}$, $\tilde{\mathcal{T}}$ and $\mathcal{C}$ operations. These are associated to particle-hole symmetry $\mathcal{P}$, chiral symmetry $\mathcal{C}$, and pseudo time-reversal symmetry $\tilde{\mathcal{T}}$.

Moreover, in order for the symmetry to hold in the magnetic field, the field should be aligned parallel to this axis. These constraints are however not as severe as they seem. We have checked the behavior of the system for fields with the orientation changing in the $x-y$ plane and its spectrum remained the same. Hence we conclude that the system is macroscopic enough that the alignment between the π-rotation axis and the magnetic field does not need to be atomically precise.

With the $\mathcal{P}$ and $\tilde{\mathcal{T}}$ symmetries combined, the BdG Hamiltonian of the nanotube is also chiral symmetric under $\mathcal{C} = \tilde{\mathcal{T}}\mathcal{P}$. This yields the final relation $v_s(\mathbf{r}) = iu_{-s}(\mathbf{r})$. Given this knowledge, we proceed in the following in the calculation of the MBS $|\Psi_M\rangle$ using an effective two-band model from section 3.6.

6.2. 1D Majorana profile

Majorana bound states are zero energy eigenstates of the BdG Hamiltonian and the particle-hole symmetry operator. The starting point is the BdG Hamiltonian (5.11)

$$\hat{\mathcal{H}}^{\pm}_{\mathrm{BdG}} = \begin{pmatrix} \tilde{\xi}_{\pm}(k) & \tilde{\Delta}_p(k) \\ \tilde{\Delta}_p(k) & -\tilde{\xi}_{\pm}(k) \end{pmatrix},$$

with the quasiparticle energy $\tilde{\xi}_{\pm}(k)$ given by

$$\tilde{\xi}_{\pm}(k) = \frac{1}{2}\left(\tilde{E}_1(k) - \tilde{E}_2(k)\right) \pm \frac{1}{2}\sqrt{\left(\tilde{E}_1(k) + \tilde{E}_2(k)\right)^2 + 4\tilde{\Delta}_s^2(k)}.$$

The functions $\tilde{\xi}_{+}(k)$ and $\tilde{\Delta}_p(k)$ are sketched in Fig. 6.2. Majorana bound states are zero energy eigenstates of the BdG Hamiltonian and the particle-hole symmetry operator. The low-energy physics is described by the block $\hat{\mathcal{H}}^{+}_{\mathrm{BdG}}$ with the particle-hole symmetry $\mathcal{P} = \tau_x\mathcal{K}$ and chiral symmetry $\mathcal{C} = \tau_y$, where $\tau_{x,y,z}$ are the Pauli matrices acting in the Nambu space.

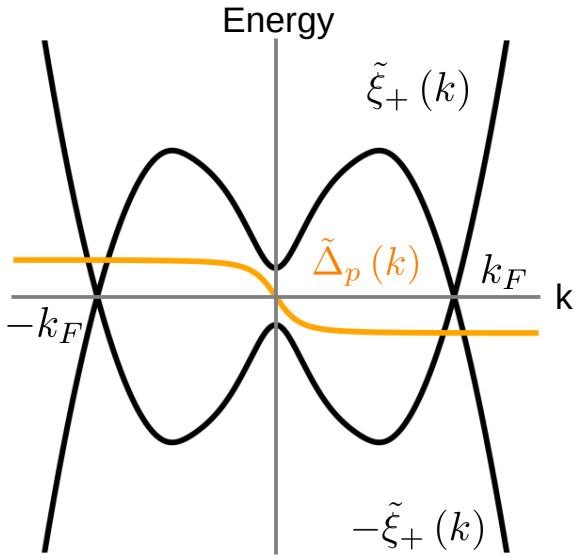

Figure 6.2: Quasiparticle energy $\tilde{\xi}_+(k)$ and superconducting order parameter $\tilde{\Delta}_p(k)$. In $\tilde{\xi}_+(k)$ we have three dominant contributions for the zero energy modes: at the Γ-point and at the $\pm k_F$-points. The superconducting order paramater is an odd function of the momentum k.

From the behavior of $\tilde{\xi}_+(k)$ we infer that the low-energy physics has three contributions: one from the Γ-point and one from each of the Fermi points. Thus, similar to some 1D models for nanowires [109], the generic form of a Majorana state can be defined as

$$|\Psi_M\rangle = \frac{A_\Gamma}{\sqrt{2}}|\Psi_\Gamma\rangle + \frac{A_R}{\sqrt{2}}|\Psi_{k_F}\rangle + \frac{A_L}{\sqrt{2}}|\Psi_{-k_F}\rangle\,. \tag{6.1}$$

We will later take into account the 3D nature of each of these three contributions and reconstruct the 3D spatial profile of the Majorana wave function. For now we approximate $\hat{\mathcal{H}}^+_{\mathrm{BdG}} \approx \hat{\mathcal{H}}^\Gamma_{\mathrm{BdG}} + \hat{\mathcal{H}}^R_{\mathrm{BdG}} + \hat{\mathcal{H}}^L_{\mathrm{BdG}}$, where we make Taylor expansions around the momenta $k = 0$ and $k = \pm k_F$, where k_F is determined by the constraint $\xi_+(k_F) = 0$.

6.2.1. Γ-point contribution

The first contribution is coming from the Γ-point. Therefore, we obtain from a Taylor expansion around the Γ-point

$$\begin{aligned}\tilde{\xi}_+(k) &\approx \tilde{\xi}_+(0) + \frac{\hbar^2 k^2}{2m^\star},\\ \tilde{\Delta}_p(k) &\approx \lambda\hbar k,\end{aligned}$$

where $\frac{1}{m^\star} = \frac{\partial^2\tilde{\xi}_+(k)}{\hbar^2\partial k^2}\Big|_{k=0}$ and $\lambda = \frac{\partial\tilde{\Delta}_p(k)}{\hbar\partial k}\Big|_{k=0}$. Then the BdG Hamiltonian for $k \approx \Gamma$ becomes

$$\hat{\mathcal{H}}^{\Gamma}_{\mathrm{BdG}} = \begin{pmatrix} \frac{\hbar^2 k^2}{2m^\star} + \tilde{\xi}_+(0) & \lambda\hbar k \\ \lambda\hbar k & -\left(\frac{\hbar^2 k^2}{2m^\star} + \tilde{\xi}_+(0)\right) \end{pmatrix}, \tag{6.2}$$

and the corresponding BdG equation reads

$$\begin{pmatrix} \frac{\hbar^2 k^2}{2m^\star} + \tilde{\xi}_+(0) & \lambda\hbar k \\ \lambda\hbar k & -\left(\frac{\hbar^2 k^2}{2m^\star} + \tilde{\xi}_+(0)\right) \end{pmatrix} \begin{pmatrix} u_\Gamma \\ v_\Gamma \end{pmatrix} = E \begin{pmatrix} u_\Gamma \\ v_\Gamma \end{pmatrix}.$$

Now, we interpret k as the momentum operator $k \to \hat{k} = -i\partial_z$ and make the ansatz

$$\begin{pmatrix} u_\Gamma(z) \\ v_\Gamma(z) \end{pmatrix} = \begin{pmatrix} u_\Gamma \\ v_\Gamma \end{pmatrix} e^{\kappa_\Gamma z}. \tag{6.3}$$

For the momentum κ_Γ we need to solve the secular equation $\det\left(\hat{\mathcal{H}}^{\Gamma}_{\mathrm{BdG}} - E\mathbb{1}\right) \stackrel{!}{=} 0$ for any energy E and we obtain

$$\kappa_\Gamma^2 = 2\frac{m^\star \tilde{\xi}_+(0)}{\hbar^2} + 2\left(\frac{m^\star\lambda}{\hbar}\right)^2 \pm \sqrt{\left(2\frac{m^\star E}{\hbar^2}\right)^2 + 4\left(\frac{m^\star\lambda}{\hbar}\right)^2 \left(\left(\frac{m^\star\lambda}{\hbar}\right)^2 + 2\frac{m^\star\tilde{\xi}_+(0)}{\hbar^2}\right)}.$$

For zero energy modes the equation can be simplified

$$\kappa_\Gamma = \pm\left(\frac{m^\star\lambda}{\hbar} \pm \sqrt{\left(\frac{m^\star\lambda}{\hbar}\right)^2 + 2\frac{m^\star\tilde{\xi}_+(0)}{\hbar^2}}\right). \tag{6.4}$$

The corresponding zero energy eigenvectors are given by

$$\begin{pmatrix} u_\Gamma \\ v_\Gamma \end{pmatrix} = \frac{1}{\sqrt{2}} \begin{pmatrix} \mp i \\ 1 \end{pmatrix}. \tag{6.5}$$

6.2.2. Fermi point contribution

For the Fermi point contribution we need to linearize $\tilde{\xi}_+(k)$ around k_F and $-k_F$, see. Fig. 6.2. Then, we can define the following two Nambu spinors $\Psi_R = (d_{k+,R},\, d_{-k+,L})$ and $\Psi_L = (d_{k+,L},\, d_{-k+,R})$. The subscripts R, L denote the right- and left-movers. The corresponding BdG Hamiltonians are given by

$$\hat{\mathcal{H}}^{R}_{\mathrm{BdG}} = \begin{pmatrix} v_F\hbar\,(k-k_F) & \tilde{\Delta}_p\,(k_F) \\ \tilde{\Delta}_p\,(k_F) & -v_F\hbar\,(k-k_F) \end{pmatrix}, \tag{6.6}$$

$$\hat{\mathcal{H}}^{L}_{\mathrm{BdG}} = \begin{pmatrix} -v_F\hbar\,(k+k_F) & \tilde{\Delta}_p\,(-k_F) \\ \tilde{\Delta}_p\,(-k_F) & v_F\hbar\,(k+k_F) \end{pmatrix}, \tag{6.7}$$

where for $\hat{\mathcal{H}}^{R}_{\mathrm{BdG}}$ we have $k > 0$ and for $\hat{\mathcal{H}}^{L}_{\mathrm{BdG}}$ we have $k < 0$. The corresponding BdG equations read

$$\begin{pmatrix} v_F\hbar\,(k-k_F) & \tilde{\Delta}_p\,(k_F) \\ \tilde{\Delta}_p\,(k_F) & -v_F\hbar\,(k-k_F) \end{pmatrix} \begin{pmatrix} u_R \\ v_L \end{pmatrix} = E \begin{pmatrix} u_R \\ v_L \end{pmatrix},$$

$$\begin{pmatrix} -v_F\hbar\,(k+k_F) & \tilde{\Delta}_p\,(-k_F) \\ \tilde{\Delta}_p\,(-k_F) & v_F\hbar\,(k+k_F) \end{pmatrix} \begin{pmatrix} u_L \\ v_R \end{pmatrix} = E \begin{pmatrix} u_L \\ v_R \end{pmatrix}.$$

With $k \to \hat{k} = -i\partial_z$ and making the ansatz

$$\begin{pmatrix} u_R\,(z) \\ v_L\,(z) \end{pmatrix} = \begin{pmatrix} u_R \\ v_L \end{pmatrix} e^{\kappa_R z} \text{ and } \begin{pmatrix} u_L\,(z) \\ v_R\,(z) \end{pmatrix} = \begin{pmatrix} u_L \\ v_R \end{pmatrix} e^{\kappa_L z},$$

we get the decaying lengths κ_R and κ_L from the secular equations $\det\left(\hat{\mathcal{H}}^{\mathrm{R/L}}_{\mathrm{BdG}} - E\mathbb{1}\right) \overset{!}{=} 0$. The decay lengths for the zero energy modes become $\kappa_R = ik_F \mp \frac{|\tilde{\Delta}_p(k_F)|}{v_F\hbar}$ and $\kappa_L = -ik_F \mp \frac{|\tilde{\Delta}_p(k_F)|}{v_F\hbar}$. Furthermore, we get the two eigenvectors

$$\begin{pmatrix} u_R \\ v_L \end{pmatrix} = \frac{1}{\sqrt{2}} \begin{pmatrix} \pm i\mathrm{sgn}\left(\tilde{\Delta}_p\,(k_F)\right) \\ 1 \end{pmatrix} = \frac{1}{\sqrt{2}} \begin{pmatrix} \mp i \\ 1 \end{pmatrix},$$
$$\begin{pmatrix} u_L \\ v_R \end{pmatrix} = \frac{1}{\sqrt{2}} \begin{pmatrix} \mp i\mathrm{sgn}\left(\tilde{\Delta}_p\,(-k_F)\right) \\ 1 \end{pmatrix} = \frac{1}{\sqrt{2}} \begin{pmatrix} \mp i \\ 1 \end{pmatrix},$$

where we used $\mathrm{sgn}\left(\tilde{\Delta}_p\,(k_F)\right) = -1$ and $\mathrm{sgn}\left(\tilde{\Delta}_p\,(-k_F)\right) = +1$.

6.2.3. 1D Majorana state

Crucially, the spinorial components of the solutions at each of the three k points are the same, which allows us to combine them into a single state which is also an eigenstate of both $\mathcal{P}$

and $\mathcal{C}$. With the three contributions we can construct the 1D solution (6.8) from the generic solution (6.1). The coefficients can be determined by the three constraints

$$\begin{aligned}
&\mathcal{P}\Psi_M(z) \stackrel{!}{=} \Psi_M(z),\\
&\Psi_M(z=0) \stackrel{!}{=} 0,\\
&\int_0^\infty dz\,|\Psi_M(z)|^2 \stackrel{!}{=} 1.
\end{aligned}$$

From our calculations we know that in the topological regime $\kappa_\Gamma \in \mathbb{R}$ and $\kappa_R, \kappa_L \in \mathbb{C}$. Moreover, we know that $\mathrm{Re}(\kappa_R) = \mathrm{Re}(\kappa_L)$ but $\mathrm{Im}(\kappa_R) = -\mathrm{Im}(\kappa_L) \Leftrightarrow \kappa_R = \kappa_L^\star$. Therefore, the wave function can be written as

$$\Psi_M(z) = \left[\frac{A_\Gamma}{\sqrt{2}}e^{\kappa_\Gamma z} + \frac{A_R}{\sqrt{2}}e^{\kappa_R z} + \frac{A_L}{\sqrt{2}}e^{\kappa_R^\star z}\right]\begin{pmatrix}\mp i\\ 1\end{pmatrix}.$$

These eigenvectors are not eigenstates of the particle-hole operator $\mathcal{P} = \sigma_x\mathcal{K}$, but we can multiply them by a complex number $c_\pm = \pm 1 + i$, such that it satifies the Majorana constraint. Then, by applying the boundary condition we get the 1D solution

$$\psi_{1D}(z) = \frac{\mathcal{N}}{2}\left(\psi_\parallel(z) + \psi_\parallel^\star(z)\right)\frac{1}{\sqrt{2}}\begin{pmatrix}1-i\\ 1+i\end{pmatrix}, \tag{6.8}$$

where $\psi_\parallel(z) = \left(e^{\kappa_F z + ik_F z} - e^{\kappa_\Gamma z}\right)$ encodes the dependence of the wave function on the longitudinal coordinate. The sum $\psi_\parallel(z) + \psi_\parallel^*(z)$ satisfies the boundary condition $\psi_{1D}(z=0) = 0$, and $\mathcal{N}$ is the normalization constant. The contribution from the Γ-point is a pure evanescent state and from the contribution from the Fermi points we get a decaying oscillation with the wavevector k_F.

6.3. 3D Majorana quasiparticle wave function

To check the validity of the ansatz (6.1), we have calculated numerically the Majorana wave function $\Psi_M(\mathbf{r})$, see Fig. 6.3(a). The associated Fourier transform for several values of $r_\perp$ (the corresponding polar angle is $\varphi = r_\perp/R$) can be seen in Fig. 6.3(b). One clearly sees one peak at the Γ-point and two peaks at opposite momenta. The peak locations are independent of φ but their height is not. Furthermore, the peak at negative k is larger. This is because of the helical spin structure of the single-particle spectrum, shown in Fig. 5.4(a). The solution at $\pm k_F$ is generated mostly by the band ①, and spin $\uparrow$ for this band is associated with $k < 0$. In the remaining of this work we provide the analytical form for $u_\uparrow(\mathbf{r})$. As we already discussed,

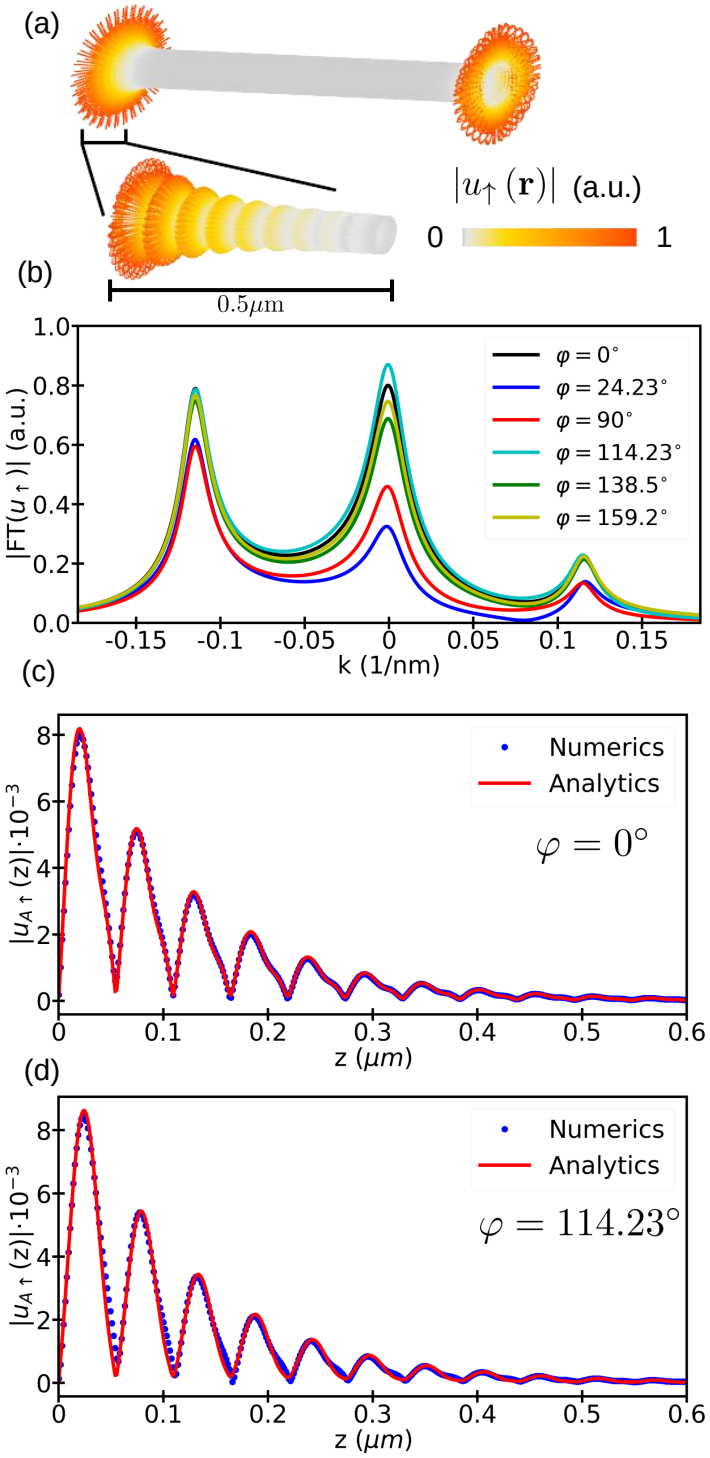

Figure 6.3: Electron component $u_\uparrow$ of the Majorana spinor. (a) The full spatial profile of the spin up particle component of the spinor, $|u_\uparrow|$ obtained by a real-space tight-binding calculation of a finite (12,4) CNT with 4000 unit cells ($L = 6.03\mu m$) for a magnetic field $B_\perp = 14$T. The amplitude of the electronic wave function is shown through both the distance from the nanotube's surface (light grey) and through the color scale. (b) Absolute values of the Fourier transformed wave functions from the tight-binding model for several values of φ. There are three momentum contributions, one from the Γ-point (k_Γ) and one from each Fermi point ($\pm k_F$). (c)-(d) Cuts along $\varphi = 0°$, $114.23°$ of the numerical $|u_\uparrow|$ together with the analytical solutions.

due to the symmetries of the system (cf. Fig. 6.1) all the other components are related to $u_{\uparrow}(\mathbf{r})$ by the $\mathcal{P}$, $\tilde{\mathcal{T}}$ and $\mathcal{C}$ symmetries. In order to find the analytical wave function we need to transform the wave function from two-band model back to four-band where we know the spatial dependence of all contributions.

The generic Majorana state (6.1) has three amplitudes, one for each contribution. These amplitudes however are not independent since Ψ_M must satisfy the Majorana condition and the open boundary condition in longitudinal direction. To express the Majorana state in the sublattice- and spin-resolved basis we need the transformations reversing (3.30), (3.34) and (5.10). The Majorana operator to create the state (6.1) is defined as

$$\gamma_M = \sum_k \begin{pmatrix} u \\ v \end{pmatrix}^T \begin{pmatrix} d_{k+} \\ d^{\dagger}_{-k+} \end{pmatrix},$$

where $k \in \{\Gamma,\, k_F,\, -k_F\}$ and $u = v^{\star} = \frac{1-i}{\sqrt{2}}$. By using all the back transformations we get

$$\gamma_M = \sum_{k,\tau,s} \left(u_{\tau s}(k)\, c_{k\tau s} + v_{\tau s}(-k)\, c^{\dagger}_{-k\tau s} \right), \tag{6.9}$$

for $k \in \{\Gamma, \pm k_F\}$, where the coefficients $u_{\tau s}(k)$ correspond to the electron and $v_{\tau s}(k)$ hole contribution, respectively. We have the following definitions for the coefficients

$$u_{\tau s}(k) = \tau s \Lambda_{\tau s}(k)\, \lambda_s(k), \tag{6.10}$$

$$v_{\tau s}(k) = \tau s \Lambda_{\tau s}(k)\, \lambda^{\star}_s(k), \tag{6.11}$$

with

$$\Lambda_{\tau s}(k) = \begin{cases} a_s(k) & \text{for } \tau = +1, \\ b_s(k) & \text{for } \tau = -1, \end{cases}$$

and

$$\lambda_s(k) = u\, m(k)\, g(sk) - s\, v\, n(k)\, h(sk).$$

By using the relations $a_s(-k) = b_{-s}(k)$, $g(-k) = h(k)$, $m(-k) = m(k)$, $n(-k) = n(k)$ we get the relations $\Lambda_{\tau s}(k) = \Lambda_{-\tau -s}(-k)$ and $\lambda_s(k) = -i\lambda^{\star}_{-s}(-k)$. As a consequence, we

obtain symmetry relations of the electron and hole coefficients $u_{\tau s}(k)$ and $v_{\tau s}(k)$, which are illustrated in Fig. 6.4.

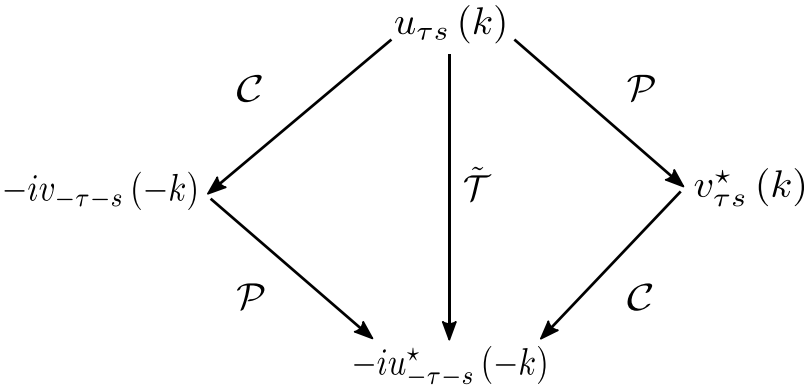

Figure 6.4: Symmetry relations of the coefficient $u_{\tau s}$ due to the three symmetries: particle-hole symmetry $\mathcal{P}$, chiral symmetry $\mathcal{C}$ and, pseudo time-reversal symmetry $\tilde{\mathcal{T}}$. Note that guided by the analogy with the definition of the $\mathcal{P}$'s action on the Hamiltonian we would expect that it should relate $u_{\tau s}(k)$ and $v^{*}_{-\tau s}(-k)$. However, due to our definition of the Nambu spinor, $\mathcal{P}$ relates $u_{\tau s}(k)$ and $v^{*}_{\tau s}(k)$, as shown above.

From the transformation we obtain the wave function in conduction basis but in order to apply the boundary condition we need the wave function in sublattice-resolved basis. In general for the transformation into the sublattice basis we need also the valence band contribution. Here we can however use the fact that due to the high chemical potential we are far away from the charge neutrality point and therefore the contribution from the valence band is negligible. With this the components in the sublattice basis are defined as $u_{p\tau s}(k) = e^{ip\eta_{\tau sk}} u_{\tau s}(k)$, where $\eta_{\tau s}(k) = \arg(\gamma_{\tau s}(k))$ is the phase of (4.8) in the low-energy regime and $p = +1$ for A sublattice and $p = -1$ for B sublattice.

Since our nanotube belongs to the zigzag class [137, 140], the open boundary conditions imply that the wave function must vanish on one end at the missing A atoms and on the other end at the missing B atoms [135]. We use therefore the open boundary condition $\Psi_A(z = 0, r_\perp) \stackrel{!}{=} 0 \ \forall r_\perp$, further focusing on $u_{A\uparrow}(\mathbf{r})$ because the components $u_{A\downarrow}(\mathbf{r})$, $v_{A\uparrow}(\mathbf{r})$ and $v_{A\downarrow}(\mathbf{r})$ are related by symmetries. The wave function $u_{A\uparrow}(\mathbf{r})$ is given by the superposition of the three contributions $k \in \{\Gamma, k_F, -k_F\}$ and the two valleys K and K', each with its specific transverse profile $e^{i\tau k_\perp x_\perp}$:

$$
\begin{aligned}
u_{\sigma\uparrow}(\mathbf{r}) = {} & \frac{A_\Gamma}{\sqrt{2}} \left[e^{i\sigma\eta_{K\uparrow\Gamma}} u_{K\uparrow}(\Gamma)\, e^{ik_\perp r_\perp} + e^{i\sigma\eta_{K'\uparrow\Gamma}} u_{K'\uparrow}(\Gamma)\, e^{-ik_\perp r_\perp} \right] e^{\kappa_\Gamma z} \\
& + \frac{A_R}{\sqrt{2}} \left[e^{i\sigma\eta_{K\uparrow k_F}} u_{K\uparrow}(k_F)\, e^{ik_\perp r_\perp} + e^{i\sigma\eta_{K'\uparrow k_F}} u_{K'\uparrow}(k_F)\, e^{-ik_\perp r_\perp} \right] e^{\kappa_F z + ik_F z} \\
& + \frac{A_L}{\sqrt{2}} \left[e^{i\sigma\eta_{K\uparrow -k_F}} u_{K\uparrow}(-k_F)\, e^{ik_\perp r_\perp} + e^{i\sigma\eta_{K'\uparrow -k_F}} u_{K'\uparrow}(-k_F)\, e^{-ik_\perp r_\perp} \right] e^{\kappa_F z - ik_F z},
\end{aligned}
\tag{6.12}
$$

where $\sigma = +1$ for A sublattice and $\sigma = -1$ for B sublattice. We have several constraints

	Analytics ($\frac{1}{\mu m}$)	Fits ($\frac{1}{\mu m}$)
κ_Γ	-7.94	-8.93
κ_F	-6.56	-8.01
k_F	118.92	115.25

Table 7: Values of k_F, κ_Γ and κ_F from the analytical calculation compared with values fitted from the numerics.

on the various parameters in this equation. The transverse momentum $k_\perp$ is quantized by the periodic boundary condition. The Fermi wavevector k_F is given by the position of the chemical potential μ, and the characteristic decay lengths at Γ and $\pm k_F$ by the parameters of the Hamiltonian at this μ. From the Majorana condition we know that $A_\Gamma \in \mathbb{R}$ and $A_R = A_L^\star$. From the open boundary condition in longitudinal direction we obtain a relation between A_R and A_Γ and the wave function can be written as

$$\begin{aligned} u_{\sigma\uparrow}(\mathbf{r}) = &\frac{1}{\sqrt{2}} \sum_\tau e^{i\tau k_\perp r_\perp} \left[A_R e^{i\sigma\eta_{\tau\uparrow k_F}} u_{\tau\uparrow}(k_F)\, \psi_\parallel(z) \right. \\ &\left. + A_R^\star e^{i\sigma\eta_{\tau\uparrow -k_F}} u_{\tau\uparrow}(-k_F)\, \psi_\parallel^\star(z) \right]. \end{aligned} \tag{6.13}$$

Note that the spatial profile of the wave function is not trivial in the sense that it cannot be factorized into separate longitudinal and transverse profiles, $u_{p\uparrow}(\mathbf{r}) \neq f(r_\perp)\, g(z)$. The absolute value $|A_R|$ is fixed by the normalization and its phase by the Majorana condition. Thus all factors in the wave function are in principle known from the analytics.

Cuts for two values of the polar angle, $\varphi = 0°$ and $\varphi = 114.23°$, of the full 3D Majorana wave function, are shown in Fig. 6.3(c) and (d). The analytical model clearly reproduces very well the numerically obtained wave functions. However, since per force we had to simplify when building the effective two-band model, there are three aspects where we have to adjust for the lost information.

(i) In the microscopic model the $\mathcal{P}$ symmetry holds exactly (by construction), but $\tilde{\mathcal{T}}$ is minimally broken by two small effects. One is the presence of the weak spin-flip terms in the Hamiltonian, due to the enhanced spin-orbit coupling [127, 128, 135]. The other is the small Peierls phase for the nearest neighbor hopping, due to the magnetic field [143]. Thus there is a $\pm 3\%$ discrepancy in the $\tilde{\mathcal{T}}$ and $\mathcal{C}$ relations between the Nambu spinor components of the numerical solutions. Removing the spin-flip and the Peierls phase restores the $\tilde{\mathcal{T}}$ and consequently also the $\mathcal{C}$ symmetries.

(ii) Due to our approximations, the neglection of correlations between band pairs due to the magnetic field and the Taylor expansions around the three contributions, the values of κ_Γ, κ_F and k_F from the analytics are slightly different than those which are obtained from fitting the numerical data using (6.13), see Tab. 7.

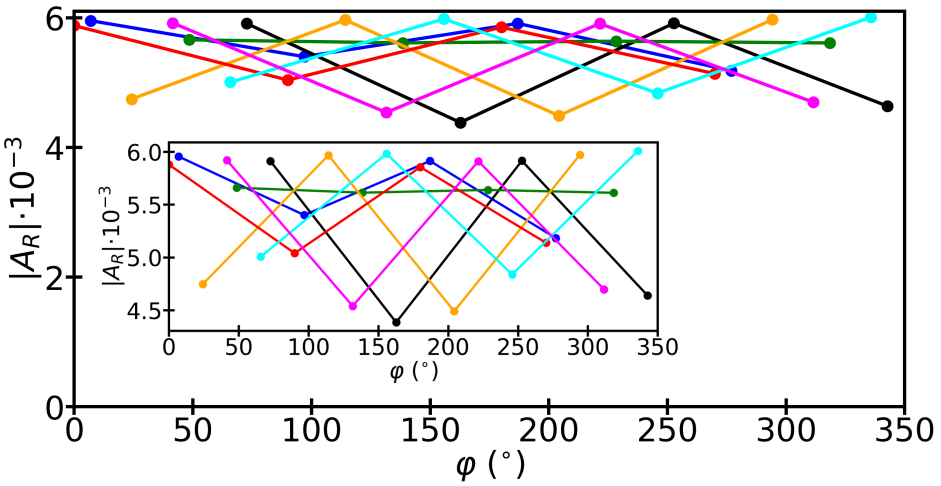

Figure 6.5: The absolute value of the fitted amplitude $|A_R|$ for 28 different φ cuts. The colors correspond to different groups of atoms related by the C_4 symmetry (i.e. atoms at the same z position). From the inset we see the π-periodicity of A_R and thus the C_2 symmetry of the MBS wave function.

(iii) We implemented the valley mixing through a continuous potential ridge along the CNT - superconductor interface. This results in the coupling between the two valleys, but also in their coupling to higher transverse momentum bands which therefore also contribute, albeit very weakly, to the final Majorana state. In consequence, although we expect A_R to be independent of φ, we obtain from the fitting procedure different A_R for 28 different φ cuts, with the resulting values of $|A_R(\varphi)|$ shown in Fig. 6.5.

We see that although not constant, the amplitude A_R is a weakly varying function of φ. Moreover, the data resolved for atoms at the same z position show that A_R is π-periodic. This is a consequence of the C_4 symmetry of our (12,4) CNT where the K'/K valley states carry the angular momentum $\ell = \pm 2$. Since the Majorana state is constructed from electron (and hole) states with $\ell = \pm 2$, the MBS wave function has C_2 symmetry, which is also visible in the Fig. 6.5 and later in Fig. 6.6(c).

6.3.1. Spin canting

In the nanowire/quantum dot setups where the character of the potential MBS is determined by analyzing its coupling to the discrete levels of the quantum dot, the spin canting of the MBS turns out to play an important role. [41, 177] If there is a mismatch between the particle spin of the MBS and that of the quantum dot, the coupling is suppressed. Thus we turn next to analyze the local spin canting angle in our Majorana nanotube.

Using the definition from the Ref. [177] this quantity is $\Theta(\mathbf{r}) = 2\arctan(u_\uparrow(\mathbf{r})/u_\downarrow(\mathbf{r}))$, thus relating the phases of particle up and down spin components of the Majorana spinor. The same information can be obtained from the local orientation of the particle spin, as we show

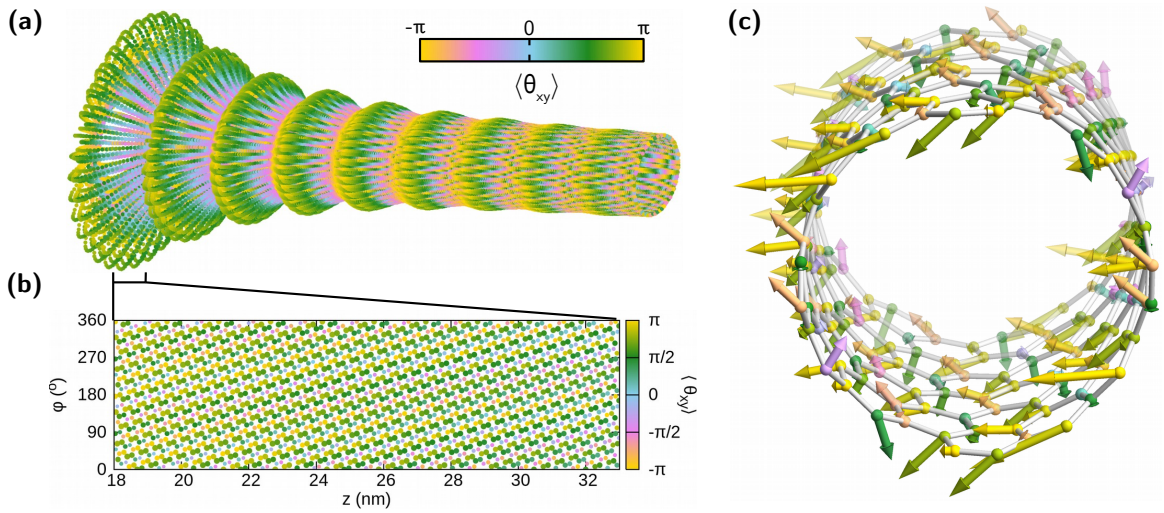

Figure 6.6: Spin canting angle $\langle\theta_{xy}\rangle(\mathbf{r})$ of the electronic component of the left Majorana state. In all panels the color corresponds to the local value of $\langle\theta_{xy}\rangle$. (a) The leftmost 0.5 μm of the Majorana state, with distance from the CNT surface encoding $|u_\uparrow(\mathbf{r})|$. (b) 2D projection of the region with the first maximum of the Majorana wave function, with point size corresponding to $|u_\uparrow(\mathbf{r})|$. (c) The left termination (i.e. the first 1.8 nm) of the CNT lattice. Vector length corresponds to $|u_\uparrow(\mathbf{r})|$, its orientation to the spin canting angle. In both (b) and (c) note the variation of $\langle\theta_{xy}\rangle$ with the polar coordinate.

below.[9] The local expectation value for each spin direction in the particle sector is given by $\langle\mathbf{u}(\mathbf{r})|s_\alpha|\mathbf{u}(\mathbf{r})\rangle$, where s_α are the Pauli matrices, $\alpha = x, y, z$, and $\mathbf{u}(\mathbf{r}) = (u_\uparrow(\mathbf{r}), u_\downarrow(\mathbf{r}))^T$ is the electron component of the wave function. Due to the symmetry relations, see Fig. 6.1,it holds

$$\begin{aligned}
\langle\mathbf{u}(\mathbf{r})\,|\,s_x\,|\,\mathbf{u}(\mathbf{r})\rangle &= -2\mathrm{Im}\left(u_\uparrow^2(\mathbf{r})\right), \\
\langle\mathbf{u}(\mathbf{r})\,|\,s_y\,|\,\mathbf{u}(\mathbf{r})\rangle &= -2\mathrm{Re}\left(u_\uparrow^2(\mathbf{r})\right), \\
\langle\mathbf{u}(\mathbf{r})\,|\,s_z\,|\,\mathbf{u}(\mathbf{r})\rangle &= 0.
\end{aligned}$$

The expectation value $\langle s_z\rangle$ is zero because of the pseudo time-reversal symmetry. Knowing the values of $\langle s_x(\mathbf{r})\rangle$ and $\langle s_y(\mathbf{r})\rangle$ we can define a local spin direction in the plane perpendicular to the nanotube,

$$\theta_{xy}(\mathbf{r}) = \arctan\left(\frac{\langle s_y(\mathbf{r})\rangle}{\langle s_x(\mathbf{r})\rangle}\right) = -2\,\arg(u_\uparrow(\mathbf{r})). \tag{6.14}$$

The definition from Ref. [177], after applying the symmetry relations from Fig. 6.1, yields $\Theta(\mathbf{r}) = -\theta_{xy}(\mathbf{r}) - 3\pi/2$, i.e. the two definitions differ only by a constant and a sign. The full 3D spatial profile of $\theta_{xy}(\mathbf{r})$ is shown in Fig. 6.6(a). The oscillation along z with the same

[9] The total spin of the Majorana particle, summed over both particle and hole contributions, is zero.

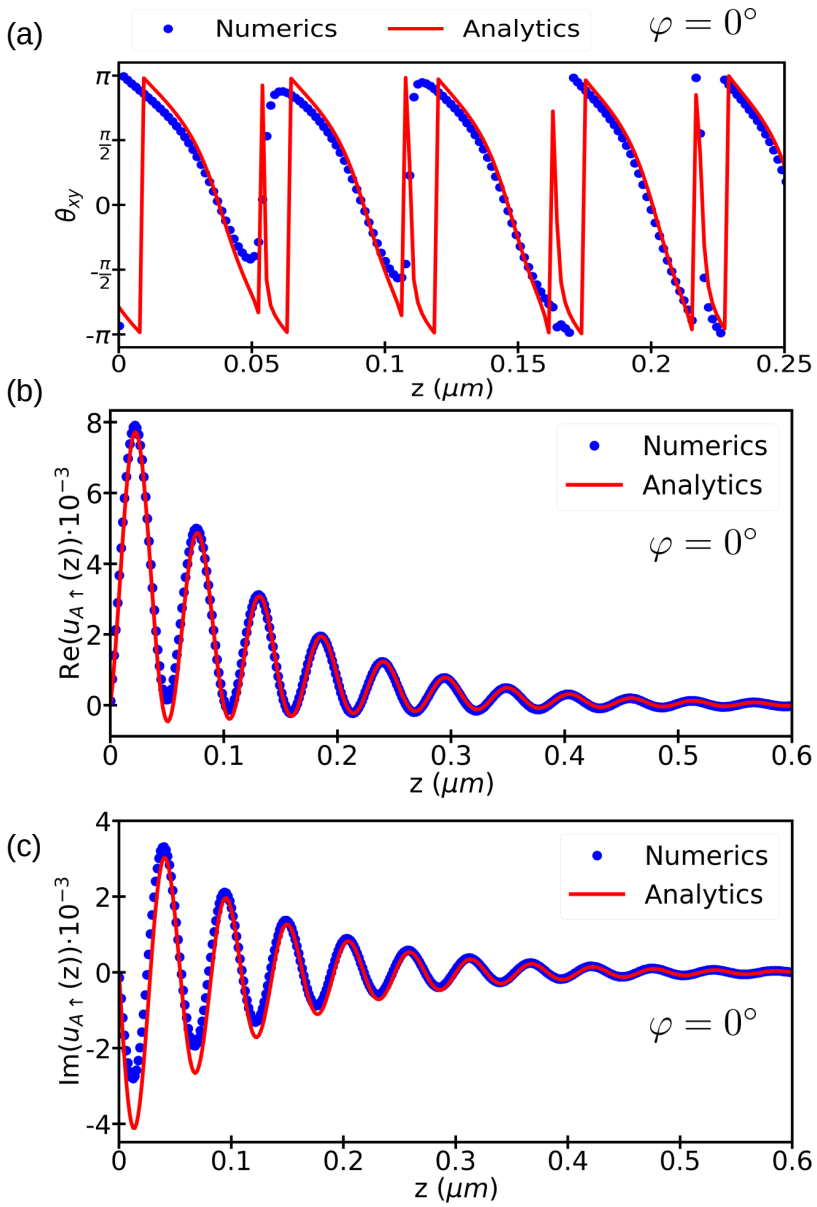

Figure 6.7: (c) The spin canting angle θ_{xy} for the cut $\varphi = 0°$ defined in Eq. (6.14). (b)-(c) Numerical and analytical Re $(u_{A\uparrow}(z))$ and Im $(u_{A\uparrow}(z))$ for the polar angle $\varphi = 0°$ from the $|u_{A\uparrow}(z)|$ fit.

period as the MBS wave function is clearly visible. Further, Fig. 6.6(b) shows a zoom of the left end of the tube for the first peak of $|u_\uparrow(\mathbf{r})|$ along z, polar angle φ resolved and showing the helical pattern of θ_{xy}. Finally, Fig. 6.6(c) visualizes the local spin canting at the very left end of the nanotube, where the electron tunneling would occur. The spin canting angle distribution also has the C_2 symmetry, and takes several different values at the edge atoms. Thus the tunneling from a putative quantum dot coupled to the left end is definitely different than in a nanowire, assumed to be isotropic. Whether this effect is helpful or detrimental for the experiment is not yet clear.

In the Fig. 6.7(a) we show a comparison between the analytical and numerical results for $\theta_{xy}(z, \varphi = 0)$. The additional phase jumps visible in the analytics are caused by the slight

discrepancy between the numerical and analytical values of the real and imaginary part of $u_\uparrow(r)$ shown in Fig. 6.7(b-c), in particular at positions where the real value in numerics is small and positive, while the analytical result is also small but negative. Nevertheless, the overall agreement is again good.

6.4. Conclusion

In this work we have shown in a combination of numerical modelling and analytical calculations how to determine the full spatial profile of the Majorana bound state in a proximitized semiconducting carbon nanotube. The wave function has three contributions: one from the Γ-point and one from each Fermi point, which is also supported by an analysis of the numerical data via a Fourier transformation. Further features which our model captures very well are: the decaying behaviour of the wave function, its oscillation, the symmetries linking the different components of the Nambu spinor and the C_2 symmetry of the Majorana state, due to its composition of the $l = \pm 2$ quasiparticle states.

The 3D spatial profile can be used to determine the 3D spin canting of the Majorana state. The total spin of the MBS is zero but still a local spin canting angle can be defined. The local spin canting angle has a nontrivial spiral pattern, varying around the CNTs circumference.

The excellent agreement between the analytically obtained and the numerically calculated spin and sublattice resolved spinor gives us confidence in the accuracy of the local observables further derived in this chapter. Despite being obtained for a CNT, our results might serve as a reference also for other systems where a microscopic calculation of the MBS spinor is not possible. Our results will be useful for modeling and interpreting the experimental results in a realistic quantum transport setup where the properties of the Majorana states are probed locally.

7. Conlusion

In summary, we investigated the topological properties of carbon nanotubes coupled to an s-wave superconductor. We analyzed the cases with and without magnetic field. In particular, we demostrated the emergence of topological edge states in a parameter region with a nontrival topological invariant and proven in both cases the bulk-edge correspondence.

In chapter 1 the topological concepts are introduced. In general a topological state of matter has a bulk gap and at its edges gapless states. We define the topological invariant for a topological system.

Then, in chapter 2 we introduced Majorana fermions, particles which are their own antiparticles. In the context of condensed matter physics this property can belong to some quasiparticles in a superconducting system, where the quantum state may be invariant under a particle-hole transformation. The emergence of such quasiparticles is discussed in a p-wave superconductor in a tight binding representation, as well as in a quantum wire with Rashba spin-orbit coupling in parallel applied magnetic field and in contact with an s-wave superconductor.

We investigated in chapter 3 the electronic spectra of ultra-clean carbon nanotubes based on the band structure of graphene. The relevance of the curvature due to the geometry of the carbon nanotubes is analyzed. The curvature enhances the intrinsic spin-orbit coupling, which then can not be neglected. An effective Hamiltonian in the reciprocal space is constructed which well reproduces the numerically calculated low-energy spectrum. Then, in the regime of low magnetic fields, an effective two-band model is derived. Moreover, we constructed an alternative model of carbon nanotubes in the helical-angular picture. Finally, we discussed the superconducting pairing terms which model proximity effect in carbon nanotubes, considering both on-site and nearest neighbor pairing between electrons.

In chapter 4 the edge states in a minimal model for topological superconductivity are studied in the time-reversal symmetric case. We demostrated that the edge states are due to the combined effect of curvature-induced shifting of the Dirac point and superconducting coupling between nearest-neighbor sites. Furthermore, the edge states with the minimal boundary are formed not by Kramer partners, but by (τ,s,r) and $(\tau,s,-r)$, where $r = \pm 1$ is the quantum number characterizing the left or right Fermi point of the spectrum. In armchair carbon nanotube it was impossible to construct an localized edge state because that required combining (τ,s,r) and $(-\tau,s,-r)$ states, whose wave functions always decay in the opposite directions.

In chapter 5 we demostrated the Majorana nature of the localized edge states in the presence of magnetic field and valley mixing using a microscopic tight-binding model. The bulk properties are discussed using the four- and two-band model and the corresponding topological phase diagram as a function of $(B_\perp, \mu)$ is calculated. We adress the point of symmetry breaking

contribution like disorder and an axial component of the magnetic field. Further, the influence of the nearest neighbor pairing term for the topological phase diagram is shown. At the end, Majorana bound states at phase boundaries are considered by tuning the chemical potential of the CNT in such a way that a part of the tube resides in the phase with $\nu = -1$ and another in the $\nu = +1$ phase.

In the final chapter the full three-dimensional spatial profile of the Majorana bound state was analytically calculated. The Majorana wave function is constructed from three contribition of the BdG spectrum: one from the Γ-point and one from each Fermi point. This result is also supported by the numerical data. The full 3D spatial profile can be used to determine the spin canting of the Majorana bound state. The local spin canting angle displays a spiral pattern, varying around the CNTs circumference. This is known to affect the electron tunneling into the MBS, although whether the effect is favorable or detrimental remains to be seen.

A. Equivalence of topological invariants

Here, we show the identity of two different expressions for the winding number: one is given by (1.26) and another is given using the flat-band Hamiltonian approach (1.21). We will omit k in the expressions for simplicity. Recall that $Q^2 = (\mathbb{1} - 2P)^2 = I - 4P + 4P^2 = \mathbb{1}$, then we have $qq^\dagger = 1$, i.e. $q^{-1} = q^\dagger$ and moreover, we also have $U^\dagger = U$, which is immediately seen from (1.25). From these two relations we have $D^{-1}U^{-1} = D^\dagger U^\dagger = D^\dagger U$ and it holds that

$$U^{-1} = DD^\dagger U = \sum_n E_n u_n u_n^\dagger. \tag{A.1}$$

Since $0 = \partial_k \left(q^{-1}q\right) = \left(\partial_k q^{-1}\right) q + q^{-1}\partial_k q$, the integrand in the expression of the winding number ν' is written as $\mathrm{Tr}\left[q^{-1}\partial_k q\right] = \frac{1}{2}\mathrm{Tr}\left[q^{-1}\partial_k q - q\partial_k q^{-1}\right]$. By using the relations $\partial_k q = (\partial_k U) D + U\partial_k D$, $\partial_k q^{-1} = \left(\partial_k D^{-1}\right) U^{-1} + D^{-1}\partial_k U^{-1}$, and the cyclic property of the trace, we have

$$\begin{aligned}
&\mathrm{Tr}\left[q^{-1}\partial_k q - q\partial_k q^{-1}\right] = \mathrm{Tr}\left[\left(D^{-1}\partial_k D - D\partial_k D^{-1}\right) + \left(U^{-1}\partial_k U - U\partial_k U^{-1}\right)\right], \\
&\mathrm{Tr}\left[U^{-1}\partial_k U - U\partial_k U^{-1}\right] = \mathrm{Tr}\left[U^{-1}\partial_k U - \partial_k\left(UU^{-1}\right) + (\partial_k U) U^{-1}\right] = 2\mathrm{Tr}\left[U^{-1}\partial_k U\right].
\end{aligned}$$

By using (A.1), we find

$$\begin{aligned}
\mathrm{Tr}\left[U^{-1}\partial_k U\right] &= \mathrm{Tr}\left[\sum_{n,n'}\left(-E_n\frac{\partial_k E_{n'}}{E_{n'}^2}\right) u_n u_n^\dagger u_{n'} u_{n'}^\dagger\right] = -\mathrm{Tr}\left[\sum_n \frac{\partial_k E_n}{E_n} u_n u_n^\dagger\right] \\
&= -\sum_n \partial_k \ln\left(E_n\right),
\end{aligned}$$

where we have used the orthogonality $u_n^\dagger u_{n'} = \delta_{n,n'}$ and $\mathrm{Tr}\left[u_n u_n^\dagger\right] = \sum_m u_{n,m} u_{n,m}^\star = 1$. Using the periodicity of $E_n(k)$ in the Brillouin zone, we finally get the identity

$$\nu' = \frac{1}{4\pi i}\int dk \mathrm{Tr}\left[D^{-1}\partial_k D - D\partial_k D^{-1}\right] = -\frac{1}{4\pi i}\int dk \mathrm{Tr}\left[\tilde{C}\mathcal{H}_C^{-1}\partial_k \mathcal{H}_C\right] = \nu.$$

Now, we prove the connection to the Chern-Simons invariant (1.20). Due to the spectral theorem of skew symmetric matrices, the matrix has purely imaginary eigenvalues that occur in complex conjugate pairs $\pm i\lambda_n$ with $\lambda_n > 0$. and we can find an orthogonal transformation $\mathcal{W}$ which transform $X\left(\tilde{k}\right)$ into a block-diagonal Jordan form [178]

$$X_J\left(\tilde{k}\right) = \mathcal{W}X\left(\tilde{k}\right)\mathcal{W}^T = \begin{pmatrix} 0 & \lambda_n\left(\tilde{k}\right) \\ -\lambda_n\left(\tilde{k}\right) & 0 \end{pmatrix}.$$

The Pfaffian of the Jordan form $X_J\left(\tilde{k}\right)$ is easy to evaluate $\mathrm{Pf}\left(X_J\left(\tilde{k}\right)\right) = \prod_n \lambda_n\left(\tilde{k}\right) > 0$. Then, the Pfaffian is given by

$$\mathrm{sgn}\left(\mathrm{Pf}\left(X\left(\tilde{k}\right)\right)\right) = \mathrm{sgn}\left(\mathrm{Pf}\left(X_J\left(\tilde{k}\right)\right)\det\left(\mathcal{W}\right)\right) = \mathrm{sgn}\left(\det\left(\mathcal{W}\right)\right).$$

Since $\mathcal{W}$ is an orthogonal matrix it follows that $\det\left(\mathcal{W}\right) = \pm 1 = e^{-i\theta}$ with $\theta = n\pi$ and $n \in \mathbb{Z}$. Then, it follows that $\theta = i\ln\left(\det\left(\mathcal{W}\right)\right) = i\int dk\partial_k \ln\left(\det\left(\mathcal{W}\right)\right)$.

The Berry connection of the ground state, i.e. the occupied state, was denoted as $\mathcal{A}_-$. It can be shown [22] that

$$\int_{-\frac{\pi}{a}}^{\frac{\pi}{a}} dk\mathrm{Tr}\left(\mathcal{A}_-\right) = \int_0^{\frac{\pi}{a}} dk\mathrm{Tr}\left(\mathcal{A}_- + \mathcal{A}_+\right) = \int_0^{\frac{\pi}{a}} dk\mathrm{Tr}\left(\mathcal{A}\right),$$

where $\mathcal{A} = \mathcal{A}_- + \mathcal{A}_+$ is the Berry connection of all states and $\mathcal{A}_+$ that of the empty states. The Berry connection is given by $\mathcal{A} = U^{-1}\partial_k U$ where U diagonalize the BdG Hamiltonian $U\mathcal{H}_{\mathrm{BdG}}U^{-1}$ and has the form $U = U_M^{-1}\mathcal{W}U_M$ [179]. With the Berry connection $\mathcal{A} = U^{-1}\partial_k U$ the Chern-Simons invariant (1.20) is given by

$$\mathrm{CS}_1 = \frac{i}{2\pi}\int \mathrm{Tr}\left(\mathcal{A}\right) = \frac{i}{2\pi}\int \partial_k \ln\left(\det\left(U\right)\right) = \frac{i}{2\pi}\int \partial_k \ln\left(\det\left(\mathcal{W}\right)\right).$$

B. Valley mixing

The possibility of tunneling between the substrate and the carbon nanotube implies close contact between both systems. With this close contact the carbon nanotube wave functions are affected by the substrate lattice potential, registering an increased electrostatic potential in the vicinity of the contact area. In order to preserve the translational symmetry of the system, which allows us to construct Bloch bands of the bulk nanotube, we treat the electrostatic potential of the substrate as a continuous ridge, adding an on-site potential term to the Hamiltonian of the CNT at the atomic sites in the proximity of the substrate. We have tested several shapes of this ridge with similar values of the resulting valley mixing energy scale, $\Delta_{KK'}$. For all calculations presented here we chose a Gaussian form of $V(\varphi)$, shown in Fig. 2.1(a) and given by

$$V(\varphi) = V_0 \exp(-(\varphi - \varphi_0)^2/\Delta\varphi^2), \tag{B.1}$$

where φ is the angular coordinate of the nanotube atom, V_0 is an arbitrarily chosen maximum height of the substrate's potential, φ_0 is the shift between nanotube coordinates and the CNT-substrate contact line, and $\Delta\varphi$ controls the sharpness of the potential. The influence of the substrate potential for three different nanotube chiralities is illustrated in Fig. 2.1b, where the atoms of the respective CNT's unit cell are colored according to the value of $V(\varphi)$ at this position. In the numerical calculations we assumed $V_0 = 0.4$ eV, $\varphi_0 = 90°$ and $\Delta\varphi = 2.5°$.

We shall now assess the hybridization between different momentum states in the CNT, $|\vec{k}\rangle$ and $|\vec{k'}\rangle$. First, we introduce the basis of LCAO plane waves

$$|\vec{k}, p\rangle = \frac{1}{\sqrt{N_c N_L}} \sum_{\vec{R}} e^{i\vec{k}\cdot\vec{R}} |\vec{R}, p\rangle, \tag{B.2}$$

with

$$\langle\vec{r}|\vec{R}, p\rangle = p_z(\vec{r} - (\vec{R} + \delta\vec{R}_p)),$$

where N_L is the number of CNT unit cells and N_c is the number of lattice sites (graphene's unit cells) in the CNT's unit cell. The index $p = A, B$ denotes the sublattice, $\vec{R}$ are the Bravais lattice vectors and $\delta\vec{R}_p$ denote the shift of the p atom from the center of graphene's unit cell. We approximate the wave functions of electronic p_z orbitals by Dirac deltas

This means that our $V(\varphi)$, which is diagonal in position and hence diagonal in sublattice, will only yield nonzero coupling between LCAO plane waves on the same sublattice,

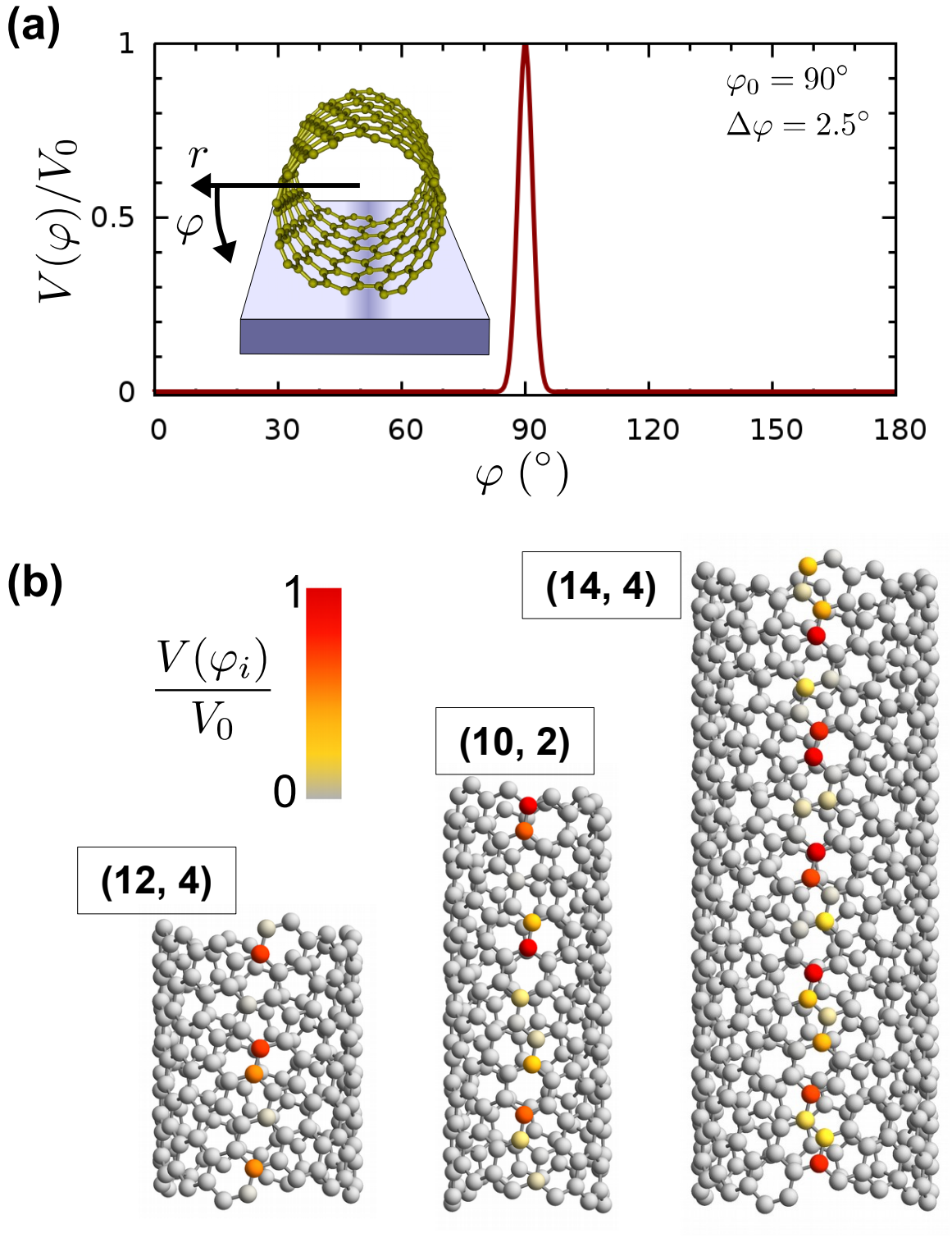

Figure 2.1: (a) The substrate potential $V(\varphi)$ in the Gaussian form. The inset shows the nanotube coordinates in relation to the substrate. (b) Examples of unit cells of nanotubes with different chiralities, with the atoms along the contact area colored by their value of $V(\varphi)$.

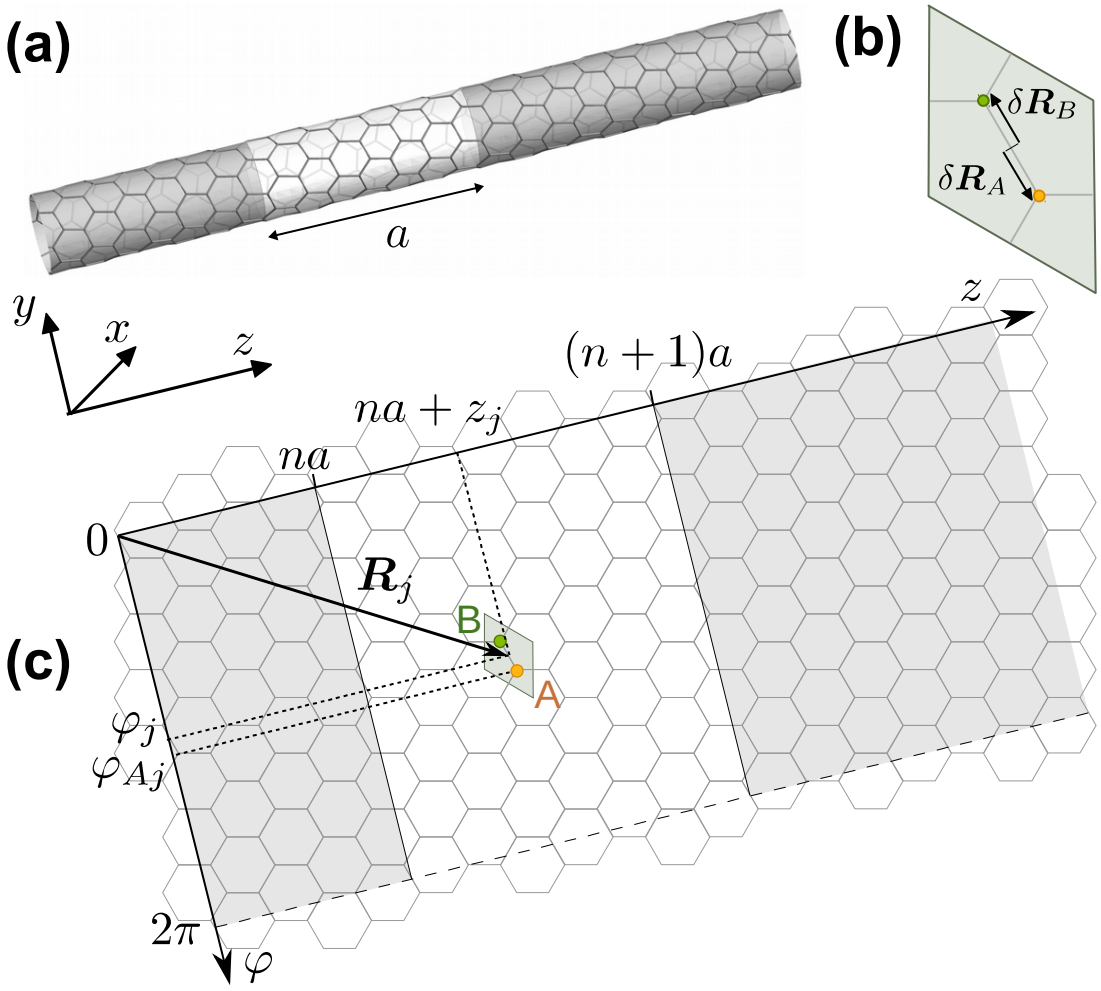

Figure 2.2: (a), Fragment of a (6,2) CNT lattice. The white area marks the translational unit cell of the CNT. (b), The unit cell of graphene, with the A and B sublattice atoms and their shifts $\delta\vec{R}_{A/B}$ from the center of the unit cell. (c), Unrolled nanotube lattice and the quantities used in equations (B.2) and (B.3).

$$V_p(\vec{k},\vec{k'}) = \langle \vec{k}, p|V(\varphi)|\vec{k'}, p\rangle = \frac{1}{N_c N_L}\sum_{\vec{R}} V(\varphi_{\vec{R},p})\, e^{i(\vec{k}-\vec{k'})\cdot\vec{R}}$$
$$= \frac{1}{N_L}\sum_{n=1}^{N_L} e^{i(k-k')na} \times \frac{1}{N_c}\sum_{j=1}^{N_c} V(\varphi_{pj}) e^{i(l_\perp - l'_\perp)\varphi_j} e^{i(k-k')z_j}, \tag{B.3}$$

where in the last step we split the sum over lattice sites $\vec{R}$ into a sum over nanotube unit cells indexed by n and a sum over all atoms in one unit cell, indexed by j. The lattice constant a is the length of the CNT's unit cell, φ_j is the angular coordinate of the lattice site $\vec{R}_j$ and φ_{pj} the angular coordinate of the p sublattice atom belonging to this site. The quantities $l_\perp, l'_\perp$ are the angular momentum components of $\vec{k}$ and $\vec{k'}$, respectively. The summation over the unit cells in an infinite CNT yields the selection rule for the longitudinal momentum, $k = k'$, while the summation over lattice sites determines the strength with which different angular momentum states at the same k are coupled. The angular momenta in the K and K' valley have opposite signs, $l_K = -l_{K'}$. When the l_K appropriate for a given chirality is inserted into (B.3), we obtain the k-independent coupling between LCAO plane waves from K and K' valley,

$$V_{KK',p} = \frac{1}{N_c}\sum_{j=1}^{N_c} V(\varphi_{pj}) e^{2il_K\varphi_j}. \tag{B.4}$$

This quantity is in general complex, with different phases on the A and B sublattice, but with the same absolute value, $|V_{KK',A}| = |V_{KK',B}| =: |V_{KK'}|$, shown in Fig. 2.3. The value of $|V_{KK'}|$ is not sensitive to the precise placement of the CNT on the substrate, i.e. to the value of φ_0, provided the decay angle $\Delta\varphi$ is large enough ($> 2-4°$).

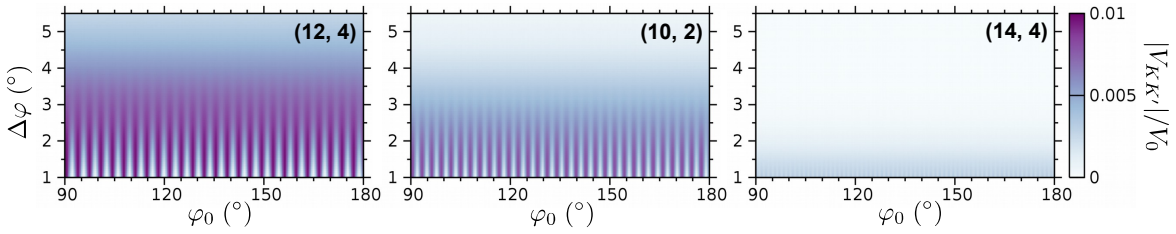

Figure 2.3: Calculated plane wave coupling $|V_{KK'}|$ as a function of the substrate potential parameters $\varphi_0, \Delta\varphi$. It is most effective in nanotubes with shorter unit cells, and in all of them the dependence on φ_0 vanishes beyond some value of $\Delta\varphi$.

Upon conversion to the conduction/valence band basis (i.e. the basis of the CNT Bloch states) we obtain the valley mixing $\Delta_{KK'}(k)$ which is proportional to $|V_{KK'}|$ but depends on the value of k. As a result, the minimum of the bands is displaced from the curvature-shifted Dirac points, as can be seen by comparing the colored and grey lines in Fig. 5.1(b). For the sake of simplicity in the effective model we accomodate this displacement through a

modification of the curvature shift $\Delta k_{\parallel}^{C}$, defined in Section 3.5, and take the value of $\Delta_{KK'}$ to be constant in k, fitted from the width of the K/K' anticrossing in the numerically obtained band structure. This simplification eases greatly the analytical calculation, while keeping the agreement between our numerical and effective model results, as the following sections will show.

C. Analysis of the 1D continuum model

In this appendix, we will show the detailed calculation of the modes of the 1D continuum model introduced in Sec. 4.4. The condition that the determinant of the matrix in Eq. (4.26) is zero is written as

$$\left(\tilde{\mu}_{\tau s}-ips\Delta_0\right)^2-\left[v_F\hbar\left(q+\tau\Delta k_{\parallel}^c\right)+ipcs\Delta_1 q\right]^2+\left[iv_F\hbar\left(k_\perp+\tau\Delta k_\perp^c+s\Delta k_\perp^{SO}\right)-pcs\Delta_1 k_\perp\right]^2 = 0.$$

This is a second-order equation in q, and the two solutions are given by,

$$\begin{aligned} q_{\mp}^{(\tau,s)} =& \frac{1}{c\left(t+ips\Delta_1\right)}\left[\pm\sqrt{\left(\tilde{\mu}_{\tau s}-ips\Delta_0\right)^2-\left[v_F\hbar\left(k_\perp+\tau\Delta k_\perp^c+s\Delta k_\perp^{SO}\right)+ipcs\Delta_1 k_\perp\right]^2}-v_F\hbar\Delta k_{\parallel}^c\right] \\ \simeq& \frac{t-ips\Delta_1}{v_F\hbar t}\left[\pm\sqrt{\tilde{\mu}_{\tau s}^2-\left[v_F\hbar\left(k_\perp+\tau\Delta k_\perp^c+s\Delta k_\perp^{SO}\right)\right]^2}\sqrt{1-2ipsF}-v_F\hbar\tau\Delta k_{\parallel}^c\right], \end{aligned}$$

where the signs $-$ and $+$ in the index of $q_{\mp}^{(\tau,s)}$ correspond to the signs of $+$ and $-$ in the right-hand side, respectively, and

$$F=\frac{1}{\tilde{\mu}_{\tau s}}\frac{\Delta_0+\Delta_1 E_\perp^{(\tau,s)}\left(E_\perp^{(\tau,s)}+\varepsilon_\perp^{(\tau,s)}\right)\frac{\tilde{\mu}_{\tau s}}{t}}{1-\left(E_\perp^{(\tau,s)}\right)^2}.$$

Note that F is of the order of $\Delta_{0/1}/\tilde{\mu}_{\tau s}$. By using the formula

$$\sqrt{a+ib}=\sqrt{\frac{a+\sqrt{a^2+b^2}}{2}}+i\mathrm{sgn}(b)\sqrt{\frac{-a+\sqrt{a^2+b^2}}{2}},$$

for $a,b\in\mathbb{R}$, the term $\sqrt{1-2ipsF}$ becomes,

$$\sqrt{1-2ipsF}=R+iI,$$

where R and I are given by

$$
\begin{aligned}
R &= \sqrt{\frac{1+\sqrt{1+(2psF)^2}}{2}} \simeq \sqrt{\frac{1+1+\frac{1}{2}(2psF)^2}{2}} \simeq 1, \\
I &= \mathrm{sgn}(-2psF)\sqrt{\frac{-1+\sqrt{1+(2psF)^2}}{2}} \\
&\simeq -ps\mathrm{sgn}(F)\sqrt{\frac{-1+1+\frac{1}{2}(2psF)^2}{2}} = -psF.
\end{aligned}
$$

Then, for the real part of $q_{\pm}^{(\tau,s)}$, we get

$$
\begin{aligned}
\mathrm{Re}\left(q_{\pm}^{(\tau,s)}\right) &= \mp\frac{tR+ps\Delta_1 I}{v_F\hbar t}\sqrt{\tilde{\mu}_{\tau s}^2 - \left[v_F\hbar\left(k_\perp+\tau\Delta k_\perp^c+s\Delta k_\perp^{SO}\right)\right]^2} - \tau\Delta k_\parallel^c \\
&\simeq \pm\sqrt{\left(\frac{\tilde{\mu}_{\tau s}}{v_F\hbar}\right)^2 - \left(k_\perp+\tau\Delta k_\perp^c+s\Delta k_\perp^{SO}\right)^2} - \tau\Delta k_\parallel^c = k_{\pm}^{(\tau,s)}.
\end{aligned}
$$

On the other hand, for the imaginary part of $q_{\pm}^{(\tau,s)}$,

$$
\mathrm{Im}\left(q_{\pm}^{(\tau,s)}\right) = \frac{1}{v_F\hbar}\left(\pm\frac{tI-ps\Delta_1 R}{t}|\tilde{\mu}_{\tau s}|\sqrt{1-\left(E_\perp^{(\tau,s)}\right)^2} + ps\tau\frac{\Delta_1}{t}v_F\hbar\Delta k_z\right),
$$

and the numerator of the first term in the right-hand side is calculated as,

$$
tI - ps\Delta_1 R = \frac{-ps}{1-\left(E_\perp^{(\tau,s)}\right)^2}\left[\frac{t}{\tilde{\mu}_{\tau s}}\Delta_0 + \left(1+E_\perp^{(\tau,s)}\varepsilon_\perp^{(\tau,s)}\right)\Delta_1\right].
$$

Then, we get

$$
\begin{aligned}
\mathrm{Im}\left(q_{\pm}^{(\tau,s)}\right) &= \mp\frac{ps}{v_F\hbar}\left\{\frac{1}{\sqrt{1-\left(E_\perp^{(\tau,s)}\right)^2}}\left[\frac{t}{\tilde{\mu}_{\tau s}}\Delta_0 + \left(1+E_\perp^{(\tau,s)}\varepsilon_\perp^{(\tau,s)}\right)\Delta_1\right]\frac{|\tilde{\mu}_{\tau s}|}{t} \mp \tau\Delta_1\varepsilon_\parallel^{(\tau,s)}\frac{\tilde{\mu}_{\tau s}}{t}\right\} \\
&= \mp\frac{ps}{v_F\hbar}\frac{\mathrm{sgn}(\tilde{\mu}_{\tau s})}{\sqrt{1-\left(E_\perp^{(\tau,s)}\right)^2}}\left[\Delta_0 + \Delta_1\frac{\tilde{\mu}_{\tau s}}{t}\left(1+E_\perp^{(\tau,s)}\varepsilon_\perp^{(\tau,s)} \mp \mathrm{sgn}(\tilde{\mu}_{\tau s})\tau\varepsilon_\parallel^{(\tau,s)}\sqrt{1-\left(E_\perp^{(\tau,s)}\right)^2}\right)\right] \\
&= \mp\frac{ps}{v_F\hbar}\frac{\mathrm{sgn}(\tilde{\mu}_{\tau s})}{\sqrt{1-\left(E_\perp^{(\tau,s)}\right)^2}}\frac{\varepsilon_{g,\pm}^{(\tau,s)}}{2},
\end{aligned}
$$

which is the expression given in Eq. (4.28).

List of Figures

List of Tables

References

[1] G. E. Volovik, *The Universe in a Helium Droplet* (Oxford University Press, 2003).

[2] X.-G. Wen, *Quantum Field Theory of Many-Body Systems: From the Origin of Sound to an Origin of Light and Electrons* (Oxford University Press, 2007).

[3] L. D. Landau, Sov. Phys. JETP **5**, 101 (1957).

[4] L. D. Landau, Sov. Phys. JETP **3**, 920 (1957).

[5] W. Nolting, *Grundkurs Theoretische Physik 7: Viel-Teilchen-Theorie* (Springer-Lehrbuch, 2009).

[6] Y. Jompol *et al.*, Science **325**, 597 (2009).

[7] L. D. Landau, Zh. Eksp. Teor. Fiz. **7**, 19 (1937).

[8] V. L. Ginzburg and L. D. Landau, Zh. Eksp. Teor. Fiz. **20**, 1064 (1950).

[9] K. v. Klitzing, G. Dorda, and M. Pepper, Phys. Rev. Lett. **45**, 494 (1980).

[10] D. C. Tsui, H. L. Stormer, and A. C. Gossard, Phys. Rev. Lett. **48**, 1559 (1982).

[11] D. J. Thouless *et al.*, Phys. Rev. Lett. **49**, 405 (1982).

[12] C. L. Kane and E. J. Mele, Phys. Rev. Lett. **95**, 226801 (2005).

[13] B. A. Bernevig and S.-C. Zhang, Phys. Rev. Lett. **96**, 106802 (2006).

[14] M. KÃűnig *et al.*, Science **318**, 766 (2007).

[15] V. L. Berezinskii, Sov. Phys. JETP **32**, 493 (1971).

[16] J. M. Kosterlitz and D. J. Thouless, Journal of Physics C. Solid State Physics **6**, 1181 (1973).

[17] P. M. Chaikin, *Principles of Condensed Matter Physics* (Cambridge University Press, 2000).

[18] M. Nakahara, *Geometry, Topology and Physics, Second Edition* (CRC Press, 2003).

[19] T. Frankel, *The Geometry of Physics: An Introduction* (Cambridge University Press, 2011).

[20] C. Nash and S. Sen, *Topology and Geometry for Physicists* (Dover Books on Mathematics, 2011).

[21] V. Mourik *et al.*, Science **336**, 1003 (2012).

[22] C.-K. Chiu *et al.*, Rev. Mod. Phys. **88**, 035005 (2016).

[23] E. Majorana, Nuovo Cimento **5**, 171 (1937).

[24] A. Y. Kitaev, Phys. Usp. **44**, 131 (2001).

[25] L. Fu and C. L. Kane, Phys. Rev. Lett. **100**, 096407 (2008).

[26] J. Alicea, Phys. Rev. B **81**, 125318 (2010).

[27] R. M. Lutchyn, J. D. Sau, and S. D. Sarma, Phys. Rev. Lett. **105**, 077001 (2010).

[28] Y. Oreg, G. Refael, and F. von Oppen, Phys. Rev. Lett. **105**, 177002 (2010).

[29] J. D. Sau *et al.*, Phys. Rev. Lett. **104**, 040502 (2010).

[30] J. Knolle *et al.*, Pyhs. Rev. Lett. **112**, 207203 (2014).

[31] S. Nadj-Perge *et al.*, Science **346**, 602 (2014).

[32] R. Lutchyn *et al.*, Nature Reviews Materials **3**, 52 (2018).

[33] Ã. GÃijl *et al.*, Nature Nanotechnology **13**, 192 (2018).

[34] H. Zhang *et al.*, Nature **556**, 74 (2018).

[35] M. T. Deng *et al.*, Science **354**, 1557 (2016).

[36] S. M. Albrecht *et al.*, Nature **531**, 206 (2016).

[37] D. A. Ivanov, Pyhs. Rev. Lett. **86**, 268 (2001).

[38] J. K. Pachos, *Introduction to Topological Quantum Computation* (Cambridge University Press, 2012).

[39] T. D. Stanescu, *Introduction to Topological Quantum Matter and Quantum Computation* (CRC Press, 2016).

[40] M. M. Shulaker *et al.*, Nature **501**, 526 (2013).

[41] E. Prada, R. Aguado, and P. San-Jose, Phys. Rev. B **96**, 085418 (2017).

[42] M. V. Berry, Proc. Roy. Soc. London A **392**, 45 (1984).

[43] F. Wilczek and A. Zee, Phys. Rev. Lett. **52**, 2111 (1984).

[44] Y. Aharonov and J. Anandan, Phys. Rev. Lett. **58**, 1593 (1987).

[45] A. Bohm *et al.*, *The Geometric Phase in Quantum Systems* (Springer, 2003).

[46] G. P. Mikitik and Y. V. Sharlai, Phys. Rev. Lett. **82**, 2147 (1999).

[47] G. P. Mikitik and Y. V. Sharlai, Phys. Rev. Lett. **93**, 106403 (2004).

[48] J. Zak, Phys. Rev. Lett. **62**, 2747 (1989).

[49] Q. Niu and D. J. Thouless, J. Phys. A: Math. Gen. **17**, 2453 (1984).

[50] D. J. Thouless, Phys. Rev. B **27**, 6083 (1983).

[51] R. D. King-Smith and D. Vanderbilt, Phys. Rev. B **47**, 1651 (1993).

[52] G. Ortiz and R. M. Martin, Phys. Rev. B **49**, 14202 (1994).

[53] E. P. Wigner, *Group theory: And its application to the quantum mechanics of atomic spectra* (Academic Press, 1959).

[54] J. B. G. Akemann and P. D. Francesco, *The Oxford Handbook of Random Matrix Theory* (Oxford Handbooks, 2005).

[55] G. D. M. S. Dresselhaus and A. Jorio, *Group Theory: Application to the Physics of Condensed Matter* (Springer, 2007).

[56] L. Fu and C. L. Kane, Phys. Rev. B **76**, 045302 (2007).

[57] J. C. Y. Teo, L. Fu, and C. L. Kane, Phys. Rev. B **78**, 045426 (2008).

[58] L. Fu and E. Berg, Phys. Rev. Lett. **105**, 097001 (2010).

[59] T. L. Hughes, E. Prodan, and B. A. Bernevig, Phys. Rev. B **83**, 245132 (2011).

[60] A. P. Schnyder and S. Ryu, Phys. Rev. B **84**, 060504(R) (2011).

[61] K. Shiozaki and M. Sato, Phys. Rev. B **90**, 165114 (2014).

[62] K. Shiozaki, M. Sato, and K. Gomi, Phys. Rev. B **93**, 195413 (2016).

[63] B. Bradlyn *et al.*, Nature **547**, 298 (2017).

[64] K. H. A. Kramers, Proc. Amsterdam Acad. **33**, 959 (1930).

[65] E. P. Wigner, *Proceedings of the Conference on Neutron Physics by Time-of-Flight* (Oak Ridge National Laboratory, 1965).

[66] E. P. Wigner, SIAM Rev. **9**, 1 (1967).

[67] F. J. Dyson, J. Math. Phys. **3**, 140 (1962).

[68] J. J. M. Verbaarschot, Phys. Rev. Lett. **72**, 2531 (1994).

[69] J. J. M. Verbaarschot and T. Wettig, Annu. Rev. Nucl. Part. Sci. **50**, 343 (2000).

[70] A. Altland and M. R. Zirnbauer, Phys. Rev. B **55**, 1142 (1997).

[71] P. Heinzner, A. H. Huckleberry, and M. R. Zirnbauer, Commun. Math. Phys. **257**, 725 (2005).

[72] S. Helgason, *Differential Geometry, Lie Groups and Symmetric Spaces* (Oxford University Press, 2001).

[73] M. Caselle, cond-mat/9610017 (1996).

[74] E. de Faria and W. de Melo, *Mathematical Aspects of Quantum Field theory* (Cambridge University Press, 2010).

[75] A. P. Schnyder *et al.*, Phys. Rev. B **78**, 195125 (2008).

[76] K. B. Efetov, *Supersymmetry in Disorder and Chaos* (Cambridge University Press, 1999).

[77] F. Wegner, Z. Phys. B **35**, 207 (1979).

[78] P. W. Anderson, Phys. Rev. **109**, 1492 (1959).

[79] E. Abrahams, *50 Years of Anderson Localization* (World Scientific Pub Co Inc, 2010).

[80] B. Simon, Phys. Rev. Lett. **51**, 2167 (1983).

[81] X.-G. Wen and A. Zee, Nucl. Phys. B **316**, 641 (1989).

[82] M. Sato *et al.*, Phys. Rev. B **83**, 224511 (2011).

[83] A. P. Schnyder and S. Ryu, Phys. Rev. B **84**, 060504(R) (2011).

[84] S. Ryu *et al.*, New J. Pjys. **12**, 065010 (2010).

[85] J. Bardeen, L. N. Cooper, and J. R. Schrieffer, Phys. Rev. **108**, 1175 (1957).

[86] M. Tinkham, *Introduction to Superconductivity* (Dover Books, 2004).

[87] H. Bruss and K. Flensberg, *Many-Body Quantum Theory in Condensed Matter Physics* (Oxford University Press, 2004).

[88] N. N. Bogoliubov, Sov. Phys. JETP **7**, 47 (1958).

[89] A. Leggett, *Quantum Liquids: Bose Condensation and Cooper Pairing in Condensed-Matter Systems* (Oxford University Press, 2006).

[90] G. E. Blonder, M. Tinkham, and T. M. Klapwijk, Phys. Rev. B **25**, 4515 (1982).

[91] J. Alicea, Rep. Prog. Phys. **75**, 076501 (2012).

[92] Y. Takane and R. Ando, J. Phys. Soc. Jpn. **83**, 014706 (2014).

[93] T. D. Stanescu *et al.*, Phys. Rev. B **81**, 241310(R) (2010).

[94] J. D. Sau *et al.*, Phys. Rev. B **82**, 214509 (2010).

[95] A. C. Potter and P. A. Lee, Phys. Rev. B **83**, 184520 (2011).

[96] P. A. M. Dirac, Proc. R. Soc. A **117**, 610 (1928).

[97] S. Weinberg, *The Quantum Theory of Fields, Volume 1: Foundations* (Cambridge University Press, 2005).

[98] M. E. Peskin and D. V. Schroeder, *An Introduction To Quantum Field Theory* (Westview Press, 1995).

[99] M. Maggiore, *A Modern Introduction to Quantum Field Theory* (Oxford University Press, 2005).

[100] T. M. Rice and M. Sigrist, J. Phys.: Condens. Matter **7**, 643 (1995).

[101] K. Ishida *et al.*, Nature **396**, 658 (1998).

[102] Y. Ueno, A. Yamakage, and M. Sato, Phys. Rev. Lett. **111**, 087002 (2013).

[103] M. Sato and Y. Ando, Rep. Prog. Phys **80**, 076501 (2017).

[104] L. Fu and C. L. Kane, Phys. Rev. B **79**, 161408 (2009).

[105] S. Nadj-Perge *et al.*, Phys. Rev. B **88**, 020407 (2013).

[106] R. Winkler, *Spin-orbit Coupling Effects in Two-Dimensional Electron and Hole Systems* (Springer, 2010).

[107] S. Tewari and J. D. Sau, Phys. Rev. Lett. **109**, 150408 (2012).

[108] S. Tewari *et al.*, Phys. Rev. B **86**, 024504 (2012).

[109] J. Klinovaja and D. Loss, Phys. Rev. B **86**, 085408 (2012).

[110] B. Braunecker *et al.*, Phys. Rev. B **82**, 045127 (2010).

[111] S. Gangadharaiah *et al.*, Phys. Rev. Lett. **107**, 036801 (2011).

[112] T.-P. Choy *et al.*, Phys. Rev. B **84**, 195442 (2011).

[113] M. Kjaergaard, K. WÃűlms, and K. Flensberg, Phys. Rev. B **85**, 020503(R) (2012).

[114] K. Flensberg, Phys. Rev. B **82**, 180516(R) (2010).

[115] C.-X. Liu *et al.*, Phys. Rev. B **96**, 075161 (2017).

[116] E. H. H. Lee *et al.*, Phys. Rev. Lett. **109**, 186802 (2012).

[117] R. Saito, G. Dresselhaus, and M. S. Dresselhaus, *Physical Properties of Carbon Nanotubes* (Imperial College Press, London, 1998).

[118] E. A. Laird *et al.*, Rev. Mod. Phys. **87**, 703 (2015).

[119] B. Uchoa and A. H. C. Neto, Phys. Rev. Lett. **98**, 146801 (2007).

[120] A. H. C. Neto *et al.*, Rev. Mod. Phys. **81**, 109 (2009).

[121] S. Iijima, Nature Lett. **354**, 56 (1991).

[122] M. Niklas, *Current and noise properties of interacting nanojunctions* (PhD thesis, 2018).

[123] D. P. DiVencenzo and E. Mele, Phys. Rev. B **29**, 1685 (1984).

[124] P. Wallace, Phys. Rev. **71**, 622 (1947).

[125] V. N. Kotov *et al.*, Rev. Mod. Phys. **81**, 109 (2009).

[126] D. C. Elias *et al.*, Nature **7**, 701 (2011).

[127] T. Ando, J. Phys. Soc. Jpn. **69**, 1757 (2000).

[128] W. Izumida, K. Sato, and R. Saito, J. Phys. Soc. Jpn. **78**, 074707 (2009).

[129] F. Kuemmeth *et al.*, Nature **452**, 448 (2008).

[130] J. Klinovaja *et al.*, Phys. Rev. B **84**, 085452 (2011).

[131] M. Niklas, *Electronic spectra of ultra-clean carbon nanotubes in a magnetic fields* (Bachelor thesis, 2013).

[132] N. Hamada, S. Sawada, and A. Oshiyama, Phys. Rev. Lett. **68**, 1579 (1992).

[133] R. Saito, M. Fujita, and G. Dresselhaus, Appl. Phys. Lett. **60**, 2204 (1992).

[134] C. L. Kane and E. J. Mele, Phys. Rev. Lett. **78**, 1932 (1997).

[135] M. del Valle, M. Marganska, and M. Grifoni, Phys. Rev. B **84**, 165427 (2011).

[136] G. A. Steele *et al.*, Nat. Commun. **4**, 1573 (2013).

[137] M. Marganska, P. Chudzinski, and M. Grifoni, Phys. Rev. B **92**, 075433 (2015).

[138] D. TomÃąnek and S. G. Louise, Phys. Rev. B **37**, 8327 (1988).

[139] S. H. Jhang *et al.*, Phys. Rev. B **82**, 041404 (2010).

[140] W. Izumida *et al.*, Phys. Rev. B **93**, 195442 (2016).

[141] W. Liang, M. Bockrath, and H. Park, Phys. Rev. Lett. **88**, 126801 (2002).

[142] D. H. Cobden and J. Nygard, Phys. Rev. Lett. **89**, 046803 (2002).

[143] R. Peierls, Z. Phys. **80**, 763 (1933).

[144] Y. Aharonov and D. Bohm, Phys. Rev. **115**, 485 (1959).

[145] W. Izumida, R. Okuyama, and R. Saito, Phys. Rev. B **91**, 235442 (2015).

[146] C. T. White, D. H. Robertson, and J. W. Mintmire, Phys. Rev. B **47**, 6596 (1993).

[147] R. Okuyama, W. Izumida, and M. Eto, J. Phys. Soc. Jpn. **86**, 013702 (2017).

[148] A. M. Black-Schaffer and C. Honerkamp, J. Phys. Condens. Matter **26**, 423301 (2014).

[149] H. B. Heersche *et al.*, Nature **446**, 56 (2007).

[150] A. Y. Kasumov *et al.*, Science **284**, 1508 (1999).

[151] A. F. Morpurgo *et al.*, Science **286**, 263 (1999).

[152] L. G. Herrmann *et al.*, Phys. Rev. Lett. **104**, 026801 (2010).

[153] S. D. Franceschi *et al.*, Nat. Nanotech. **5**, 703 (2010).

[154] J.-D. Pillet *et al.*, Nat. Phys. **6**, 965 (2010).

[155] B.-K. Kim *et al.*, Phys. Rev. Lett. **110**, 076803 (2013).

[156] J.-D. Pillet *et al.*, Phys. Rev. B **88**, 045101 (2013).

[157] J. Schindele *et al.*, Phys. Rev. B **89**, 045422 (2014).

[158] A. Kumar *et al.*, Phys. Rev. B **89**, 075428 (2014).

[159] J. Gramich, A. Baumgartner, and C. SchÃűnenberger, Phys. Rev. Lett. **115**, 216801 (2015).

[160] K. L. Hur, S. Vishveshwara, and C. Bena, Phys. Rev. B **77**, 041406 (2008).

[161] E. Polizzi, Phys. Rev. B **79**, 115112 (2009).

[162] L. Chico, M. P. Lopez-Sancho, and M. C. Munoz, Phys. Rev. Lett. **93**, 176402 (2004).

[163] D. Huertas-Hernando, F. Guinea, and A. Brataas, Phys. Rev. B **74**, 155426 (2006).

[164] A. Haim *et al.*, Phys. Rev. B **94**, 161110 (2016).

[165] D. N. Sheng *et al.*, Phys. Rev. Lett. **97**, 036808 (2006).

[166] L. Fu, C. L. Kane, and E. J. Mele, Phys. Rev. Lett. **98**, 106803 (2007).

[167] J. D. Sau and S. Tewari, Phys. Rev. B **88**, 054503 (2013).

[168] X. Xi *et al.*, Nat. Phys. **12**, 139 (2016).

[169] J. Gramich, A. Baumgartner, and C. SchÃűnenberger, Appl. Phys. Lett. **108**, 172604 (2016).

[170] J. Cao, Q. Wang, and H. Dai, Nat. Mater. **4**, 745 (2005).

[171] L.-M. Peng *et al.*, AIP Adv. **2**, 041403 (2012).

[172] H. Ajiki and T. Ando, J. Phys. Soc. Jpn. **62**, 1255 (1993).

[173] C. L. Huang *et al.*, Phys. Rev. B **76**, 212504 (2007).

[174] J. S. Lim, R. Lopez, and L. Serra, EPL (Europhysics Letters) **103**, 37004 (2013).

[175] J. Osca, R. López, and L. Serra, The European Physical Journal B **87**, 84 (2014).

[176] A. Manolescu *et al.*, Phys. Rev. B **96**, 125435 (2017).

[177] A. Schuray, A. L. Yeyati, and P. Recher, arXiv:condmat/1807.05176 (2018).

[178] B. Zumino, J. Math. Phys. **3**, 1055 (1962).

[179] J. C. Budich and E. Ardonne, Phys. Rev. B **88**, 075419 (2013).